Accretion in High Mass X-ray binaries

Manousakis, Antonios

Université de Genève
Département d'astronomie

Faculté des Sciences
Dr Roland Walter

Accretion in High Mass X-ray Binaries

Thèse

**présentée à la Faculté des sciences de l'Université de Genève
pour obtenir le grade de Docteur ès sciences,
mention Astronomie et Astrophysique**

par

Antonios MANOUSAKIS

de

Canée, Crète (Grèce)

Thèse N° 4395

**Genève
ISDC & Observatoire de Genève
2011**

UNIVERSITÉ
DE GENÈVE

FACULTÉ DES SCIENCES

Doctorat ès sciences
Mention astronomie et astrophysique

Thèse de *Monsieur Antonios MANOUSAKIS*

intitulée :

"Accretion in High Mass X-ray Binaries"

La Faculté des sciences, sur le préavis de Messieurs R. WALTER, docteur et directeur de thèse (Département d'astronomie), Th. COURVOISIER, professeur ordinaire (Département d'astronomie), G. MEYNET, professeur ordinaire (Département d'astronomie) et J. WILMS, professeur (Astronomisches Institute der Universität Erlangen-Nürnberg, Bamberg, Deutschland), autorise l'impression de la présente thèse, sans exprimer d'opinion sur les propositions qui y sont énoncées.

Genève, le 21 décembre 2011

Thèse - 4395 -

Le Doyen, Jean-Marc TRISCONE

N.B.- La thèse doit porter la déclaration précédente et remplir les conditions énumérées dans les "Informations relatives aux thèses de doctorat à l'Université de Genève".

The publications contained in this work are listed in page 118.

ὡς πρὸς ἀστρονομίαν ὄμματα πέπηγεν,
ὡς πρὸς ἐναρμόνιον φορὰν ὦτα παγῆναι,
καὶ αὗται ἀλλήλων ἀδελφαί τινες αἱ ἐπιστῆμαι εἶναι

Πλάτων, Πολιτεία

the eyes are framed for astronomy
so the ears are framed for the movements of harmony
and these are in some sort kindred sciences

Plato, Republic

Résumé en français

Cette thèse porte sur le travail effectué à l'ISDC pendant la période de septembre 2007 à octobre 2011.

Les binaires X de grande masse sont des systèmes binaires formés d'un trou noir ou d'une étoile de neutrons accrétant de la matière provenant d'une étoile massive compagnion. Cette dernière peut être une étoile Be (p. ex. XMMU J054134-7682550) ou une étoile OB super-géante (le système est alors identifié comme un sgHMXB).

On distingue plusieurs types de sgHMXB en fonction de leurs propriétés observées en rayons X: les systèmes persistants classiques (p. ex. Vela X-1) ou très absorbés (p. ex. IGR J17252-3616), ainsi que les systèmes transitoires rapides (identifiés comme un SFXT). Les SFXTs montrent une variabilité extrême sur des échelles de temps de la minute à quelques heures, séparées par des périodes d'inactivité qui peuvent durer plusieurs semaines.

Nous avons observé le système binaire Be XMMU $J054134-7682550$ du grand nuage de Magellan lors d'une éruption en août 2007, avec les satellites $XMM-Newton$ et $RXTE$. Grâce à une raie cyclotron, nous avons pu déterminer la taille de la magnétosphère du pulsar. Nous avons observé d'intenses variations dans le flux de rayons X à faible énergie (<2 keV) que nous avons interprétées par le reflet de l'émission de rayons X énergétique émis proche du pulsar sur la face interne du disque d'accrétion.

Nous avons étudié la binaire X super-géante très absorbée IGR $J17252-3616$ avec $XMM-Newton$ pour un total de 10 observations. Une absorption importante est observée tout au long de l'orbite avec d'importantes variations à une phase de 0.4. La largeur équivalente de la raie du Fer Kα varie aussi, mais les autres paramètres spectraux varient peu le long de l'orbite. Combinant ces observations avec un modele du vent stellaire de l'étoile massive, nous avons pu montrer que la variabilité observée suggère une vitesse de vent significativement plus faible qu'attendu usuellement pour ces étoiles.

Pour étudier cette hypothèse, nous avons modélisé le système à l'aide du code hydrodynamique VH1. Nous avons calculé une grille de simulations pour des taux de perte de masse de $(0.2-5)\times10^{-6}$ $M_\odot$ yr^{-1} et pour des vitesses terminales typiques et basses. Il s'avère qu'une vitesse terminale faible ($\upsilon_\infty = 500$ km s^{-1}) et une perte de masse modérée sont nécessaires pour reproduire les observations. Pour une vitesse faible, la variabilité de l'absorption dépend fortement de la masse de l'étoile de neutrons. Les observations requièrent une masse de 1.9-2.0 $M_\odot$, qui contraint l'équation d'état de la matière ultra-dense.

Ce manuscrit est organisée en 3 parties. La première partie introduit les sources et les instruments qui ont été utilisés pour les étudier, et passe en revue certaines connaissances théoriques liées à l'accrétion et aux vents stellaires. La deuxième partie présente les résultats observationels qui sont déjà publiés ainsi que les simulations hydrodynamiques. La troisième partie décrit d'autres articles et travaux réalisés au cours de mon travail à l'ISDC.

Abstract in English

This thesis is based on the work carried out at the ISDC Data Center for Astrophysics part of the Observatoire de Genève and Université de Genève between September 2007 and

October 2011.

High Mass X-ray Binaries (HMXBs) consist of a massive OB star and either a black hole (BH) or a neutron star (NS) orbiting each other. The massive donor can be either a Be star forming a Be/X-ray binary (e.g., XMMU $J054134.7-682550$) or a supergiant OB star forming a sgHMXB. Based on their X-ray properties, sgHMXB can be classified as classical, obscured (e.g., IGR J17252-3616), or supergiant fast X-ray transient (SFXT). Both classical and obscured sgHMXB are persistent sources with minor variation in their X-ray flux. In contrast, SFXTs show extreme variability on timescales of minutes to hours, separated by periods of quiescence that can last for of several weeks.

We have observed the Be/X-ray binary system XMMU $J054134.7-682550$ in the LMC with $XMM-Newton$ and $RXTE$ during a type II outburst in August 2007. Thanks to the detection of a cyclotron feature around 10 keV, we were able to constrain the magnetosphere of the pulsar. Remarkable soft X-ray (< 2 keV) variation were observed and interpreted as the reprocessing of hard X-rays at the inner edge of the accretion disk.

We have observed the obscured sgHMXB IGR $J17252-3616$ with $XMM-Newton$ for a total of 10 observations, covering the orbital phase space. The spectra of this source were always significantly absorbed and showed remarkable variations of the absorbing column density and of the equivalent width of the Fe Kα line. Other spectral parameters (e.g. cut-off energy, photon index, iron line energy) did not vary throughout the orbit. The observed variability suggests that the wind velocity is significantly lower than expected in classical sgHMXBs.

To study this hypothesis, we have modeled the system with the hydrodynamical code VH1. We implemented a grid of simulation for weak (2×10^{-7} $M_\odot$ yr^{-1}) to strong (5×10^{-6} $M_\odot$ yr^{-1}) mass-loss rates and for typical ($v_\infty = 1200$ km s^{-1}) and low ($v_\infty = 500$ km s^{-1}) terminal velocities. It turned out a low terminal wind velocity and a moderate mass loss rate are needed to reproduce the observed properties of this system.

Details of the variability of the absorbing column density with orbital phase strongly depend on the mass of the neutron star. The observations require a wind terminal velocity of $v_\infty = 500$ km s^{-1}, a mass-loss rate of 10^{-6} $M_\odot$ yr^{-1} and a neutron star mass of $M_X = 1.9-2.0$ $M_\odot$. Such a large neutron star mass constrains the equation of state of hyper-dense matter.

The two observational papers (XMMU $J054134.7-682550$ and IGR $J17252-3616$) have been published. The hydrodynamical modeling will be reported in a paper in preparation.

This manuscript is organized in 3 parts. The first part introduces the sources and the instruments that have been used and reviews some theoretical background related to accretion and stellar wind structures. The second part presents the observational results that were already published as well as the hydrodynamical simulation which were conducted. The third part describes other papers and work performed at the ISDC during these four years.

Acknowledgements

It is obvious that the work presented in this thesis has been influenced by many people. They spent their time and provided feedback on a number of questions regarding the topics included in this thesis. I would like to thank all of them for their support.

I am indebted to Dr Roland Walter, my supervisor, for his guidance, time, encouragement, and support over all these years. He not only served as my supervisor but also encouraged and challenged me throughout my academic training. I find myself very lucky for this interaction, resampling the connection between the mentor and protégé.

I want to express my gratitude to Prof. John Blondin (North Carolina) for his guidance on the issues of computational fluid dynamics. He has always time to spent on my (naive) questions and provide a useful guidance throughout the last quarter of my Ph.D. Studies. I am glad for this collaboration and am looking forward for more to come.

In addition, my deepest thanks are going to Prof. Thierry Courvoisier (Geneva) who always has had an open eye on my work although he prefers to work on extragalactic objects.

I would like to thank Prof. Jörn Wilms (Erlangen-Nürnberg) and Prof. Georges Meynet (Geneva) for accepting being member of the jury. Moreover, I would like to thank them for their time for reading and providing feedback on my thesis.

Indeed the warmth of the Local Working Environment (LWE) is a key feature. The life at the office P106 could not be better without Daniela and Enrico. I enjoyed our discussions with Enrico on many aspect of science and not only. However, I realized that I can bake or burn sweets thanks to Daniela and GCC (Geneva Cookie Conspiracy).

Working at a french speaking country, without speaking french, life can be very tricky. I am grateful to the ISDC ladies, Martine, Franca, and Marie-Claude for helping me though all the procedures and bureaucracy here. I do not know if I could survive without their support.

In addition, I would like to thank all people at ISDC. From those in Pavillon for the coffee breaks to those at Castle and Barn although that I did not spend much time there.

Last but not least, I would like to thank those people outside Switzerland and ISDC. I would like to thank my family, friends from Greece, and those who are now spread around the globe.

Contents

PART I: Introduction

Chapter 1

High Mass X-ray Binaries

1.1 General view

X-Ray binaries (XRBs) are accreting systems hosting a star and a compact object(White, Nagase & Parmar 1995; Tauris & van den Heuvel 2006). Giacconi *et al.* (1962) serendipitously discovered the first of these sources, Sco X-1, during an X-ray observation of the Moon. The accretion and emission mechanisms depend on the nature of the companion star and of the compact object.

There are three types of compact objects that can take part in a binary system: a white dwarf (WD), a neutron star (NS), or a black hole (BH). Figure 1.1 shows the different types of XRBs depending on the nature of the compact object. If the compact object is either a NS or a WD, it can feature a strong surface magnetic field $B \sim 10^{12-15}$ Gauss, or $B \sim 10^{6}$ Gauss, respectively. The magnetic field influences the accretion flow, by driving matter to the *accreting column*. The strong magnetic field in NS also imprints the X-ray spectrum emitted by the compact object, in the form of absorption/emission lines, referred to as *cyclotron lines*.

A further distinction is based on the mass (and therefore the spectral type) of the companion star. If the mass of the companion is more than 10 $M_{\odot}$ the system is referred to as a High Mass X-ray Binary (HMXB). If the mass of the companion star is less than 1 $M_{\odot}$ then it is referred to as a Low Mass X-ray binary (LMXB). Finally, if the mass of the companion falls in between 1 $M_{\odot}$ and 10 $M_{\odot}$ then it is referred to as an Intermediate Mass X-ray Binary (IMXB). In this thesis we focus on the class of HMXBs, hosting high mass, early type stellar companion (OB spectral classification). HMXBs can be further divided by the luminosity class of the companion star. If the companion is a dwarf of the main sequence (luminosity class V-III) the system is known as a Be/X-ray Binary (or BeX). If the companion is a supergiant (luminosity class I-II) the system is known as a sgHMXBs.

1.2 Be/X-ray binaries

In Be/X-ray binaries the optical companions are Be stars (Slettebak 1988). Be stars are dwarf, fast-rotating stars, featuring spectral emission lines[1]. The best studied lines are those of hydrogen (e.g. Balmer series) but Be stars also show He and Fe in emission (Hanuschik 1996). Be stars also show an infrared (IR) excess, that is larger than that emitted by an absorption-line B-type star of the same spectral type. The IR excess is

[1]The letter 'e' on their spectral classification stands for line in emission.

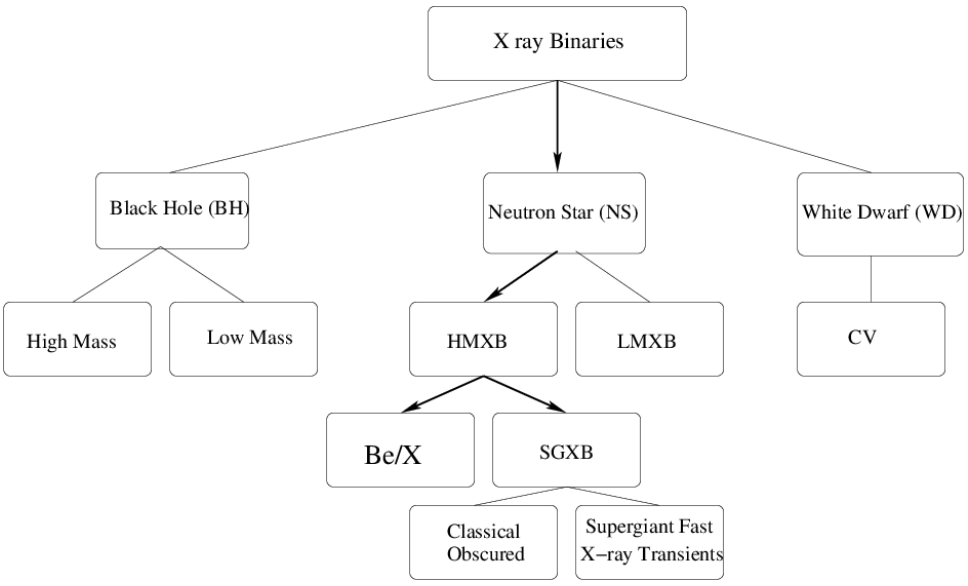

Figure 1.1: Classification of the X-ray binaires based on the nature of the compact object.

related to the presence of a circumstellar disk expelled by the star (equatorial stellar winds). In Be/X-ray binary systems, the neutron star is orbiting in an eccentric orbit (see fig 1.2) crossing the expelled material regularly. This triggers more accretion and therefore more X-ray activity. Be/X-ray binaries can show three different types of activity.

- *Type I (or normal) outburst*: This re-occurring outburst is related to the periastron passage of the neutron star. At its closest proximity to the Be star, the NS is passing through the circumstellar disk. The frequency of these outbursts is related to the orbital period of the source. All Be/X-ray binaries produce type I outbursts. The peak luminosity in X-rays is $L_X \sim 10^{36} - 10^{37}$ erg s^{-1}.

- *Type II (or giant) outburst*: This event is rare and very powerful. It is not related to any orbital modulation, although it occurs close to the periastron. The recurrence of the event is irregular and likely to happen every couple of years. Type II outbursts are related to recurrent activity (likely a dramatic expansion of the equatorial disk) of the Be star. Typical peak X-ray luminosity is $L_X \sim 10^{38}$ erg s^{-1}. The latter is close to the Eddington luminosity limit for a NS (see next chapter).

The third type consists of a persistent, low level activity. It is observed and named after the system in which it was first detected: *X-Per like (or persistent outburst)* emission (Roche *et al.* 1997). Figure 1.3 summarizes the above phenomenology.

1.3 Supergiant High Mass X-ray Binaries

Over the years, the classical sgHMXBs (e.g. Vela X-1, GX 301-2, 4 $U1700-37$, 4 $U1538-52$, Cyg X-1, SAX $J1802.7-2017$, 4 $U1907+09$, XTE $J1855-026$) have been studied extensively: in particular, Vela X-1, the prototype of its class (Watanabe *et al.* 2006, and references therin). These sources show a persistent X-ray emission, related to continuous accretion by the NS of the stellar wind of the companion star. The typical characteristics of

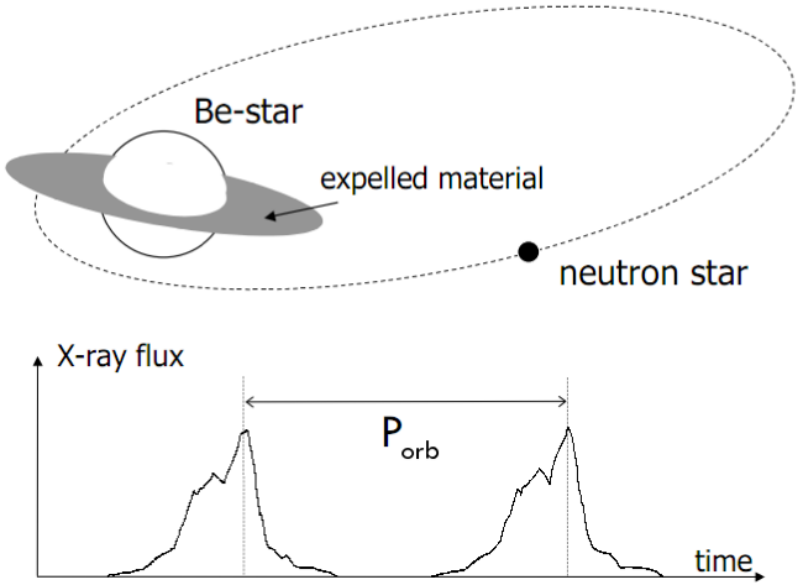

Figure 1.2: Schematic view of a Be/X-ray binaries system. The neutron star moves around the Be star, in an eccentric orbit. Close to periastron the neutron star crosses the equatorial disk, accretes material, and gives an outburst *Credit:* Tauris & van den Heuvel (2006)

classical sgHMXB are as follows, (Liu, van Paradijs & van den Heuvel 2006, and references therein),

- Orbital period $\sim$ 5–20 days,
- Spin Period $\sim$ 100–700 seconds,
- Almost circular orbits at $\alpha \sim 2R_*$,
- Moderate to low absorption $N_{\rm H} \sim (0.8-3) \times 10^{22}{\rm cm}^{-2}$,
- Evolved early type star (OB),
- Typical X-ray luminosity of $L_{\rm X} \sim 10^{36}$ erg s^{-1},

The above characteristics do not fit all of the classical sgHMXB. For example, GX 301-2 has an eccentric orbit $e \sim 0.5$ (Koh *et al.* 1997) and an high absorbing column density $N_{\rm H} \sim 10^{24}$ cm^{-2} due to the formation of an accretion disk (Leahy & Kostka 2008).

Two new classes of sgHMXB have been discovered by *INTEGRAL*:

- *The heavily obscured sources* exhibiting large X-ray absorption when compared to the classical sgHMXBs.
- *The Supergiant Fast X-ray Transient* (SFXTs) showing fast ($\sim$ 1 hour) outbursts and much lower quiescent emission.

A review of these new types of sgHMXBs is given in chapter 5.

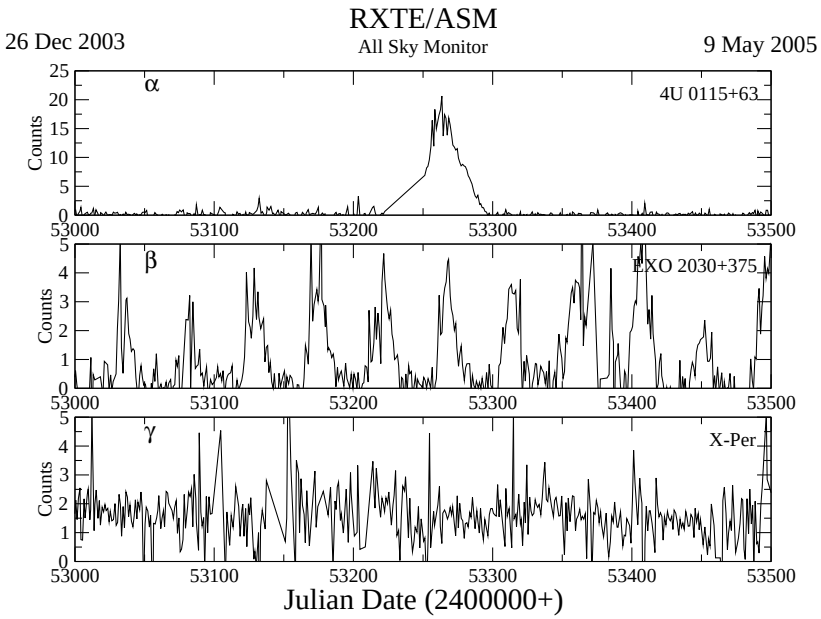

Figure 1.3: Types of outbursts observed in Be/X-ray binaries systems obtained with RXTE ASM. Top panel (α) shows a giant outburst (type II). Middle panel (β) shows normal outbursts (type I). Bottom panel (γ) shows a persistent outburst.

1.4 Corbet diagram

All the different classes of HMXBs can be placed in a spin vs orbital period diagram (see figure 1.4) referred to as the Corbet diagram (Corbet 1986). The different classes of objects occupy different regions in this diagram, reflecting different types of mass transfer. The classical and obscured sgHMXBs and SFTXs (green triangles) show no correlation or anti-correlation at all. In general, these sources are characterized by long spin periods (100–1000 sec; for SFXTs even longer) and rather short orbital periods (5-15 days). They are located on the upper left side of the diagram on a rather narrow stripe parallel to the orbital period$-axis$. Be/X-ray binaries (black points) show a remarkable correlation between the orbital period and the spin period. This correlation has been explained as the result of the rotation of the neutron star at the equilibrium velocity between the spin-up and the spin-down led by centrifugal effects of their strong magnetic field (Waters & van Kerkwijk 1989). As a result, these sources are located in a rather narrow stripe, $\log P_s = 2.29 \log P_{orb} - 2.62$ where P_s and P_{orb} are spin period (in seconds) and the orbital period (in days), respectively. Finally, disk-fed accretion (or Roche Lobe overflow; RLO) systems show short orbital and spin periods. In these systems, the evolved companion fills its Roche lobe and material is transferred to the compact object through an accretion disk. There are few (3) RLO systems.

The knowledge of the spin of the neutron star and of the orbital period allows to estimate the mass transfer mechanism.

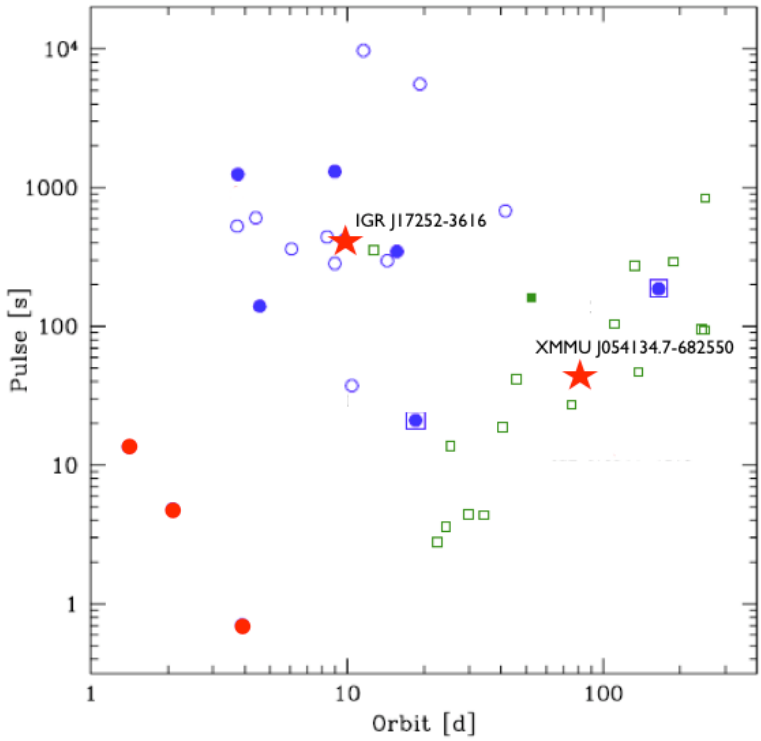

Figure 1.4: The spin-period vs orbital-period diagram, also known as Corbet diagram (Corbet 1986). Green squares represent Be/X-ray binaries, blue circles represent sgHMXB, circles in squares are SFXTs. Red circles represent the three Roche lobe overflow (RLO) systems. The stars show the position of the sources discussed in this thesis. *Credit:* Rodriguez *et al.* (2009)

1.5 Secular evolution of HMXBs

The formation of a HMXB system can be described in a ten-stage process (Tauris & van den Heuvel 2006). First, one needs the ingredients, two massive (>10 $M_\odot$) stars orbiting each other. The more massive star will evolve faster. It will depart from the main sequence (MS), fill its Roche lobe (see chapter 3) and transfer mass to its lighter companion.

During that time the core of the star is evolving. When the mass of the core is sufficient ($M \gtrapprox 3\ M_\odot$), the star explodes as a supernova, leaving either a NS or a BH. Such an explosion is likely to change the orbit significantly (initial orbital period of 100 days; after explosion 5000 days). The system will stay in this stage for about 10 Myrs while the second massive star continues to burn its fuel. The neutron star will emit X-rays when matter is captured from its companion. This is known as a HMXB system. Observational evidences shows that Be/X-ray binaries have eccentric orbit likely related to a supernova "kick" (Reig 2011).

The winds of a main sequence Be star is concentrated on an equatorial disk (also known as a cirumstellar disk). As the donor star evolves towards the giant phase, the orbital radius decreases when compared to the companion radius and continuous wind accretion may start. When the companion fills its Roche Lobe the accretion flow tends to form an accretion disk. Finally, the orbital radius could become smaller than the stellar radius and the system enters the common envelope phase. When the companion stellar

core reaches the critical mass ($\gtrapprox 3\ M_\odot$) it undergoes a supernova explosion. The outcome of this explosion could be a BH/NS or NS/NS binary system. Figure 1.5 summarizes this evolutionary path.

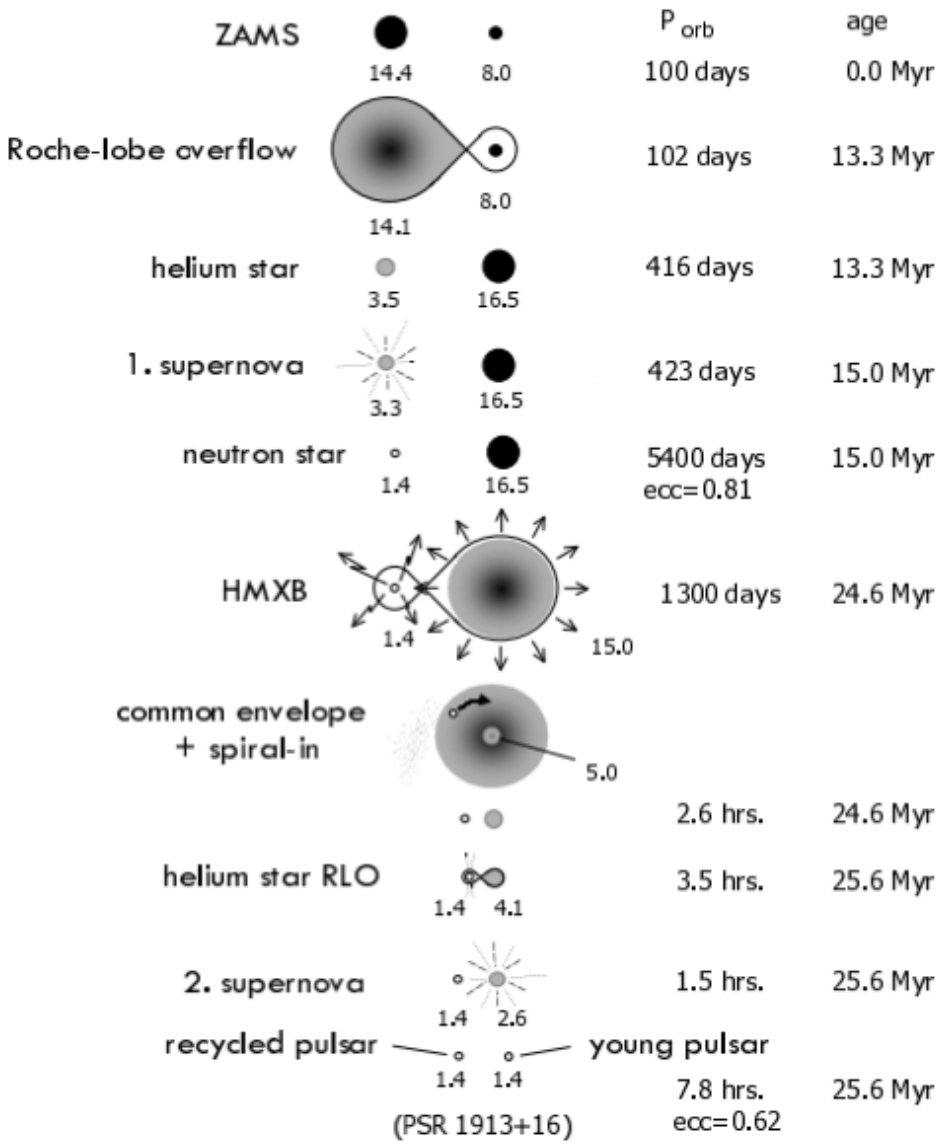

Figure 1.5: Schematic view of the evolution of an HMXBs. Masses are given in $M_\odot$. *Credit*: Tauris & van den Heuvel (2006)

Chapter 2

High-Energy Observatories

In the work carried out in this thesis, we have made use of data from three satellites. XMM-Newton (observations are discussed in chapter 6 and 8), INTEGRAL (observations are discussed in chapter 6 and 9), and finally RXTE (observations are discussed in chapter 8).

2.1 XMM-Newton

$XMM-Newton$ (Jansen *et al.* 2001) is a cornerstone mission of ESA's Horizons 2000, launched on December 10, 1999.

The payload consists of three Wolter type-1 X-ray telescopes with different X-ray detectors on the focal plane, and of a 30 cm optical/UV telescope with a CCD detector. A view of the telescope is shown in figure 2.1.

The angular resolution of the three telescopes is ~ 6 *arcsec*. The total field of view (FoV) is about 30 *arcmin*. Moderate spectral resolution ($E/\Delta E \sim 20$–50) can be achieved using the European Photon Imaging Camera (EPIC), which consists of two MOS (see Turner *et al.* 2001) and one *pn* CCD arrays (see Strüder *et al.* 2001) operating in the energy range from ~ 0.2 to ~ 15 keV. High resolution spectroscopy ($E/\Delta E \sim 200$–800) can be obtained by utilizing the Reflection Grating Spectrometers (RGS) that deflect about half of the light of two of the X-ray telescopes. A summary of the $XMM-Newton$'s capabilities is given in table 2.1.

All EPIC CCDs operate in photon counting mode. This mode produces event lists, i.e. tables with one entry line per event, and lists attributes of the events such as the position at which they were registered, their arrival time and their energies. The two types of EPIC cameras differ in some major aspects. Below we describe the two cameras separately.

- *MOS*: Each of the MOS camera is composed of seven front-illuminated CCDs. The central CCD is at the focal point on the optical axis of the telescope while the outer six are stepped towards the mirror by 4.5 mm to follow approximately the focal plane curvature. This improves the focus for off-axis sources. The imaging area is $\sim$2.5×2.5 cm^2, so that a mosaic of seven covers about 28.4 arcmin. The imaging section has 600×600 40 μm square pixels, one pixel covers 1.1×1.1 arcsec on the FOV, and 15 pixels cover the mirror PSF half width of 15 arcsec.

- *PN*: The pn camera comprises twelve 3×1 cm CCDs on a single waver. The four individual quadrants each having three CCD subunits with a format 200×64 pixels

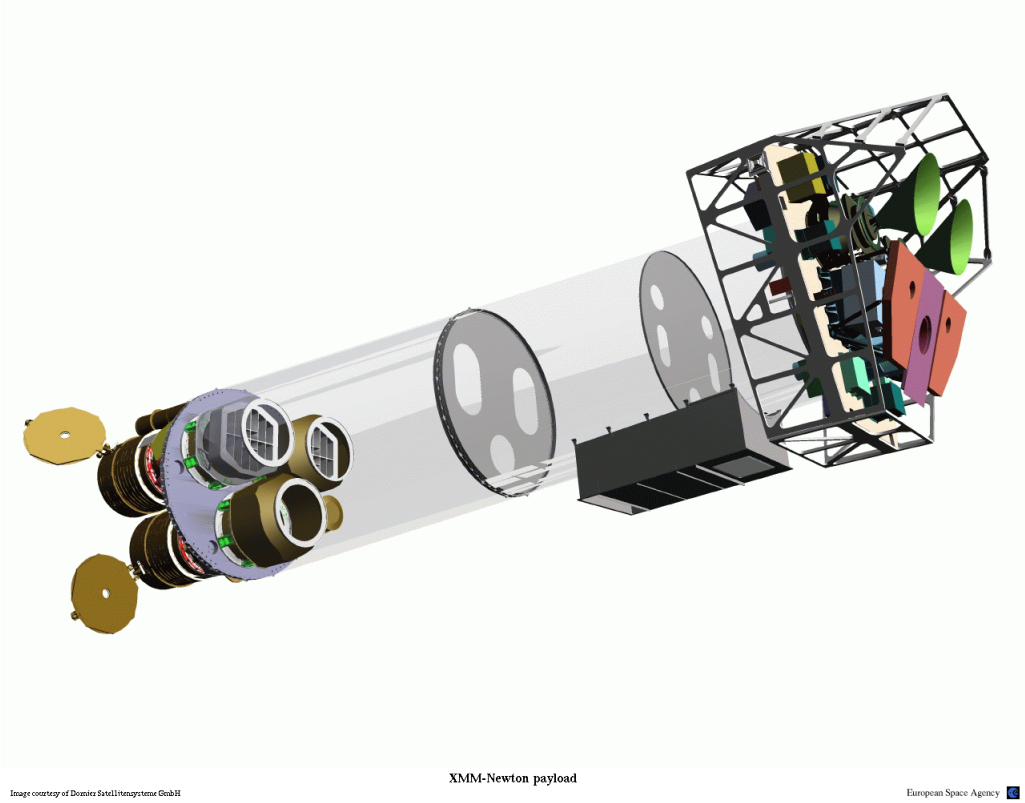

Figure 2.1: A sketch of $XMM - Newton$. The three mirror modules (with their doors) can be seen at the lower left. The focal plane is located at the right end. The distance between mirrors and focal plane is about 7.5 m. EPIC-MOS cameras (Black and Green), EPIC-pn camera (violet), and RGS detectors (pink) are visible. The OM camera is located on the mirror module. *Credit: Dornier Satellitensysteme GmbH*

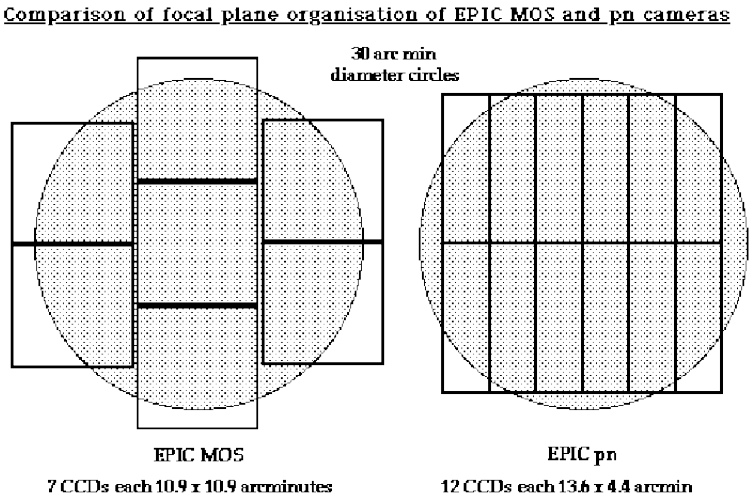

Figure 2.2: A sketch of the field of view of the two types of EPIC cameras: The MOS cameras (left) and the pn camera (right). The shaded area corresponds to a 30' diameter area. *Credit*: $XMM - Newton$ User Handbook

are operated in parallel. The pn camera has an imaging area of 6×6 cm, covering about 97% of the FOV, and a pixel size of 150×150 μm with a position resolution of 120 μm, resulting in an equivalent angular resolving capability for a single photon of $\sim$ 6 arcsec.

In addition to full frame mode, MOS and pn have large and small windows modes for faster read out. Also both, MOS and pn, are able to perform timing mode observations with temporal resolution of ms for MOS and 0.01 ms for pn.

Table 2.1: $XMM - Newton$ Characteristics

Instrument	EPIC MOS	EPIC PN	RGS	OM
Bandpass	0.15-12 keV	0.15 15 keV	0.35-2.5 keV	180-600 nm
Orbital target visibility	5-135 ks	5-135 ks	5-135 ks	5-145 ks
Sensitivity (after 10 ks)	$\sim 10^{-14}$ (1)	$\sim 10^{-14}$ (1)	$\sim 8^{-5}$ (2)	20.7 mag (3)
FOV	30'	30'	$\sim$ 5'	17'
PSF (FWHM/HEM)	5"/14"	6"/15"	N/A	1.4"-2.0"
Pixel size	40μ m (1.1")	150 μ m (4.1")	81 μ m (9 x 10^{-3} A)	0.476513"
Timing resolution	1.5 ms	0.03 ms	0.6 s	0.5 s
Spectral resolution	$\sim$ 70 eV	$\sim$ 80 eV	0.04/0.025 A	350

(1): erg cm^{-2} s^{-1}.
(2): ph cm^{-2} s^{-1}.
(3): 5σ detection of an $A0$ spectral type star in 1 ksec.

2.2 INTEGRAL

The INTErnational Gamma-Ray Astrophysics Laboratory, $INTEGRAL$ (Winkler *et al.* 2003), is a medium-size mission of ESA's Horizon 2000. It was launched on October 17, 2002, by a Russian $PROTON$ rocket from Baikonur, in Kazakhztan. Figure 2.3 shows the expanded view of the INTEGRAL spacecraft. All hard X- and γ-ray instruments on board $INTEGRAL$ are using coded-masks. Focusing hard X- and γ-rays is almost impossible. A coded mask is a planar array of opaque and transparent elements, whose distribution is chosen for optimal performance. The mask is placed in front of the detector plane. Each source within the field-of-view projects a shadow of the mask on the detector. Each photon is recorded (position, arrival time, energy, etc). Once the observation is finished, the sky image should be reconstructed from the detector image (shadow) and the mask geometry.

The instruments on board INTEGRAL are,

- The hard X- and γ-ray imager, IBIS (Ubertini *et al.* 2003). IBIS has a field of view, FOV, of 29° × 29° and an angular resolution of 12 $arcmin$. Above the detector layers, the coded mask is a parallelepiped of 1064 × 1064 × 16 mm^3, with 95 × 95 individual cells. Fifty percent of them are opaque in the IBIS energy range. There are two detectors layers at he bottom of IBIS,

  - The top layer *INTEGRAL Soft Gamma-Ray Imager - ISGRI* (Lebrun *et al.* 2003) is operational in the range 20 keV to 1 MeV. It is an array of 128 × 128 independent pixels (4×4 mm^2, 2 mm thick) made of Cadmium-Telluride (CdTe) crystals. The sensitivity of ISGRI peaks in the range 25-55 keV and ISGRI can achieve a 3σ detection of a 0.3 mCrab source within 1 Msec.

  - *Pixellated Imaging Caesium Iodide Telescope - PICsIT* (Labanti *et al.* 2003) is sensitive in the range 200 keV up to 10 MeV. It is composed of Caesium-Iodide (CsI) scintillator crystals divided in an array of 64×64 pixels (8.55×8.55 mm^2, 30 mm thick).

- The hard X- and γ-ray spectrometer SPI (Vedrenne *et al.* 2003, SPectrometer on board INTEGRAL) is sensitive in the energies from 20 keV to 8 MeV. It has a FOV of $\sim 31^\circ$ and an angular resolution of 2°. The detector consists of 19 hexagonal (highly pure) Germanium detectors (70 mm thick) providing spectral resolution of 2.1 keV at 1 MeV. Since the launch of *INTEGRAL*, four of them failed decreasing the instrument's sensitivity. The SPI detector is screened by the Anti-Coincidence Shield (ACS) made of BGO crystals surrounding the detector and the coded mask outside of the FoV.

- The two (co-aligned) X-ray monitors, JEM-X (Lund *et al.* 2003), operational in the energies from 3 to 30 keV, have a FOV of $\sim 13^\circ$, and an angular resolution of $\sim 3.5\, arcmin$. The detector is made of micro-strip gas chamber where incident photons are absorbed by photo-electric processes and the resulting ionization is amplified towards the strip anodes using high voltage.

- The optical monitor camera, OMC (Mas-Hesse *et al.* 2003), consists of an optical system focused onto a CCD detector. The optics are refractive with an entrance aperture of 5 cm diameter and a square field of view of about $5^\circ \times 5^\circ$. A Johnson V filter allows photometric calibration using standard stars.

The spacecraft is tracked by two ground stations, Redu in Belgium and Goldstone in California, USA. Telemetry is then sent to the Mission Operation Center (MOC) in Darmstadt, Germany which delivers it to the *INTEGRAL* Science Data Center (ISDC) near Geneva, Switzerland.

The ISDC (Courvoisier *et al.* 2003) receives the telemetry and processes the data before release to the community. An archive of all *INTEGRAL* data is maintained at ISDC. In addition, ISDC offers the Off-line Science Analysis software (OSA) and performs a Quick-Look Analysis (QLA) with a delay of approximately 3 hours. The Hard X-ray sky is highly variable on time-scales of hours, therefore QLA is essential to detect transient phenomena. We will discuss again this aspect in chapter 10.

2.3 Rossi-XTE

The Rossi X-ray Timing Explorer (RXTE) was launched on December 30, 1995 from NASA Kennedy Space Center. It was named after the pioneer Bruno Rossi (1905-1993). Figure 2.4 shows the design of RXTE. The payload of RXTE includes three instruments:

- The Proportional Counter Array (PCA; Jahoda *et al.* 1996, 2006) consist of 5 large proportional counter units (PCU) with an anti-coincidence shield providing a very low background. The 5 PCU provides a net effective area of 6250 cm^2 and are filled with xenon gas. The energy range covers 2-60 keV. An hexagonal collimator gives a 1° FWHM resolution. Sources at mCrab level can be detected in a few seconds.

- The High Energy X-ray Timing Experiment (HEXTE; Rothschild *et al.* 1998) has a large area and low background with a FOV of 1^o co-aligned with the PCA. HEXTE

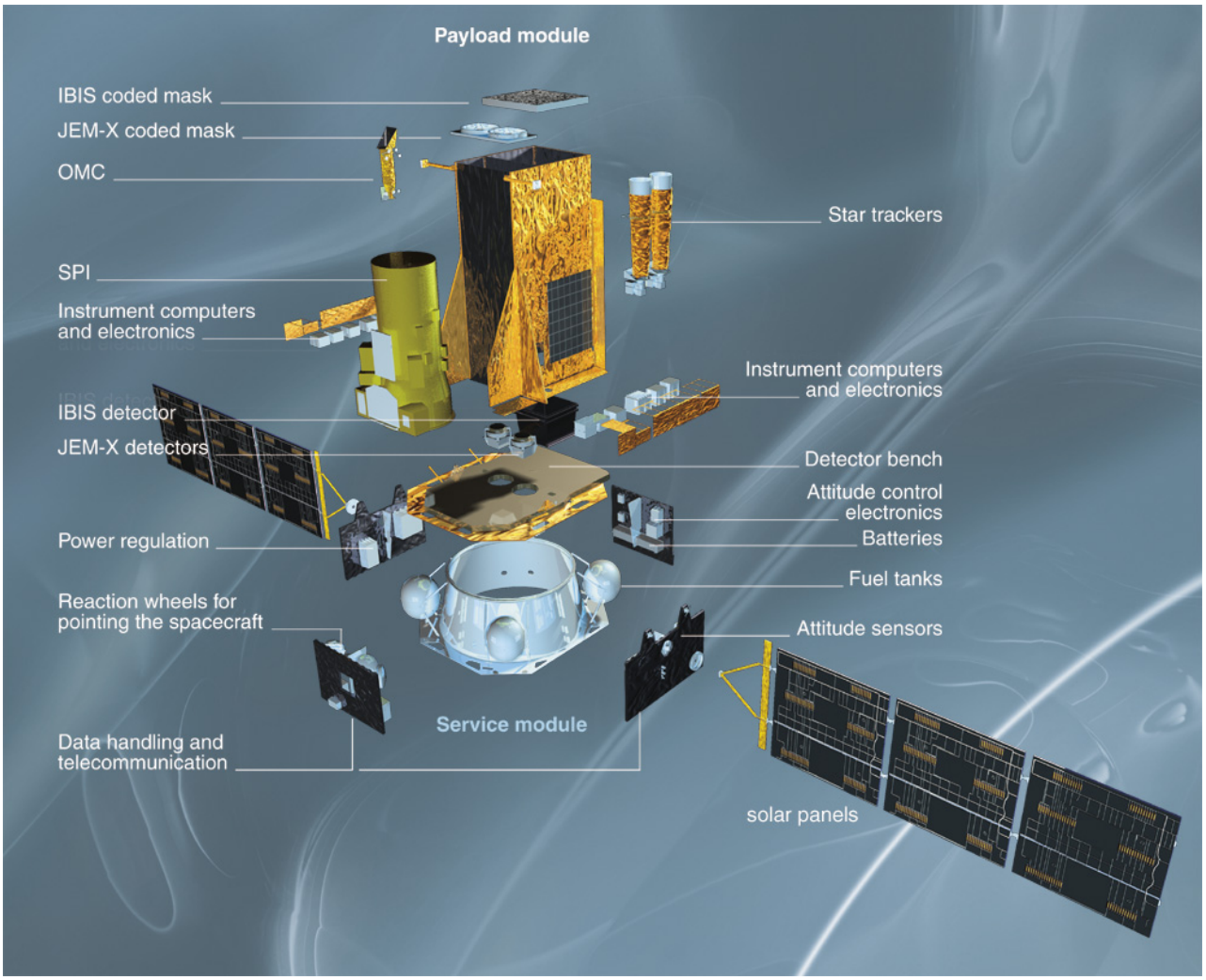

Figure 2.3: A sketch of *INTEGRAL* and of its payload. The service module at the bottom supports all the systems. The four instruments can be seen, IBIS imager, SPI spectrometer, JEM-X monitors and OMC. *Credit: ESA*

is split into 2 clusters of eight NaI/CsI detectors each. HEXTE operates in the energy range of 20-200 keV and an has effective area of 1600 cm^2.

- The All-Sky Monitor (ASM; Levine *et al.* 1996) completes the payload of RXTE. ASM scans roughly 80% of the sky every 1.5 hours. ASM data are used to alert the community in case of flares or changes of the state of an X-ray source. ASM consists of three rotation Scanning Shadow Cameras (SSC). Each SSC detector is a sealed proportional counter using Xenon-CO_2 gas. It is sensitive in the range 2–10 keV.

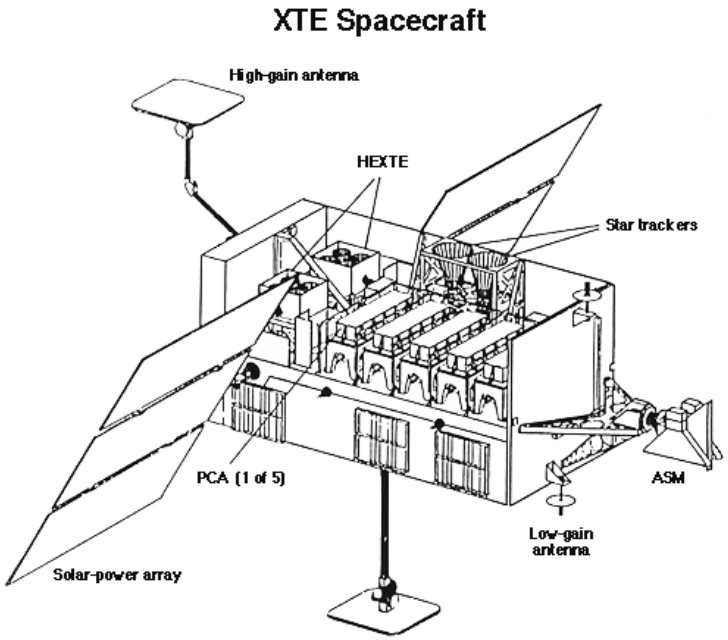

Figure 2.4: A sketch of the Rossi X-ray Timing Explorer (RXTE) and of its payload. *Credit: NASA*

Chapter 3

Accretion

3.1 Introduction

Among the X-ray and γ-ray galactic sources are those known as accretion powered sources. The luminosity of an accreting source can be expressed as,

$$L_{acc} = \eta G M \dot{M} / R_* \tag{3.1}$$

where R_* is the radius of the compact object and $\dot{M}$ the accretion rate. The coefficient η measures the efficiency at which radiation is extracted from the accretion flow, in the gravitational field of the compact object. The latter can have a mass ranging from 1.4 to 2.0 $M_\odot$ for neutron stars (NS) and from $\gtrsim 3$ $M_\odot$ for black hole candidates (BHC).

3.2 Accretion Flow

3.2.1 Spherically symmetric accretion

Here, we consider the case of a steady, spherically symmetric accretion flow (Bondi & Hoyle 1944; Frank, King & Raine 1992). We consider a compact object of mass M accreting material form a large spherical cloud of gas. In order to develop and study the problem we introduce spherical coordinates (r, θ, ϕ) with the origin located at the center of the accreting object. For a steady flow, the continuity equation reduces to

$$\frac{1}{r^2}\frac{d}{dr}(r^2 \rho \upsilon) = 0 \tag{3.2}$$

where r is the distance from the star, υ the velocity of the infalling material, and ρ the density. A constant mass accretion rate can be defined as

$$\dot{M} = 4\pi r^2 \rho(-\upsilon) \tag{3.3}$$

If the only external force is the gravity,

$$f_g = -GM\rho/r^2 \tag{3.4}$$

where, G is the Gravitational constant and M is the mass of the accreting object, the Euler equation can be written,

$$\upsilon\frac{d\upsilon}{dr} + \frac{1}{\rho}\frac{dP}{dr} + \frac{GM}{r^2} = 0 \tag{3.5}$$

Assuming the equation of state of a perfect gas:

$$T = \frac{\mu m_H P}{\rho k}, \tag{3.6}$$

and introducing the polytropic relation $P \sim \rho^\gamma$ where $\gamma = 5/3$ for an adiabatic compression, the Euler equation reduces to

$$\frac{1}{2}\Big(1 - \frac{c_s^2}{v^2}\Big)\frac{d}{dr}(v^2) = -\frac{GM}{r^2}\Big[1 - \frac{2c_s^2 r}{GM}\Big] \tag{3.7}$$

where c_s is the speed of sound.

There are a number of solutions to this equation. Figure 3.1 summarizes the families of solution, in a Mach number squared ($\mathcal{M}^2 = c_s^2/v^2$) vs radius plot. Only one curve (noted 1) is adequate to describe accretion. The right-hand side of eq. 3.7 eventually reaches zero at,

$$r_s = \frac{GM}{2c_s^2} \approx 7.5 \cdot 10^{13} \left(\frac{T}{10^4\mathrm{K}}\right)\left(\frac{M}{M_\odot}\right) \mathrm{cm} \tag{3.8}$$

(using $c_s \approx 10(T/10^4\mathrm{K})$ km s^{-1}). At r_s , the Mach number is 1, i.e. $v^2 = c_s^2$ and $\frac{d}{dr}(v^2)$=0. The mass accretion rate can thus be written, $\dot{M} = 4\pi r_s^2 \rho(r_s) c_s(r_s)$ and using $\rho(r_s) = \rho(\infty)\Big[\frac{c_s(r_s)}{c_s(\infty)}\Big]^{2/(\gamma-1)}$, we obtain

$$\dot{M} = \pi G^2 M^2 \frac{\rho(\infty)}{c_s^3(\infty)}\Big[\frac{2}{5-3\gamma}\Big]^{\frac{5-3\gamma}{2(\gamma-1)}} \tag{3.9}$$

3.2.2 Eddington limit

At extreme accretion rates the radiation pressure can increase to a point at which it can counterbalance the gravitational force. This is referred to as the *Eddington limit*. The Eddington limit can be derived by equalizing the radiation and hydrostatic gravitational pressure to obtain

$$\begin{aligned} L_{Edd} &= 4\pi G M m_p c/\sigma_T \\ &\approx 1.3 \times 10^{38}(M/M_\odot)\ \mathrm{erg\,s^{-1}} \end{aligned} \tag{3.10}$$

At luminosities larger than L_{Edd} the outward radiation pressure will exceed the gravitational pressure and therefore accretion could be halted. In other words, this limit is the maximum (in rough terms) luminosity that can be achieved by accretion. The maximum luminosity emitted from an accreting NS ($M_{NS} = 1.4M_\odot$) $L_{Edd} \approx 2 \times 10^{38}$ erg s^{-1}, is indeed observed during type II outbursts of Be/X-ray binaries (see chapter 1).

3.3 Accretion in Binaries

3.3.1 Interacting binaries and Roche lobe Geometry

The motion of a test particle in the gravitational potential of two massive bodies orbiting each other was studied by the French Mathematician Edouard Roche. Roche's approximation assumes that the bodies are orbiting in circular orbits and also assumes that the stars are point sources.

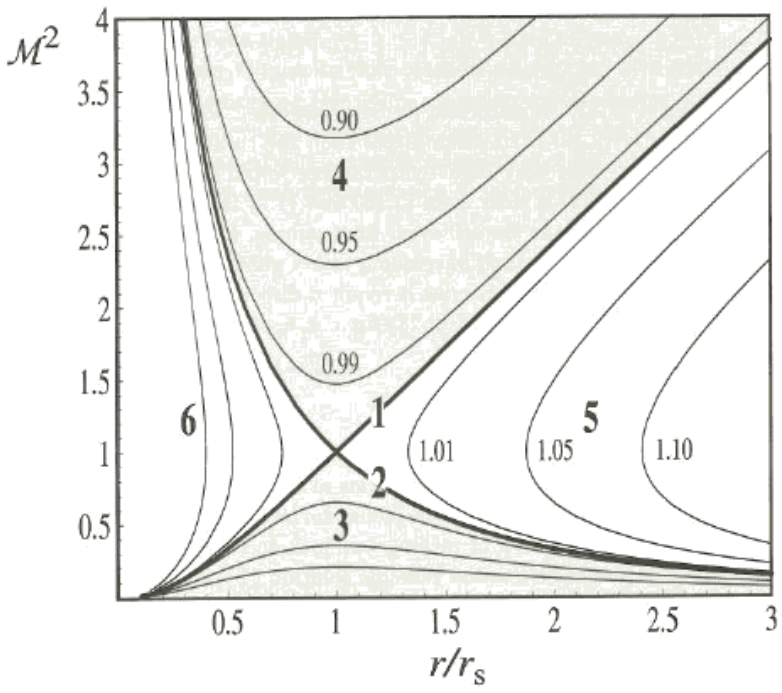

Figure 3.1: A family of solution for the accretion flow in a Mach numbered squared as a function of radius r_s plot for a spherically symetric adiabatic gas flow. *Credit:* Frank, King & Raine (1992)

The binary separation, α, is derived from the orbital period, through Kepler's 3rd law.

$$\alpha \approx 2.9 \times 10^{11} m_1^{1/3} (1+q)^{1/3} P_d^{2/3} cm \tag{3.11}$$

where, $P_{\rm d}$ is the orbital period in days, m_1 is the mass of the primary star in $M_\odot$, and $q = m_2/m_1$ is the mass-ratio.

The effective potential that accounts for the two stars plus the centrifugal force is given by the so called Roche potential, $\Phi_R(\mathbf{r})$, as follows,

$$\Phi_r(\mathbf{r}) = -\frac{GM_1}{|\mathbf{r}-\mathbf{r_1}|} - \frac{GM_2}{|\mathbf{r}-\mathbf{r_2}|} - \frac{1}{2}(\omega \times \mathbf{r})^2 \tag{3.12}$$

where, $\mathbf{r_1}$, $\mathbf{r_2}$ are the position vector of the centers of the two stars, $\omega = \left[\frac{GM}{\alpha^3}\right]^{1/2}\mathbf{e}$ is the vector of the angular momentum, and $\mathbf{e}$ is the unit vector normal to the orbital plane. Figure 3.2 shows the equipotentials of a binary system (with q=0.25), in the orbital plane.

The morphology of the Roche potential has two deep lobes at the places of the two massive objects. A figure-of-eight shape (see figure 3.2, in two dimension) shows how these two lobes are connected at the inner Lagrangian point L1. In three dimension this critical surface has a dumbbell shape. A test particle will pass through the lowest potential at the vicinity of L1 in the other lobe than to escape the critical surface.

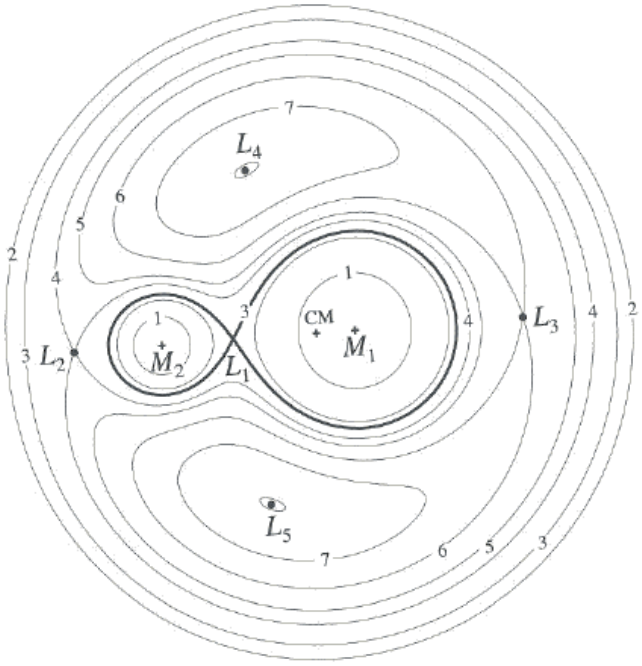

Figure 3.2: Section in the orbital plane of Roche equipotential Φ =const. for a binary system with q=0.25. Critical Lagrangian points are denoted by L and the inner lagrangian point by L_1. The thick solid line draws the Roche lobes projected on the orbital plane. *Credit:* Frank, King & Raine (1992)

An approximate analytic formula to define the Roche lobe size (Eggleton 1983) is,

$$\frac{R_L}{\alpha} = \frac{0.49q^{2/3}}{0.6q^{2/3} + ln(1+q^{1/3})} \tag{3.13}$$

When one star for some reason (e.g. stellar evolution) fills its Roche lobe, material will fall through the L_1 point to the other star. If the companion star is a compact object, the formation of an accretion disc is likely (see 3.3.4). Another quantity, useful for the next paragraph, is the distance between the L1 point and the center of the compact object. The distance from the L1 point can be approximated by, $b_1/\alpha = 0.5 - 0.227\log(q)$ (Frank, King & Raine 1992).

3.3.2 Orbital parameters in eclipsing binaries

An important parameter necessary for determining the properties of a X-ray binary is the mass function, given by

$$f(M) = \frac{4\pi^2(\alpha_x \sin i)^3}{GP_{\rm orb}} = \frac{M_{\rm oc}\sin^3 i}{(1+q)^2} \tag{3.14}$$

where $M_{\rm oc}$ is the mass of the optical counterpart , $q = M_x/M_{\rm oc}$, $\alpha_x \sin i$ is the projected semi-major axis of the neutron star, and i is the inclination of the orbit with respect to the line-of-sight (LOS). Another way to express the mass ratio, q, is

$$q = \frac{\alpha_{\rm oc} \sin i}{\alpha_x \sin i} = \frac{K_{oc} P_{\rm orb} \sqrt{1-e^2}}{2\pi \alpha_x \sin i} \tag{3.15}$$

where $\alpha_{\rm oc} \sin i$ is the projected semi-major axis of the orbit of the companion star, $K_{\rm oc}$ is the semi-amplitude of the optical Doppler velocity curve of the massive star, and e is the eccentricity.

For an eclipsing binary the inclination angle can be determined by assuming that the radius of the OB star is compatible with a sphere of radius R_{oc}, and therefore one gets,

$$R_{oc} \approx \alpha \sqrt{\cos^2 i + \sin^2 i \sin^2 \theta_e} \tag{3.16}$$

where $\alpha = \alpha_x + \alpha_{oc}$ is the separation of the centers of mass of the two stars, and θ_e is the eclipse half angle, for eclipsing systems. Thus, the orbital inclination is

$$\sin i \approx [1 - \beta^2 (R_L/\alpha)^2]^{1/2} / \cos\theta_e \tag{3.17}$$

where $\beta = R_{\rm oc}/R_L$ is the fraction of the ratio of the companion star to its corresponding Roche lobe. Although we have already given some approximation to the Roche Lobe radius, here we make use of the approximation (Joss & Rappaport 1984, and references therein),

$$R_L \approx \alpha [A + B \log q + C \log^2 q] \tag{3.18}$$

where $A \approx 0.398 - 0.026\Omega^2 + 0.004\Omega^3$, $B \approx -0.264 + 0.052\Omega^2 - 0.015\Omega^3$, and $C \approx -0.023 - 0.005\Omega^2$; Ω is the ratio of the angular velocity of the optical counterpart to the orbital velocity of the system. The above expression can provide an accuracy of about 2% over the range $0 \leq \Omega \leq 2$ and $0.02 \leq q \leq 1$.

From the above set of equations, we see that quantities such as, K_{oc}, $\alpha_x \sin i$, and θ_e are observables. If we are unable to fully determine them, we can use reasonable assumptions on the co-rotation of the companion star (Ω) or on the fraction of the Roche Lobe filled by the star (β). For instance, in the case of sgHMXBs, one can assume a synchronous rotation ($\Omega = 1$) and an almost filled Roche lobe ($\beta \gtrsim 0.9$).

3.3.3 Wind accretion

We now consider the case of a massive, most likely evolved star, that is part of a binary system hosting a neutron star, orbiting in an almost circular orbit. Typical mass loss rates are in the range, $\dot{M}_w \approx 10^{-7} - 10^{-5}$ M$_\odot$ yr^{-1}. The velocity profile and the mechanism responsible for the acceleration of the wind are described in chapter 4. The escape velocity in these type of stars $v_{esc} = \sqrt{2GM_*/R_*}$ is comparable to the wind velocity, v_w. Both escape and wind velocity are highly supersonic ($c_s \sim 10$ km s^{-1}). The neutron star is orbiting with a velocity which is $v_{ns} \approx 440 \sqrt{M_{OB}/\alpha}\,{\rm km\,s^{-1}} \approx 50\alpha/P\,{\rm km\,s^{-1}} \approx 200 M_{OB}^{1/3}(1+q)^{1/3} P^{-1/3}\,{\rm km\,s^{-1}}$, where M_{OB} is the mass of the companion star in solar masses, α is the separation between the two stars in solar radii, and P is the orbital period of the system in days, assuming a circular orbit. The NS is orbiting supersonically within the wind of the star and able to create shocks.

A NS, orbiting close to its companion ($\alpha \sim 1-2$ R$_*$), accretes material from the wind. An effective accretion radius can be determined by $r_{acc} \sim GM/v^2$, where v is the velocity

of the wind relative to the neutron star[1]. An effective cross-section of the capturing radius is πr_{acc}^2 and the mass accretion rate is therefore given by,

$$\dot{M}_{acc} = \pi r_{acc}^2 \rho_0 \upsilon \tag{3.19}$$

where ρ_0 is the density in the vicinity of the accretion radius.

More quantitative expression can be derived for the accretion radius (Bondi & Hoyle 1944), as given by,

$$r_{acc} = \frac{2\xi G M_{ns}}{\upsilon^2} \sim 10^{10} m_{ns} \upsilon_8^{-2} \,\mathrm{cm} \tag{3.20}$$

where m_{ns} is the mass of the neutron star in $M_\odot$, ξ is a dimensionless plasma-capture process parameter, and υ_8 is the velocity as determined above in 10^8 cm s^{-1}. The velocity is the relative velocity of the neutron star within the wind of the donor star. Also in the above determination we have assumed a supersonic velocity and neglected the speed of sound, c_s.

The accretion of material will lead to an emission of X-ray radiation. As we have see in equation 3.1, we can translate mass accretion rate into luminosity. In particularly we have $L \approx 10^{36} \times \dot{M}_{-9}$ erg s^{-1}, where $\dot{M}_{-9}$ is the mass accretion rate in $10^{-9} M_\odot$ yr^{-1}. For a typical wind-fed systems the X-ray luminosity is $L_X \sim 10^{36}$ erg s^{-1}.

This luminosity is adequate to ionize the material around the NS and effectively stop the acceleration of the stellar wind locally. In order to describe the ionization of the wind we introduce the ionization parameter,

$$\xi = \frac{L_X}{n r^2} \tag{3.21}$$

where n is the number density, and r is the distance from the X-ray source. To calculate the number density from a smooth stellar wind, we have to assume a mass continuity ($\dot{M} = 4\pi r^2 \upsilon^2$) and the CAK velocity law (see chap. 4). Assuming a spherically symmetric distribution of material, we can determine the ionization parameter and (number) density contours. The number density distribution can be written

$$n(R) = \frac{\dot{M}_w}{4\pi \mu m_p R^2 \upsilon(R)} \approx 2 \times 10^{10} \dot{M}_{-6} \upsilon_8^{-1} R_{12}^{-2} \,\mathrm{cm}^3 \tag{3.22}$$

where, R is the distance from the massive star, $\dot{M}_{-6}$ is the mass loss rate in $10^{-6} M_\odot$ yr^{-1}, υ_8 is the wind velocity in 10^8 cm s^{-1}, and R_{12} is the distance from the massive star in 10^{12} cm. In all the derivations we have assumed spherical symmetry. One, then, obtains,

$$\xi = \xi_0 \Big(\frac{R}{r}\Big)^2 \Big(1 - \frac{R_*}{R}\Big)^\beta, \tag{3.23}$$

where $\xi_0 = 4\pi\mu m_p \upsilon_\infty L / \dot{M}_w \approx 50 L_{36} \upsilon_8 M_{-6}^{-1}$ erg cm s^{-1} and β is the wind velocity gradient (see eq. 4.1). For a constant velocity field ($\beta = 0$) one gets (Hatchett & McCray 1977; Ghosh 2007)

$$\Big(\frac{R}{\alpha}\Big)^2 \Big(1 - \frac{\xi_0}{\xi}\Big) - 2\Big(\frac{R}{\alpha}\Big)\cos\Theta + 1 = 0 \tag{3.24}$$

A sphere of highly ionized material will enclose the X-ray source. In this Strömgren sphere the wind is not radiatevely driven (see chapter 4).

[1] The velocity $\boldsymbol{\upsilon} = \boldsymbol{\upsilon}_w - \boldsymbol{\upsilon}_{orb}$ where $\boldsymbol{\upsilon}_w$ is the wind velocity far from the neutron star and $\boldsymbol{\upsilon}_{orb}$ is the orbital velocity for the NS. For simplicity we have assumed circular orbit, $\upsilon = \sqrt{\upsilon_w^2 + \upsilon_{orb}^2}$

3.3.4 Formation of an accretion disk

When the Roche lobe is filled, the atmosphere of the companion star fuels the compact object through the Lagrangian point, L1. The in-falling material has high specific angular momentum hence, cannot directly fall onto the compact object but spirals around it and drops. Let's consider the stream with two (velocity) components, $\upsilon_\perp \sim b_1\omega$, and $\upsilon_\parallel \lesssim c_s \approx 10(T/10^4K)^{1/2}$ km s^{-1}, in the non-rotating frame. One can obtain $\upsilon_\perp \sim 100M_X^{1/3}(1+q)^{1/3}P_{day}^{-1/3}$km s^{-1}, where M_X is the mass of the X-ray source. We also know that $\upsilon_\parallel \sim c_s \sim 10$ km s^{-1} for a typical stellar envelope temperature.

A good approximation is to consider the stream trajectory as the orbit of a test particle allowed to 'fall' from the point L1 in the gravitational field of the compact object. This will lead to an elliptical orbit lying in the orbital plane of the star. The steam is located close to the orbital plane as the velocity normal to the plane is negligible. Assuming that the stream dissipates energy via shocks it tends to orbit along a circular orbit. We expect therefore a critical circularization radius, R_{circ}, where the Kepler orbit has the same specific angular momentum as that of the transferring gas had on passing through L1. This circular velocity is $\upsilon_\phi(R_{circ}) = \left(\frac{GM_{CO}}{R_{circ}}\right)^{1/2}$, resulting in a circularization radius of, $R_{circ} \approx 4(1+q)^{4/3}\,(0.5 - 0.227log q)^4 P_{day}^{2/3} R_\odot$.

3.3.5 Accretion disk structure

Following Frank, King & Raine (1992), we consider a steady Keplerian accretion disk, geometrically thin. In other words the material lies very close to the plane of the orbit, at z=0. The problem is solved using cylindrical polar coordinates (R, ϕ, z). The circular velocity is given by, $\upsilon_\phi = R\Omega_K(R)$, where, $\Omega_K(R) = (GM/R^3)^{1/2}$ is the Keplerian angular velocity. In addition, we assume that there is a small radial 'drift' velocity υ_R. The disc will be characterized by its surface density distribution, $\Sigma(R,t)$ in units of mass per unit surface area of the disc. The density is integrated over the z-axis, which is normal to the disc.

A annulus of this disc between R and $R+\Delta R$ has a total mass of $2\pi R\Delta R\Sigma$ and a total angular momentum of $2\pi R\Delta R\Sigma R^2\Omega_K$. Therefore the rate of change of mass over time is given by

$$\frac{\partial}{\partial t}(2\pi R\Delta R\Sigma) = \upsilon_R(R,t)2\pi R\Sigma(R,t) - \upsilon_R(R+\Delta R)2\pi(R+\Delta R)\Sigma(R+\Delta R)$$
$$\sim -2\pi\Delta R\frac{\partial}{\partial R}(R\Sigma\upsilon_R)$$

At the limit where $\Delta R \to 0$, we end up with the mass conservation equation,

$$R\frac{\partial\Sigma}{\partial t} + \frac{\partial}{\partial R}(R\Sigma\upsilon_r) = 0 \tag{3.25}$$

Similarly we can obtain for the angular momentum,

$$\frac{\partial}{\partial t}(2\pi R\Delta R\Sigma R^2\Omega_K) \approx -2\pi\Delta R\frac{\partial}{\partial R}(R\Sigma\upsilon_R R^2\Omega_K) + \frac{\partial G}{\partial R}\Delta R$$

where, $G(R,t)$ accounts for the net effect of the viscous torques. Again, at the limit of $\Delta R \to 0$ one gets,

$$R\frac{\partial}{\partial t}(\Sigma R^2\Omega_K) + \frac{\partial}{\partial R}(R\Sigma\upsilon_R R^2\Omega_K) = \frac{1}{2\pi}\frac{\partial G}{\partial R} \tag{3.26}$$

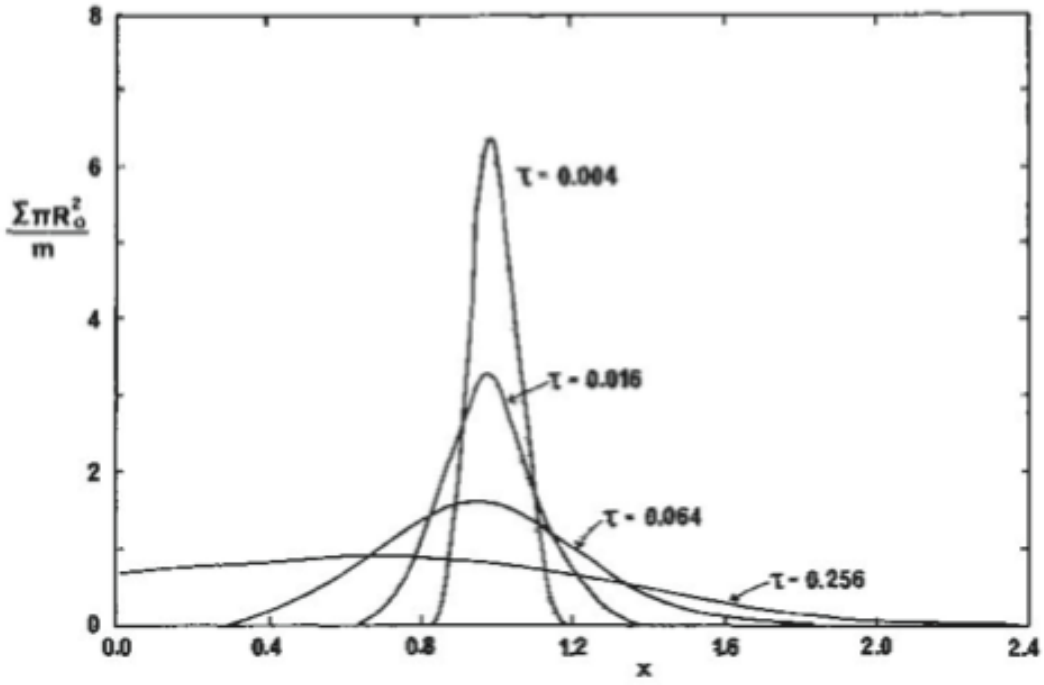

Figure 3.3: A ring of mass m placed in a Kepleria orbit at $R = R_0$ spreads out under the action of viscous torques. The surface density is given as a function of $x = \frac{R}{R_0}$ where τ is the dimensionless time. *Credit:* Frank, King & Raine (1992)

Equations 3.25 and 3.26 combined with $G(R) = 2\pi R\nu\Sigma R^2\Omega'$ [2], defining the torque, determine the disc structure in the radial direction. After appropriate transformation one can get the radial distribution of the material on the disk, considering a ring of mass m at $R = R_0$, given by $\Sigma(R, t = 0) = \frac{m}{2\pi R_0\delta(R-R_0)}$, where $\delta(R - R_0)$ is the Dirac delta distribution. Therefore,

$$\Sigma(\chi, \tau) = \frac{m}{\pi R_0^2}\tau^{-1}\chi^{-1/4}e^{-\frac{1+\chi^2}{\tau}}I_{1/4}(2\chi/\tau) \tag{3.27}$$

where, $I_{1/4}(z)$ is the modified Bessel function,; $\chi = R/R_0$, and $\tau = 12\nu t R_0^{-2}$ are dimensionless radius and time variable respectively. Figure 3.3 shows the $\Sigma(\chi, \tau)$ as a function of χ for various values of τ (Frank, King & Raine 1992).

Emitted Spectrum

Each element of the disk surface radiates, approximately, as a blackbody of temperature $T(R)$. The temperature $T(R)$ can be obtained by equations the viscous dissipation rate, $D(R)$, to the blackbody flux, i.e., $\sigma T^4(R) = D(R)$ (Frank, King & Raine 1992).

The temperature is therefore given by,

$$T(R) = \left[\frac{3GM\dot{M}}{8\pi R^3\sigma}\left(1 - \sqrt{\frac{R_{in}}{R}}\right)\right]^{1/4} \text{where, } D(R) = \frac{3GM\dot{M}}{8\pi R^3}\left[1 - \left(\frac{R_*}{R}\right)^{1/2}\right] \tag{3.28}$$

[2] $G(R)$ is the differential torque between the layer R and $R + dR$. Therefore, the differential torque can be written as $G(R + dR) - G(R) = (dG/dR)dR$. Here we denote $\Omega' = d\Omega/dR$

where, R_{in} is the inner radius of the accretion disk. For $R \gg R_{in}$, one gets $T = T_{in}(R/R_{in})^{3/4}$, where,

$$T_{in} = \left(\frac{3GM\dot{M}}{8\pi R_{in}^3\sigma}\right)^{1/4} = 1.3\times10^7 \dot{M}_{17}^{1/4} m_{ns}^{1/4} R_6^{-3/4}\,\mathrm{K} \tag{3.29}$$

where, $\dot{M}_{17} = \dot{M}/10^{17}\,\mathrm{g\ s^{-1}}$, m_{ns} is the mass of the neutron star in solar masses, and $R_6 = R_{in}/10^6$ cm. For typical parameters of a neutron star ($m_{ns} \sim R_6 \sim \dot{M}_{17} \sim 1$) we can estimate the temperature of the inner disk to be $\sim 10^7$ K. Each element of the surface of the disk emits as a blackbody,

$$I_\nu = \frac{2h\nu^3}{c^2(e^{h\nu/kT(R)}-1)} \tag{3.30}$$

For an observer at distance D, whose line-of-sight makes an angle i to the disc plane, the flux as a function of frequency, ν, is given as,

$$\begin{aligned} F_\nu &= \frac{2\pi cos(i)}{D^2}\int_{R_{in}}^{R_{out}} I_\nu R dR \\ &= \frac{4\pi h\, cos(i)\nu^3}{c^2D^2}\int_{R_{in}}^{R_{out}} \frac{R\,dR}{e^{h\nu/kT(R)}-1} \end{aligned} \tag{3.31}$$

An important note here, is that the flux, and temperature as well, are independent of the disc viscosity. This comes out of the assumptions of the steady disc and blackbody approximation.

The Standard model: α-discs

In the further study of accretion disks, we now examine the case of a steady state disc for a simple case. The structure of the disk was first studied by Shakura & Sunyaev (1973), who assumed a viscosity prescription given by, $\nu = \alpha c_s H$, where H is the disk thickness, and that the Rosseland mean opacity is well approximated by the Kramer's law, given by $\kappa_R = 5\times10^{24}\rho T_c^{-7/2}$ cm^2 gr^{-1}. One can derive several quantities ($\alpha \lesssim 1$) from the above equations:

$$\begin{aligned} \Sigma &= 5.2\alpha^{-4/5}\dot{M}_{16}^{7/10} m_{co}^{1/4} R_{10}^{-3/4} f^{14/5}\mathrm{gr\,cm^2} \\ H &= 1.7\times10^8\alpha^{-1/10}\dot{M}_{16}^{3/20} m_{co}^{-3/8} R_{10}^{9/8} f^{3/5}\mathrm{cm} \\ \rho &= 3.1\times10^{-8}\alpha^{-7/10}\dot{M}_{16}^{11/20} m_{co}^{5/8} R_{10}^{-15/8} f^{11/5}\mathrm{gr\,cm^{-3}} \\ T_c &= 1.4\times10^4\alpha^{-1/5}\dot{M}_{16}^{3/10} m_{co}^{1/4} R_{10}^{-3/4} f^{6/5}\,\mathrm{K} \\ \tau &= 190\alpha^{-4/5}\dot{M}_{16}^{1/5} f^{4/5} \\ \nu &= 1.8\times10^{14}\alpha^{4/5}\dot{M}_{16}^{3/10} m_{co}^{-1/4} R_{10}^{3/4} f^{6/5}\,\mathrm{cm^2 s^{-1}} \\ \upsilon_R &= 2.7\times10^4 \\ f &= \left[1-\sqrt{\tfrac{R_{in}}{R}}\right]^{1/4} \end{aligned} \tag{3.32}$$

where, $\dot{M}_{16}$ is the mass accretion rate in 10^{16} gr sec^{-1} $\sim 1.5\times10^{-10}$ M$_\odot$ yr^{-1}, m_{co} is the mass of the compact object in solar masses (M$_\odot$), and R_{10} is the distance from the compact object in 10^{10} cm.

One can then extract some additional information about the disk. First, one can see that $H \sim 10^8 R_{10}^{9/8}$ cm $\rightarrow$ H/R $\sim 10^{-2}\mathrm{R}_{10}^{1/8}$ which is indeed a thin disk. The mass of the disk,

$$M_{disk} = 2\pi \int_{R_{in}}^{R_{out}} \Sigma R dR \lesssim 10^{-10} \alpha^{-4/5} \dot{M}_{16}^{7/10} \, \mathrm{M}_\odot$$

is negligible when compared to the compact object which holds a typical mass of about 1 $M_\odot$ (Frank, King & Raine 1992).

Another step is to examine under which conditions the Kramers opacity and the disregard of the radiation pressure are valid assumptions. From equation 3.32 we get, $\kappa_R = \tau/\Sigma \approx 36 \dot{M}_{16}^{-1/2} m_{co}^{1/4} R_{10}^{3/4} f^{-2}$ which is independent of α. For an ionized gas at high temperature, $T \gtrsim 10^4$ K, the main source of opacity is electron scattering, $\kappa_R \approx \sigma_T/m_p \approx 0.4$ cm^2 s^{-1}. Kramer's opacity will dominate in the range $R \gtrsim 2.5 \times 10^7 \dot{M}_{16}^{2/3} m_{co}^{1/3} f^{8/3}$ cm which is larger than the magnetosphere of a neutron star, assuming typical parameters. The ratio to the radiation-to-gas pressure is given,

$$\frac{P_r}{P_g} = 2.8 \times 10^{-3} \alpha^{1/10} \dot{M}_{16}^{7/10} R_{10}^{-3/8} f^{7/5} \tag{3.33}$$

which is small in the region where Kramer's opacity dominates (Frank, King & Raine 1992). For R$\lesssim 10^7$ cm, where electron scattering is the dominant source of opacity, we still have $P_r \ll P_g$. However, in the inner disk $R \lesssim 24 \alpha^{2/21} \dot{M}_{16}^{16/21} m_{co}^{-3/21} f^{4/21}$ km, the geometrical thin disk assumption breaks for $\dot{M}_{16} \gtrsim 1$. In that region, the main source of opacity is electron scattering, therefore, $\tau = \Sigma\kappa_R \approx \rho H \sigma_T/m_p$. The speed of sound is $c_s = 3GM\dot{M}\sigma_T H f^4/8\pi R^3 m_p c$ and hence, $H = 3\sigma_T \dot{M} f^4/8\pi m_p c \approx \frac{3R_{in}}{4\eta} \frac{\dot{M}}{\dot{M}_{Edd}} f^4$. The height of a radiatively pressured disk is independent of R. This shows that at high accretion rate, where $\dot{M} = \dot{M}_{Edd}$ and for $\eta = 0.1$ the thin disk approximation is no more valid close to the compact object (Frank, King & Raine 1992).

3.3.6 Spin evolution of accretion powered pulsars

The formation of the accretion disk, and its interaction with the neutron star's magnetosphere will have an impact on the spin evolution of the pulsar. From the very early years of X-ray astronomy and the discovery of two famous accretion-powered pulsars, Cen X-3 and Her X-1, it became clear that their intrinsic pulse period (or spin) were showing a long-term decrease. This secular evolution is referred to as spin-up of accretion-powered pulsar, which is in contrast to the spin-down of rotation powered pulsars.

We consider a magnetized neutron star with $B \sim 10^{12}$ Gauss with a magnetic momentum

$$\mu = B_* R_*^3, \tag{3.34}$$

where B_* is the magnetic field strength at the surface of the neutron star ($B \sim \mu/r^3$) and R_* is radius of the neutron star. For an order of magnitude approximation, we have $B_* \sim 10^{12}$ Gauss and $R_* \sim 10$ km. Therefore, the magnetic momentum is of the order of $\mu \sim 10^{30}$ Gauss cm^3. This number is similar for magnetic white dwarfs ($B_* \sim 10^4$ Gauss, $R_* \sim 5 \times 10^8$ cm).

The size of the magnetosphere can be obtained by equation the magnetic pressure to the gas and ram pressures of the in-falling material (White & Stella 1988; Frank, King & Raine 1992). By setting $P_{mag}(r_M) = \rho v^2|_{r_M}$ we find,

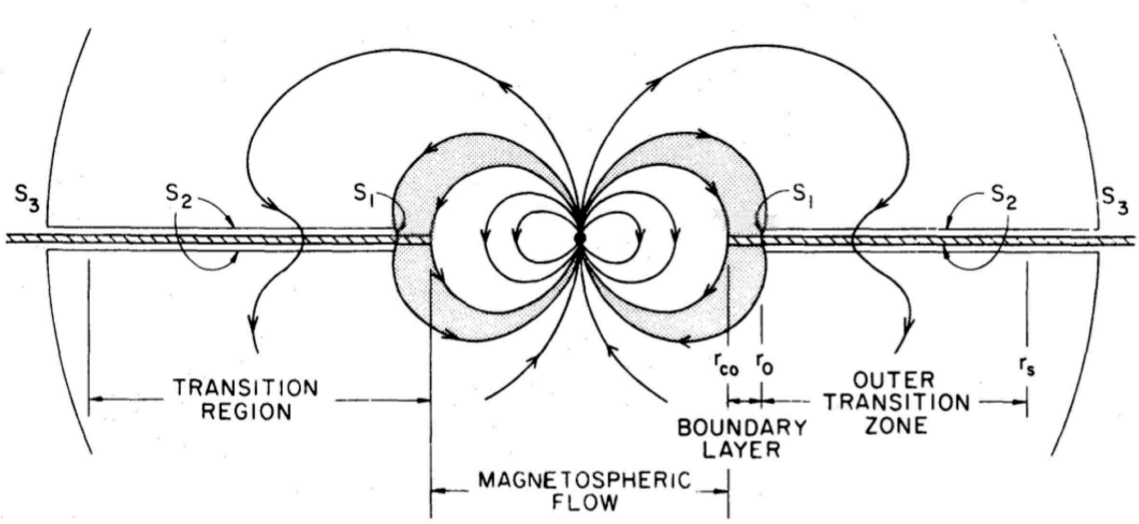

Figure 3.4: Side-view of an accretion flow and the surface S used for accretion torque calculation. See the text for details. *Credit:* Ghosh & Lamb (1979b).

$$\left[\frac{4\pi}{\mu_0}\right]\frac{\mu^2}{8\pi r_M^6} = \frac{(2GM)^{1/2}\dot{M}}{4\pi r_M^{5/2}} \tag{3.35}$$

and derive the Alfvén radius $r_M \approx 8\times10^8 \dot{M}_{-9}^{-2/7} m_{ns}^{-1/7} \mu_{30}^{4/7}$ cm, where $\dot{M}_{-9}$ is the mass accretion rate in $10^{-9}\,M_\odot$ yr $^{-1}$. It is often convenient to replace the mass accretion rate with the observable X-ray luminosity. One gets, $r_M \approx 3\times10^8 m_{ns}^{1/7} R_{10km}^{-2/7} L_{37}^{-2/7} \mu_{30}^{4/7}$ cm, where L_{37} is the X-ray luminosity in 10^{37} erg s^{-1}. Within this radius, the infalling material will flow along the magnetic field lines. At r_M the torque exerted by the magnetic field on the disk is of the order of the viscous torque $G(r_M)$.

Torques on Disk-fed Pulsars

Here we will describe an accurate way to determine the accretion torque using the approach of Ghosh and Lamb (Ghosh, Pethick & Lamb 1977; Ghosh & Lamb 1979a,b, GL hereafter) work.

Consider a surface S enclosing the star (see figure 3.4). Assuming an axisymmetric steady flow of gas, N, or the rate of flow of angular momentum integrated over the whole surface S is given by,

$$N = \int_S \Big(-\rho v_p r^2 \Omega + r\frac{\mathbf{B}_p B_\phi}{4\pi} + \eta r^2 \nabla\Omega \Big)\cdot \hat{\mathbf{n}} dS \tag{3.36}$$

Here, ρ is the matter density, v_p and Ω are the poloidal velocity and the angular velocity of the plasma, respectively. Moreover, $\mathbf{B}_p$ and B_ϕ are respectively the poloidal and toroidal components of the magnetic field, η is the effective viscosity, and $\hat{\mathbf{n}}$ is the outward unit vector normal on the surface S. The three terms of the above formula represent the contributions of the material, magnetic and viscous stress to the total accretion torque. Depending on the selection of the surface S the relative sizes of each component will vary. For example, if we select to place the surface close to the neutron-star surface the

magnetic stress will dominate with decreasing radius and the other two contribution will be negligible. Viscous contribution will significantly contribute only in the outer zone. The torque is communicated to the star almost entirely by the magnetic stress.

To evaluate the torque we will follow the 'recipe' described in GL papers. This is done by using the surfaces shown in figure 3.4, consisting of three parts: 1) a cylindrical surface ($S1$) of height $2h$ located at the border between the boundary layer, and the outer transition zone, 2) a surface of 2 sheets ($S2$) running just above and below the disk, from the location of $S1$ to ∞, and 3) a surface ($S3$) consisting of two hemispherical pieces at infinity. The angular momentum flow-rate through $S1$ is denoted N_0 and is communicated to the neutron star through the field lines that define the boundary layer. Accordingly, the flow-rate through $S2$ is the torque denoted N_{out} which is communicated by the field lines that thread the outer transition zone, and the integral over $S3$ vanishes.

The torque through $S1$, is caused by the accretion material. The viscous stress on the surface is negligible and the magnetic stress has no component normal to $S1$. Also, the angular velocity on the plasma at the iner boundary, r_0 is Keplerian (by definition). So N_0 can be written,

$$N_0 \approx \rho v_r r_{in}^2 \Omega_K(r_{in}) 4\pi r_{in} h = \dot{M}\sqrt{GMr_{in}} \tag{3.37}$$

where, $\Omega_K = (GM/r^3)^{1/2}$ is the Keplerian angular velocity at r in terms of the mass of the NS. N_{out} is given by the magnetic stress on the surface $S2$, since viscous stresses have no component normal to this surface and the material stress is negligible. Therefore,

$$N_{out} = \int_{S_2} r\frac{B_z B_\phi}{4\pi}\, dS = \int_{r_{in}}^{r_s} \gamma_\phi B_z^2 r^2\, dr \tag{3.38}$$

where $\gamma_\phi = -(B_\phi/B_p)_{z=h} = (B_\phi/B_p)_{z=-h}$ by definition. The latter, is the average azimuthial pitch of the magnetic field of the NS at the upper ($z = h$) and lower ($z = -h$) surfaces of the disk between the inner (r_0) and outer (r_s) radius of the transition zone.

Combining the above equations (see GL papers) we can write the net torque as,

$$N = N_0 + N_{out} = n(\omega_s) N_0 \tag{3.39}$$

where $n(\omega_s) = 1.39(1-\omega_s(4.03(1-\omega_s)^{0.173} - 0.878))(1-\omega_s)^{-1}$ is the dimensionless torque and

$$\omega_s = \frac{\Omega_s}{\Omega_K(r_{in})} \approx 1.2 P^{-1} \dot{M}_{17}^{-3/7} \mu_{30}^{-3/7} \Big(\frac{M}{M_\odot}\Big)^{-5/7} \tag{3.40}$$

is the fastness parameter, where P is the spinning period of the neutron star in seconds, $\dot{M}_{17}$ is the mass accretion rate in 10^{17} gr s^{-1}, and μ_{30} is in units of 10^{30} gauss cm^3.

In general, one can write $\dot{\Omega}_s = N/I_{eff}$ where, the moment of inertia (I_{eff}) can be assumed to be roughly constant. Therefore,

$$-\dot{P} = 5 \times 10^{-5} \mu_{30}^{2/7} n(\omega_s) S_1(M) (P L_{37}^{3/7})^2 \,\mathrm{s\,yr}^{-1} \tag{3.41}$$

where ω_s is given from equation 3.40 and $S_1(M) = R_6^{6/7}(M/M_\odot)^{-3/7} I_{45}^{-1}$ where I_{45} is the moment of inertia in units of 10^{45} gr cm^2, R_6 is the NS radius in 10^6 cm, and M the mass of the NS.

The spin-up rate can thus be re-written as $\frac{-\dot{P}}{P} = f_N(\mu, M) P L^{6/7}$. A plot of $-\dot{P}$ against $PL^{3/7}$ avoids any intrinsic scatter due to varying fastness. Figures 3.5 shows the observed dependency for varying M (left panel) and on varying magnetic moment μ_{30} (right panel).

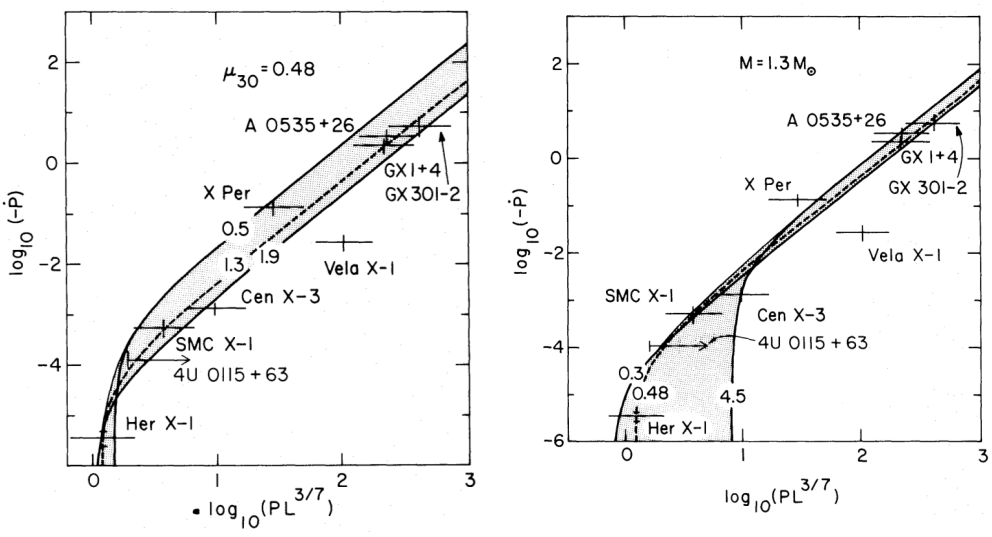

Figure 3.5: Theoretical prediction between spin up rate $-\dot{P}$ against the quantity PL^{37} from the GL model. The stellar magnetic moment is set to $\mu_{30} \sim 0.5$ (on left panel) and the mass of the neutron star $M = 1.3M_\odot$ (on right panel). *Left:* Stellar mass ranges form 0.5 $M_\odot$ to 1.9 $M_\odot$. The shaded area represents this mass span while dashed line corresponds to a mass of $M_{ns} \approx 1.3M_\odot$. *Right:* Magnetic moment scales form $\mu_{30} = 0.3$ to $\mu_{30} = 4.5$. The shaded area represents the magnetic moment span, while the dashed line corresponds to $\mu_{30} = 0.48$. *Credit:* Ghosh & Lamb (1979b).

On very short time scale, Perna, Bozzo & Stella (2006) had modeled the interaction between an accretion disk and the oblique rotator (a NS) resulting in multiple accretion states along the spin period. These states are characterized by different accretion rate at the magnetospheric boundary, regardless of the steady mass-loss rate of the donor star.

3.4 Spectrum of Accreting Neutron Stars

3.4.1 Continuum X-ray emission

The continuum photon spectrum of an accreting pulsar, $N(E)$ (number of photons on the detector per unit time, e.g. sec, per unit energy, e.g. keV) between 2 and 100 keV, can be characterized by a power-law $E^{-\Gamma}$ with a photon index Γ in the range 1 to 2, up to a cut-off energy, $E_{cut} \sim 10 - 20$ keV above which it exponentially drops (White, Swank & Holt 1983; White, Nagase & Parmar 1995; Coburn *et al.* 2002):

$$N(E) = N_0 E^{-\Gamma} exp(E/E_{cut}) \tag{3.42}$$

Figure 3.7 displays the continuum (mostly featureless) emission of a number of accreting pulsars. In each spectrum, the top panel gives the counts spectrum (crosses), the inferred photon spectrum (grey line) and the model spectrum (histogram) while the residuals are displayed in the bottom panel.

An explanation of the continuum emission of accreting pulsars was proposed by Becker & Wolff (2007). In the binary system, the accreted material reaches the magnetic field lines on *the magnetosphere*. Then it follows the magnetic field lines all the way to the stellar

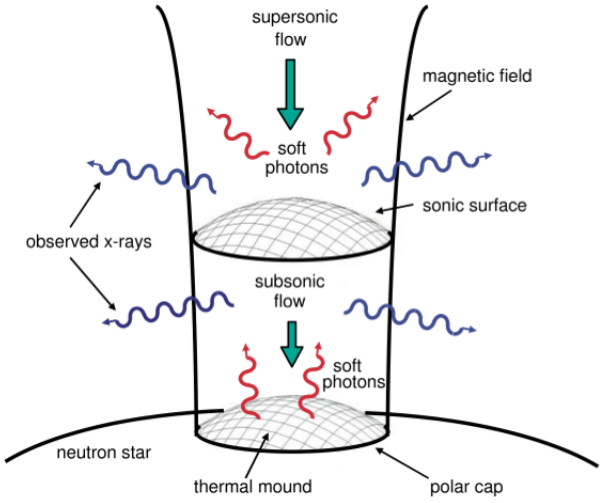

Figure 3.6: A sketch of accretion column. *Credit:* Becker & Wolff (2007)

surface. The geometry close to the stellar surface is limited in a cylinder-like shaped region referred to as *the accretion column*. Material in this column will accelerate and eventually become supersonic. When the accreted matter reaches the NS, it decelerates forming a shock between the in-falling material and the sub-sonic flow close to the NS surface (Davidson 1973).

Within the accretion column, radiative shocks occur above the stellar surface. Seed photons produced via a combination of different processes such as cyclotron, bremsstrahlung, and blackbody radiation, are scattered by high energy electrons. Blackbody seed photons are produced at the surface of the dense thermal mound located at the base of the flow, where local thermodynamic equilibrium prevails. Cyclotron and bremsstrahlung seed photons are produced in the optically thin region above the thermal mound. The geometry is illustrated in figure 3.6.

3.4.2 Cyclotron Lines

Truemper *et al.* (1978) first discovered cyclotron features in Her X-1, at energies slightly larger than 10 keV, that are commonly known as Cyclotron Resonance Scattering Features (CRSFs). CRSFs are of fundamental importance because they allow to directly probe the neutron star magnetic field. The energy, E_c of these features is a measure of the magnetic field, B, in the neutron star's magnetosphere:

$$E_c = \hbar\Omega_c \approx 11.6\, B_{12}(1+z)^{-1}\ \text{keV} \tag{3.43}$$

where, z is the gravitational redshift ($z \sim 0.3$), B_{12} the strength of the magnetic field in 10^{12} Gauss, and $\Omega_c = (eB/m_e c)(1+z)^{-1}$ is the cyclotron resonance frequency. The physical processes underlying these features is the resonant scattering of X-ray photons by electrons whose energy states are the quantized Landau levels in the strong magnetic field. Cyclotron features are also expected to be detected at harmonics, such as $2E_c, 3E_c, ...$

Figure 3.8 displays the cyclotron features as observed by INTEGRAL in V 0332+53 (Kreykenbohm *et al.* 2005). More specifically, the combined JEM-X (red) and IBIS/ISGRI (blue) spectra host three harmonics. The fundamental cyclotron line lies at 25 keV, the

first harmonic at 51 keV, and the 2nd at 72 keV allowing to determine the NS's magnetic field as $B = 2.7 \times 10^{12}$ Gauss. The figure also shows the parametrization: a) the data and the folded high energy cut-off power-law model, b) residuals for model without any CRSFs, c) after fitting the fundamental 25 keV line, d) the fundamental line and the first harmonic at 50 keV have been fitted, and e) all three lines have been fitted.

3.4.3 Fluorescence lines

The iron Kα fluorescence line has been discovered since the very early years of X-ray astronomy, specifically in Her X-1 by Pravdo *et al.* (1977). A metal atom, or an ion with one or more L-shell electron yields the Kα line when a K-shell electron is removed and an L-shell electron makes a radiative transition to the free slot of the K-shell. In accreting pulsars the ionizing X-ray emission ejects the K-shell electron.

A key question is where the fluorescent material is located. Both K-edge and centroid of Kα line depend on the ionization of iron atoms (see fig. 6.4 in chap. 6). Kallman *et al.* (2004) noticed that the center of iron Kα line departs from the 6.4 keV value for iron atom which is at least 18 time ionized. In addition, the iron edge depends more on the ionization and can provide better constrain (e.g. for IGR J17252−3616). Given that the iron Kα line is mainly observed at 6.4 keV, the fluorescent material cannot be too ionized. This rules out any place close to the neutron star, especially the magnetic poles, where the X-ray radiation originally comes from. Another possibility is the atmosphere of the companion star. However, the expected iron fluorescent line is too weak to explain the observations (EW$\sim 100 - 1000$ eV).

In the case of Her X-1, hosting a low mass companion, and fed by Roche Lobe Overflow, most of the fluorescent material might be in the accretion disk or close to the Alfvén surface. On the other hand, in HMXB, the material lies within the wind. Figure 3.9 shows the iron line at 6.4 keV of the sgHMXB Vela X-1, observed with *Chandra*. Recent analysis of a census of accreting pulsar (Torrejón *et al.* 2010a) shows that the iron $K\alpha$ line seems ubiquitous in all X-ray pulsars and that most of the emission is likely compatible with a spherically symmetric distribution of material.

3.4.4 Soft excess

The term *Soft excess* refers to the excess of soft X-ray radiation observed in accreting pulsar when the continuum is modeled using a cutoff power-law. A number of physical processes could be responsible for the soft excess. Hickox, Narayan & Kallman (2004) studied a number of possible emission mechanisms (illustrated schematically in figure 3.10).

- Emission from the accretion column

  The first likely origin of soft excess may be within the accretion column as it provides the harder X-rays. This scenario can explain weak soft X-ray emission but is unlikely for luminous HMXBs, where a region much larger that the size of the neutron star is needed.

- Collisional excitation and emission

  A second possibility is that the emission comes from a collisionally energized cloud. In this case the energy is coming through the wind of the star, $\dot{E} = \dot{M} v_w^2/2$. This emission mechanism, resulting in some 10^{35} ergs s^{-1} can only explain the emission of weak X-ray pulsars.

- Reprocessing by optically thin gas

  In this scenario, material can be energized by the X-ray emission of the neutron star and about 10% can be reprocessed in the soft X-rays. As a forest lines is impossible to resolve using low resolution instruments, a soft excess will be detected. A number of soft X-ray lines has indeed been detected in the spectrum of Vela X-1 (Schulz *et al.* 2002; Watanabe *et al.* 2006).

- Reprocessing by optically thick gas

  The most likely location of the optically thick material is close to the inner edge of an accretion disk. Only a fraction of the hard X-ray radiation will be released as a soft excess, $L_{soft} = \Omega L_X$, where Ω is the solid angle of the reprocessing area. We will study X-ray reprocessing by optically thick material in chapter 8.

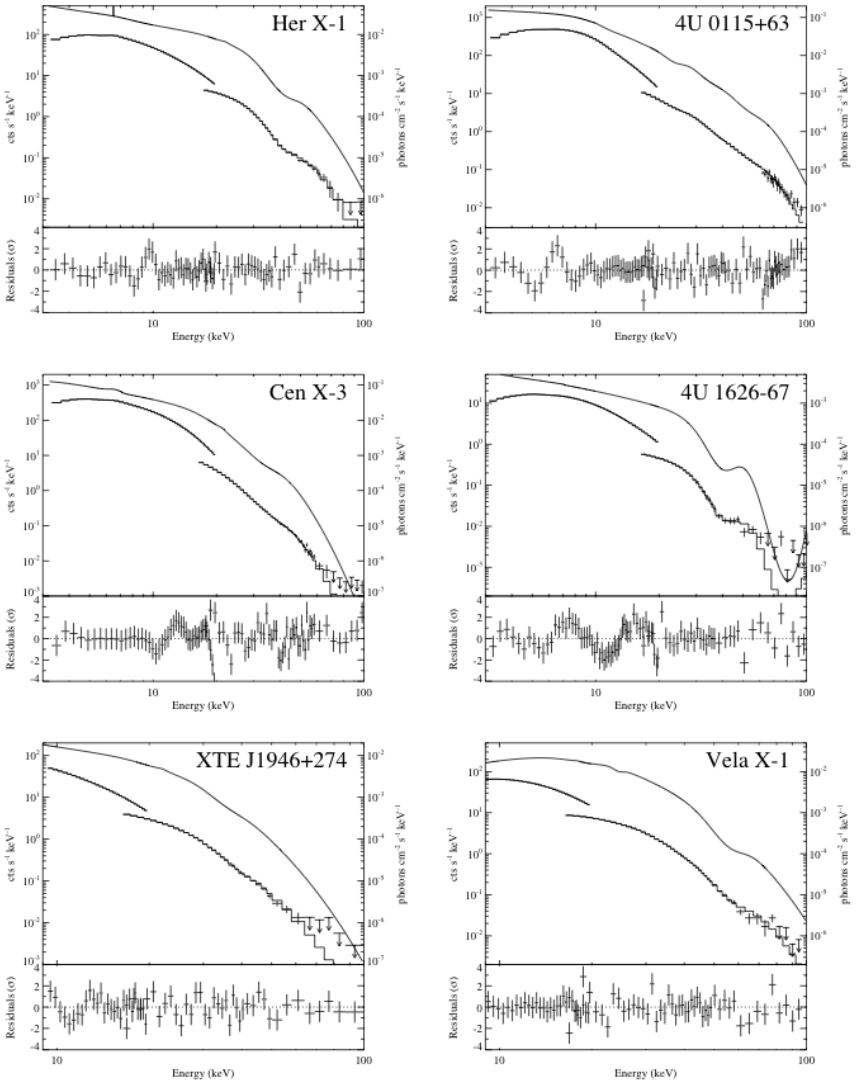

Figure 3.7: X-ray spectra of accreting pulsars from *RXTE*. See the text for details. *Credit:* Coburn *et al.* (2002)

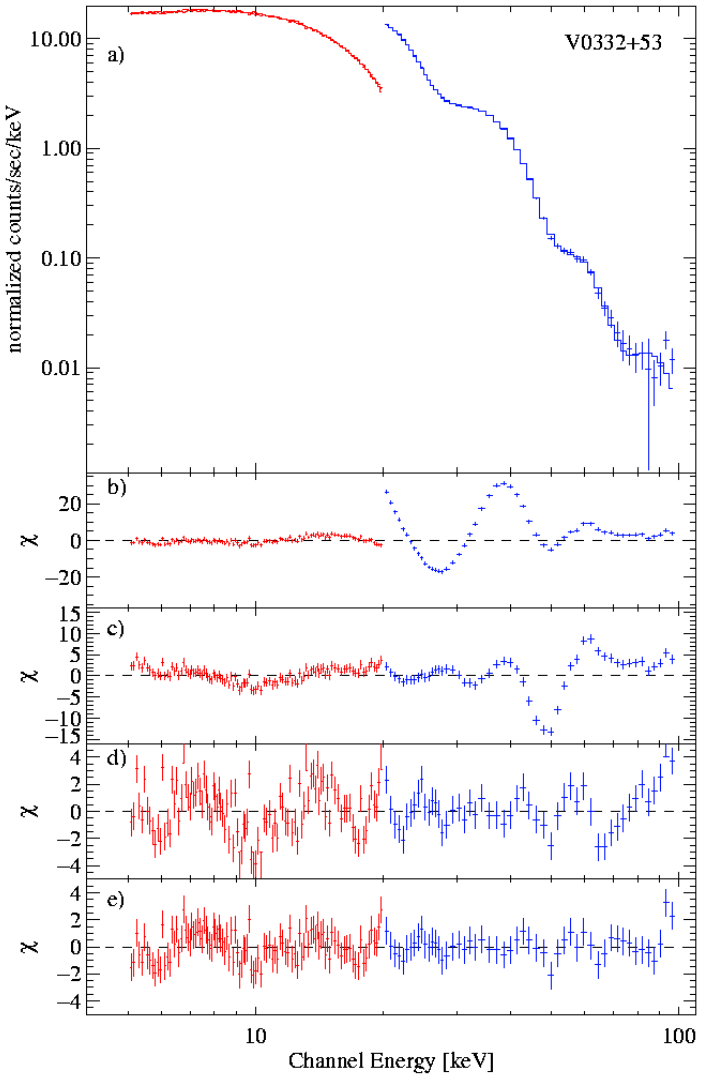

Figure 3.8: V 0332+53 during the 2004-2005 outburst. The fundamental cyclotron line is at 25 keV, the first higher harmonic at 51 keV, and the 2nd at 72 keV allowing to determine the NS's magnetic field to be $B = 2.7 \times 10^{12}$ Gauss. *Credit:* Kreykenbohm *et al.* (2005)

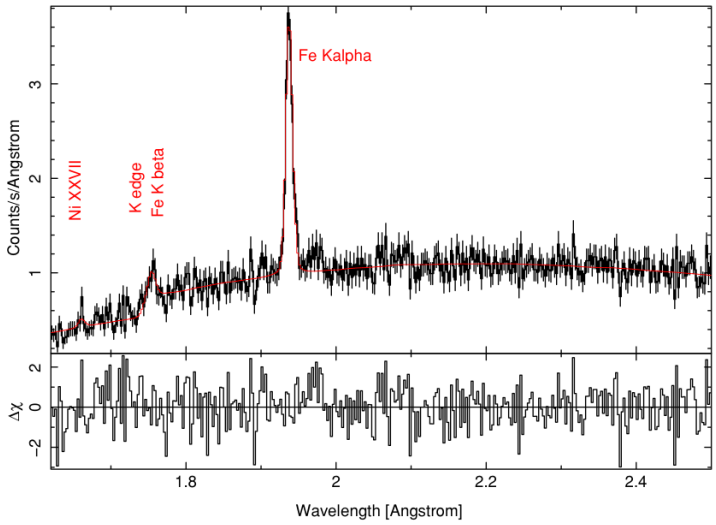

Figure 3.9: *Chandra* observation of Vela X-1. Fe Kα and Kβ lines can be seen. *Credit:* Torrejón *et al.* (2010a)

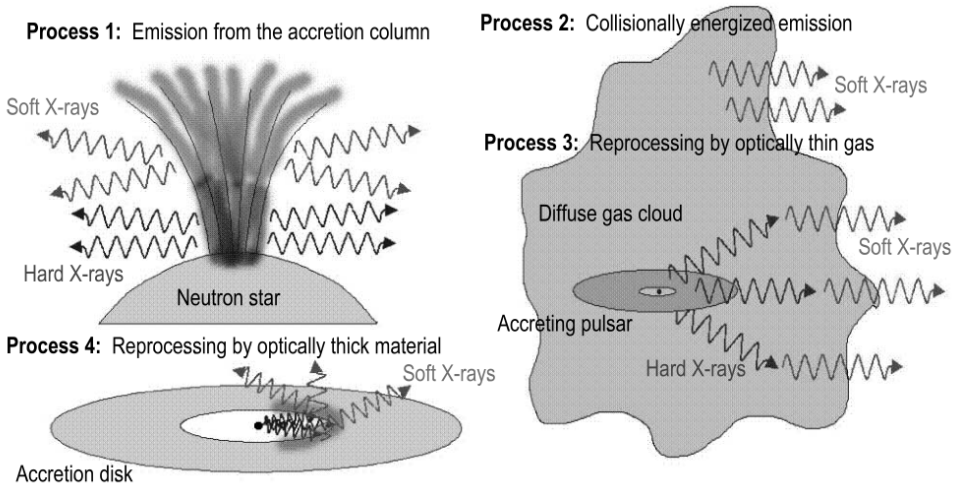

Figure 3.10: The soft excess emission processes discussed in this section. See the text for details. *Credit:* Hickox, Narayan & Kallman (2004)

Chapter 4

Stellar Winds

4.1 Introduction

The spectrum of a hot massive star can be understood, at first-order approximation, as that of a black-body with temperature $T \sim 3 - 5 \times 10^4$ K. Bulk of the emission at that temperature is coming out in the ultraviolet (UV) . This radiation is efficiently absorbed by ions within the stellar wind, which gain momentum. Those ions are responsible for the acceleration of the wind and trace the wind terminal velocity in a spectrum.

Stellar wind can be characterized by two parameters: i) the mass loss rate ($\dot{\mathrm{M}}$) and ii) the terminal velocity (υ_∞). The *mass loss rate* refers to the amount of mass expelled by the massive star per unit of time. Typical mass loss rate of massive stars are of the order of $\dot{\mathrm{M}} \sim 10^{-6}$ $\mathrm{M}_\odot$/year. The *terminal velocity* refers to the velocity of the stellar wind at large distances from the star. Typical values of the terminal velocity in massive stars are of the order of $\upsilon_\infty \sim 1500$ km/sec. Acceleration of the stellar wind in massive stars is discussed in section 4.4.2.

Assuming a spherically symmetric (stationary) stellar wind, the mass loss rate can be derived from the equations of mass continuity, $\dot{\mathrm{M}} = 4\pi r^2 \rho(r) \upsilon(r)$, where r is the distance from the center of the star, $\rho(r)$ is the density and $\upsilon(r)$ is the velocity at that distance. The radial density profile can be parametrized assuming a β-velocity law (Castor, Abbott & Klein 1975):

$$\upsilon(r) = \upsilon_\infty \big(1 - R_*/r\big)^\beta, \tag{4.1}$$

where υ_∞ is the terminal velocity of the wind, R_* is the stellar radius and β is the gradient of the velocity. Figure 4.1 shows the wind velocity as a function of radius for different β values. The gradient describes the density profile, and hence the wind structure.

4.2 Observational aspects

4.2.1 Spectrum of OB stars

In the photosphere of OB stars, a number of elements are responsible for the observed spectral lines. These lines can give a wealth of information regarding the chemical composition, the gravity, rotational velocity, excitation, and ionization. These lines form a fingerprint of the star. The velocity field of the stellar wind adds another imprint on the spectra of massive stars, in particular the P-Cyg profile. Spectral lines formed within the wind can be easily distinguished from those formed in photosphere as they have much

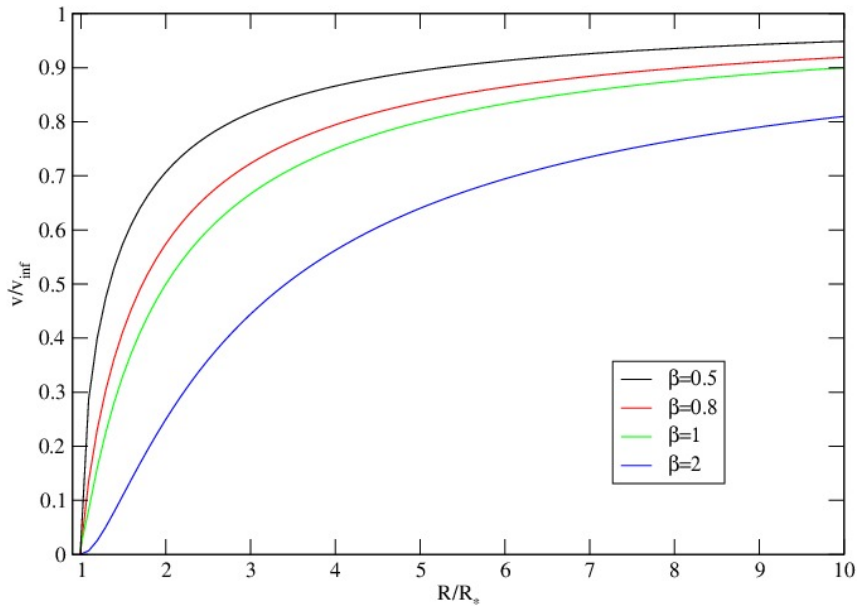

Figure 4.1: The velocity profile of the stellar wind for different values of β.

larger width and/or wavelength shift due to the outflowing motion. The four processes for the line formation in the winds are:

- Line scattering
  If a photon is absorbed by an atom in the wind it will photo-excite an electron to a higher level. After a very short time, the photon will be re-emitted by electro de-excitation to the same original level. The emitted photon will have a slightly different energy, than the original photon, due to the motion of the atom within the wind. Most of the observed P-Cyg profiles are formed by this process.

- Line emission by recombination
  If an atom is excited after a recombination, then a number of transition will occur producing spectral lines. This process is responsible for the formation of the Hα and IR emission lines in the winds of hot stars.

- Line emission from collisional excitation
  Within the wind atoms might collide and excite to higher levels. A subsequent photo-deexcitation to a lower level is then likely. This process is efficient in hot plasmas where collisions are energetic.

- Pure absorption
  Photo-excitation of an atom to a higher level can be followed by spontaneous de-excitation to another, lower, level. This process is the least important in the stellar winds.

4.2.2 P Cygni profile

The observation of a P-Cygni (P-Cyg, hereafter) line profile allows the determination of important stellar wind parameters. The lines showing P-Cyg profile are an essential tool to measure wind terminal velocities and mass loss rates in massive stars. In rough terms,

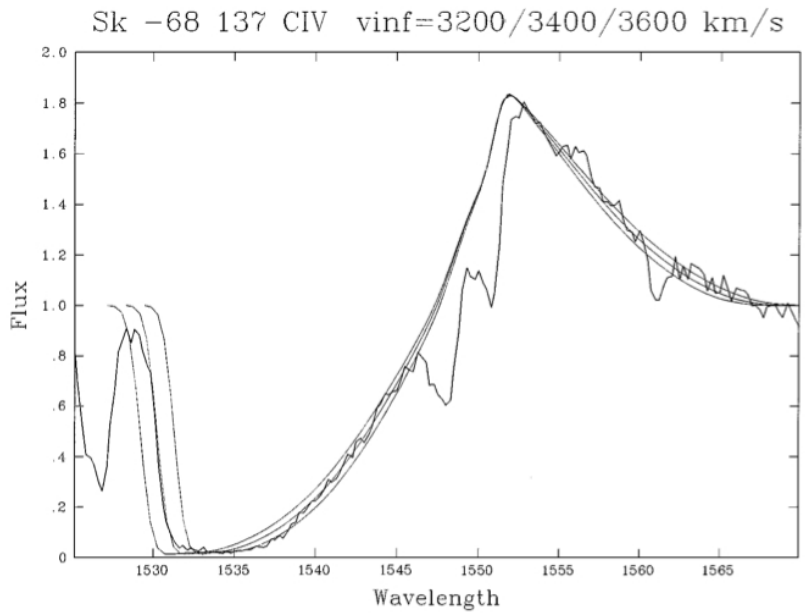

Figure 4.2: P-Cyg Profile of the C IV line from an O3 star SK-68^o 137 in the large magelanic cloud. Simulated line profiles for different values of terminal velocity are shown(υ_∞ = 3200, 3400, 3600 km/s; $\beta = 1.0$). *Credit:*Kudritzki & Puls (2000).

P-Cyg profile consists of a blue-shifted absorption followed by a red-shifted peak. A typical example of a P-Cyg profile is coming from a resonance line, e.g. the C IV line, illustrated in figure 4.2. P-Cyg profiles are observed for the resonance transitions of N V, Si IV, O VI, and C IV in the UV. Similar profiles might also be found in lines at longer wavelength. These lines are also responsible for the acceleration of the stellar wind. Figure 4.2 shows the P-Cyg line and a fit with different terminal velocities.

Although the P-Cyg lines in the UV range are indicative of the terminal velocity of the wind, the basic problem remains that one has to know the mean ionization/excitaion fraction in order to derive a reliable estimate on mass loss rate. An alternative way to determine the mass loss rate is to use of stellar wind emission profile of Hα and to fit it to theoretical models (see figure 4.3, Olson & Ebbets 1981; Leitherer 1988).

Terminal Velocities

A correlation between the effective temperature (T_{eff}) and the escape velocity has been demonstrated by Abbott (1978, 1982) (figure 4.4). The higher the effective temperature (or the earlier the spectral type), the higher the terminal velocity of the wind. We see that for supergiants (LC I) the terminal velocity ranges between 200 and 3000 km/s. For the main sequence and sub giant systems the velocity ranges from 1000 to 3000 km/s. Lower terminal velocities are found in inflated supergiant stars. Stars with similar luminosity class and T_{eff} will show a variety of different gravities and different escape velocities, leading to a wider distribution and a significant spread of terminal velocities.

The photospheric escape velocity is given by,

$$\upsilon_{esc} = \sqrt{\frac{2GM_*}{R_*}} \approx \sqrt{2g_* R_* (1-\Gamma)} \tag{4.2}$$

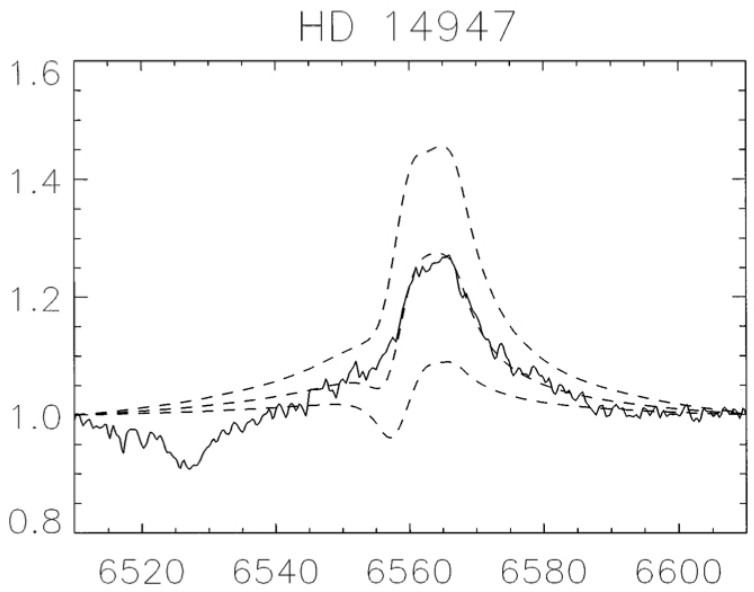

Figure 4.3: P-Cyg Profile of the Hα line from an O5Ia f^+ star HD 14947 compared with mass loss rate of 10,7.5, and 5 $\times 10^{-6}$ $M_\odot$/yr. *Credit:* Kudritzki & Puls (2000).

where, $g_* = GM_*/R_*^2$ is the gravity of the star and $\Gamma = \frac{\sigma_T L}{4\pi G M m_p c}$ is the ratio of the radiative to gravitational accelerations. One can find that the ratio of υ_∞ to υ_{esc} is roughly constant at temperatures larger than $\sim$ 21000 K. Below 21000 K a sudden decrease can be observed. A rough estimate on the connection between the terminal and escape velocities can be parametrized (Kudritzki & Puls 2000):

$$\frac{\upsilon_\infty}{\upsilon_{esc}} = \begin{cases} 2.65, & T_{eff} \geq 21000 \text{ K} \\ 1.4, & 10000 \text{ K} < T_{eff} < 21000 \text{ K} \\ 1.0, & T_{eff} \leq 10000 \text{ K} \end{cases}$$

4.3 Isothermal winds with forces

4.3.1 Isothermal winds

In this chapter we will describe some fundamental properties of stellar winds. In a stationary wind, the velocity at a given distance does not change with time. If we only have gas pressure and gravity the equation of motion is,

$$\upsilon \frac{d\upsilon}{dr} + \frac{1}{\rho}\frac{dp}{dr} + \frac{GM_*}{r^2} = 0 \tag{4.3}$$

The above equations is referred to as the momentum equation, describing the motion of gas for a stationary wind. The first term describes the acceleration which is produced by the pressure gradient (2nd term), under the gravitational field of the primary star (third term). We have assumed that the wind is isothermal, i.e., $T(r) = T$ =constant assuming that the thermal structure is somehow maintained constant.

Assuming that the behavior of the flow is typical of a perfect gas, we have $p = \mathcal{R}\rho T/\mu$, where $\mathcal{R}$ is the gas constant and $\mu \approx 0.6$ is the mean atomic weight. By substituting

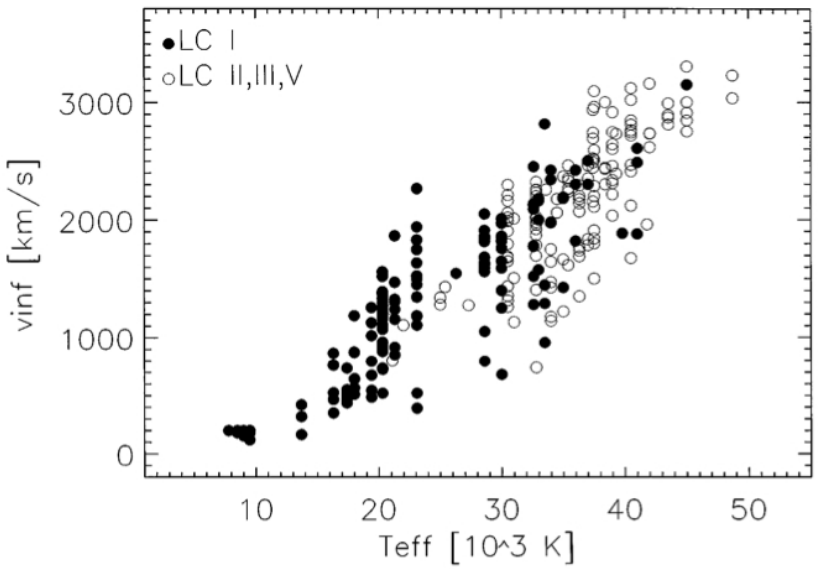

Figure 4.4: Wind terminal velocities as a function of effective temperatures of hot massive star for different luminosity classes. *Credit:* Kudritzki & Puls (2000).

pressure into equation 4.3 and converting density gradient to velocity gradient by using the continuity equation, on can conclude,

$$\upsilon\frac{d\upsilon}{dr}+\frac{\mathcal{R}T}{\mu}\Big\{-\frac{1}{\upsilon}\frac{d\upsilon}{dr}-\frac{2}{r}\Big\}+\frac{GM_*}{r^2}=0 \text{ or}$$
$$\frac{1}{\upsilon}\frac{d\upsilon}{dr}=\Big\{\frac{2a}{r}-\frac{GM_*}{r^2}\Big\}/\{\upsilon^2-a^2\} \tag{4.4}$$

where $a=(\mathcal{R}T/\mu)^{1/2}$ is the isothermal speed of sound. The latter is constant for an isothermal wind. One has to define the lower boundary condition for this equation. We set $\upsilon(r_0)=\upsilon_0$, where r_0 is similar or larger than the photospheric radius.

From the previous equation we can extract a singularity at the point where $a=\upsilon$. One sees that the numerator of equation 4.4 goes to zero at $r=r_c=GM_*/2a^2$. This is referred to as the *critical point*. If the critical point is located within the photosphere ($r_c<r_0$), the assumption of an isothermal wind is no more valid. From the above equation one can derive the velocity as,

$$\upsilon\exp\Big(-\frac{\upsilon^2}{2\alpha^2}\Big)=\alpha\Big(\frac{r_c}{r}\Big)^2\exp\Big\{-\frac{2r_c}{r}+\frac{3}{2}\Big\} \tag{4.5}$$

under the condition $\upsilon(r_c)=\alpha$ at the critical point.

We also need to describe the initial velocity at the lower boundary of the isothermal region by applying the above equation at r_0. At the lower boundary condition ($\upsilon_0<<\alpha$) the initial velocity is given by,

$$\upsilon_0\approx\alpha\Big(\frac{\upsilon_{esc}(r_0)}{2\alpha}\Big)^4\exp\Big\{\frac{\upsilon^2_{esc}(r_0)}{2\alpha^2}+\frac{3}{2}\Big\} \tag{4.6}$$

The above equation shows that an isothermal wind that is only driven by gas pressure can become supersonic if and only if the initial velocity υ_0 has a very specific value.

The velocity gradient throughout the wind can then be written,

$$\frac{\upsilon}{\upsilon_0}\exp\Big(-\frac{\upsilon^2}{2\alpha^2}\Big)=\Big(\frac{r_0}{r}\Big)^2\exp\Big\{\frac{GM_*}{\alpha^2}\Big(\frac{1}{r_0}-\frac{1}{r}\Big)\Big\} \tag{4.7}$$

For large distances, where $r >> r_0$ the velocity law goes like, $\upsilon \approx 2\alpha\sqrt{\ln(r/r_0)}$. This increases infinitely as a consequence of the assumption that the wind is isothermal at large distances. In reality winds can be isothermal up to a certain distance. After that distance the velocity does not increase significantly.

The density structure can now be obtained through the mass continuity equation, and this yields,

$$\frac{\rho}{\rho_0}\exp\Big\{\frac{1}{2}\Big(\frac{\upsilon_0\rho_0 r_0^2}{\alpha\rho r^2}\Big)\Big\}=\exp\Big\{-\frac{GM_*}{\alpha^2}\Big(\frac{1}{r_0}-\frac{1}{r}\Big)\Big\} \tag{4.8}$$

This can be solved numerically. A good approximation in the subsonic region can be achieved by assuming a hydrostatic atmosphere. In this case the density will be given by $(1/\rho)*(dp/dr)+GM_*/r^2=0$. Therefore, the distribution can be derived as follows,

$$\frac{\rho(r)}{\rho_0}=\exp\Big\{-\frac{(r-r_0)}{\mathcal{H}_0}\frac{r_0}{r}\Big\} \tag{4.9}$$

where, $\mathcal{H}_0=\mathcal{R}T/\mu g_0$ and $g_0=GM_*/r_0^2$. Figure 4.5 shows the distribution of velocity and density from an isothermal wind. The behavior of both analytic and numerical solutions are very similar in the subsonic part of the flow at r/r_0 <1. After that point a deviation can be seen (dashed line).

From the density and velocity distributions, we can derive the mass loss rate of the star. We suppose a star of radius R_* and mass M_* with a coronal temperature T_c which has a density ρ_0 at the base of the atmosphere. We have assumed that the coronal temperature is roughly constant. As the density in the subsonic region varies exponentially out to r_c we have:

$$\dot{\mathrm{M}}=4\pi\rho_c\alpha r_c^2\approx 4\pi\rho_0\alpha r_0^2\Big(\frac{r_c}{r_0}\Big)^2\exp\Big\{-\frac{r_c-r_0}{\mathcal{H}_0}\cdot\frac{r_0}{r_c}\Big\} \tag{4.10}$$

For the Sun ($T_c=10^6$ K, $\rho_0=10^{-14}$ gr cm^{-3}, $r_0=10^{11}$ cm) the mass loss rate is estimated to be $\dot{M}\approx 1.5\cdot10^{-14}$ M$_\odot$ yr^{-1}, in good agreement with an observed value of $\sim 2\cdot10^{-14}$ M$_\odot$ yr^{-1}.

4.3.2 Case I: Force $f\sim r^{-2}$

In this paragraph we examine the case of an isothermal wind with a simple force of the form $f\sim r^{-2}$. Force of this form can be produced by radiation pressure due to optically thin lines or continua such as electron scattering or dust scattering. In this case, the radiative flux varies as r^{-2} and thus the radiation acceleration $g=\kappa_F F(r)/c=\kappa_F F(R_*)(r/R_*)^{-2}/c\sim r^{-2}$ where κ_F is the flux-mean opacity independent of distance.

Equation 4.3 can now be modified to include the new term, $f=c\cdot r^{-2}$ as follows,

$$\upsilon\frac{d\upsilon}{dr}+\frac{1}{\rho}\frac{dp}{dr}+\frac{GM_*}{r^2}-\frac{c}{r^2}=0 \tag{4.11}$$

In this equation c is a positive constant in the region where the force acts, and zero outside that region. Similarly equation 4.4 can be re-written as,

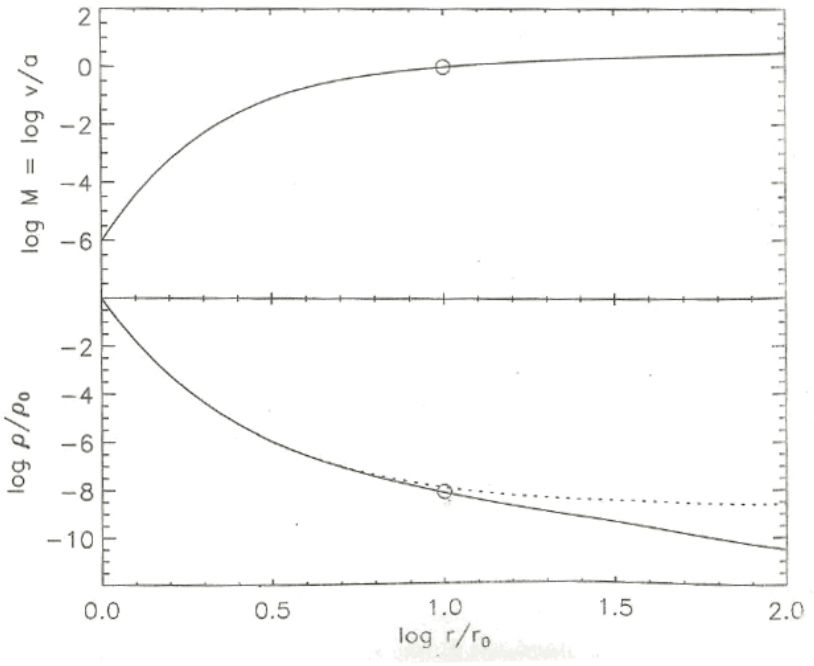

Figure 4.5: Velocity (in terms of Mach number) and the density (in terms of density at r_0) as a function of r/r_0. The distance at critical point $r_c = 10r_0$ is shown by a circle. The dashed line represents the density distribution by a hydrostatic atmosphere at the same temperature. The two density distribution are very similar in the subsonic region. *Credit:* Lamers & Cassinelli (1999)

$$\frac{1}{\upsilon}\frac{d\upsilon}{dr} = \left\{\frac{2a}{r} - \frac{GM_*}{r^2} + \frac{c}{r^2}\right\}/\{\upsilon^2 - a^2\}. \tag{4.12}$$

We can have a critical solution if the nominator and denominator reaches zero at the same point. Therefore the structure of this equation is rather similar to the case of an isothermal wind with gas pressure only. This implies, as we have seen, that there is one critical solution for one particular value of the initial velocity υ_0 and mass loss rate if the lower boundary conditions of the isothermal region are known. This solution depends on ρ_0, T, and r_0 for a region where $c \neq 0$.

We will now discuss the case of $c > 0$ applied throughout the wind as expected e.g. from an ionized wind with radiation pressure due to electron scattering. In this case equation 4.12 is equivalent to that of a wind without an extra force if the stellar mass is also modified accordingly by an effective mass, $M_{eff} = M_* - c/G = M_*(1 - \Gamma)$, where $\Gamma = c/GM_*$ with $\Gamma_{max} \approx 1$ if $2\alpha << \upsilon_{esc}(r_0)$.

For $\Gamma = 0$ we obtain the previous solution of the gas pressure only solution. For Γ <1 or $M_{eff} > 0$ the conditions of the critical point are the same as equation 4.12. Although that the velocity remains the same ($\upsilon(r_c) = \alpha$) at the critical point, the point itself, r_c is now closer to the star by a factor of $(1 - \Gamma)$.

Therefore, the critical point is defined as a function of Γ, when it changes from zero to possitive values. $r_C(\Gamma) = \{GM_*(1 - \Gamma)\}/2\alpha^2$ until Γ reaches its maximum value such as $r_c = r_0$ at the bottom of the isothermal regions, where $\Gamma_{max} = 1 - (2\alpha^2 r_0)/(GM_*) = 1 - \{2\alpha/\upsilon_{esc}(r_0)\}^2$

Velocity and density structure in the subcritical part of the plot are affected by $\Gamma > 0$

only. The same is also valid for the mass loss rate. For a force with $0 < \Gamma < \Gamma_{max}$ applied in the subsonic part of the wind the velocities gradient will be smaller but the velocities will be larger and the critical point moves closer to the star.

Adopting the scaling of some parameters of the form, $r_c \rightarrow r_c(1-\Gamma)$, $\upsilon_{esc}^2 \rightarrow \upsilon_{esc}^2(1-\Gamma)$, and $\mathcal{H} \rightarrow \mathcal{H}/(1-\Gamma)$, the mass loss rate increases by,

$$\frac{\dot{M}}{\dot{M}(\Gamma=0)} = (1-\Gamma)\cdot\exp\Big\{\frac{\Gamma r_0}{\mathcal{H}(\Gamma=0)}\Big\} \tag{4.13}$$

4.3.3 Case II: Force $f \sim \upsilon(d\upsilon/dr)$

In this paragraph we discuss a second example of a force which can be expressed in a simple analytic form. The acceleration of the wind in OB stars occurs through radiatively driven winds. The responsible ions for the acceleration absorb a photon which is seen redshifted from its rest wavelength. The amount of radiative momentum absorbed per cm^3 per sec by the optically thick lines (e.g. C IV) is $F_\nu(r)\Delta\nu/c$, where F_v is the monochromatic flux at distance r and $\Delta\nu$ is the Doppler shift due to the velocity gradient over a distance Δr =1 cm, so $\Delta\nu = (\nu_0/c)(d\upsilon/dr)\Delta r$. The force is proportional to the momentum of the absorbed radiation per unit volume and per unit mass is, $f_{rad} \sim \rho^{-1}r^{-2}(d\upsilon/dr) \sim \upsilon(d\upsilon/dr)$. This example is of particular interest for hot massive stars. We will discuss in details this acceleration mechanism in paragraph 4.4.2.

The newly derived momentum equation is of the form,

$$\upsilon\frac{d\upsilon}{dr} + \frac{1}{\rho}\frac{dp}{dr} + \frac{GM_*}{r^2} - c\cdot\upsilon\cdot\frac{d\upsilon}{dr} = 0, \tag{4.14}$$

where c is a positive constant which accounts for the number of optically thick lines and on the flux at their wavenumbers. The velocity gradient can be re-written accordingly,

$$\frac{1}{\upsilon}\frac{d\upsilon}{dr} = \Big\{\frac{2\alpha^2}{r} - \frac{GM_*}{r^2}\Big\}/\{\upsilon^2(1-c) - a^2\} \tag{4.15}$$

The radiative acceleration, the last term in equation 4.14, introduces an extra factor of the form (1-c) in the denominator of the momentum equation. The latter equation is similar to equation 4.4 if we transform $\upsilon(r) \rightarrow \upsilon'(r) = \upsilon(r)(1-c)^{-1/2}$ for $c < 1$. This implies that the properties of the critical point also apply here.

Therefore at the critical point $r_c = GM_*/2\alpha^2$, the velocity is given by, $\upsilon(r_c) = \alpha/(1-c)^{-1/2}$. The location of the critical point here is the same as in the wind without external forces. However, with a velocity decreased by a factor of $(1-c)^{1/2}$.

The velocity transformation described above allows an easy derivation of the mass-loss rate from an isothermal wind with a radiative force of the form $f = c\upsilon(d\upsilon/dr)$ and, one gets

$$\dot{M} \approx \frac{4\pi\rho_0\alpha r_0^2}{\sqrt{(1-c)}}\Big\{\frac{\upsilon_{esc}}{2\alpha}\Big\}^2\exp\Big\{-\frac{\upsilon_{esc}^2(r_0)}{2\alpha^2} + \frac{3}{2}\Big\} \tag{4.16}$$

The mass loss rate is a factor of $(1-c)^{1/2}$ smaller than the one obtained with gas pressures only. With a velocity that is always larger by a factor of $(1-c)^{-1/2}$ and a mass loss rate which is larger by the same factor, the density distribution will be identical to the one derived in the force-free case.

For $c > 1$ when the force is large, one derives a negative denominator of the momentum equation for all the values of v. So the velocity will increase in the region $r_0 < r < r_c$ reaching its maximum at r_c and decrease outwards. This situation is physically unrealistic as we will see in section 4.4.

4.4 Line driven winds

Hot stars are emitting most of their radiation in the UV where the atmosphere of the star has many absorption lines. The opacity of the C IV resonance line at 1550 Å is much (almost a factor of a million) larger than the opacity of the continuum due to electron scattering.

A static atmosphere, with strong lines absorbing the radiation of the underlying photosphere, will absorb or scatter the radiation. Therefore, the outer layer will not receive direct radiation from the photosphere at the wavelength of the lines. As a result, the acceleration of the outer layer of the stellar atmosphere due to spectral lines will be significantly reduced. However, in the case of a moving atmosphere (outflow) the velocity gradient will allow the atoms in the atmosphere to 'see' the photosphere of the star redshifted. As a consequence, the atoms of the outer layers of the atmosphere will be able to absorb radiation from the photosphere that is not attenuated by the intermediate layers. Thus, the Doppler shift allows the atoms to absorb an unattenuated continuum in their spectral line transitions. This makes the radiative acceleration due to spectral line in the atmosphere of hot massive stars a very efficient driving mechanism.

4.4.1 Sobolev Approximations

Absorption (and/or scattering) in an expanding atmosphere takes place in a very limited frequency window. This region is referred to as the 'line interaction region' defined by,

$$(\nu_0 - 1.5\Delta\nu_G) \leq \nu_p \leq (\nu_0 + 1.5\Delta\nu_G)(1 + v_\infty/c) \tag{4.17}$$

where ν_p is frequency of the photon emitted by the photosphere, ν_0 is the frequency of the transition line, $1.5\Delta\nu_G$ is defined as the 90% content of the line (assuming a gaussian line profile), v_∞ is the terminal velocity of the wind, and c is the speed of light. Photons with frequencies $\nu_p < \nu_0 - 1.5\Delta\nu_G$ will not have an interaction region within the wind, photons with frequencies $\nu_p > (\nu_0 + 1.5\Delta\nu_G)(1 + v_\infty/c)$ cannot be absorbed either. Specific geometry and velocity profile define the line interaction region geometrically.

The Sobolev approximation assumes that this interacting region is infinitely narrow. The limit can be reached when the width of the line profile function, $\phi(\Delta\nu)$, is so small that ϕ can be treated as a delta-function, $\phi(\Delta\nu) \rightarrow \delta(\Delta\nu)$. In this case, the optical depth depends only on the local conditions where the absorption occurs. Also, in Sobolev approximation the line interaction region tends to be a point. This is called the Sobolev point in frequency domain.

$$\nu_0 = \nu_p\big(1 - v_z(r_S)/c\big) \tag{4.18}$$

where $v_z(r_S)$ is the component of the wind velocity at r_S in the direction of z (Note: the observer is placed at $z = +\infty$).

A schematic illustration of the line profile and the corresponding optical depth is given in figure 4.6. The Sobolev approximation is shown in figure 4.6 (bottom) by representing the line profile by a δ-Dirac function and the corresponding optical depth by a step function.

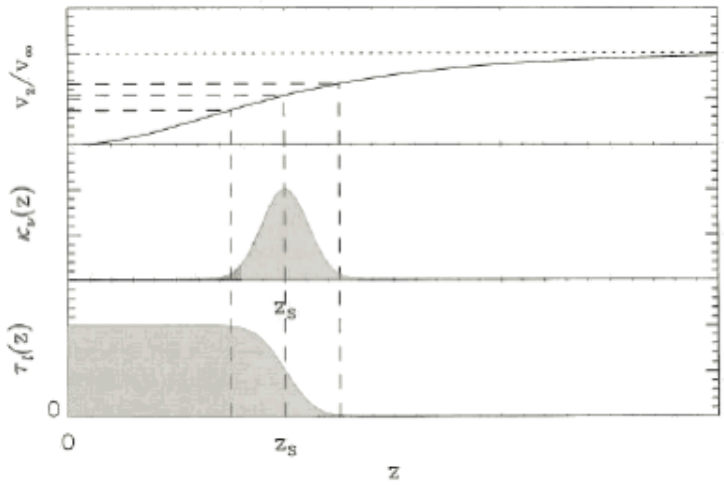

(a) No approximation

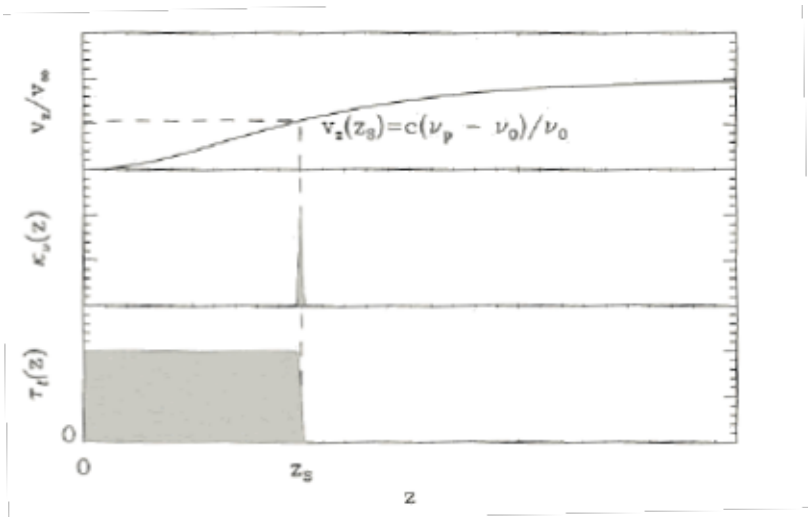

(b) Sobolev apprximation

Figure 4.6: Schematic view of the Soboloev approximation *Credit:* Lamers & Cassinelli (1999)

4.4.2 A realistic approach: CAK/Sobolev model

The winds of hot luminous stars are driven by absorption in spectral lines and referred to as line driven winds. The bulk emission of hot stars is in the ultraviolet where the outer atmosphere of these stars have many absorption lines. Radiatively driver stellar wind were developed by Castor, Abbott & Klein (1975). This model assumes that UV resonance lines (like C IV, N IV, O IV, etc) are able to accelerate the stellar wind.

The net radiative force, accelerating the stellar wind, due to spectral transitions lines is given by

$$g_L = \frac{2\pi}{c} \sum_l \kappa_l \int_{\mu_*}^{1} I_{\nu,l} \frac{1 - e^{-\tau_{\nu,l}}}{\tau_{\nu,l}} \mu d\mu \tag{4.19}$$

The above equation add the contribution of each spectral line, denoted by the index l.

CAK assumes that the total radiative acceleration due to all spectral lines can be derived as a result of the radiative acceleration due to electron scattering times a multiplication factor, $M(t)$, which is called force multiplier.

$$g_L = g_e^{ref} M(t) \tag{4.20}$$

where,

$$g_e^{ref} \equiv \frac{\sigma_e^{ref} \mathcal{F}}{c} = \frac{\sigma_e^{ref} L_*}{4\pi r^2 c} \tag{4.21}$$

where $\sigma_e^{ref} = 0.325$ cm^{-2} gr^{-1} (Castor, Abbott & Klein 1975) is the reference value for the electron scattering opacity. The core problem is the investigation of the force multiplier, $M(t)$, which depends on the ionization, excitation, and chemical composition of the wind. The ionization is also affected by the stellar parameters (e.g. T_{eff}). The situation is getting more complicated in binary systems where the ionization is also affected by the compact object. This scenario is discussed in chapter 7.

CAK approximated the force multiplier by

$$M(t) = kt^{-\alpha}(10^{-11} n_e / W)^{\delta} \tag{4.22}$$

where the quantities k, α, and δ are called the force multiplier parameters. The parameter n_e is the electron density and $W(r)$ is called the geometrical dilution factor. Parameter $t \equiv \sigma_e^{ref} \upsilon_{th} \rho (dr/d\upsilon)$ is the dimensionless optical depth parameter, where υ_{th} is the mean thermal velocity of the protons in the wind with a temperature T_{eff}.

Therefore, the radiative acceleration due to spectral line can be re-written as

$$g_L = \frac{\sigma_e^{ref}}{4\pi r^2} \frac{L_*}{r} k t^{-\alpha} (10^{-11} n_e / W)^{\delta} \tag{4.23}$$

We used the VH1 hydrodynamic code (see chapter 7) to calculate the wind mass loss rate and the terminal velocity of the wind as a function of the CAK parameters. The only forces applied for acceleration are the gravity and the radiative force based on the CAK/Sobolev approximation. Several simulations were performed for various set of parameters (see tables 7.1 and 7.2). This simulation starts with an initial ($t = 0$) velocity field of 0 km s^{-1} and follows the wind evolution. The wind relaxes to a stationary solution after after a few days. Figure 4.7 shows the wind velocity profile evolving with time for the parameters of Vela X-1/HD 77581 (CAK k=0.35, CAK-α=0.55, and $\rho_{in} = 1E-12$ gr cm^{-3}). The wind was then fit with the β velocity law (eq. 4.1) resulting in $\upsilon_\infty = 1.75 \times 10^8$ cm s^{-1} and $\beta = 0.8$, corresponding to a mass loss rate of $\sim 2 \times 10^{-6}$ M$_\odot$ yr^{-1}.

4.5 Stellar Wind Instabilities: Clumpy structures

4.5.1 Observational evidences

The presence of clumping as extreme density fluctuations in hot stars was first invoked by Osterbrock & Flather (1959). Besides studying wind clumping in X-ray binaries (in't Zand 2005; Walter & Zurita Heras 2007), Cherepashchuk, Khaliullin & Eaton (1984) observed V444 Cyg and first noticed differences in the shape and depth of eclipses in the UV and IR. This results could not be interpreted using a smooth wind. Individual density condensation were needed.

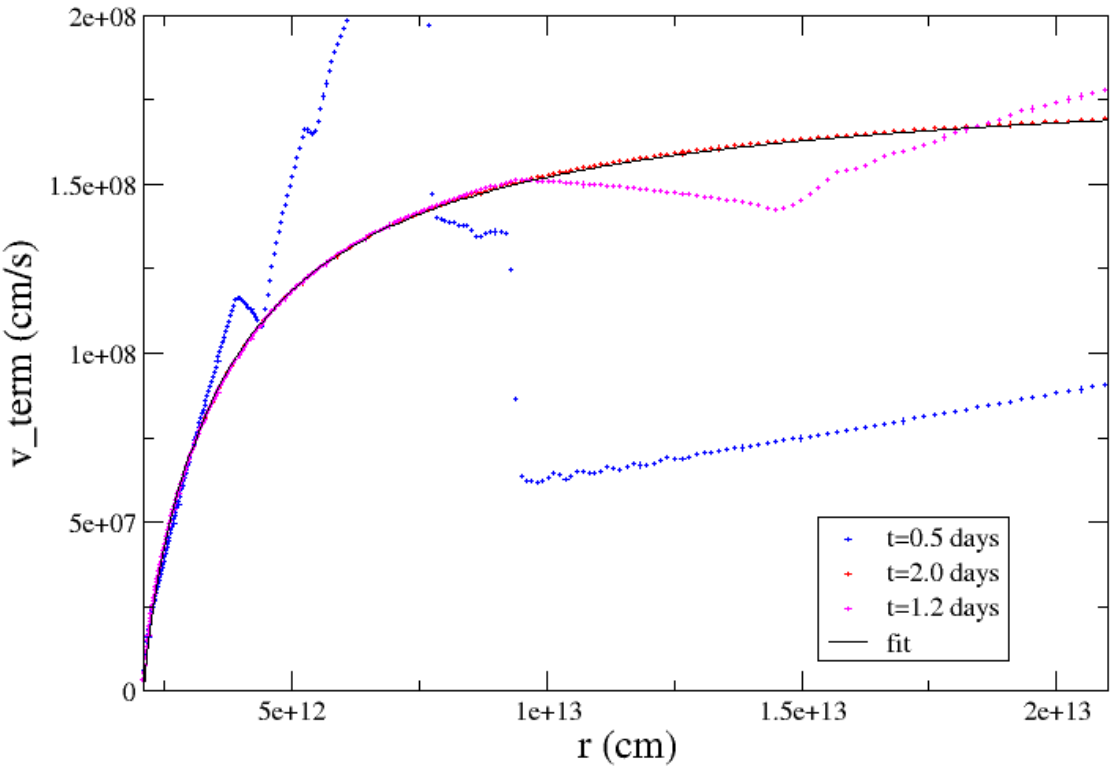

Figure 4.7: Velocity profile as a function of radius for a number of time steps. Symbols show the velocity profile evolution while the solid line shows the fit to eq. 4.1. The resulting fit parameters are are $\upsilon_\infty = 1.75 \times 10^8$ cm s^{-1} and $\beta = 0.80$.

For OB stars, first investigations were carried out by Eversberg, Lepine & Moffat (1998) on the He II 4686 line in z Pup, which revealed outward moving inhomogeneities in its wind, starting near the stellar surface up to at least ~ 2 R$_*$. The clumping properties of O and WR stars are similar. Lépine & Moffat (2008) showed that the moving sub-peaks identified on top of the broad emission lines in WR-stars appear also in the Of stars z Pup and HD93129A and concluded that stochastic wind clumping is a universal phenomenon in the radiation-driven, hot winds of massive stars. In addition, X-ray observation of Galactic O stars revealed that the emission line profile require the presence of a hot plasma embedded in a highly clumped cool wind (Oskinova, Feldmeier & Hamann 2006).

For O-stars, we have to rely mostly on indirect methods to address the clumping properties. By comparing the observed and predicted wind-momentum luminosity relationship (WLR) for a sample of galactic O-stars, Markova *et al.* (2004) demonstrated that a clumping factor, f_{cl} ∼5, of the clumped matter, was needed resulting in a net reduction of the mass-loss rate by a factor of ~ 3.

4.5.2 Theoretical predictions

Applying a perturbation analysis to the CAK/Sobolev steady state wind, the radiatively driven wind becomes highly unstable. The growth of perturbations with a length smaller than $v_{th}/(dv/dr)$ creates small scale structures (Owocki 1994). These instabilities will lead to the creation of shocks (Owocki, Castor & Rybicki 1988). Clumpy wind can affect the interpretation of observable quantities (e.g. $\dot{M}$) by a factor of $\sim 5 - 10$.

Figure 4.8 (left panel) illustrates the results of a 1D simulation, starting from an initial condition set by a smooth, steady-state CAK/Sobolev model. Instabilities lead to extensive structure in both velocity and density. In the outer wind, the velocity variations become highly nonlinear, with amplitudes approaching 1000 km s^{-1}, leading to formation of strong shocks. For most of the wind mass, the dominant overall effect of the instability is to concentrate material into dense clumps, leading to a density contract up to 10^{4-5}. The right panel of the same figure shows the resulting 2D density structure at fixed time intervals of 4000 sec starting from the CAK initial condition at the top.

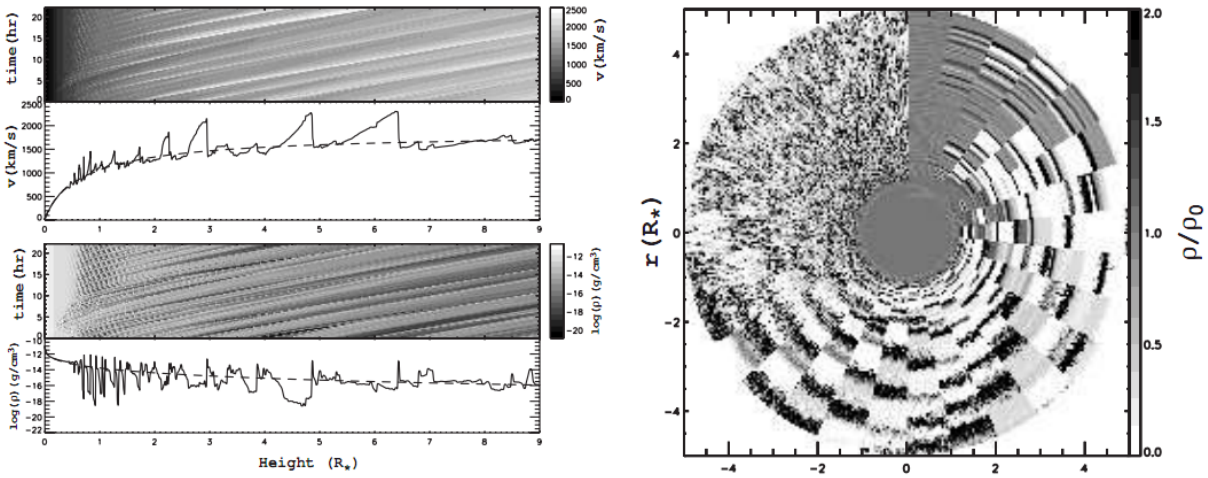

Figure 4.8: *Left:* Results of 1D simulation. The line plots show the spatial variation of velocity (upper) and density (lower) at a xed, arbitrary time snapshot. The dashed curve shows the corresponding smooth, steady CAK model. *Right:* For 2D simulation, grayscale representation for the density variations rendered as a time sequence of 2-D wedges of the simulation model azimuthal range $\Delta\phi = 12^o$ stacked clockwise from the vertical in intervals of 4000 sec from the CAK initial condition. *Credit:* Owocki (2004)

Figure 4.9 shows the effect of clumping on spectral lines in O-star spectra (a clumping factor of $f_{cl} =< \rho^2 > / < \rho >^2 = 50$ was used in that model (Bouret, Lanz & Hillier 2005b)). The mass-loss rate derived in this example, assuming a clumpy wind, is reduced by a factor of ~ 7, when compared to the value obtained assuming a smooth wind. In general, mass loss estimates are reduced by $f_{cl}^{1/2}$ when clumpy wind are considered.

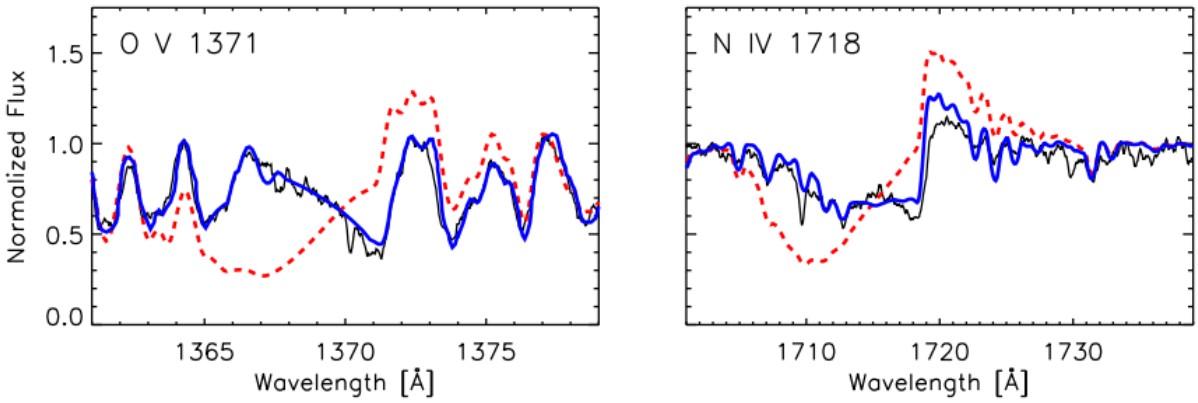

Figure 4.9: Black lines show observed line profiles of O V (1371Å) and NIV (1718Å) for an O4 star. The blue lines show the results of a clumpy stellar wind model. Dotted lines show the profiles predicted by a smooth wind model . *Credit:* Bouret, Lanz & Hillier (2005a)

PART II: Accretion in High Mass X-ray Binaries

Chapter 5

INTEGRAL discovery of new HMXB systems

5.1 Introdution

INTEGRAL has been observing the galactic plane for a very long time since 2002. The large field of view of the INTEGRAL/IBIS imager (see chap. 2) and its hard X-ray sensitivity make of *INTEGRAL* an efficient tool to detect strongly obscured sources that could not be recognized in the X-rays and fast transients sources discovered serendipitously. Figure 5.1 shows the INTEGRAL/IBIS exposure map (in galactic coordinates) for the first 800 revolutions, from 2002 to 2009. The figure highlights that the galactic plane has been extensively observed .

Among the newly discovered sources two are of particular interest, i.e. IGR $J16318-4848$ and IGR $J17544-2619$. Both are the archetypes of heavily obscured persistent sgHMXB and supergiant fast X-ray transients, respectively. These source types have been revealed by *INTEGRAL*. Table 5.1 lists the sources discovered by *INTEGRAL* that are members of these two classes.

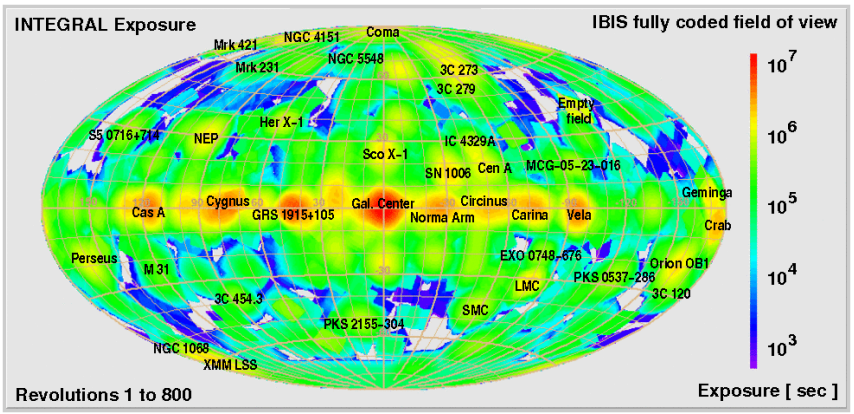

Figure 5.1: *INTEGRAL* exposure map. The exposure time is color-coded. *Credit:* ISDC.

Although *INTEGRAL* is a very efficient instrument to identify these sources, the source localization is limited to ~ 2 *arcmin*. Within this *error box* a large number of possible optical/IR counterparts could be found. Thanks to high resolution X-ray observatories, such as $XMM-Newton$, *Chandra*, and *swift* resolution of $\sim$ *arcsec* could be

obtained. Follow-up observations allow to accurately pin-point the X-ray counterpart and then the optical/IR counterpart. Due to the heavy inter-stellar absorption in the direction of these sources (GC, galactic arms), most of the counterparts were detected in the near IR. The properties of the X-ray identified INTEGRAL sources were then determined through optical and IR spectroscopy (an extensive work has been carried out by Masetti 2006; Masetti *et al.* 2006a,b,c,d, 2008, 2009, 2010; Chaty *et al.* 2008; Rahoui *et al.* 2008).

5.2 Population of sgHMXBs

A comprehensive study of the population of sources detected by *INTEGRAL* has been provided by Bodaghee *et al.* (2007). In the Galactic bulge one finds mostly LMXBs and a small number of HMXBs. Most HMXBs (in particular sgHMXBS) are found in the regions created by the spiral arms. Figure 5.2 (blue) shows the distribution of HMXBs across the galactic place, summed over the galactic latitude ($|b| < 6^o$). This plot also shows the number of star-forming complexes divided by 3 (red) and of ultra compact H II regions divided by 10 (black). The distribution of HMXBs shows two peaks at galactic longitude of -40^o and 30^o. These two peaks correspond roughly to the position of the tangent to the Norma and Scutum galactic arms (Binney & Merrifield 1998).

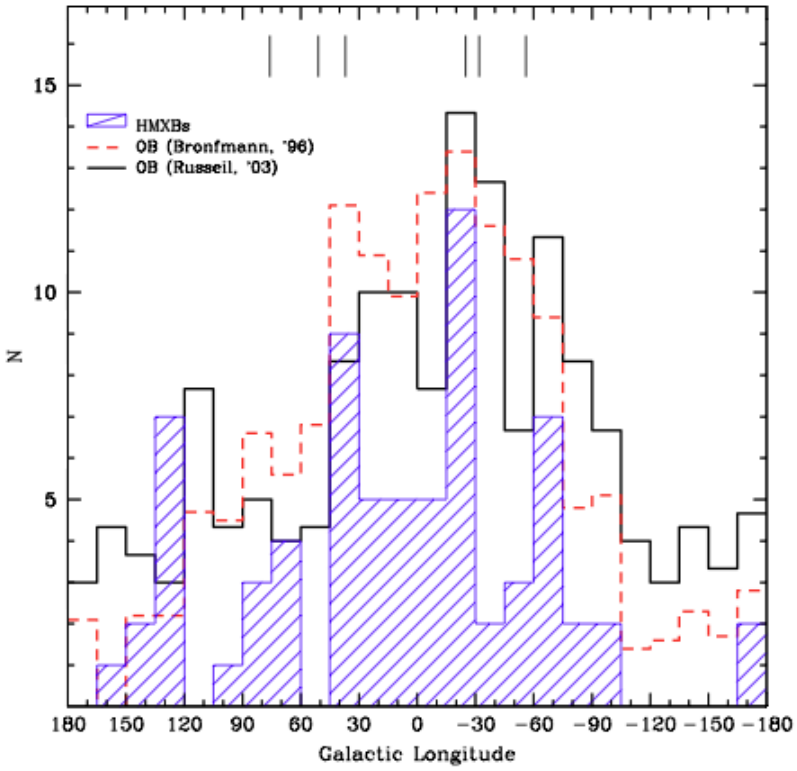

Figure 5.2: Distribution of HMXBs. *Credit:* Bodaghee *et al.* (2007).

5.3 Classical sgHMXB

Classical sgHMXBs have been studied extensively over the years (see chap. 1). The neutron stars are located at a distance of $\alpha \sim 1.5 - 2$ R$_*$ from their companion star. Typical mass-loss rates of $\sim 10^{-6}$ M$_\odot$ yr^{-1} and wind terminal velocities of 1500 km s^{-1} are observed in most of them. Blondin *et al.* (1990); Blondin, Stevens & Kallman (1991) modeled Vela X-1 (the prototype of the class) using hydrodynamic code and revealed that the wind of the massive star is heavily disrupted. The X-ray radiation from the neutron star ionizes the local material and can further disrupt the wind. High-resolution soft X-ray spectroscopy of the brightest sources revealed a number of lines in emission, constraining the ionization level of the gas (Watanabe *et al.* 2006).

5.4 Obscured sgHMXB

5.4.1 Overview

The new category of heavily obscured sgHMXBs shares some of characteristics of the classical sgHMXBs. The main difference between classical and obscured sgHMXBs is that the latter ones are much more absorbed in the X-rays. The absorbing column density (N_H) is, on average, 10 times larger than in classical systems and well above the galactic absorption in the direction of the sources. Spin periods, orbital periods, and donor's spectral type are similar to those of classical sgHMXBs. Walter *et al.* (2006) studied a number of these sources with $XMM-Newton$ and showed that all of them are heavily obscured ($N_H \sim 10^{23}$ cm^{-2}) and feature prominent iron Kα line.

5.4.2 Individual sources

IGR $J17252-3616$

IGR $J17252-3616$(=EXO 1722-363) is a heavily obscured sgHMXB. $XMM-Newton$ observations revealed an absorbing column density, $N_H \sim 10^{23}$ cm^{-2}, almost ten times higher than the galactic absorption in this direction (Zurita Heras *et al.* 2006). Moreover, the $INTEGRAL$ light-curves showed clearly that the source is an eclipsing binary. $RXTE$ observations of the system are consistent with a spin period of 414 seconds and an orbit of $P \approx 9.74$ days with an upper limit for eccentricity $e < 0.2$ (Thompson *et al.* 2007; Manousakis & Walter 2011). Optical and IR observations confirmed the supergiant nature and showed prominent P-Cygni profile (Chaty *et al.* 2008). Recent VLT observations suggested a B0-5I or B0-1Ia spectral type star and a distance of about 8 kpc (Mason *et al.* 2009a).

IGR $J18027-2016$

IGR $J18027-2016$ (=SAX $J1802.7-2017$) has been observed by $XMM-Newton$ which revealed an absorbing column density of $N_H \sim 9 \times 10^{22}$ cm^{-2} (Walter *et al.* 2006). The system hosts a neutron star with a spin period of about 140 sec orbiting its massive companion with an orbital period of about 5 days showing deep eclipses (Hill *et al.* 2005). Optical and IR observations revealed hydrogen and He I lines in emission with a rather tentative P-cyg profile suggesting a B supergiant at a distance of 12 kpc (Chaty *et al.*

2008). The spectral type and the distance of the object were confirmed to be B1 Ib and ∼12 kpc (Torrejón *et al.* 2010b; Mason *et al.* 2011).

IGR $J19140+0951$

RXTE observation of IGR $J19140+0951$(=EXO 1912+097) revealed an absorbed spectrum ($N_H \sim 5\times10^{22}$ cm^{-2}) and a strong iron line (Swank & Markwardt 2003). Additional RXTE observations revealed a sinusoidal modulation compatible with a period of 13.5 days (Wen *et al.* 2006). There is no evidence for a spin period besides an unconfirmed pulsation at 6.5 ksec (in't Zand *et al.* 2006). Optical and nearIR observations revealed a number of line in emission (Paschen, Brackett Hydrogen lines, He I and He II) implying a supergiant nature of the companion (Hannikainen *et al.* 2007; Chaty *et al.* 2008). More recently, the nature of the object was confirmed as a supergiant B0.5 Ia at a distance of 3.5 kpc (Torrejón *et al.* 2010b). Based on simultaneous RXTE and INTEGRAL observations the evolution of absorbing column density was found to correlate with the orbit of the system and a weak mass loss rate of $\sim 10^{-8}$ M$_\odot$ yr^{-1} was inferred (Prat *et al.* 2008).

IGR $J16320-4751$

IGR $J16320-4751$(=AX $J1631.9-4752$) is a source exhibiting a high absorbing column density, $N_H \sim 2\times10^{23}$ cm^{-2} (Rodriguez *et al.* 2003). X-ray observation revealed pulsation of ∼ 1300 sec (Lutovinov *et al.* 2005) and an orbital period of about 8.9 days (Corbet *et al.* 2005). An iron line at 6.4 keV and a soft excess are also detected (Rodriguez *et al.* 2006). IR observations of the counterpart (Negueruela & Schurch 2007) revealed a number of Brackett lines with P-Cyg profile, indicating a supergiant OB nature (Chaty *et al.* 2008). Mid-IR observation and SED fitting are consistent with an O8 I star, suggesting a distance to 3.5 kpc (Rahoui *et al.* 2008).

IGR $J00370+6122$

IGR $J00370+6122$ (=1RXS $J003709.6+612131$) has been observed with RXTE and revealed a highly variable absorbing column density $N_H \sim (7-15)\times10^{22}$ cm^{-2} (den Hartog *et al.* 2006; in't Zand *et al.* 2007). *RXTE* and *INTEGRAL* observation revealed an orbital period of ∼ 16 days (Wen *et al.* 2006) and speculation of a ∼360 seconds spin period, corresponding to the regime of wind accretion in the Corbet diagram.

IGR $J16283-4838$

The source is absorbed in the X-rays with $N_H \sim 5\times10^{22}$ cm^{-2} without any indication for pulsations (Markwardt, Swank & Smith 2005). Subsequent observations with *swift*, *INTEGRAL* revealed a variable absorbing column density in the range $\sim 5-15\times10^{22}$ cm^{-2} with a flat spectrum (Beckmann *et al.* 2005) placing the system in the class of the obscured systems. ESO-NTT observations revealed that the most likely counterpart is an OB supergiant at a distance in the range 14 to 21 kpc (Pellizza, Chaty & Chisari 2011).

IGR $J16207-5129$

IGR $J16207-5129$ has been observed by *Chandra* indicating a moderate absorbing column density $N_H \sim 4\times10^{22}$ cm^{-2}, slightly higher than the galactic absorption towards the source direction (Tomsick *et al.* 2006). *XMM − Newton* observations confirmed its absorbed

nature with a lack of pulsation (Tomsick *et al.* 2009). Infrared spectroscopy revealed a B1 Ia companion, placing it at a distance of ~ 6 kpc (Nespoli, Fabregat & Mennickent 2008). *Suzaku* observation showed a strongly absorbed source $N_H = 1.6 \times 10^{23}$ cm^{-2} with an evidence for a partial eclipse (Bodaghee *et al.* 2010)

IGR $J16393-4643$

IGR $J16393-4643$(=AX $J1639.0-4642$) has been observed with INTEGRAL and XMM-Newton and revealed a pulse period of ~ 912 seconds. Spectroscopy also revealed an iron line at 6.4 keV and a highly obscured spectrum with $N_H \sim 2 \times 10^{23}$ cm^{-2} (Bodaghee *et al.* 2006). Subsequent observations with RXTE showed an orbital period of 3.7 days and a spin period of 911 sec (Thompson *et al.* 2006). Mid-IR observations and spectral energy distribution fit (SED) revealed a B type star at a distance 10-20 kpc (Chaty *et al.* 2008). Corbet *et al.* (2010b) confirmed the orbital period using *swift* and *RXTE*.

IGR $J16318-4848$

IGR $J16318-4848$ was the first source discovered by *INTEGRAL*. It exhibits enormous absorption and features a prominent iron line at 6.4 keV (Walter *et al.* 2003). The source is persistently obscured with only small variations of $N_H = (1-2) \times 10^{24}$ cm^{-2} (Ibarra *et al.* 2007). IGR $J16318-4848$ is the second HMXB with an sgB[e] mass donor (Filliatre & Chaty 2004). The distance to the source is constrained to 1.6 kpc through IR spectroscopy (Rahoui *et al.* 2008).

5.5 Supergiant Fast X-ray Transients

5.5.1 Overview

The main property of an SFXT is its flaring activity. This activity lasts from several minutes to up several hours. The dynamic range of the outburst is 10^{2-4} when compared to the quiescent level. The luminosity (1-100 keV) during the outbursts reaches up to 10^{37} erg s^{-1}, which corresponds to an ingestion of mass of the order of 10^{22} gr. The outburst spectrum is similar to these of accreting pulsar. Some sources have large spin periods and orbital period of several weeks. The above characteristics place the SFXTs in a position between the wind accretors and the Be/X-ray binaries in the Corbet diagram.

The quiescent properties consist of minor variability in the range of $L_X \sim 10^{33-34}$ erg s^{-1} (Sidoli *et al.* 2008). The lowest observed X-ray luminosity of SFXTs is about 10^{32} erg s^{-1} and is related to a very soft spectrum (in't Zand 2005; Bozzo *et al.* 2010). The flares rise fast in order of dozen of minutes and have a total duration of about an hour. Flares are separated by weeks, and their peak luminosity is $L_X \sim 10^{36-37}$ erg s^{-1}.

Pulsations are difficult to detect, or when detected are in general long, e.g. IGR $J16465-4507$ with spin period of 228 sec (Lutovinov *et al.* 2005), IGR $J16418-4532$ with spin period of 1246 sec (Walter *et al.* 2006). When non detected, the lack of pulsation during an outburst may imply that the spin period is longer than $\sim$ an hour. The possibility that some systems host a BH candidate can also not be ruled out.

Orbital period for SFXTs ranges between $\sim$3 days (IGR $J16479-4514$ Jain, Paul & Dutta 2009) and 165 days (IGR $J11215-5952$ Romano *et al.* 2009). The variability of SFXTs is related to the perisatron passages. These flares could be related with accretion when also crosses a high-density area, or a clumpy wind (Leyder *et al.* 2007).

5.5.2 Individual sources

IGR $J18483-0311$

IGR $J18483-0311$ detected in 2007, shows an absorbed cut-off power-law spectrum (indication of an accretion pulsar) during its outbursts and is likely to be either a SFTX or a Be/X-ray binary, given its position in the Corbet diagram (Sguera *et al.* 2007a). Optical and IR observations revealed a supergiant companion star, B0.5Ia, to a distance of about 3 kpc (Rahoui *et al.* 2008; Chaty *et al.* 2008; Torrejón *et al.* 2010b). $XMM-Newton$ and $swift$ observations detected a 21 sec spin period. The X-ray flux variability was explained in terms of changes in the accretion rate rather than by eclipses (Giunta *et al.* 2009). Variation of an order of 1000 between peak flux and quiescence luminosity are explained in term of an accretion of an isotropic clump with a mass of 10^{18-21} gr (Romano *et al.* 2009).

IGR $J18410-0535$

IGR $J18410-0535$(=AX $J1841.0-0536$) is an SFXT at a distance of about 3 kpc with a spin period at about 5 sec and shows a spin-up trend (Sidoli *et al.* 2008; Nespoli, Fabregat & Mennickent 2008). Swift monitoring revealed (Romano *et al.* 2009) a dynamical range of up to 2000 in flux variation, hard power-law spectrum with a high energy cut-off, harder during the outburst. Time-resolved analysis of a bright flare by $XMM-Newton$ concluded that the flare was due to an ingestion of a clump of mass 10^{22} gr (Bozzo *et al.* 2011).

IGR $J18450-0433$

IGR $J18450-0435$(=AX $J1845.0-0433$) is an SFXT observed with $INTEGRAL$ and $swift$ indicating fast flaring activity on timescales of minutes (Sguera *et al.* 2007b). Further $XMM-Newton$ observations revealed a rather high 10^{35} erg s^{-1} quiescence luminosity (0.2-100 keV) and two short bright flares at a level of 10^{36} erg s^{-1} indicating a maximum dynamical range of about 50 (Zurita Heras & Walter 2009). In addition, soft excess and highly ionized iron is detected during quiescence.

IGR $J17544-2619$

IGR $J17544-2619$ was discovered in 2003 with a typical $N_H \sim 10^{22}$ cm^{-2} and exhibits a repeating activity about every 2 hours (González-Riestra *et al.* 2004). Optical and IR observation revealed an O9Ib companion at a distance of about 3.5 kpc (Pellizza, Chaty & Negueruela 2006; Rahoui *et al.* 2008). A Suzaku observation revealed an intense flare with a peak flux about 10000 times larger than that of quiescence with a sudden increase of the absorbing column density and hardening of the spectrum during the outburst (Rampy, Smith & Negueruela 2009).

IGR $17391-3021$

IGR $17391-3021$(=XTE $J1739-302$) is a SFXT with flaring activity lasting for minutes to hours (Sguera *et al.* 2005). Optical and IR observations suggest the presence of a supergiant companion at a distance of ~ 3 kpc (Rahoui *et al.* 2008; Chaty *et al.* 2008). The source tends to be absorbed, especially during flares (Sidoli *et al.* 2008; Romano *et al.*

2009; Bodaghee *et al.* 2011). INTEGRAL analysis ($\sim$ 12 Msec) revealed a modulation of about 50 days interpreted as a highly eccentric obit ($e \sim 0.8$) orbit inside an inhomogeneous clumpy wind (Drave *et al.* 2010).

IGR 16328 − 4726

IGR 16328 − 4726 is a new member of the class of SFXTs. INTEGRAL observation revealed a dynamical range of about 200 with a sporadic emission behavior (Fiocchi *et al.* 2010). Using $swift/BAT$ (15-100 keV) a 10d orbital modulation was found. The source shows signature of an intrinsic absorption (Corbet *et al.* 2010a).

5.5.3 Models of SFXTs outburst activity

Although a vast amount of observation was obtained, several issues concerning the nature of SFXTs are still open. The observed orbital period of SFTXs can be divided in two categories, i) long orbital periods (> 15 days) and ii) short orbital periods (< 15 days). Different phenomenology can arise from these categories. A number of possible scenarios have been proposed:

1. Clumpy stellar wind
   Many authors (in't Zand 2005; Walter & Zurita Heras 2007; Ducci, Sidoli & Paizis 2010) proposed that clumps (from highly structured stellar winds) are swallowed by the neutron star. In *short* period systems are likely to orbit close to their companion stars and to accrete clumps. The X-ray variability of SFXTs provides insights on the wind clump structure. Parameters, such as the mass, the size, and the number of the clumps and the clumping parameters can be estimated (Walter & Zurita Heras 2007).

2. Magnetar
   Bozzo, Falanga & Stella (2008) explained SFXT with the interplay between a magnetar, having a magnetic field $B \sim 10^{14}$ Gauss and a variable stellar wind. The variability is driven through Kelvin-Helmholtz instability. This model can explain fast variability with smaller density contrast than the pure clumpy wind model.

3. Circumstellar disk
   To explain *long* orbital period SFXTs Sidoli *et al.* (2007) proposed of a circumstellar disk, similar to those found in Be/X-ray binaries, but placed perpendicularly to the orbital plane. This can provide short outburst when the NS crosses the disk.

Table 5.1: Sample of INTEGRAL source. We list the name of the source, the region of the Galaxy (either *No* for Norma arm or *GC* for Galactic Center), their spin and orbital period, the interstellar absorbing column density (on the line of sight), the X-ray absorbing column density. Eclipsing srouces are marked with E.

Source	P_s (s)	P_o (d)	N_H (10^{22} cm^{-2})	Type	Ref.
Obscured sgHMXBs					
IGR J17252-3616	414	9.74	18	E	AM11, JZ07, RW06
IGR J18027-2016	140	4.5	9.1	E	H05, RW06
IGR J19140+0951	-	13.5	10	-	W06
IGR J16320-4751	1300	8.96	12	-	L05, C05, RW06
IGR J16393-4643	911	3.68	25	-	B06, RW06
IGR J00370+6122	-	15.6	13	-	W06
IGR J16283-4838	-	-	17	-	B05
IGR J16207-5129	-	-	4	-	T06
IGR J16318-4848	-	-	193	-	I07, RW06
SFTXs					
IGR J17544-2619	-	-	2	-	G04
IGR J18410-0535	5	-	-	-	S08
IGR J17391-3021	-	50	3	-	D10
IGR J18483-0311	-	-	-	-	-
IGR J18450-0433	-	-	-	-	-
IGR J16328-4726	-	-	-	-	-

References: AM11:Manousakis & Walter (2011), JZ07:Zurita Heras *et al.* (2006), H05: Hill *et al.* (2005), L05:Lutovinov *et al.* (2005),C05:Corbet *et al.* (2005), W06:Wen *et al.* (2006), B05:Beckmann *et al.* (2005), T06: Tomsick *et al.* (2006), B06:Bodaghee *et al.* (2006), I07:Ibarra *et al.* (2007), S08:Sidoli *et al.* (2008), G04:González-Riestra *et al.* (2004), D10:Drave *et al.* (2010), RW06: Walter *et al.* (2006).

Chapter 6

The nature of the absorbing material in the highly obscured HMXB IGR $J17253-3616$

6.1 Introduction

In 1987, *Ginga* performed a pointed observations and revealed a highly variable X-ray source, X1722-363, with a pulsation period of ~ 413.9 sec (Tawara *et al.* 1989). Additional *Ginga* observations revealed the orbital period of 9-10 days and a mass of the companion star of $\sim 15\ M_{\odot}$ (Takeuchi, Koyama & Warwick 1990). IGR $J17252-3616$ was detected as a bright hard X-ray source by $ISGRI$ onboard $INTEGRAL$ on February 9, 2004 among other hard X-ray sources. Both studies concluded that the system is a high mass X-ray binary (HMXB).

$INTEGRAL$ and $XMM-Newton$ observations of IGR $J17252-3616$, allowed Zurita Heras *et al.* (2006) to identify the infrared counterpart of the system, to accurately measure the absorbing column density, and refine the spin period of the system. Thanks to the deep eclipses, an accurate orbital period could be derived from $INTEGRAL$ data. Further RXTE observations helped identify a highly inclined system ($i > 61^{o}$) with a companion star of $\mathrm{M}_{*} \lesssim 20\,\mathrm{M}_{\odot}$ and $\mathrm{R}_{*} \sim 20-40\,\mathrm{R}_{\odot}$ (Thompson *et al.* 2007; Corbet, Markwardt & Swank 2005). Recent VLT observations help to infer the companion spectral type (between B0–B5 I and B0–B1 Ia) and radial velocity measurements (Mason *et al.* 2009a).

IGR $J17252-3616$ is discussed in detail in the paper that follows (sect. 6.2). We have observed IGR $J17252-3616$ with $XMM-Newton$ for a total of 10 observations. The observations were scheduled to cover the orbit of IGR $J17252-3616$ which allowed to perform X-ray wind tomography. Phase-resolved spectroscopy revealed significant variations of the absorbing column density (N_H) and of the EW of the Fe Kα line. Other spectral components (e.g. cutoff energy, power-law index) remained constant throughout the orbit. An ad-hoc model of the wind and of a trailing tail were implemented to account for the observations. The main assumption of the model was that the wind terminal velocity is of the order of 500 km s^{-1}, significantly lower than what is usually expected for supergiant OB stars. If confirmed in the obscured system, it may turn out that half of the sgHMXB have stellar wind velocities several times lower than usually measured.

6.2 Scientific Article on IGR J17252 – 3616

A&A 526, A62 (2011)
DOI: 10.1051/0004-6361/201015707

Astronomy & Astrophysics

X-ray wind tomography of the highly absorbed HMXB IGR J17252–3616⋆

A. Manousakis[1,2] and R. Walter[1,2]

[1] ISDC Data Center for Astrophysics, Université de Genève, Chemin d'Ecogia 16, 1290 Versoix, Switzerland
e-mail: Antonios.Manousakis@unige.ch
[2] Observatoire de Genève, Université de Genève, Chemin des Maillettes 51, 1290 Versoix, Switzerland

Received 7 September 2010 / Accepted 6 November 2010

ABSTRACT

Context. About ten persistently highly absorbed super-giant high-mass X-ray binaries (sgHMXB) have been discovered by INTEGRAL as bright hard X-ray sources lacking bright X-ray counterparts. Besides IGR J16318-4848, which has peculiar characteristics, the other members of this family share many properties with the classical wind-fed sgHMXB systems.
Aims. Our goal is to understand the characteristics of highly absorbed sgHMXB and in particular the companion stellar wind, which is thought to be responsible for the strong absorption.
Methods. We monitored IGR J17252–3616, a highly absorbed system featuring eclipses, with *XMM-Newton* to study the variability of the column density and the Fe Kα emission line along the orbit and during the eclipses. We also compiled a 3D model of the stellar wind to reproduce the observed variability.
Results. We first derive a refined orbital solution based on *INTEGRAL*, *RXTE*, and *XMM-Newton* data. We find that the *XMM-Newton* monitoring campaign reveals significant variations in the intrinsic absorbing column density along the orbit and the Fe Kα line equivalent width around the eclipse. The origin of the soft X-ray absorption is associated with a dense and extended hydrodynamical tail, trailing the neutron star. This structure extends along most of the orbit, indicating that the stellar wind has been strongly disrupted. The variability of the absorbing column density suggests that the wind velocity is smaller ($\upsilon_\infty \approx 400$ km s^{-1}) than observed in classical systems. This may also explain the much stronger density perturbation inferred from the observations. Most of the Fe Kα emission is generated in the innermost region of the hydrodynamical tail. This region, which extends over a few accretion radii, is ionized and does not contribute to the soft X-ray absorption.
Conclusions. We present a qualitative model of the stellar wind of IGR J17252–3616 that can represent the observations, and we suggest that highly absorbed systems have lower wind velocities than classical sgHMXB. This proposal could be tested with detailed numerical simulations and high-resolution infrared/optical observations. If confirmed, it may turn out that half of the persistent sgHMXB have low stellar wind speeds.

Key words. X-rays: binaries – stars: winds, outflows – pulsars: individual: IGR J17252–3616 – supergiants

1. Introduction

High mass X-ray binaries (HMXB) consist of a neutron star or a black hole fueled by the accretion of the wind of an early-type stellar companion. Their X-ray emission, a measure of the accretion rate, shows a variety of transient to persistent patterns. Outbursts are observed on timescales from seconds to months and dynamical ranges varying by factors of 10^4. The majority of the known HMXB are Be/X-ray binaries (Liu et al. 2006), with Be stellar companions. These systems are transient, featuring bright outbursts with typical durations on the order of several weeks (White 1989; White et al. 1995; Charles & Coe 2006). A second class of HMXBs harbor OB supergiant companions (sgHMXBs) that feed the compact object by means of strong, radiatively driven stellar winds or Roche lobe overflow. Thanks to INTEGRAL, the number of known sgHMXB systems has tripled in the past few years (Walter et al. 2006).

Highly absorbed sgHMXB were discovered by *INTEGRAL* (Walter et al. 2004) and are characterized by strong and persistent soft X-ray absorption ($N_{\rm H} > 10^{23}$ cm^{-2}). When detected, these systems have short orbital periods and long spin periods (Walter et al. 2006). They correspond to the category of wind-fed accretors in the Corbet diagram (Corbet 1986).

IGR J17252–3616 was detected by *ISGRI* onboard *INTEGRAL* on February 9, 2004 among other hard X-ray sources (Walter et al. 2004, 2006). The source was first detected by *EXOSAT* (EXO 1722-3616) as a weak soft X-ray source, back in 1984 (Warwick et al. 1988). In 1987, *Ginga* performed a pointed observations and revealed a highly variable X-ray source, X1722-363, with a pulsation period of ∼413.9 s (Tawara et al. 1989). Additional *Ginga* observations revealed the orbital period of 9−10 days and a mass of the companion star of ∼15 $M_\odot$ (Takeuchi et al. 1990). Both papers concluded that the system was a high mass X-ray binary (HMXB).

INTEGRAL and *XMM – Newton* observations of IGR J17252–3616 allowed Zurita Heras et al. (2006) to identify the infrared counterpart of the system, to accurately measure the absorbing column density, and refine the spin period of the system. Thanks to the eclipses, an accurate orbital period could be derived from *INTEGRAL* data. Further RXTE observations helped identify a highly inclined system ($i > 61°$) with a companion star of $M_* \lesssim 20\ M_\odot$ and $R_* \sim 20$–$40\ R_\odot$

⋆ Based on observations obtained with XMM-Newton and INTEGRAL, two ESA science mission with instruments, data centers, and contributions directly funded by ESA Member States, NASA, and Russia.

A&A 526, A62 (2011)

Table 1. XMM-Newton observation log.

ObsID	#	Revolution	Start time (UT)	Effective exposure (ks)	Source counts	Phase (± 0.01)
0405640201	1	1231	2006-08-29T03:02:58	19.2	5.4×10^2	0.03
0405640301	2	1232	2006-08-31T16:37:44	4.1	1.4×10^4	0.27
0405640401	3	1234	2006-09-04T06:35:33	5.6	7.9×10^3	0.65
0405640501	4	1235	2006-09-06T19:33:10	5.4	9.5×10^2	0.91
0405640601	5	1236	2006-09-08T10:03:38	7.9	3.8×10^2	0.08
0405640701	6	1239	2006-09-15T07:23:45	2.8	1.7×10^3	0.79
0405640801	9	1247	2006-10-01T03:24:26	9.4	2.3×10^4	0.40
0405640901	8	1246	2006-09-28T14:36:53	11.3	1.9×10^4	0.15
0405641001	7	1245	2006-09-27T07:27:58	9.4	6.5×10^2	0.01
0206380401	10	785	2004-03-21T13:23:09	8.6	4.7×10^4	0.37

Notes. The revolution number, the start time, the effective exposure, the source counts, and the phase, calculated at the middle of each observation using the orbital solution obtained with fixed orbital period (table 3 are shown.

(Thompson et al. 2007). Recent VLT observations help us to infer the companion spectral type (Chaty et al. 2008; Mason et al. 2009) and radial velocity measurements (Mason et al. 2010). Its spectral energy distribution can be characterized by a temperature of $T_* \sim 30$ kK and a reddening of $A_V \sim 20$ (Rahoui et al. 2008).

In this paper, we report on a monitoring campaign of IGR J17252–3616 performed with *XMM-Newton* along the orbit in order to estimate the structure of the stellar wind and the absorbing material in the system. We describe the data and their analysis in Sect. 2 and a refined orbital solution in Sect. 3, and we present the evolution of the X-ray spectrum during the orbit in Sect. 4. In Sect. 5, we present and discuss a 3D model of the stellar wind that can reproduce the observations and present our conclusions in Sect. 6.

2. Data reduction and analysis

2.1. XMM-Newton

Pointed observations of IGR J17252–3616 were performed between August and October 2006 with *XMM-Newton* (Jansen et al. 2001). We scheduled 9 observations to cover the orbital phases 0.01, 0.03, 0.08, 0.15, 0.27, 0.40, 0.65, 0.79, and 0.91. In addition, we used one observation of 2004 with a phase of 0.37. The observations are summarized in Table 1.

The Science Analysis Software (XMM-SAS) version 9.0.0[1] was used to produce event lists for the EPIC-pn instrument (Strüder et al. 2001) by running `epchain`. Barycentric correction and good time intervals (GTI) were applied. Photon pile-up and/or out-of-time events were not identified among the data. High level products (i.e., spectra and lightcurves) were produced using `evselect`[2]. Spectra and lightcurves were built by collecting double and single events in the energy range 0.2−10 keV. The lightcurves were built using 5 s time bins. The spectra were re-binned to obtain 25 counts/bin for low count-rate observations and 100 counts/bin for high count-rate observations.

In one dataset (ObsID 0405640701, ∼19 ks), the count rate above 10 keV has a very peculiar behavior, increasing monotonically with time. As this does not affect the background subtracted source lightcurve significantly, we used the entire set of data in the pulse arrival-time determination. Standard GTI was used for spectral analysis.

2.2. INTEGRAL

We analyzed the hard X-ray lightcurve of IGR J17252–3616 obtained with *ISGRI* (Lebrun et al. 2003) on board *INTEGRAL* (Winkler et al. 2003). We extracted the 22−40 keV lightcurve using the HEAVENS[3] interface (Walter et al., in prep.). The lightcurve includes all data available on IGR J17252–3616 from Jan. 29, 2003 06:00:00 to Apr. 8, 2009 00:28:48 UTC. The effective exposure time on source is ∼3.6 Ms.

3. Timing analysis and orbit determination

3.1. Orbital period from INTEGRAL

We used the Lomb-Scargle (Press & Rybicki 1989) technique to determine the orbital period from the *INTEGRAL* light-curve and obtained $P_{orb} = 9.742 \pm 0.001$ days. Figure 1 shows (upper panel) the Lomb-Scargle power around the orbital period (dashed line). This period was used to refine the orbital solution (Sect. 3.3). The lower panel of Fig. 1 shows the lightcurve folded with the newly derived orbital period. The eclipse is clearly detected with the count rate dropping to zero.

3.2. Pulse arrival times

Pulse arrival times (PATs, hereafter) were obtained from the broad-band 0.2−10 keV lightcurves obtained by *XMM-Newton*. Close to the eclipse ($\phi = 0.03, 0.08, 0.91, 0.01$), when the compact object is behind the massive star, pulses could not be detected. We did not extract PATs for the observation of 2004.

To determine the PATs, we used a pulse profile template. This template is derived by folding the lightcurve from observation 0405640801 with a period of 414.2 s, obtained using the Lomb-Scargle technique (Press & Rybicki 1989). This observation was selected because the source was very bright for a long and almost uninterrupted exposure.

A sequence of pulse profile template was fit to each individual lightcurve. This sequence is characterized by: (i) the time of a pulse at the middle of the observation; (ii) the pulse period; and (iii) the amplitudes of each pulse. This assumes that the pulse period is reasonably constant during each observation.

[1] http://xmm.esac.esa.int/sas/

[2] http://xmm.esac.esa.int/sas/current/howtousesas.shtml

[3] http://www.isdc.unige.ch/heavens

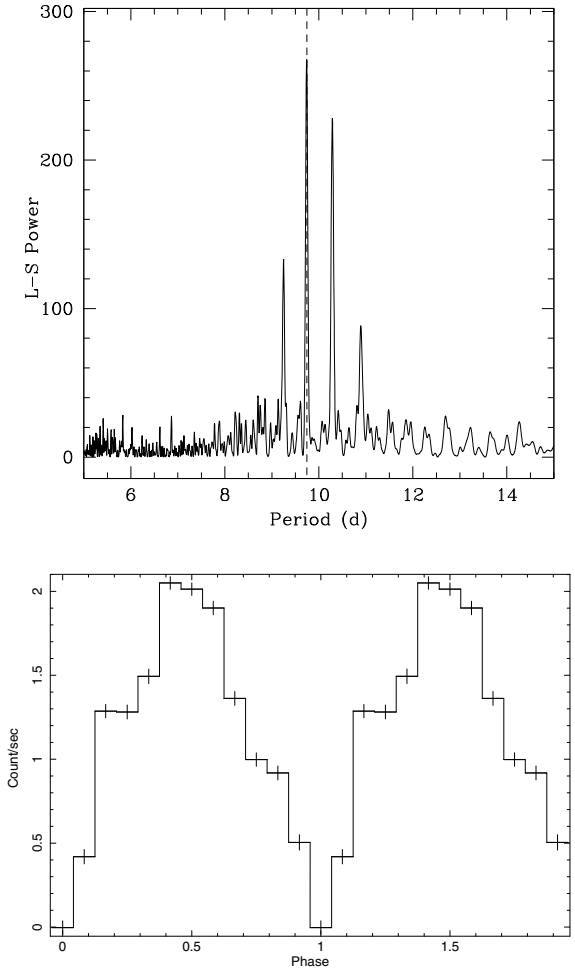

Fig. 1. *Top*: Lomb-Scargle periodogram obtained from the *INTEGRAL* 22−40 keV lightcurve. *Bottom*: *INTEGRAL* lightcurve folded with a period of 9.742 days.

Table 2. Pulse arrival times and derived pulse period.

ObsID	PAT (HJD) (±0.00011)	Pulse period (s)
0405640301	53 978.74948	414.3 ± 0.1
0405640401	53 982.32329	414.0 ± 0.1
0405640701	53 993.45320	414.2 ± 0.2
0405640801	54 009.24191	414.2 ± 0.1
0405640901	54 006.75737	413.8 ± 0.1

The statistical errors in the pulse time and period are typically 0.01 s and 0.1 s, respectively. Table 2 lists the pulse times and the pulse period obtained at the middle of each observation.

The PAT accuracy is limited by the systematic error related to the assumed pulse profile template. Using a different pulse profile template (derived from observation 0405640901) produces PAT with an offset between 8 s and 12 s from the values listed in Table 2. We adopted a systematic error of 10 s.

Table 3. Orbital solution for IGR J17252–3616.

	Units	Free $P_{\rm orb}$	Fixed $P_{\rm orb}$	RXTE Epoch 3
$t_0^{\rm XTE}$	HJD	53 761.73144	53 761.73142	53 761.73126
$P_0^{\rm XTE}$	s	413.889 ± 0.004	413.889 ± 0.005	413.894 ± 0.002
$\dot{P}^{\rm XTE}$	μs s^{-1}	–0.010 ± 0.002	–0.010 ± 0.003	–0.0106 ± 0.0001
$t_0^{\rm XMM}$	HJD	53 978.7494	53 978.7495	–
$P_0^{\rm XMM}$	s	413.86 ± 0.04	413.84 ± 0.04	–
$\dot{P}^{\rm XMM}$	μs s^{-1}	0.98 ± 0.04	1.01 ± 0.03	–
$\alpha_x \sin i$	lt-s	102 ± 8	101 ± 2	101 ± 4
$P_{\rm orb}$	d	9.76 ± 0.02	9.742 (fixed)	9.78 ± 0.04
T_{90}	HJD	53 761.62 ± 0.1	53 761.69 ± 0.1	53 761.60 ± 0.09
χ^2_ν		1.5 (30)	1.65 (31)	1.45 (28)

Notes. The errors have been calculated at 90% confidence level. The errors in the arrival times t_0 are 0.00001 and 0.0001 days for *RXTE* and *XMM*, respectively. The last column shows the result from Thompson et al. (2007) for comparison.

3.3. Orbital solution

We derived the orbital solution using the PATs of the *RXTE* observation obtained by Thompson et al. (2007, Epoch 3, see Fig. 2), and the PATs derived above from *XMM* data.

The orbital solution was obtained by comparing the observed pulse arrival delays ($t_n - t_0 - nP_0 - \frac{1}{2}n^2P_0\dot{P}$) to the expected ones $\alpha_x \sin i \cos[2\pi(t_n - T_{90})/P_{\rm orb}]$ (Levine et al. 2004). The orbital parameters (the orbital period, $P_{\rm orb}$; the projected semi-major axis, $\alpha_x \sin i$; the reference time corresponding to mid-eclipse, T_{90}) were assumed to be constant. To account for pulse evolution, two sets of pulse parameters (spin period at time t_0, P_0; spin period derivative, $\dot{P}$) were used for the *RXTE* and *XMM* campaigns. The pulse number n was given by the nearest integer to $n = (t_n - t_0)/(P_0 + 0.5\dot{P}(t_n - t_0))$.

We performed a combined fit of the *RXTE* and *XMM* observations. We derived the orbital solutions by (i) allowing all parameters to vary freely and (ii) fixing the orbital period to the value derived from the *INTEGRAL* data. The resulting parameters are listed in Table 3. We were also able to obtain an upper limit (90%) of $e < 0.15$ on the eccentricity by adding the first-order term in a Taylor series expansion in the eccentricity (Levine et al. 2004). The *RXTE* and *XMM* orbital solutions are comparable and the resulting parameters are consistent within the errors.

The folded lightcurve obtained with the *INTEGRAL* derived orbital period (Fig. 1, lower panel) results in a pulse fraction ∼100%. For the rest of the analysis, we used the orbital solution obtained with fixed $P_{\rm orb}$ (Table 3).

Figure 2 shows the resulting pulse arrival-time delays (fixed $P_{\rm orb}$) for both *RXTE* and *XMM* data together with the best-fit orbital solution.

4. Spectral analysis

The spectral analysis was performed using the XSPEC[4] package version 11.3.2ag (Arnaud 1996). To use the χ^2_ν statistics, we grouped the data to have at least 25 (faint spectra) and up to 100 (bright spectra) counts per bin. We initially fitted the observed spectra using a phenomenological model made of an intrinsically absorbed cutoff power-law, a blackbody soft excess, and a gaussian Fe Kα line (`wabs*(bb+gauss+vphabs*cutoff)`). The

[4] http://xspec.gsfc.nasa.gov

A&A 526, A62 (2011)

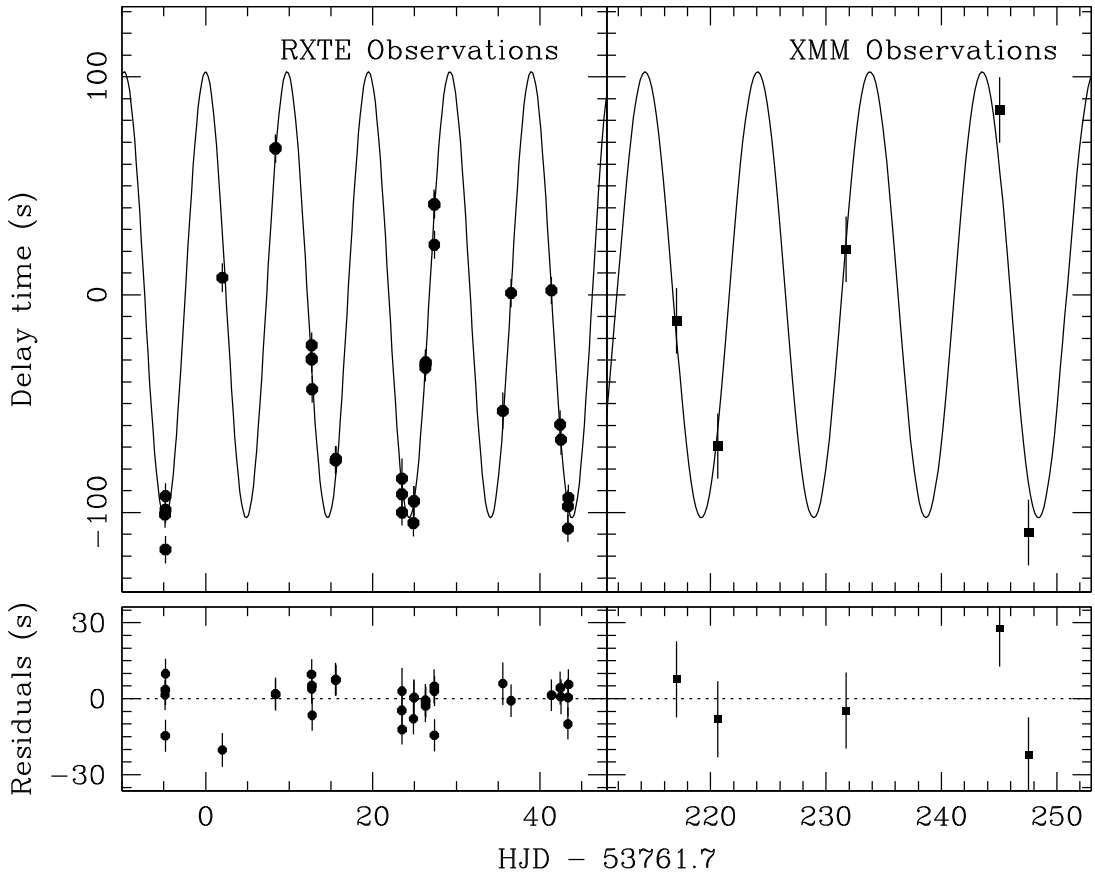

Fig. 2. Delays (*top*) and residuals (bottom) derived from the fixed $P_{\rm orb}$ orbital solution compared to the data. *Left*: *RXTE* data are taken from Thompson et al. (2007). *Right*: *XMM − Newton* data from this work.

centroid of the iron line is compatible with $E_{\rm c} \sim 6.40 \pm 0.03$ keV at all epochs.

The spectra are always strongly absorbed below ~3 keV and display an iron K-edge at ~7.2 ± 0.2 keV. We first fit each spectrum by assuming all parameters to be free, apart from the Galactic absorption, which was fixed to $N_{\rm H} = 1.5 \times 10^{22}$ cm^{-2} (Dickey & Lockman 1990).

Some parameters (photon index, cutoff energy, blackbody temperature, and absorber Fe metallicity) did not vary (within the 90% errors) among the observations and were fixed to their average values of $E_{\rm C} = 8.2$ keV, $\Gamma = 0.02$, and $kT_{\rm BB} = 0.5$ keV, $Z = 1\ Z_{\odot}$. The Fe line was fixed to an energy of 6.4 keV, with a narrow width. Two representative spectra are displayed in Fig. 3.

The intrinsic absorbing column density and the normalization of each component were allowed to vary freely. The best-fit model parameters are listed in Table 4. Figure 4 shows the variation in all these parameters and in both the unabsorbed 2−10 keV flux and Fe Kα equivalent width (EW). The unabsorbed Fe Kα EW was calculated by setting the intrinsic absorbing column density to zero. All the spectral fits were good resulting in $\chi^2_\nu \approx 0.8$−1.4, apart from the $\phi = 0.03$ observation for which a poor fit was obtained. For the observations made during the eclipse, some parameters are poorly constrained.

The unabsorbed continuum flux (Fig. 4f) is on the order of ~5 × 10^{-11} erg cm^{-2} s^{-1} outside the eclipse. Variations

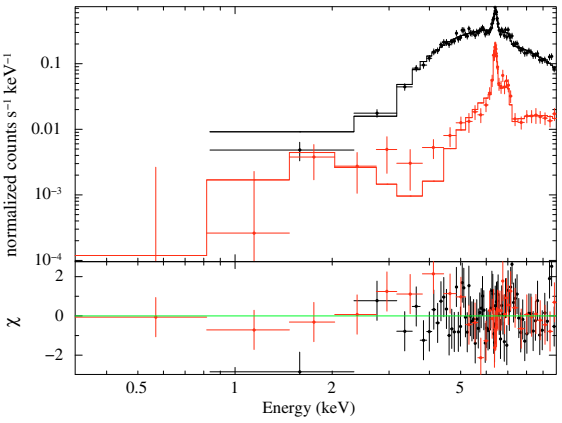

Fig. 3. *Top*: folded model and data for $\phi = 0.65$ (black) and $\phi = 0.91$ (red). *Bottom*: the corresponding residuals using the model described in the text with the parameters from Table 4.

are observed across the range (2−10) × 10^{-11} erg cm^{-2} s^{-1} and can be interpreted as variations in the accretion rate ($\dot{M}$). During the eclipse, the continuum flux drops by a factor of

Table 4. Spectral analysis results.

Phase (±0.01)	$N_{\rm H}$ 10^{22} cm^{-2}	unabs *EW* (Fe) keV	Fe line flux 10^{-5} ph cm^{-1} s^{-1}	Blackbody Luminosity 10^{33} erg s^{-1} @ 8 kpc	$I_\nu^{\rm cutoffpl}$ (1 keV) 10^{-3} ph keV^{-1} cm^{-2} s^{-1}	$F^{\rm unabs}_{\rm 2-10\ keV}$ 10^{-10} erg s^{-1} cm^{-2}	χ^2_ν (d.o.f.)
0.01	17^{+14}_{-9}	0.50 ± 0.4	0.34 ± 0.21	<0.88	$0.015^{+0.009}_{-0.006}$	0.0054 ± 0.003	1.34 (23)
0.03	26^{+9}_{-6}	0.81 ± 0.4	$0.66^{+0.12}_{-0.15}$	<0.33	$0.018^{+0.009}_{-0.005}$	0.006(8) ± 0.003	2.6 (17)
0.08	18^{+10}_{-9}	1.1 ± 0.6	1.1 ± 0.3	<0.57	$0.023^{+0.012}_{-0.007}$	0.008(8) ± 0.003	1.06 (11)
0.15	15.7 ± 0.5	0.04 ± 0.01	$2.6^{+0.8}_{-0.6}$	1.6 ± 1.4	1.44 ± 0.03	0.48 ± 0.02	0.90 (172)
0.27	$9.4^{+0.4}_{-0.3}$	0.14 ± 0.02	14 ± 02	$4.4^{+0.3}_{-0.1}$	2.29 ± 0.05	0.77 ± 0.02	1.05 (128)
0.37	12.1 ± 0.3	0.09 ± 0.006	16^{+1}_{-2}	$3.4^{+0.2}_{-0.3}$	$3.86^{+0.05}_{-0.06}$	1.29 ± 0.04	1.09 (396)
0.40	19.1 ± 0.5	0.11 ± 0.01	11 ± 1	$2.81^{+0.06}_{-0.1}$	2.26 ± 0.05	0.76 ± 0.02	1.45 (207)
0.65	24 ± 1	0.11 ± 0.02	$7.6^{+0.9}_{-1.5}$	$1.87^{0.1}_{-0.06}$	$1.55^{+0.06}_{-0.05}$	0.52 ± 0.02	0.99 (73)
0.79	23 ± 3	0.09 ± 0.03	$2.5^{+1.0}_{-0.7}$	<1.48	0.60 ± 0.06	0.20 ± 0.04	0.97 (31)
0.91	89^{+11}_{-14}	0.12 ± 0.03	$3.2^{+0.5}_{-0.7}$	$1.41^{+0.1}_{-0.05}$	$0.6^{+0.2}_{-0.1}$	0.20 ± 0.07	0.82 (33)

Notes. All free parameters are listed below together with the unabsorbed 2−10 keV flux and χ^2_ν. All uncertainties have been calculated at 90% confidence level.

~200 and remains stable at the level of $F^{\rm 2-10\ kev}_{\rm unabs} \approx (7 \pm 1) \times 10^{-13}$ erg cm^{-2} s^{-1}.

The intrinsic absorbing column density (Fig. 4b) is persistently high ($\gtrsim 10^{23}$ cm^{-2}). Significant variations are detected for $\phi = 0.2-0.4$ and close to the eclipse, reaching values of $N_{\rm H} \sim 9 \times 10^{23}$ cm^{-2}.

The normalization of the blackbody component (Fig. 4c) does not show any variability, although the low energy part of the spectrum is poorly constrained. The normalization of the blackbody component is compatible with $\sim 10^{33}$ erg s^{-1} assuming a distance of 8 kpc. The very high intrinsic absorbing column density rules out the neutron star as the origin of the soft excess.

The flux and *EW* of the Fe Kα line are displayed in Figs. 4d and 4e, respectively. Both components display significant variations indicating that the region emitting the line is at least partially obscured by the mass-donor star.

As the X-ray continuum illuminating the gas emitting the Fe fluorescent line cannot be measured during the eclipse, we calculated a corrected Fe Kα *EW* by assuming a constant continuum flux of 1.8×10^{-3} ph keV^{-1} cm^{-2} s^{-1} (Table 4).

5. Discussion

5.1. Constraining the physical parameters of the system

In the previous sections, we have derived an orbital solution (Table 3) yielding a mass function $f = 4\pi^2(\alpha_x \sin i)^3/GP^2_{\rm orb} = M_{\rm OB} \sin^3 i/(1+q)^2 \approx 11.7 \pm 0.7\ M_\odot$. This is consistent with a high mass X-ray binary system.

Adopting an inclination $i = 90°$, we infer a mass $M_{\rm OB} \sim 14\ M_\odot$ for the donor star. Radial velocity observations showed that $q = M_{\rm X}/M_{\rm OB} \sim 0.1$ (Mason et al. 2010). Using an upper limit on the mass of ~20 $M_\odot$ (Thompson et al. 2007) constrains the inclination of the orbit $i > 70°$. Mason et al. (2010) estimated an inclination $i \approx 75°-90°$. Within this range, the mass of the donor star is constrained to be $M_{\rm OB} \approx 14-17\ M_\odot$. The mass ratio and the donor mass imply a neutron star mass of $M_{\rm NS} = 1.4-1.7\ M_\odot$. The masses of both the donor star and the compact object are roughly similar (within a factor of 2) to that of Vela X-1 (Quaintrell et al. 2003; van Kerkwijk et al. 1995).

The separation of the system could be derived from the duration of the eclipse and the inclination (Joss & Rappaport 1984). For the eclipse duration of $\Delta\phi \approx 0.18 \pm 0.02$ (i.e. 1.75 days), we can estimate the separation to be $\alpha_x \approx 1.7-1.8\ R_*$. The Roche lobe of the system is $R_{\rm L} = 0.99-1.06\ R_*$ assuming a synchronous rotation (Joss & Rappaport 1984). This means that the system is very close to filling its Roche lobe and to forming an accretion disk, although no significant spin-up has been observed.

Using our VLT observations, Mason et al. (2009) performed near-IR spectroscopy of IGR J17252–3616 and concluded that the donor star is between B0−B5 I and B0−B1 Ia with an effective temperature $T_{\rm eff} = 22-28\ kT$ and a stellar radius of $R_* = 22-36\ R_\odot$. On the basis of this spectroscopic determination, we obtain absolute numbers for the separation ($\alpha_x \approx 37-64\ R_\odot$) and the Roche lobe radius ($R_{\rm L} \approx 22-38\ R_\odot$).

The unabsorbed 2−10 keV source flux is in the range $(0.2-1.3) \times 10^{-10}$ erg s^{-1} cm^{-2}. Adopting a mean value of $(0.8 \pm 0.3) \times 10^{10}$ erg s^{-1} cm^{-2} and assuming a distance of 8 kpc (Mason et al. 2009), the inferred 2−10 keV unabsorbed luminosity is $L_{\rm X} \sim 10^{36}$ erg s^{-1}. Assuming accretion as the source of energy (where $L_{\rm X} = \epsilon \dot{M} c^2$), we can estimate a mass accretion rate of $\dot{M} \sim 10^{-9}\ M_\odot$ yr^{-1}, which is similar to that of Vela X-1 (Fürst et al. 2010).

During the eclipse, the X-ray luminosity drops by a factor of ~200 resulting in $L_{\rm X} \sim 5 \times 10^{33}$ erg s^{-1}. As OB stars emit in X-rays with a luminosity $L_{\rm X} \sim 10^{31-32}$ erg s^{-1} (Güdel & Nazé 2009), this emission is probably dominated by X-ray scattering in the stellar wind (Haberl 1991). Hickox et al. (2004) discussed the origins of the soft X-ray excesses of many types of accreting pulsars. It is likely that the fairly constant soft X-ray excess observed in IGR J17252–3616 is emitted by recombination lines (Schulz et al. 2002) in a region of the wind larger than the stellar radius (Watanabe et al. 2006).

For a spherically symmetric stellar wind, one would expect to have smooth and predictable variations in the absorbing column density along the orbit. In particular, observations along the same line of sight or symmetric when compared to the eclipse must result in different, respectively identical, column densities. Our observing strategy resulted in $N_{\rm H}(\phi = 0.15) \approx N_{\rm H}(\phi = 0.37)$, $N_{\rm H}(\phi = -0.35) > N_{\rm H}(\phi = 0.37)$ and $N_{\rm H}(\phi = -0.35) \approx N_{\rm H}(\phi = -0.21)$, ruling out a spherical geometry.

5.2. Stellar wind structure

We constructed a 3D model of the OB supergiant stellar wind to simulate the variability of the intrinsic column density ($N_{\rm H}$)

A&A 526, A62 (2011)

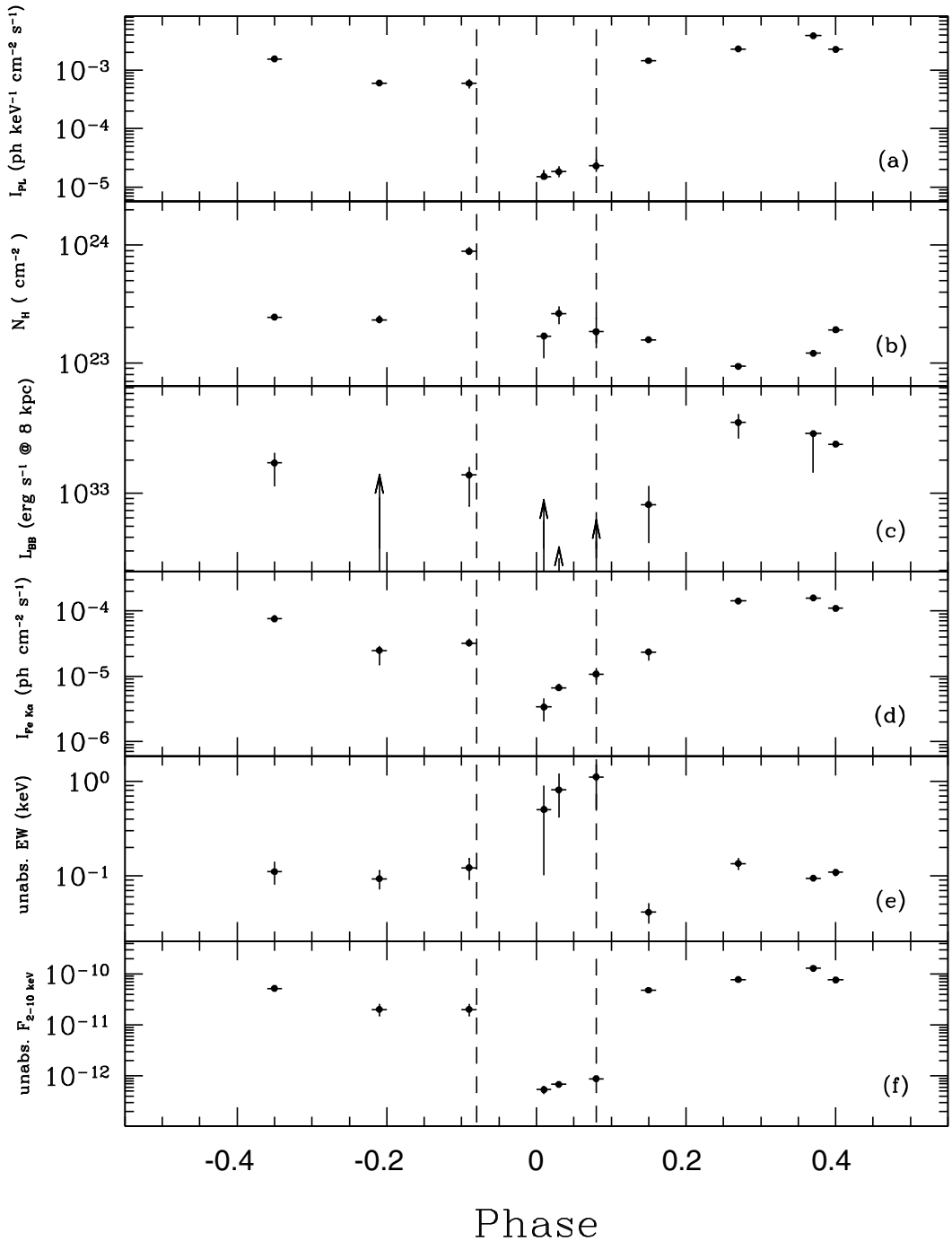

Fig. 4. Spectral variability along the orbit illustrated by **a)** the cut-off power-law normalization at 1 keV, **b)** the intrinsic hydrogen column density, **c)** the soft excess blackbody luminosity, assuming a distance of 8 kpc, **d)** the iron line flux, **e)** the iron line equivalent width calculated for the unabsorbed continuum, and **f)** the unabsorbed flux. Dashed vertical lines indicate the eclipse boundary.

and the Fe Kα line equivalent width (EW), during the orbit, and compare them with the observations. We assumed a distance $D \approx 8$ kpc (Mason et al. 2009), a circular orbit ($e = 0$), and an edge-on geometry ($i = 90°$).

Variability of absorption along the orbit

We first investigated the behavior of the intrinsic column density, $N_{\rm H}$, as a function of phase, to identify the structure of the wind during the orbit. We approximated the wind structure with two components, the unperturbed wind ($\rho_{\rm wind}$) and a tail-like hydrodynamic perturbation ($\rho_{\rm tail}$) related to the presence of the neutron star. Tail-like structures are expected for the photoionization and heating of the wind leading to strong shock formation and dense sheets of gas trailing the neutron star (Fransson & Fabian 1980). These shocks are produced by hydrodynamical simulations (Blondin et al. 1990) but produce a $N_{\rm H}$ of up to $\sim 10^{22}$ cm^{-2}, which is too small to account for the variability observed in IGR J17252–3616.

The unperturbed stellar wind was modeled by assuming a standard wind profile (Castor et al. 1975)

$$\upsilon(r) = \upsilon_\infty \left(1 - \frac{R_*}{r}\right)^\beta ,$$

where $\upsilon(r)$ is the wind velocity at distance r from the stellar center, υ_∞ is the terminal velocity of the wind, and β is a parameter describing the wind gradient. The conservation of mass provides the radial density distribution of the stellar wind. The unperturbed stellar wind is a good approximation within the orbit of the neutron star. Hydrodynamical simulations (Blondin et al. 1990, 1991; Blondin 1994; Blondin & Woo 1995; Mauche et al. 2008) of HMXB have shown that the wind can be highly disrupted by the neutron star beyond the orbit.

To estimate the terminal velocity of the unperturbed wind, we studied the $N_{\rm H}$ variability using three different sets of parameters (Fig. 5). The mass-loss rate and terminal velocity are constrained by the data to be in the range $\dot{M}_{\rm w}/\upsilon_\infty \sim (0.7–2) \times 10^{-16}$ $M_\odot$/km (β has a very limited impact on the results, so we used 0.7).

The fraction of the wind captured by the neutron star could be estimated from the accretion radius $r_{\rm acc} = 2GM_{\rm X}/(\upsilon_{\rm orb}^2+\upsilon^2) \sim 2 \times 10^{11}$ cm (where $\upsilon_{\rm orb} = 250$ km s^{-1} is the orbital velocity) as $f \sim \pi r_{\rm acc}^2/4\pi R_{\rm orb}^2 \sim 7.5 \times 10^{-4}$. The mass-loss rate is therefore $\dot{M}_{\rm w} \sim f^{-1}\dot{M} \approx 1.5 \times 10^{-6}$ $M_\odot$/yr and the terminal velocity of the wind is constrained to be in the interval $\upsilon_\infty \sim 250–600$ km/h.

In our simulation, we adopted a terminal velocity $\upsilon_\infty = 400$ km s^{-1}, a stellar radius $R_* = 29$ $R_\odot$, a wind gradient $\beta = 0.7$, and a mass loss rate $\dot{M}_* = 1.35 \times 10^{-6}$ $M_\odot$ yr^{-1}. The assumed, observed, and inferred model parameters are listed in Table 5. The variability of $N_{\rm H}$ along the orbit indicates that the unperturbed wind is adequate for phases $\phi \approx 0–0.35$. For $\phi \gtrsim 0.35$, $N_{\rm H}$ increases at a value of $\sim 2 \times 10^{23}$ cm^{-2}. This indicates that a high density tail-like structure lies on one side of the orbit, trailing the neutron star. The tail-like component is still present up to $\phi \gtrsim 0.8$.

We assumed that the tail-like structure is created very close to the neutron star and opens up with distance. The density of the material inside the "tail" decreases with distance to ensure mass conservation. Its distribution follows a "horn"-like shape with a circular section. We adjusted the density of the tail-like structure to match the observations. The density distribution $\rho_{\rm wind} + \rho_{\rm tail}$ is displayed in Fig. 6. The supergiant is located at the center (black disk). The tail-like structure covers about half of the orbit.

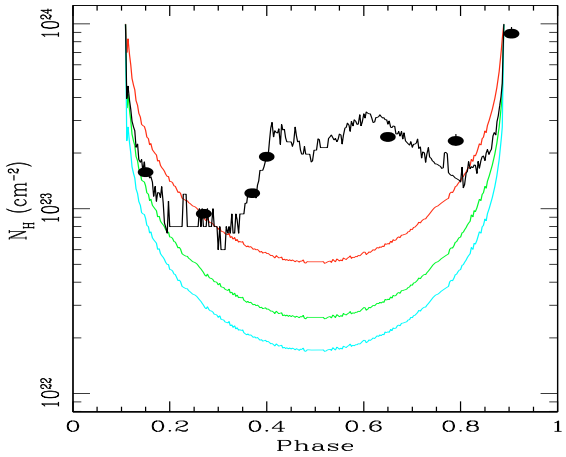

Fig. 5. Simulated $N_{\rm H}$ variations plotted together with the data. We illustrate three different smooth wind configurations, for $\dot{M}/\upsilon_\infty = 0.7$ (cyan), 1 (green), and 2 (red) $\times 10^{-16}$ $M_\odot$/km, keeping all the other parameters fixed. The solid black line shows the total $N_{\rm H}$ consisting of the unperturbed stellar wind (green line) and the tail-like extended component. The observations during the eclipse have been omitted.

Table 5. Wind model parameters.

Parameter	Value	Reference
Observed		
$q = M_{\rm X}/M_{\rm OB}$	0.1	Mason et al. (2010)
$M_{\rm OB}$	15 $M_\odot$	Takeuchi et al. (1990)
α	1.75 R_*	This work.
$\dot{M}$	10^{-9} $M_\odot$/yr	This work.
Assumed		
R_*	29 $R_\odot$	
$M_{\rm X}$	1.5 $M_\odot$	
i	90°	
β	0.7	
Inferred		
υ_∞	400 km s^{-1}	
$\dot{M}_{\rm w}$	1.35×10^{-6} $M_\odot$/yr	

Figure 5 displays the simulated $N_{\rm H}$ variability from the above density distribution together with the observed data points. The data and the model shows that the tail-like perturbation is essential to understand the observed variations.

Variability of the Fe Kα line during the orbit

Assuming that the intrinsic X-ray flux is unaffected by the eclipse, the Fe Kα equivalent width drops by a factor of ~10 during the eclipse in an orbital phase interval of ~0.1. This indicates that the radius of the region emitting Fe Kα is smaller than half of the stellar radius ($<10^{12}$ cm) and far more compact than the tail structure responsible for the absorption variability profile.

Vela X-1 shows a similar behavior, which was interpreted as an emitting region of the size of (Ohashi et al. 1984), or even within (Endo et al. 2002) the accretion radius.

Outside the eclipse, the equivalent width of the Fe Kα line is of the order of 100 eV. Following Matt (2002) and assuming a spherical transmission geometry, this corresponds to a column density of $N_{\rm H} \sim 2 \times 10^{23}$ cm^{-2}. As this additional absorption

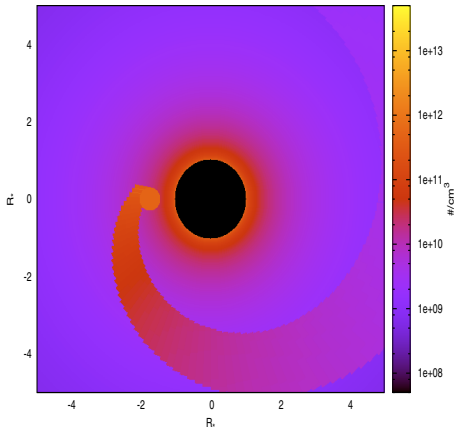

Fig. 6. Number density distribution in the plane of the orbit including a smooth wind and a tail-like perturbation. The black disk at the center represents the supergiant star.

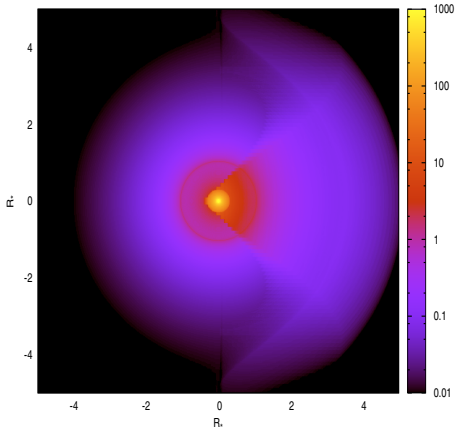

Fig. 8. Integrated Fe Kα emissivity (relative units) centered on the neutron star at phase $\phi = 0.5$. The smooth circular halo shows the rim of the supergiant star. The tail structure can be observed on the right.

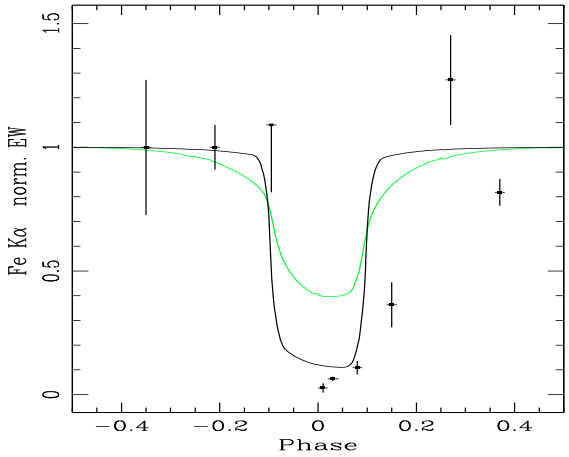

Fig. 7. Corrected unabsorbed Fe Kα line equivalent width along the orbit. *Green curve* indicates the prediction of the hydrodynamical tail and the *black curve* the addition of the central cocoon.

is not observed, the region emitting Fe Kα must be partially ionized.

An ionization parameter $\xi = L/nR^2$ in the range 10–300 is required to fully ionize light elements contributing to the soft X-ray absorption and keep an Fe Kα line at the energy of 6.4 keV (Kallman et al. 2004; Kallman & McCray 1982). The density of the Fe Kα emitting region is therefore $\sim\xi^{-1}{R_{12}}^{-2} \times 10^{12}$ cm^{-3}, where R_{12} is the distance from the neutron star in units of 10^{12} cm. As $N_{\rm H} = nR \sim 2 \times 10^{23}$ cm^{-2}, we have $\xi \sim 5/R_{12}$. A dense cocoon is therefore needed around the neutron star with a size $0.5 > R_{12} > 0.02$ and a density 10^{11} cm^{-3} $< n <$ 3×10^{12} cm^{-3}.

The majority of the Fe Kα is formed in a region that is small enough to allow for pulsation of the Fe Kα line, as observed in Cen X–3 (Day et al. 1993) and Her X–1 (Choi et al. 1994). We searched for such pulsations in our longest and almost uninterrupted observation (obsID 0405640801; $\phi = 0.40$). Folded lightcurves were built in the energy bands 6.2–6.7 keV, 2–6.1 keV, and 6.8–10 keV and resulted in a pulse fraction of 49 ± 5%, 58 ± 3%, and 57 ± 4%, respectively. The ratio of the line flux to the continuum in the energy range 6.2–6.7 keV is ∼0.25. Assuming that the line is not pulsed, we infer an Fe Kα pulse fraction of ∼50%, which is in good agreement with the above measurement. Weak Fe Kα pulsation can be explained if the cocoon is isotropic.

To match the observed column density variability, the radius and the density of the inner region of the tail structure were set to 4×10^{11} cm and 3×10^{11} cm^{-3}, respectively. It is therefore very likely that the dense cocoon corresponds to the inner and ionized region of the hydrodynamical tail. We thus added this partially ionized cocoon in our simulations, using a density of 3×10^{11} cm^{-3} within a radius of $\sim 6 \times 10^{11}$ cm $\sim 3\ R_{\rm acc}$. The Fe Kα emissivity map (Fig. 8) was calculated by applying an illuminating radiation field ($\sim 1/r^2$) to the density distribution. Figure 7 displays the resulting simulated profile of the Fe Kα equivalent width together with the observed data. The green curve shows the variations in the Fe Kα equivalent width expected from the wind density profile excluding the central cocoon, which obviously could not reproduce the data. The black curve accounts for the dense central cocoon. The exact profile of the eclipse is related to the size and density profile of the cocoon. No effort has been made to obtain an exact match to the data.

The ionized cocoon is expected to produce an iron K-edge at ∼7.8 keV. For a column density of $N_{\rm H} \sim 2 \times 10^{23}$ cm^{-1}, its optical depth $\tau \sim 0.2$ (Kallman et al. 2004) remains difficult to detect. Even our observation at an orbital phase 0.15 (the best candidate for the detection of the ionised edge) does not have enough signal.

The mass of the tail-like structure $M_{\rm tail} \sim 10^{-8}\ M_\odot$ can be accumulated in $t_{\rm tail} = M_{\rm tail}/\dot{M}$, where $\dot{M} = (\pi r_{\rm eff}^2/4\pi R_{\rm orb}^2)\dot{M}_{\rm w}$ and $r_{\rm eff}$ is an effective radius for the funneling of the wind in the tail. For a tail accumulation timescale ($t_{\rm tail}$) comparable to the orbital period of (∼10 days), this effective radius is $12\ R_{\rm acc}$.

The orientation of the tail-like structure depends on the wind and orbital velocities. The angle between the wind velocity and the orbital velocity is given by $\tan(\alpha) = \upsilon_{\rm orb}/\upsilon$. The tail obtained in our simulations is tilted by $\alpha \sim 80°$. This corresponds to $\upsilon \sim 0.2\ \upsilon_{\rm orb} \approx 50$ km s^{-1}, which is lower than $\upsilon(R_{\rm orb}) \approx 250$ km s^{-1} because of the ionization of the stellar wind in the vicinity of the neutron star.

6. Conclusions

We have presented the analysis of an observing campaign performed with *XMM-Newton* on the persistently absorbed sgHMXB IGR J17252–3616. Nine observations have been performed over about four weeks, distributed across various orbital phases. Three of them were scheduled during the eclipse of the neutron star by the companion star.

We first refined the orbital solution, using in addition archival *INTEGRAL* and *RXTE* data and found an orbital period of 9.742 d and a projected orbital radius of 101 ± 2 lt-s. The pulsar spin period varies between 414.3 and 413.8 s during the observing campaign.

The X-ray spectrum (0.2–10 keV), which varies during the orbit, was successfully fitted using an absorbed cut-off power-law continuum, a soft excess, and a gaussian emission line. The soft excess, modeled with a black body, remained constant.

The continuum component varies in intensity (a measure of the instantaneous accretion rate) but displays a constant spectral shape, as usually observed in accreting pulsars.

The absorbing column density and the Fe Kα emission line show remarkable variations. The column density, always above 10^{23} cm^{-2}, increases towards 10^{24} cm^{-2} close to the eclipse, as expected for a spherically symmetric wind. The wind velocity is unusually small close to $\upsilon_\infty = 400$ km s^{-1}. An additional excess of absorption of 2×10^{23} cm^{-2} is observed for orbital phases $\phi > 0.3$, which is found to represent a hydrodynamical tail trailing the neutron star.

During the eclipse, the equivalent width of the Fe Kα line drops by a factor >10 indicating that most of the line is emitted in a cocoon surrounding the pulsar, with a size of a few accretion radii. This cocoon is ionized and corresponds to the inner region of the hydrodynamical tail.

The parameters of the IGR J17252–3616 are very similar to these of Vela X-1, except for the smaller wind velocity. We argue that the persistently large absorption column density is related to the hydrodynamical tail, which has been strengthened by the low wind velocity. The tail is a persistent structure dissolving on a timescale comparable to the orbital period.

Our interpretation can be tested using numerical hydrodynamical simulations and high resolution optical/infrared spectroscopy. If confirmed, it may turn out that half of the persistent sgHMXB have stellar wind speeds several times lower than usually measured.

References

Arnaud, K. A. 1996, in Astronomical Data Analysis Software and Systems V, ed. G. H. Jacoby, & J. Barnes, ASP Conf. Ser., 101, 17

Blondin, J. M. 1994, ApJ, 435, 756

Blondin, J. M., & Woo, J. W. 1995, ApJ, 445, 889

Blondin, J. M., Kallman, T. R., Fryxell, B. A., & Taam, R. E. 1990, ApJ, 356, 591

Blondin, J. M., Stevens, I. R., & Kallman, T. R. 1991, ApJ, 371, 684

Castor, J. I., Abbott, D. C., & Klein, R. I. 1975, ApJ, 195, 157

Charles, P. A., & Coe, M. J. 2006, Optical, ultraviolet and infrared observations of X-ray binaries, ed. W. H. G. Lewin, & M. van der Klis, 215

Chaty, S., Rahoui, F., Foellmi, C., et al. 2008, A&A, 484, 783

Choi, C. S., Nagase, F., Makino, F., et al. 1994, ApJ, 437, 449

Corbet, R. H. D. 1986, MNRAS, 220, 1047

Day, C. S. R., Nagase, F., Asai, K., & Takeshima, T. 1993, ApJ, 408, 656

Dickey, J. M., & Lockman, F. J. 1990, ARA&A, 28, 215

Endo, T., Ishida, M., Masai, K., et al. 2002, ApJ, 574, 879

Fransson, C., & Fabian, A. C. 1980, A&A, 87, 102

Fürst, F., Kreykenbohm, I., Pottschmidt, K., et al. 2010, A&A, 519, A37

Güdel, M., & Nazé, Y. 2009, A&ARv, 17, 309

Haberl, F. 1991, A&A, 252, 272

Hickox, R. C., Narayan, R., & Kallman, T. R. 2004, ApJ, 614, 881

Jansen, F., Lumb, D., Altieri, B., et al. 2001, A&A, 365, L1

Joss, P. C., & Rappaport, S. A. 1984, ARA&A, 22, 537

Kallman, T. R., & McCray, R. 1982, ApJS, 50, 263

Kallman, T. R., Palmeri, P., Bautista, M. A., Mendoza, C., & Krolik, J. H. 2004, ApJS, 155, 675

Lebrun, F., Leray, J. P., Lavocat, P., et al. 2003, A&A, 411, L141

Levine, A. M., Rappaport, S., Remillard, R., & Savcheva, A. 2004, ApJ, 617, 1284

Liu, Q. Z., van Paradijs, J., & van den Heuvel, E. P. J. 2006, A&A, 455, 1165

Mason, A. B., Clark, J. S., Norton, A. J., Negueruela, I., & Roche, P. 2009, A&A, 505, 281

Mason, A. B., Norton, A. J., Clark, J. S., Negueruela, I., & Roche, P. 2010, A&A, 519, A79

Matt, G. 2002, MNRAS, 337, 147

Mauche, C. W., Liedahl, D. A., Akiyama, S., & Plewa, T. 2008, in Am. Inst. Phys. Conf. Ser., ed. M. Axelsson, 1054, 3

Ohashi, T., Inoue, H., Koyama, K., et al. 1984, PASJ, 36, 699

Press, W. H., & Rybicki, G. B. 1989, ApJ, 338, 277

Quaintrell, H., Norton, A. J., Ash, T. D. C., et al. 2003, A&A, 401, 313

Rahoui, F., Chaty, S., Lagage, P., & Pantin, E. 2008, A&A, 484, 801

Schulz, N. S., Canizares, C. R., Lee, J. C., & Sako, M. 2002, ApJ, 564, L21

Strüder, L., Briel, U., Dennerl, K., et al. 2001, A&A, 365, L18

Takeuchi, Y., Koyama, K., & Warwick, R. S. 1990, PASJ, 42, 287

Tawara, Y., Yamauchi, S., Awaki, H., et al. 1989, Astron. Soc. Japan, 41, 473

Thompson, T. W. J., Tomsick, J. A., in 't Zand, J. J. M., Rothschild, R. E., & Walter, R. 2007, ApJ, 661, 447

van Kerkwijk, M. H., van Paradijs, J., Zuiderwijk, E. J., et al. 1995, A&A, 303, 483

Walter, R., Bodaghee, A., Barlow, E. J., et al. 2004, The Astronomer's Telegram, 229, 1

Walter, R., Zurita Heras, J., Bassani, L., et al. 2006, A&A, 453, 133

Warwick, R. S., Norton, A. J., Turner, M. J. L., Watson, M. G., & Willingale, R. 1988, MNRAS, 232, 551

Watanabe, S., Sako, M., Ishida, M., et al. 2006, ApJ, 651, 421

White, N. E. 1989, A&ARv, 1, 85

White, N. E., Nagase, F., & Parmar, A. N. 1995, in X-ray Binaries, ed. W. H. G. Lewin, J. van Paradijs, & E. P. J. van den Heuvel, 1

Winkler, C., Courvoisier, T., Di Cocco, G., et al. 2003, A&A, 411, L1

Zurita Heras, J. A., de Cesare, G., Walter, R., et al. 2006, A&A, 448, 261

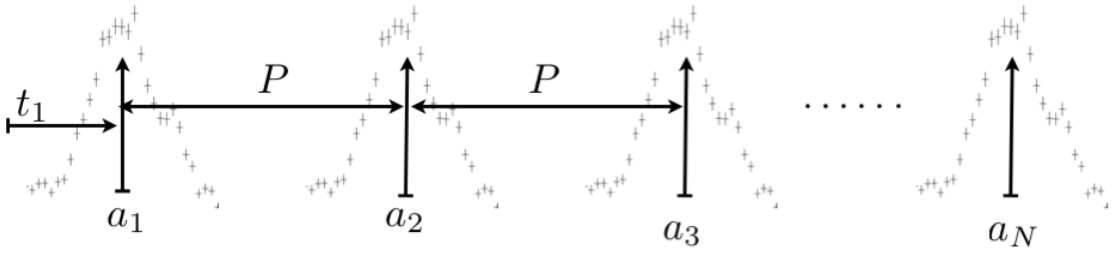

Figure 6.1: A sequence of pulse profile templates with the free parameters indicated.

6.3 Pulse Arrival Times

To obtain the pulse arrival times (PATs) for IGR $J17252-3616$ we have used XMM-Newton light-curves in the energy range 0.2-10 keV. We derived a pulse profile template obtained for the longest and least interrupted observation (obsID 0405640801). Performing a Lomb-Scargle (Press & Rybicki 1989) periodogram, we obtained a period of 414.2 sec The pulse profile template was obtained by folding the observed light-curve using this period.

A sequence of profile template was constructed in order to fit each observation separately. Figure 6.1 shows a sequence of profile template characterized by the initial shift (t_1), the period (P), and the amplitude of each pulse (α_N). The parametrized sequence was then fit to each observation individually, to obtain a series of periods and PATs for a pulse at the middle of each observation. An example of this technique on observation 0405640801is shown in figure 6.2. With this technique we could produce PATs with an accuracy of about 10 sec. If we would have fit each pulse separately, the resulting accuracy on each PAT would have been limited to 60-100 sec, roughly 1/4th of the spin period.

With the PATs, we are able to constrain the orbital solution, indeed for a circular orbit, the n-th pulse arrival time is given by,

$$t_n = t_0 + nP_0 + \frac{1}{2}n^2 P_0 \dot{P} + \frac{1}{c}\alpha_x \sin i \cos[2\pi(t_n - T_{90})/P_{orb}] \tag{6.1}$$

where n is given by the nearest integer to $n = (t_n - t_0)/(P_0 + 0.5\dot{P}(t_n - t_0))$, where P_0 is the period at the arrival time t_0, $\dot{P}$ is the period derivative, $\alpha_x \sin i$ is the projected semi-major axis, P_{orb} is the orbital period, and T_{90} is the reference time corresponding to mid-eclipse. To test the eccentricity, we added a Taylor expansion term in eq. 6.1 of the form, $-\frac{e}{2c}\alpha_x \sin i \sin[4\pi(t_n - T_{90})/P_{orb} - \omega_p]$, where e is the eccentricity and ω_p is the longitude of the periastron. By adding this perturbation, we were able to obtain an upper limit on the eccentricity $e < 0.15$ at a 90% confidence level. We obtained a $T_{90} = 53761.69$ HJD for the mid-eclipse and an orbital period of $P = 9.742$ days.

With the above parameters, we can determine the mass function of the system,

$$f(M) = \frac{4\pi^2(\alpha_x \sin i)^3}{GP_{orb}^2} = \frac{M_{OB}\sin^3 i}{1+q^2} \tag{6.2}$$

where, M_{OB} is the mass of the donor star, and $q = M_X/M_{OB}$ is the mass ratio. For IGR $J7252-3616$, $f(M) = 11.7 \pm 0.7$

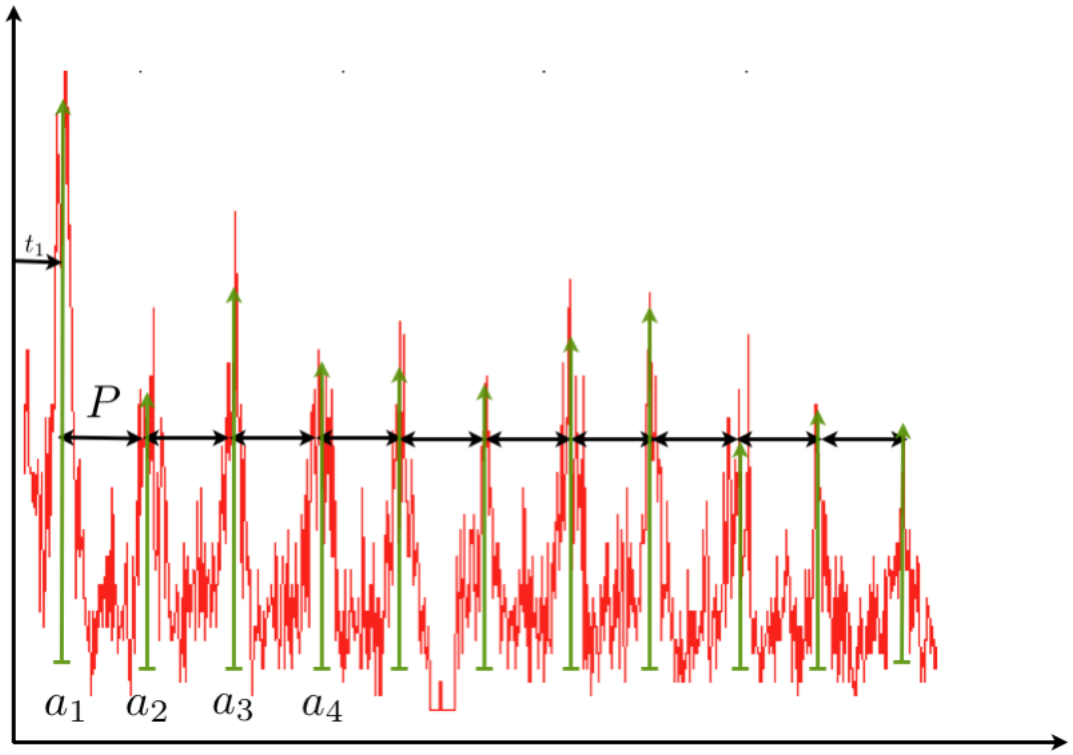

Figure 6.2: A sketch of applying the pulse profile template on one light-curve.

6.4 Phase resolved spectroscopy

The $XMM-Newton$ observations were scheduled to cover the orbital phases, 0.01, 0.03, 0.08, 0.15, 0.27, 0.37, 0.40, 0.65, 0.79, and 0.91 inferred from the orbital solutions. The spectra are always heavily absorbed below ~ 3 keV and contain an iron K-edge at 7.2 keV. We have used XSPEC (Arnaud 1996) to perform the spectral analysis. The model is characterized by an absorbed high-energy cut-off power-law, an gaussian line and a blackbody component. The overall spectrum is absorbed by the inter-stellar absorption. The model in XSPEC is written, `wabs*(bbody+vphabs*(cutoffpl+gauss))`. Throughout our observations an iron Kα line, at 6.40$\pm$0.03 keV, is always present. Some parameters (photon index, cut-off energy, blackbody temperature) did not vary significantly among the observations. To search for spectral variability we decided to fix them to their average values (E_C=8.2 keV, Γ = 0.02, kT_{BB}=0.5 keV). The model was built by using an intrinsically absorbed high energy cut-off power-law with a gaussian line, a black-body component responsible for the observed soft X-ray excess, and an overall absorption responsible for the interstellar absorption fixed to the Galactic absorption N_H=1.5$\times 10^{22}$ cm^{-2} (Dickey & Lockman 1990). Figure 6.3 shows the XMM-Newton spectra of two observations at orbital phases $\phi = 0.65$ (black) and $\phi = 0.91$ (red).

6.5 The absorber distribution

For IGR $J17252-3616$, we found that the iron edge is at 7.2 ± 0.2 keV. Figure 6.4 illustrates the energies of the Fe K edge and the Fe Kα line as a function of ionization.

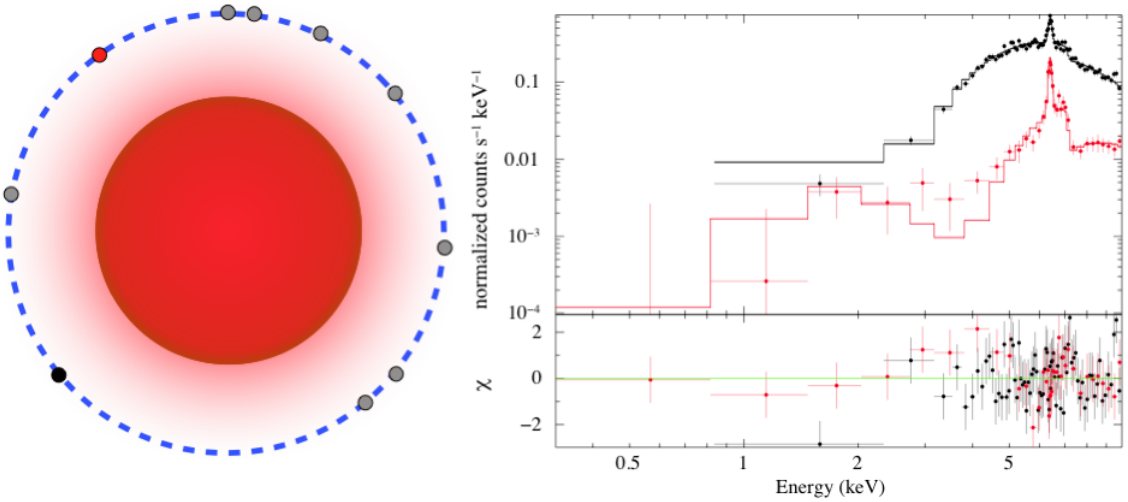

Figure 6.3: A sketch of the observation as a function of orbital phase (left) and the representing spectra (right). The points show the observations. Red and black point (left) correspond to the spectra (right).

From figure 6.4a, we see that for the iron edge energy at 7.2 ± 0.2 keV we conclude an ionization level up to Fe VI (or Fe X, for the upper limit of 7.4 keV). The corresponding ionization parameter is $\xi \sim 300$ erg cm s^{-1} (see fig 3*b* from Kallman & McCray 1982), for which the light elements do not contribute to the X-ray absorption.

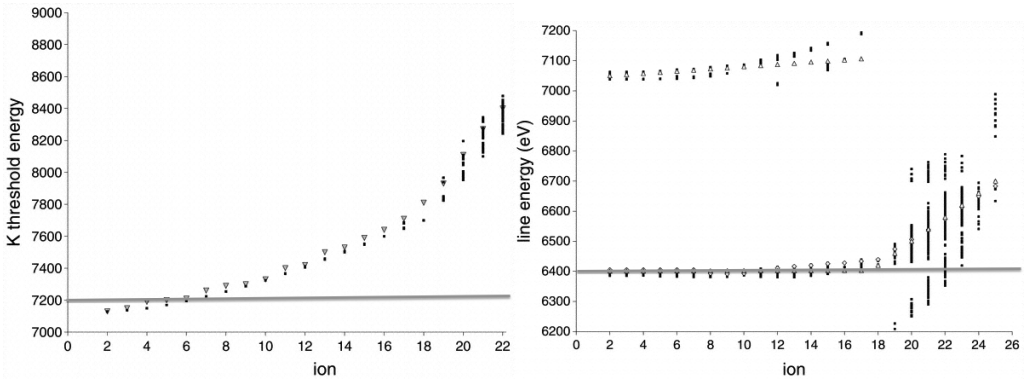

(a) Iron edge energy (b) Iron line energy

Figure 6.4: The above figures show the a) Iron K edge energy (eV) and the b) iron K line energy (eV) as a function of ionization state. The grey horizontal lines shows the observed values. *Credit:* Kallman *et al.* (2004)

We, therefore, expect a dense, but not absorbing cocoon around the neutron star. The likely geometry is illustrated in figure 6.5 (left panel) together with the corresponding curve of growth (equivalent width of the iron line vs N_H). For a centrally illuminating source, which is the case for IGR $J17252-3616$ (grey point in both figures), a more detailed curve of growth is shows in figure 6.5 (right panel), for different metallicities (for 0.5, 1.0 and 2.0 $Z_\odot$.).

A tail, far away from the highly ionized region, completes the model. The tail accounts for the accretion wakes formed within the wind of the OB star, trailing the NS. The

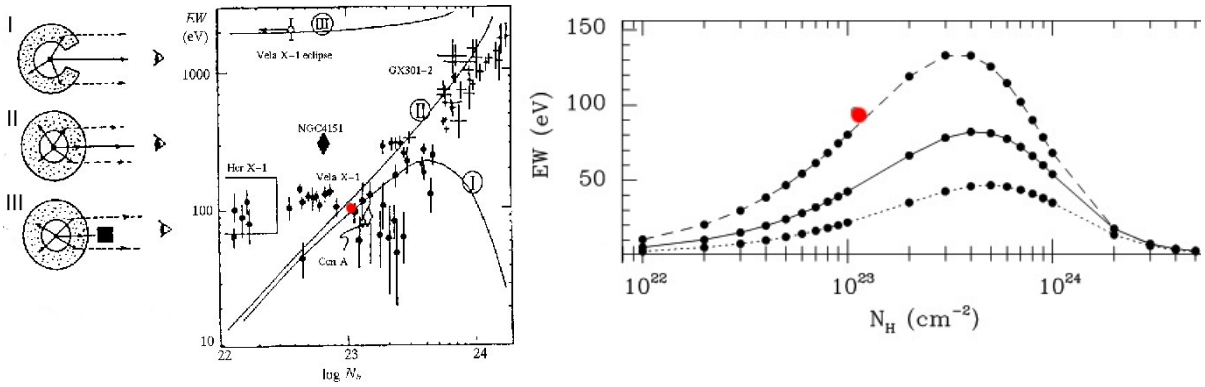

Figure 6.5: In both figures we show the relation between absorbing column density and the equivalent width of the iron Kα line. *Left:* Monte-Carlo calculation of the N_H vs Fe Kα EW for different geometries (illustrated from I to III). *Left:* The same as previous, for a spherically symmetric. The position of IGR J17252−3616 is shown by a red filled circle. *Credits:* Makishima (1986) (for the left) and Matt (2002) (for the right)

modeling ofthe accretion wake is presented in chapter 7

Chapter 7

Hydro-dynamical simulations of absorbed HMXBs

7.1 Introduction

A fluid, free to flow ideally, can be described by four parameter: density, pressure, velocity, and energy. The density (ρ) changes as the fluid moves. The velocity field ($\mathbf{u}$) is the mass-weighted average of all the individuals velocities within a microscopic cell. The pressure, p, gives the momentum flux of particles across an infinitesimal element of area. Since the kinetic energy may be stored temporally in atomic excitation, the internal energy (e) includes both the kinetic and excitation energy, to make e a conserved quantity.

Euler Equation

The motion of the fluid is described by the Euler equations which assume that the mass of all particles is conserved, the total momentum of the particles is conserved, and that the internal energy in the cell is described by the first law of thermodynamics.

For the conservation of mass, the rate of change of mass in a given volume V is the (negative) of the mass flux over the surface of the volume V.

$$\frac{d}{dt}\int_V \rho dV = -\int_S \rho \mathbf{u}\, d\mathbf{A}$$

By applying the divergence theorem[1] we can re-write the above to obtain the first Euler equation,

$$\partial_t \rho + \nabla \cdot (\rho \mathbf{u}) = 0 \tag{7.1}$$

where, for simplicity, we use $\partial_t = d/dt$ hereafter.

The momentum conservation is therefore, $\partial_t(\rho\mathbf{u}) + \nabla \cdot (\rho\mathbf{u}\mathbf{u}) + \nabla p = \mathbf{F}$. Here, the surface integral contains not only the flux of momentum being carried out across the boundary, $[-(\rho\mathbf{u})\mathbf{u} \cdot d\mathbf{A}]$, but also the momentum flux related to the pressure, $[-pd\mathbf{A}]$. An additional force (F) can be a momentum source per unit volume.

[1] The divergence theorem is also known as Gauss theorem. Assume a compact volume (V) which has a smooth boundary surface (A). If $\mathbf{f}$ is a (continuously differentiable) vector field in the neighbor of V, then $\iiint_V (\nabla \cdot \mathbf{f}) dV = \oint_S (\mathbf{f} \cdot \mathbf{n}) dA$, where $\mathbf{n}$ is the outward unit vector.

The conservation of energy can therefore be derived. Following the 1st law of thermodynamics, the Lagrangian rate[2] of change of the specific internal energy plus the rate per unit mass at the point that the pressure is doing work, equals the rate per unit mass at which heat is being deposited from the external sources, q.

$$\frac{De}{Dt} + p\frac{D(1/\rho)}{Dt} = q$$

Here we can re-write the above conservation law as follows,

$$\partial_t\Big(\rho e + \frac{1}{2}\rho u^2\Big) + \nabla\cdot\Big(\rho\mathbf{u}e + \frac{1}{2}\rho\mathbf{u}u^2 + p\mathbf{u}\Big) = \rho q + \mathbf{u}\cdot\mathbf{F} \tag{7.2}$$

The sum of the internal and of the kinetic energies is equal to the energy flux, as part of advection with fluid and another part due to the pressure.

The Hydrodynamic Code, VH-1

The code used here, VH1[3] (Written by John Blondin) is written as a Lagrangian hydrodynamics code coupled with a remap onto the original Eulerian grid (PPMLR).

Let us now consider the equations of ideal hydrodynamics in Lagrangian coordinates in 1-D, planar geometry an with no source terms. The conservation laws can be written as,

$$\begin{aligned}
\partial_t V - \partial_m u &= 0 \\
\partial_t u + \partial_m p &= 0 \\
\partial_t E + \partial_m up &= 0
\end{aligned}$$

where, $\rho = 1/V$, $E = e + u^2/2$, and $p = (\gamma - 1)\rho e$.

The above equation can be finite differenced as,

$$\begin{aligned}
\rho_{j+1/2}^{n+1} &= \rho_{j+1/2}^{n} + \Delta t\bar{u}_{j+1/2} \\
u_j^{n+1} &= u_j^n + \frac{\Delta t}{\Delta m_j}(\bar{p}_{j-1/2} - \bar{p}_{j+1/2}) \\
E_j^{n+1} &= E_j^n + \frac{\Delta t}{\Delta m_j}(\bar{u}_{j-1/2}\bar{p}_{j-1/2} - \bar{u}_{j+1/2}\bar{p}_{j+1/2})
\end{aligned}$$

where the subscript j refers to the zone averaged values, and subscript $j-1/2$ and $j+1/2$ refer to values at the left and right boundary of the zone, respectively. The superscript n refer to the time step. The values $\bar{u}$ and $\bar{p}$ are the time-averageed values of the velocity and pressure at the Lagrangian zone interfaces. Accurate and stable estimates of these quantities are essential.

[2] Here we have to start with the Lagrangian framework to define the first law of thermodynamics. The time derivative, taken into account the fluid motion, can be define as $Df/Dt = \partial_t + \mathbf{u}\cdot\nabla f$. We also assume that the volume occupied by the unit mass is $1/\rho$. The volume of this parcel of mass is therefore given by $D(1/\rho)/Dt$.

[3] http://astro.physics.ncsu.edu/pub/VH-1/

Godunov (1959) tried to obtain time-averaged quantities by approximating the flow at each zone interface during each time-step with a Riemann shock tube problem[4]. At the beginning of the time-step, the zone interface is modelled as a discontinuity separating two uniform stages given by the zone averages on the left and right side of the zone (e.g. $i-1$ and i). This constructed Riemann problem is therefore solved to derive the time-averaged value of the velocity and the pressure at the discontinuity. The solution of the non-linear problem demands an iterative procedure.

The piece-wise parabolic method (PPM, hereafter) improves upon this method by using more accurate guesses for the input states to the Riemann problem (the values on either side of the interface). Using a quadratic interpolation of the fluid variables in each zone, the Riemann input states are taken to be the average over that part of the zone that can be reached by a sound wave in a time dt, i.e., the characteristic domain of dependence. PPMLR (Colella & Woodward 1984) is a higher order extension of Godunov (1959) method. The integration and interpolation steps are performed in Lagrangian framework (co-moving), which is followed by a remap onto the fixed computational grid (Euler). VH-1 uses the PPMLR implementation of Colella & Woodward (1984).

Once the hydrodynamic equations have been differenced to obtain the values at t+dt, the fluid variables can be instantaneously remapped from the Lagrangian coordinate system to the stationary Eulerian grid. This remap step uses the same quadratic interpolation method that was used in the hydrodynamics step.

7.2 Modeling High Mass X-ray Binaries

Building a model to simulate and reproduce observable quantities of a HMXB system is a tricky and difficult job. In order to reproduce the observed absorption profile of HMXB we use the Virginia Hydrodynamic code (VH1) written by John Blondin in 1990. The code has been used in 1-D and 2-D mode. In 2-D we use spherical co-ordinates (r, θ) where the code solves the hydro equation along the orbital plane. This simulations assume an ideal gas[5] with an adiabatic index $\gamma = 5/3$.

A test particle will be affected by the effective gravity force of the two stars (the massive star and the neutron star; F_{grav}) and by the force related to the photon absorption (F_w) from the underlying photosphere of the main star. The ionizing X-ray radiation of the neutron star is taken into account to determine where the wind acceleration stops, within the Strömgren sphere.

X-ray heating and radiative cooling of the wind (Kallman & McCray 1982; Blondin *et al.* 1990) are also implemented in the code. The heating of the wind occurs through, (i) photo-ionization, (ii) Compton effect, and (iii) collisional excitation. The cooling mechanisms are, (i) recombination, (ii) bremsstrahlung, (iii) collisional ionization, and (iv) collisional de-excitation. The modeling of heating/cooling requires much more spatial and temporal resolution resulting in demanding computing time. For this reason we have not used it in this thesis. The X-ray Heating and radiative cooling can create additional instabilities in the wind. This can make the wind more variable, unstable, and create asymmetries in the trailing tail, such as filamentary structure. The impact of the heating

[4] The shock tube problem is the best shock wave example, often used as a test problem. In a laboratory, we can use a long gas cell initially at a high pressure gas on one side and a lower pressure gas on the other site separated by a membrane.

[5] The equation of state for an ideal gas is given by, $pV = nRT$, where $p = \rho(\gamma - 1)e$. The adiabatic index is $\gamma = C_p/C_v$ and e is the internal energy.

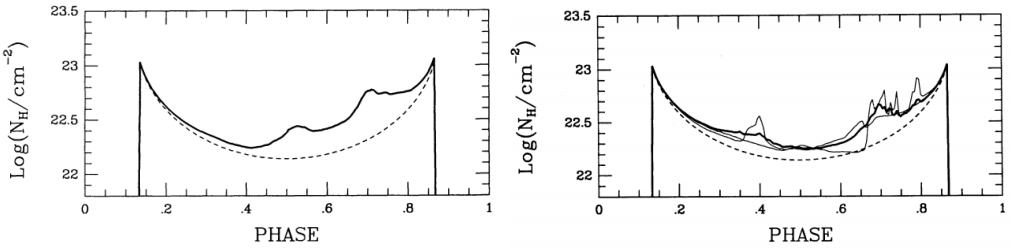

(a) Without heating/cooling (b) With heating/cooling

Figure 7.1: Time-averaged absorbing column (thick line) density for Vela X-1 using VH1: a) N_H variation when heating and cooling is not taken into account; b) shows the N_H variation when heating and cooling is taken into account; thin lines shows the column density at different times. Dashed line indicated the N_H from an unperturbed wind. *Credit:* Blondin *et al.* (1990)

and cooling is shown in figure 7.1, which can vary by a factor up to 3-4 with respect to the mean value.

We have assumed a circular orbit and a system viewed edge-on (i.e. $i = 90^o$) when deriving observable quantities (e.g. N_H). The computational grid is an important parameter. In 2-D, the key parameter of the grid is the resolution at the position of the neutron star. Resolution is also needed close to the surface of the companion star to model the acceleration of the wind. A higher resolution reveals small-scale structure close to the vicinity of the NS. In order to optimize and save computational time, the grid is denser close to the surface of the primary and in the neighbor of the NS, and the cells become wider as we go away from these regions. Typical resolution used in our analysis are at the order of $\sim 10^{10}$ cm $\sim r_{acc}/3$ for IGR $J17252-3616$, close to the neutron star. Figure 7.2 shows the grid used for the simulations.

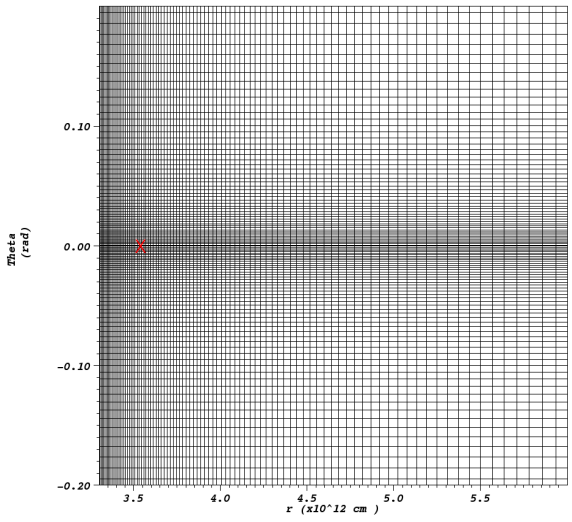

Figure 7.2: The VH1 Grid of the simulation in the vicinity of the neutron star (X).

Apart from the discretization of the grid, the model depends on number of parameters, describing the binary system. The main parameters describing the geometry of the system are:

- Mass of the primary star, M_{OB}
- Mass of the compact object M_{NS}
- Separation, the distance between the two object, α
- The radius of the primary star, R_{OB}

Another set of parameter describes the acceleration of the wind using the CAK/Sobolev approximation,

- The CAK k parameter
- The CAK α parameter
- The luminosity of the primary star, L_{OB}
- The temperature of the primary star, T_{OB}
- The density at the stellar surface, ρ_{in}

Up to now, we have not used the fact the the compact object accretes matter and therefore emits hard X-rays with luminosities, $L \sim \dot{M}$. These X-rays can efficiently ionize the local environment and stop the acceleration of the wind as we see further in this chapter. The ionization stage and the point at which the wind is no more accelerated are described by

- The X-ray luminosity of the neutron star, L_X
- A critical $\xi = \frac{L_X}{nr^2}$, at which material is highly ionized, $\xi_{crit} = 300$ erg cm s^{-1}.

Figure 7.3 shows the ionization structure of a number of elements as a function of the ionization parameter ξ. We see that most of the heavy ions (bottom lines) are fully ionized at $\xi \sim 100 - 1000$ or even larger. The above parameters control the simulation. A number of them are well constrained from the observations (e.g. the geometry). Some parameters (i.e. CAK k, CAK α, and ρ_{in}) are not related to observed quantities and need to be constrained from wind terminal velocity and mass-loss rate.

Tuning the Parameters

The parameters describing the geometry are relatively well known, for the two systems (Vela X-1 and IGR $17252 - 3616$) that we have studied in this chapter. These parameters are listed in table 7.1.

The parameters related to the radiatively driven winds are not known. We started with the 1-D code simulating only the companion star for a range of CAK parameters to obtain the velocity field and mass-loss rate. We started with k and α parameters in the range 0.05 to 0.5 (Lamers & Cassinelli 1999) and $\rho_{in} = 10^{-(13-10)}$ gr cm^{-3}, in order to obtain a steady wind. The wind terminal velocity and mass-loss rate can be measured for each simulation.

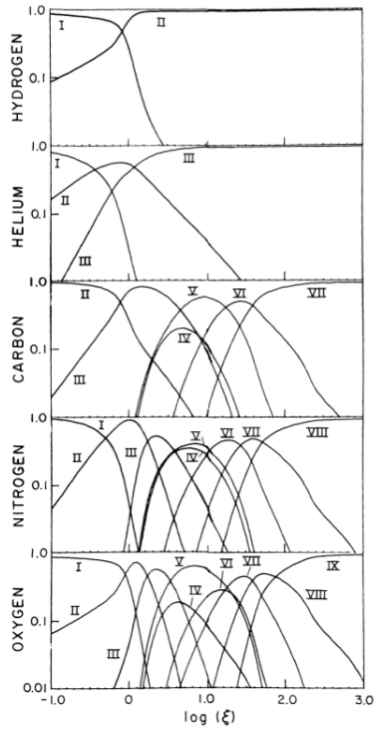

Figure 7.3: Ionization stages for a number of (light) elements. Those at the bottom (O, C, N) are responsible for the wind accelerations. *Credit:* Kallman & McCray (1982).

The parameters derived for IGR $J17252-3616$ are listed in table 7.2. For Vela X-1 we used only one set of parameters (k=0.35, α=0.55, ρ_{in}=1E-12) as the wind terminal velocity and mass-loss rate are well known.

We have run the 1-D code for a typical mass loss rate of $\sim 10^{-6}$ $M_\odot$ yr^{-1} for both $v_\infty = 1700$ km s^{-1} (e.g. Vela X-1) and for a slower wind $v_\infty = 500$ km s^{-1} (IGR $J17252-3616$). The wind-related parameters are listed in table 7.2. Figure 7.4 shows the wind velocity when the wind is relaxed, after some time ($t >> 1$ orbit). In both plots we have fitted the parameters using $\beta = 0.8$. The fit is represented by the solid black line. To demonstrate the influence of ionization we also plotted the velocity distribution disrupted by the presence of the X-ray radiation field for $\xi_{crit} = 1000$ ergs cm s^{-1}.

7.3 Testing the code using Vela X-1

Vela X-1 is the prototype of the classical sgHMXB. It is an eclipsing binary with an orbital period of about 8.96 days, a spinning pulsar, P$\sim$ 280 sec, orbiting in a close configuration with a distance to its primary star of α =1.78 R_*. Vela X-1 has been studied over the years in all regimes, from the radio to extreme gamma rays. The donor star is a B 0.5 Ib. The parameters are summarized in the table 7.1.

We ran the 2-D simulation over 4.5 orbital periods. Figure 7.5 shows the density distribution obtained after $t = 2$ P$_{orb}$, where accretion structures trailing behind the neutron star can be observed. Figure 7.6 shows the absorbing column density (N_H) variations with phase. The tail-like structure following the NS can be traced in these variations. Past work has shown that the strength of the tail structure is related to the binary separa-

Table 7.1: Physical paramater of two sgHMXBs.

Model prefix	Vela $X-1$	IGR $J17252-3616$
Donor star Parameters		
M_* ($M_\odot$)	23.1[2]	15[3]
R_* ($R_\odot$)	30[4]	29[1,6]
L_* ($10^5\,L_\odot$)	2.5[5]	4[6]
T_* (kK)	40[5]	30[6]
Wind Parameters		
$\dot{M}_W$ ($10^{-6}\dot{M}_\odot$ yr^{-1}	1[7]	1[1]
υ_∞ (km s^{-1})	1700[7]	500[1]
Binary parametrs		
M_{NS} ($M_\odot$)	1.88[2]	1.5-2.0 (see text)
α (R_*)	1.78[4]	1.75[1]
L_X (10^{36} erg s^{-1})	4[8]	1[1]

References: (1) Manousakis & Walter (2011), (2) Quaintrell *et al.* (2003), (3) (Takeuchi, Koyama & Warwick 1990), (4) van Kerkwijk *et al.* (1995), (5) Prinja & Massa (2010), (6) Mason *et al.* (2009b), (7) Dupree *et al.* (1980) (8) Kreykenbohm *et al.* (2008)

Table 7.2: Wind model parameters.

Model prefix	v12_ML2	v12_ML10	v12_ML50	v5_ML2	v5_ML10	v5_ML10
Input						
CAK α	0.55	0.55	0.55	0.35	0.35	0.35
CAK k	0.05	0.15	0.30	0.20	0.30	0.55
ρ_{in} (gr cm^{-3})	1E-12	5E-12	1E-11	5E-12	5E-11	1E-10
Outcome						
$\dot{M}_W$						
$\times 10^{-7}$ ($\dot{M}_\odot$ yr^{-1})	2	10	50	2	10	50
υ_∞ (km s^{-1})	1200	1200	1200	500	500	500

tion (Blondin, Stevens & Kallman 1991). When the wind acceleration stops closer to the surface of the companion, a more efficient disruption occurs.

The results of our simulation are in good agreement with these obtained by Blondin *et al.* (1990): the N_H is of the order of 10^{22} cm^{-2} with an increases for orbital phases > 0.6, because of an accretion wake. Only a minor difference (less than a factor of 2) between our simulations and those of Blondin *et al.* (1990) can be observed at orbital phase $\phi \approx 0.8$.

7.4 Application to IGR J17252-3616

The sgHMXB, IGR $J17252-3616$ has been observed with $XMM-Newton$ and $INTEGRAL$. The source is an eclipsing binary with an orbital period of 9.74 days, a pulsar spinning with P$\sim$ 414 sec, orbiting in a close configuration with a distance to its primary star of α =1.75 R_* with an intrinsic absorbing column density persistently high ($\geq 10^{23}$ cm^{-2}).

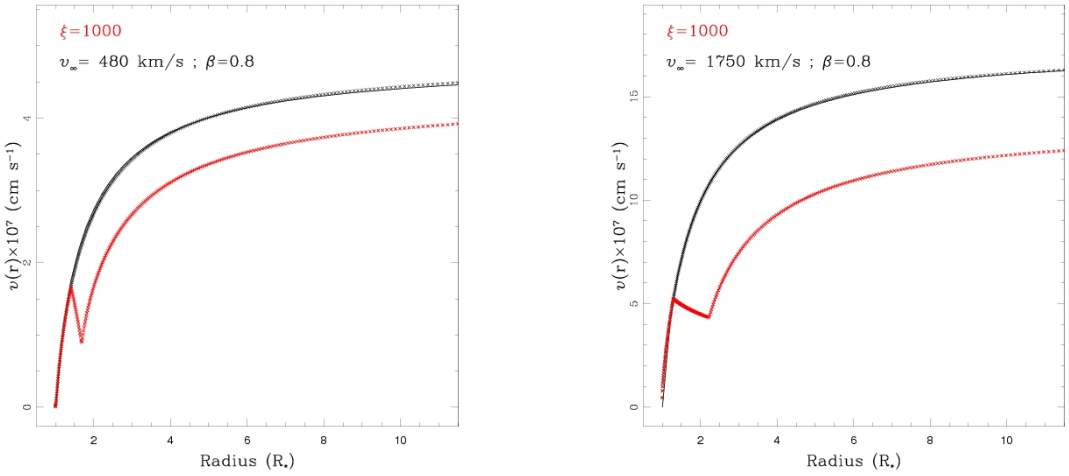

(a) IGR $J17252-3616$ (b) Vela X-1

Figure 7.4: Velocity field adopted for a classical sgHMXB (right) and an absorbed (left). The red lines indicate the velocity field perturbed by the X-ray ionization. One can notice the presence of a minimum at the position of the neutron star, $\alpha \sim 2$ R$_*$, similar for the two systems.

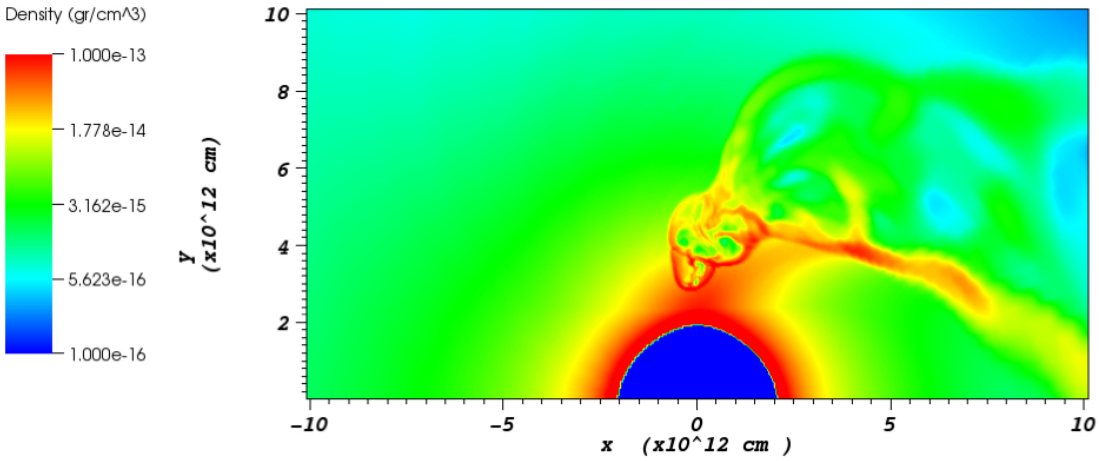

Figure 7.5: Vela X-1 after 2 orbits.

Ground-based observations (Mason *et al.* 2009b,a) showed that the donor star is likely of spectral type B0-5I or B0-1 Ia. Typical wind terminal velocities of these stars are at the order of 1500 km s^{-1}. Manousakis & Walter (2011) suggested that the wind terminal velocity of the system is significantly lower, of the order of $v_\infty \sim 500$ km s^{-1}. An ad-hoc modeling of the trailing tail allowed to reproduce the observed column density profile and the observed iron Fe Kα line emissivity.

We performed hydrodynamic simulations using the parameters of this particular system, with the aim to confirm or rule-out the hypothesis of a low terminal velocity. We have run the code for different wind parameters, for a terminal velocity between 500 km

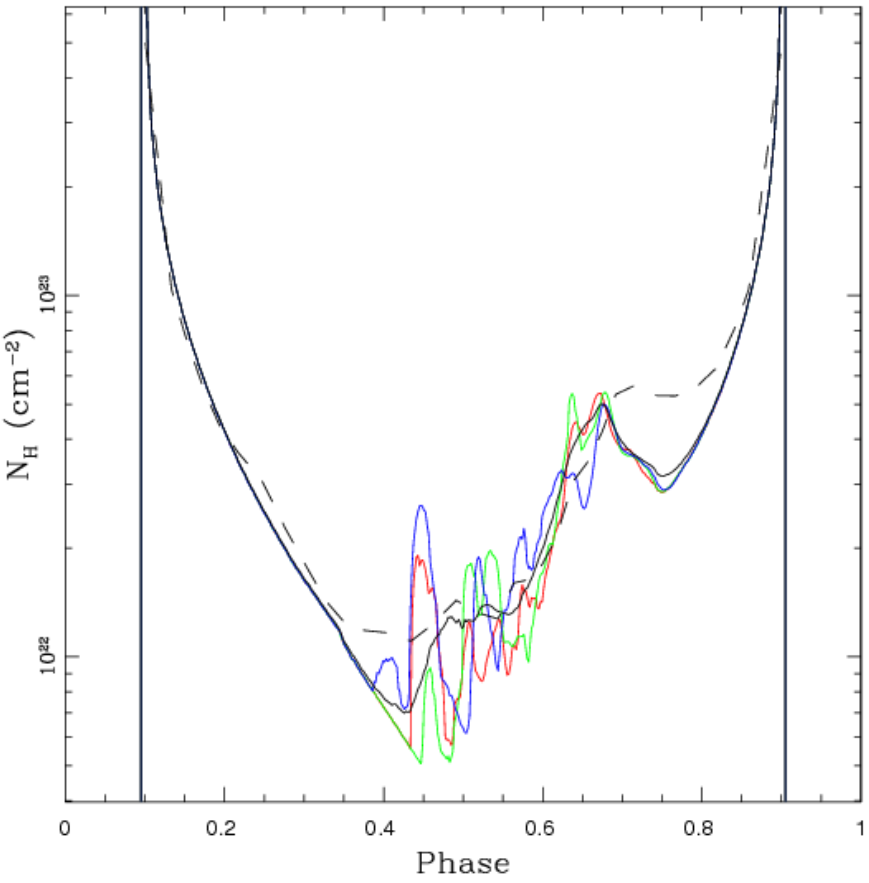

Figure 7.6: Absorbing Column Density, N_H for Vela X-1, after 1 (red), 2 (green), and 3 (blue) orbits. The black line indicates the time-averaged N_H. The dashed line indicated the resulting N_H taken from Blondin *et al.* (1990, see fig. 7.1a for comparison).

s^{-1} and 1200 km s^{-1} and for a mass loss rate between 2×10^{-7} and 5×10^{-6} $M_\odot$ yr^{-1} . The parameters of these runs are listed in tables 7.1 and 7.2.

7.5 Wind velocity and shocks

We have used the 2D code to identify the impact of a slow wind velocity. The physical parameters are selected for IGR $J17252-3616$. Figure 7.7 shows the density distribution for different wind configurations. One can see that the orientation of the accretion wake depends on the wind parameters. The slower is the wind, the more enhanced is the hydrodynamical tail. Figures 7.8 to 7.13 shows the time-averaged N_H for different wind configurations. This series of figures demonstrate the sensitivity of the obscuration on the wind parameters. The slower the wind, the larger the amount of obscuration. In addition, figure 7.14 shows results of all the wind configuration (for a given NS mass, M_X=1.95 $M_\odot$) plotted with the data from IGR $J17252-3616$. The parameters of the simulations can be constrained by the observations. We adopt a value of wind terminal velocity of $v_\infty = 500$ km s^{-1} and a mass-loss rate of $\dot{M} = 10^{-6}$ $M_\odot$ yr^{-1}.

The geometry the shock, formed around a neutron star, is affected by the wind parameters (Fransson & Fabian 1980). In a highly ionized environment, close to the neutron star, the wind acceleration stops (Stevens & Kallman 1990; Stevens 1991) and can create shocks by pilling up at that boundary (see fig. 7.4a for a slow wind and fig. 7.4b for a typical wind). The wind parameters and the relative motion of the neutron star within the wind allows to estimate the orientation of the forming shock, which depends on the mass of the NS (see section 7.6).

7.6 Neutron star mass

We investigated the dependency of the absorbing column density, N_H, profile on the mass of the neutron star. Figure 7.15 shows the density distribution of a moderate ($\dot{M}_w \sim 10^{-6}$ $M_\odot$ yr^{-1}) and a slow wind velocity (υ_∞=500 km s^{-1}) for a neutron star mass between 1.5 and 2.0 $M_\odot$, with a step of 0.1 $M_\odot$. The corresponding time-averaged absorbing column density is plotted in figure 7.16. The heavier the neutron star, the more tilted is the hydrodynamical tail. This affects the orbital phase dependence of N_H by moving the minimum of the N_H earlier in phase. The jump of N_H at mid-orbital phase is also getting larger when the neutron star mass is higher, reaching almost $N_H \sim 10^{24}$ cm^{-2}.

The comparison of the variation of N_H with orbital phase derived from observations and hydrodynamical simulations allow to evaluate the mass of the neutron star. From figure 7.16, we see that the mass of the neutron star is in the range $M_X = 1.9 - 2.0$ $M_\odot$. This mass is well bellow the (theoretical) maximum mass of a neutron star, $M_{NS}^{max} \lesssim 3$ $M_\odot$ (Müller & Serot 1996).

The neutron star mass derived above is independent from the mass function derived from the dynamical studies with the analysis of spectral lines. However, it is model-dependent. The uncertainties on the parametrization of the wind will impact on the neutron star mass determination. For a velocity of $\upsilon_\infty = 500$ km s^{-1} the simulated N_H moves, in rough terms, vertically in figure 7.16. Therefore, the mass-loss rate can be rather well constrained with an accuracy of a factor 2, resulting in the range $\dot{M} \approx (0.5-2)\times 10^{-6}$ $M_\odot$ yr^{-1}. Estimates of the uncertainty of the terminal velocity is more complicated to obtain. First, a 1-D model should be built to derive a stable wind parameter which should be fed in the 2-D code. This will be performed for the publication of these results. We see in figures 7.8 to 7.13 that the dependency on the neutron star mass is significant when the wind is slow whereas it is less significant for a typical wind velocity.

Measurement of the mass (or radius) of a neutron star can strongly constrain the equation of state (EOS) of dense matter and theoretical models of their composition (Lattimer & Prakash 2007, and references therein). Demorest *et al.* (2010) used radio observations to estimate the mass of the pulsar PSR J1614-2230 using the Shapiro delay. The Shapiro delay (Shapiro 1964) is an effect of general relativity (light bending), maximized during the eclipse of the pulsar by the primary star. Comparison between the observed pulse arrival times and model predictions allowed them to obtain the parameters of the binary system and to constrain the mass of the pulsar to $M = 1.97 \pm 0.04$ $M_\odot$.

The neutron star mass of IGR $J17252-3616$ is in the same range as that of PSR J1614-2230. Figure 7.17 shows the mass-radius diagram for a number of EOSs. The lower mass derived for IGR $J17252-3616$ is shows by a red line, while the upper mass coincides with the mass of PSR $J1614-2230$. Any of the proposed EOS whose trajectory does not intersect with the two lines can be ruled out by these mass estimate. For example, models

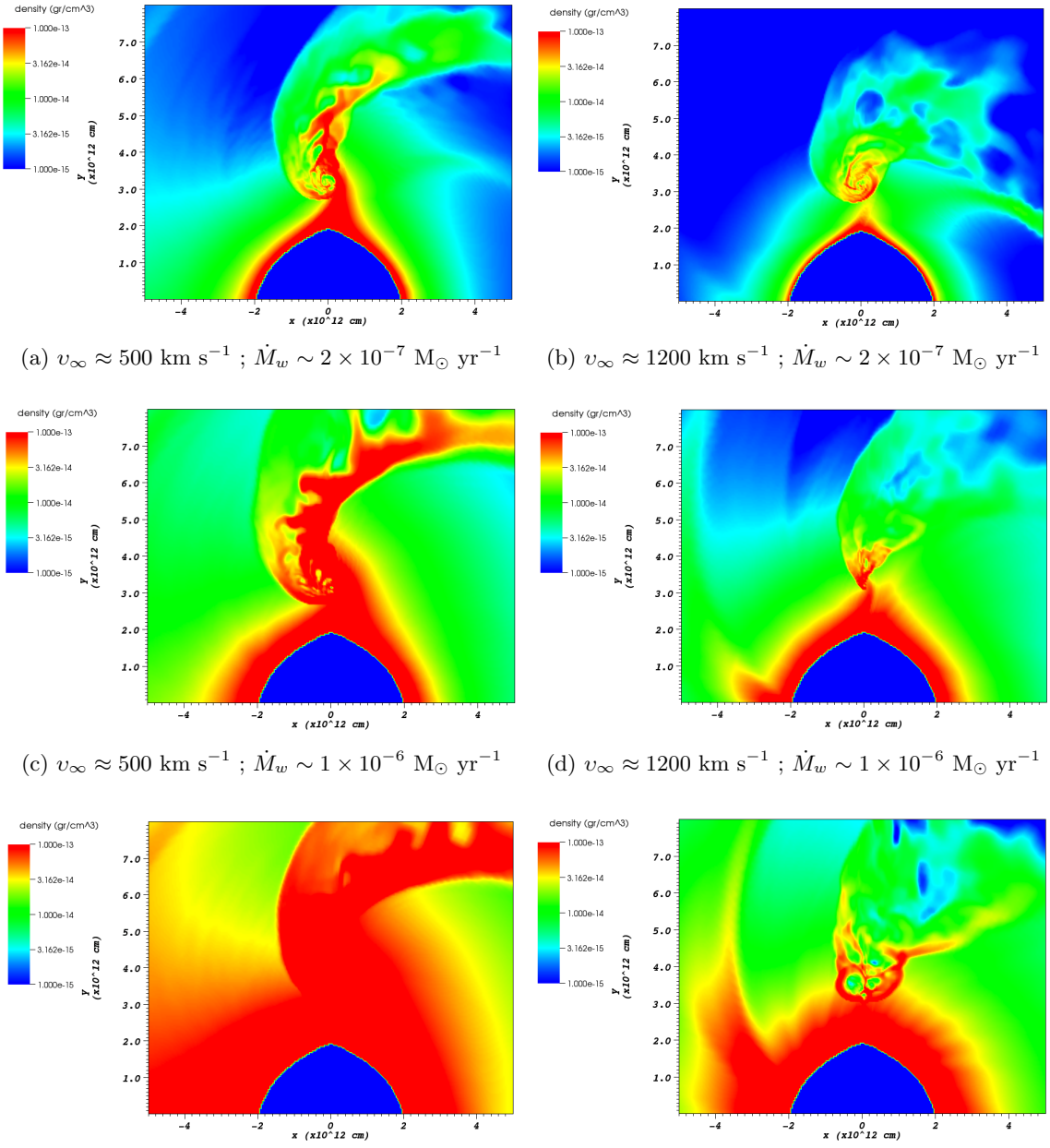

(a) $\upsilon_\infty \approx 500$ km s^{-1} ; $\dot{M}_w \sim 2 \times 10^{-7}$ M$_\odot$ yr^{-1}

(b) $\upsilon_\infty \approx 1200$ km s^{-1} ; $\dot{M}_w \sim 2 \times 10^{-7}$ M$_\odot$ yr^{-1}

(c) $\upsilon_\infty \approx 500$ km s^{-1} ; $\dot{M}_w \sim 1 \times 10^{-6}$ M$_\odot$ yr^{-1}

(d) $\upsilon_\infty \approx 1200$ km s^{-1} ; $\dot{M}_w \sim 1 \times 10^{-6}$ M$_\odot$ yr^{-1}

(e) $\upsilon_\infty \approx 500$ km s^{-1} ; $\dot{M}_w \sim 5 \times 10^{-6}$ M$_\odot$ yr^{-1}

(f) $\upsilon_\infty \approx 1200$ km s^{-1} ; $\dot{M}_w \sim 5 \times 10^{-6}$ M$_\odot$ yr^{-1}

Figure 7.7: Density distribution (gr cm^{-3}) in the plane of the orbit after ~ 3 orbits with a terminal velocity of $\upsilon_\infty \approx 500$ km s^{-1} or 1200 km s^{-1} and a mass-loss rate $\dot{M}_w \approx 0.2, 1, 5 \times 10^{-6}$ M$_\odot$ yr^{-1}. The mass of the neutron star is M$_X$=1.9 M$_\odot$. The color bar indicates the density.

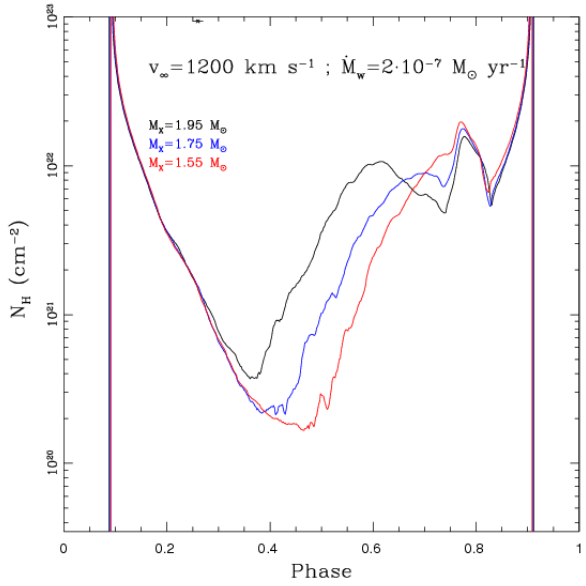

Figure 7.8: Time-averaged absorbing column density (N_H) for IGR $J17252-3616$ simulations. The stellar wind is characterized by a mass-loss rate of $\dot{M} = 2 \times 10^{-7}$ $M_\odot$ yr^{-1}, a wind terminal velocity of v_∞=1200 km s^{-1}, and M_X = 1.55, 1.75, 1.95 $M_\odot$. We also over-plotted the data from Manousakis & Walter (2011).

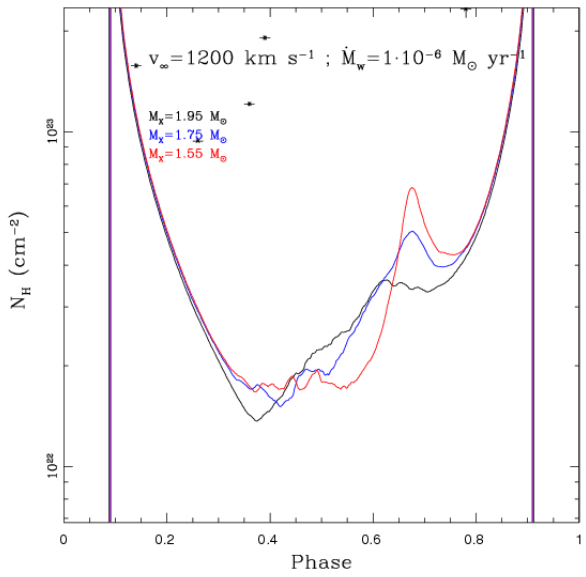

Figure 7.9: Same as figure 7.8 for $\dot{M} = 1 \times 10^{-6}$ $M_\odot$ yr^{-1}, v_∞=1200 km s^{-1} and M_X = 1.55, 1.75, 1.95 $M_\odot$.

include the appearance of exotic hadronic matter, such as hyperons or kaon condensates (GS1 and GM3 in fig. 7.17) seems to be ruled out.

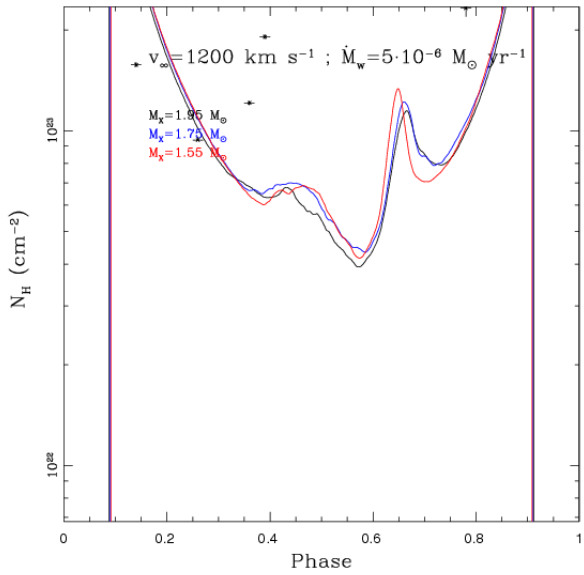

Figure 7.10: Same as figure 7.8 for $\dot{M} = 5 \times 10^{-6}$ $M_\odot$ yr^{-1}, υ_∞=1200 km s^{-1}, and $M_X = 1.55, 1.75, 1.95$ $M_\odot$.

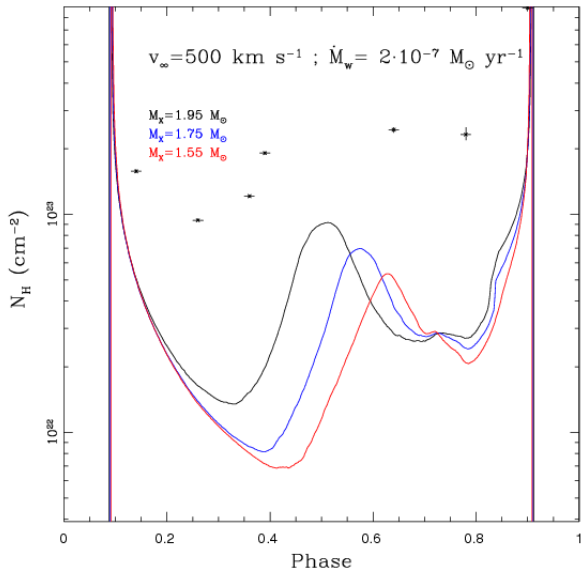

Figure 7.11: Same as figure 7.8 for $\dot{M} = 2 \times 10^{-7}$ $M_\odot$ yr^{-1}, υ_∞=500 km s^{-1}, and $M_X = 1.55, 1.75, 1.95$ $M_\odot$.

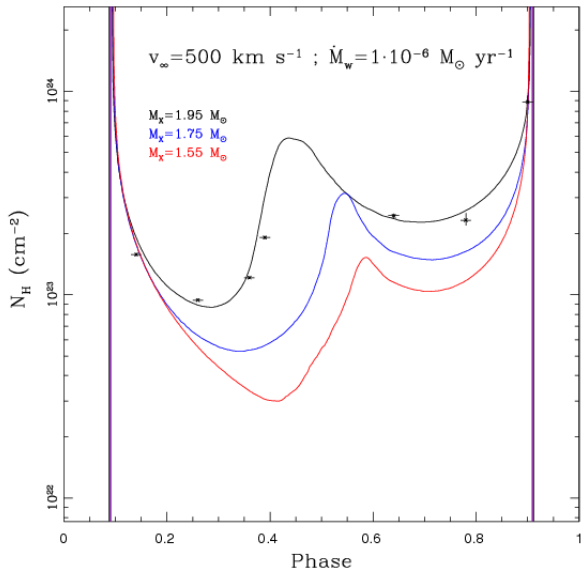

Figure 7.12: Same as figure 7.8 for $\dot{M} = 1 \times 10^{-6}$ M$_\odot$ yr^{-1}, υ_∞=500 km s^{-1}, and M_X = 1.55, 1.75, 1.95 M$_\odot$.

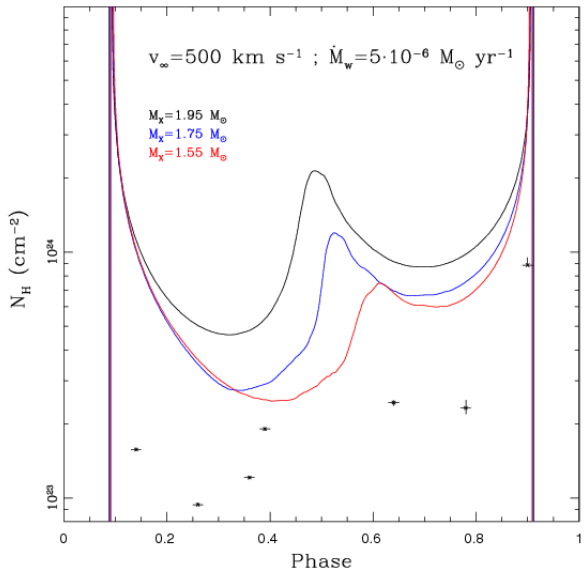

Figure 7.13: Same as figure 7.8 for $\dot{M} = 5 \times 10^{-6}$ M$_\odot$ yr^{-1}, υ_∞=500 km s^{-1}, and M_X = 1.55, 1.75, 1.95 M$_\odot$.

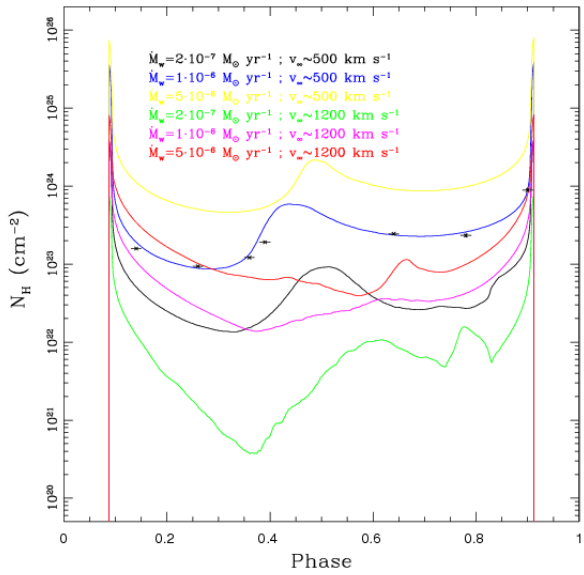

Figure 7.14: Same as figure 7.8 for a neutron star mass of M_X=1.95 $M_\odot$ and a number of different stellar winds.

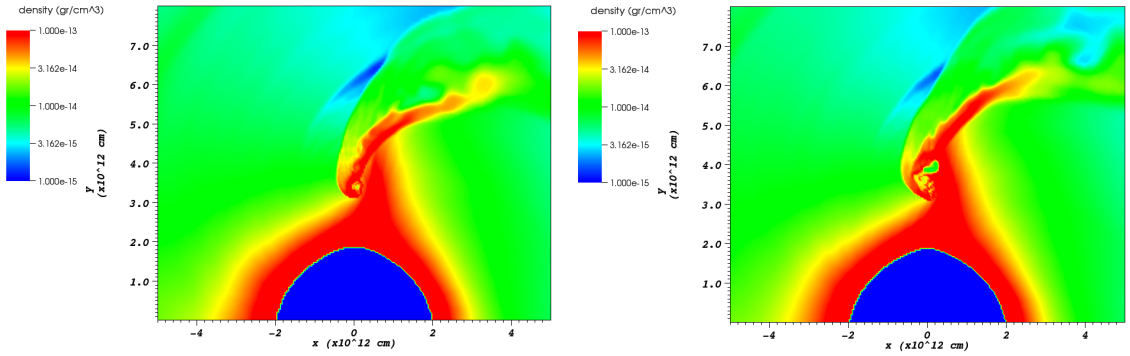

(a) $M_X = 1.5M_\odot$ (b) $M_X = 1.6M_\odot$

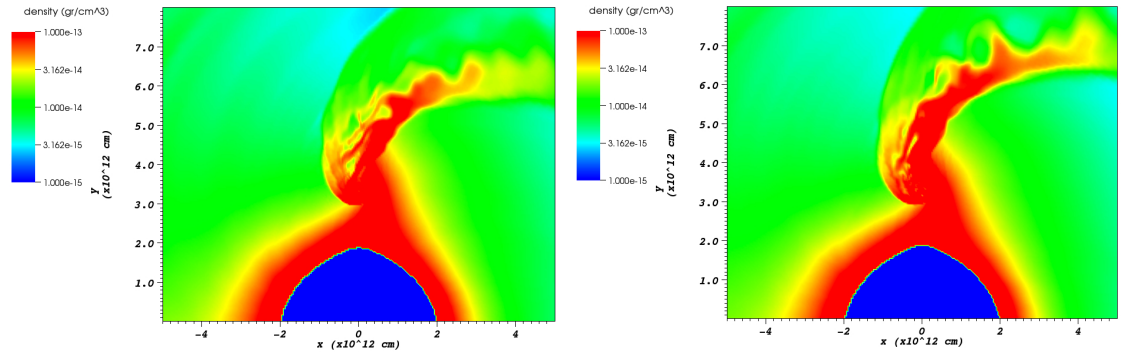

(c) $M_X = 1.7M_\odot$ (d) $M_X = 1.8M_\odot$

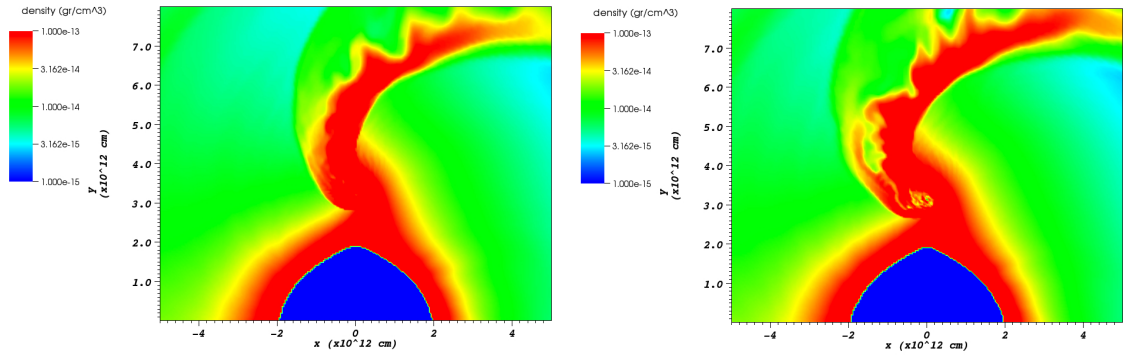

(e) $M_X = 1.9M_\odot$ (f) $M_X = 2.0M_\odot$

Figure 7.15: Density distribution (gr cm^{-3}) at the plane of the orbit after ~ 3 orbits with a terminal velocity of $\upsilon_\infty \approx 500$ km s^{-1} and a mass-loss rate $\dot{M}_w \approx 10^{-6}$ M$_\odot$ yr^{-1}. The color bar indicated the density (in gr cm^{-3}). The dependency on the mass of the compact object can be resolved. See the text for more details.

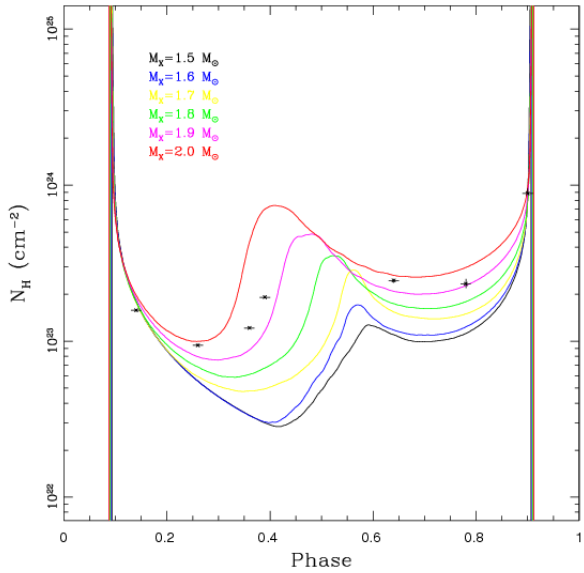

Figure 7.16: Time-averaged absorbing column density (N_H) for IGR $J17252-3616$ simulation. The stellar wind is characterized by a $\dot{M} = 1 \times 10^{-6}$ $M_\odot$ yr^{-1} and v_∞=500 km s^{-1}. The neutron star mass is M_X = 1.5, 1.6, 1.7, 1.8, 1.9, 2.0 $M_\odot$. We also over-plotted the from Manousakis & Walter (2011)

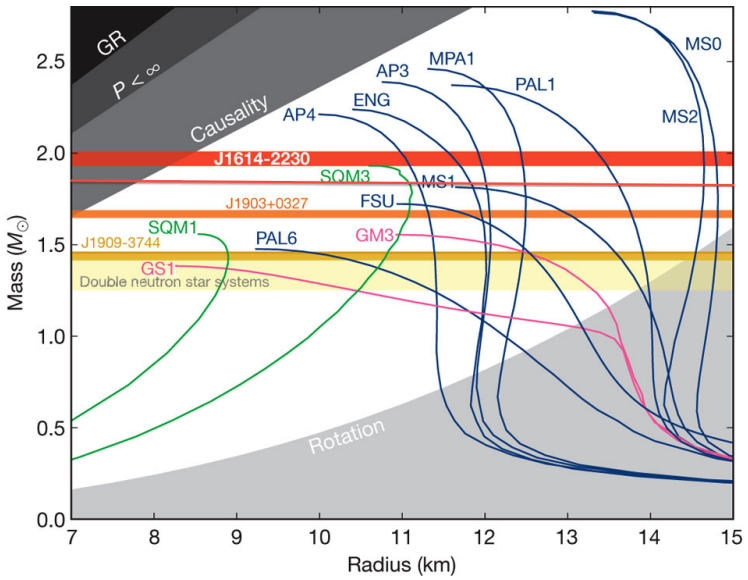

Figure 7.17: Neutron star mass-radius diagram for typical EOSs (blue, nucleons; pink, nucleons + exotic matter; green, strange quarks). The horizontal band (red) shows the observational constraint for J1614-2230 mass measurement (1.97 ± 0.04 $M_\odot$). A red line gives the lower mass value for IGR $J17252-3616$ *Credit:* Demorest *et al.* (2010)

Chapter 8

Accretion disk geometry in XMMU $J054134.7-682550$

8.1 Introduction

The X-ray spectra of Be/X-Ray binaries can be characterized by a cutoff power-law. In a few systems, when the interstellar absorption is low, there is an evidence of a soft excess below 2 keV, often modeled as a blackbody component. It has been shown that the soft excesses observed in luminous X-ray sources ($L_X > 10^{38}$ erg s^{-1}) can only be explained by reprocessing of hard X-rays by optically thick material, near the inner edge of the accretion disk (Hickox, Narayan & Kallman 2004, and references therein). Only a handful of systems, i.e., LMC X-4, SMC X-1, Her X-1, have been observed in the past, featuring remarkable soft X-ray excess.

The system XMMU $J054134.7-682550$, located in the Large Magellanic Cloud - LMC, featured a Type II outburst in August 2007. XMMU $J054134.7-682550$ had been proposed as a likely HMXB by Shtykovskiy & Gilfanov (2005). Palmer, Grupe & Krimm (2007) found XMMU $J054134.7-682550$ in a flaring state during a routine scan of the Swift-BAT data on August 3, 2007 at a level of ≈ 50 mCrab. Subsequent RXTE observations on August 9, 2007 revealed X-ray pulsations ($P_s \approx 61.601 \pm 0.017$s) and cyclotron feature at 10 keV (Markwardt, Swank & Corbet 2007). Assuming a Be system having a type II outburst, Markwardt, Swank & Corbet (2007) estimated an orbital period of about 80 days (within a factor of $\sim$2) based on the Corbet diagram. The average PCA (Proportional Counter Array on board RXTE) spectrum could be fit with a cut-off power law, with photon index 0.47 and an e-folding cut-off energy of 16 keV (Markwardt, Swank & Corbet 2007). Serendipitous observations with $XMM-Newton$ revealed significant soft excess at energies less that 2 keV and confirmed a cyclotron line at 9 keV.

The observability of the soft excess depends on the absorbing column density (N_H) and flux. One can assume that soft excesses are present in other accreting pulsars but not detectable due to too low flux or high N_H (Hickox et al. 2004). Sources far away from the galactic plane suffers less absorption than those in the galactic plane. Figure 8.1 shows flux vs N_H for a number of accreting pulsars. The left panel of figure 8.1 shows a sample of sources with detected soft excess (stars) or not detected (filled boxes). A clean boundary between the two kind of sources is seen. In the right panel, the over-plotted contour levels of χ^2_ν fitted by a simple absorbed power law supports this idea. Sources with high χ^2_ν shows soft excess while sources with $\chi^2_\nu \sim 1$ do not show soft excess. Thanks

to the type II outburst and its position in the LMC, we were able to detect a soft excess in XMMU $J054134.7-682550$.

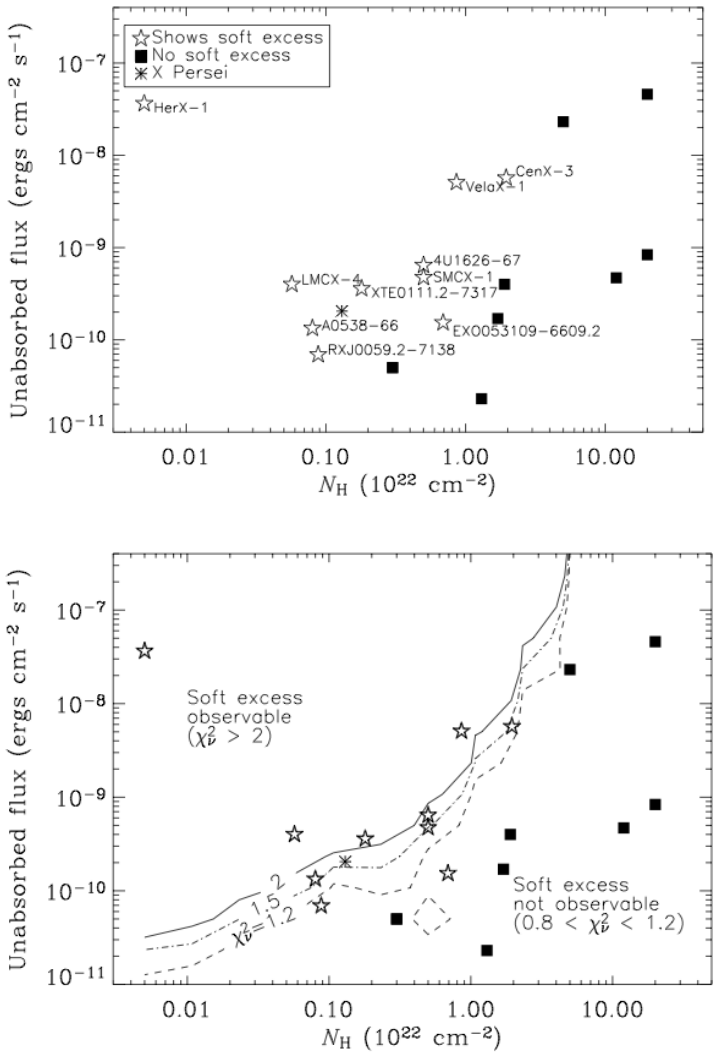

Figure 8.1: *Top*: Observed N_H and unabsorbed fuxes for X-ray binary pulsars. Sources with soft excess are shows as stars, without soft excess with filled boxes. *Bottom*: Observability of the soft excess as a function of N_H and unabsorbed fluxes. The contours show the fits of simple absorbed power law. *Credit:* Hickox, Narayan & Kallman (2004)

The soft X-ray excess, observed in several Be/X-ray binaries, has been interpreted as the signature of hard X-ray reprocessing in the inner accretion disk. Thanks to the cyclotron line of XMMU $J054134.7-682550$, we were able to constrain the magnetic field, and therefore the magnetospheric radius. We have analyzed series of simultaneous observations obtained with XMM-Newton/EPIC-MOS and RXTE/PCA in order to derive spectral and temporal characteristics of the system, before, during and after the giant outburst. The geometry of the system could be understood by studying the the soft X-ray pulsed to the hard X-ray pulses. We found that the reprocessing region corresponds to the inner edge of the accretion disk, because the soft X-ray emission showed a sinusoidal modulation, wider than of hard X-rays (Manousakis *et al.* 2009).

8.2 Scientific Article on XMMU $J054134.7 - 682550$

A&A 498, 217–222 (2009)
DOI: 10.1051/0004-6361/200811087

Astronomy & Astrophysics

Pulsed thermal emission from the accreting pulsar XMMU J054134.7-682550⋆

A. Manousakis[1,2], R. Walter[1,2], M. Audard[1,2], and T. Lanz[3]

[1] ISDC Data Center for Astrophysics, Chemin d'Ecogia 16, 1290 Versoix, Switzerland
e-mail: Antonios.Manousakis@unige.ch
[2] Observatoire de Genève, Université de Genève, Chemin des Maillettes 51, 1290 Versoix, Switzerland
[3] Department of Astronomy, University of Maryland College Park, MD 20742-2421, USA

Received 3 October 2008 / Accepted 2 February 2009

ABSTRACT

Aims. Soft X-ray excesses have been detected in several Be/X-ray binaries and interpreted as the signature of hard X-ray reprocessing in the inner accretion disk. The system XMMU J054134.7-682550, located in the LMC, featured a giant Type II outburst in August 2007. The geometry of this system can be understood by studying the response of the soft excess emission to the hard X-ray pulses.
Methods. We have analyzed series of simultaneous observations obtained with XMM-Newton/EPIC-MOS and RXTE/PCA in order to derive spectral and temporal characteristics of the system, before, during and after the giant outburst. Spectral fits were performed and a timing analysis has been carried out. Spectral variability, spin period evolution and energy dependent pulse shapes are analysed.
Results. The outburst ($L_X = 3 \times 10^{38}$erg/s $\approx L_{EDD}$) spectrum could be modeled successfully using a cutoff powerlaw, a cold disk emission, a hot blackbody, and a cyclotron absorption line. The magnetic field and magnetospheric radius could be constrained. The thickness of the inner accretion disk is broadened to a width of 75 km. The hot blackbody component features sinusoidal modulations indicating that the bulk of the hard X-ray emission is emitted preferentially along the magnetic equator. The spin period of the pulsar decreased very significantly during the outburst. This is consistent with a variety of neutron star equations of state and indicates a very high accretion rate.

Key words. X-rays: binaries – stars: emission-line, Be – accretion, accretion disks – Magelanic Clouds

1. Introduction

Be/X-ray binaries consist of a neutron star orbiting a Be star, which is defined as a non-supergiant B-type star whose spectrum shows (or showed, at some time) one or more Balmer lines in emission. Be/X-Ray binaries display X-ray pulsations, a signature of the strong magnetic field ($B \sim 10^{12}$ G) of the neutron star orbiting a massive star companion. Most known Be/X-Ray binaries undergo outbursts in which their X-ray luminosity suddenly increases by a factor of ∼10−10^4 with respect to the quiescence level.

They can feature two types of outbursts: type I (or normal) X-ray outbursts of moderate intensity ($L_X \sim 10^{36}$ erg s^{-1}) occuring during the periastron passage of the neutron star and type II (or giant) X-ray outbursts of higher intensity ($L_X \sim 10^{37-38}$ erg s^{-1}) lasting for several weeks or even months. Generally, type II outbursts start shortly after periastron passage, but do not show any other correlation with orbital parameters (Finger & Prince 1997). A small fraction of Be/X-ray binares are persistent sources (the prototype being X-Per), with a low luminosity $L_X \sim 10^{34}$ erg s^{-1} at an almost constant emitting level (Reig & Roche 1999).

During giant outbursts, the spin period of the neutron star has been observed to decrease (neutron star spin-up), indicating that angular momentum is transfered from the accreted material to the neutron star, through an accretion disk (Finger et al. 1999; Wilson et al. 2003).

Corbet (1986) has shown that Be/X-Ray binaries fall into a narrow area in the $P_{spin} - P_{orb}$ diagram. This correlation has been interpreted as a result of the rotation of the neutron star at the equilibrium velocity between the spin-up, and the spin-down led by centrifugal effects of the strong magnetic field (Waters & van Kerkwijk 1989).

The X-ray spectra of Be/X-Ray binaries are very close to those of accreting pulsars, although these depend on the physical conditions close to the neutron star. The spectra can be characterized by cutoff powerlaws. In a few systems with low interstellar absorption, there is evidence for soft excesses at low energies, often modeled as blackbody components (White et al. 1983; Hickox et al. 2004; Paul et al. 2002; Endo et al. 2000). Hickox et al. (2004) showed that the soft excesses observed in luminous X-ray sources ($L_X > 10^{38}$ erg s^{-1}) can only be explained by reprocessing of hard X-rays by optically thick material, near the inner edge of the accretion disk. Many, if not all, bright sources with low absorption have shown this feature.

XMMU J054134.7-682550, located in the Large Magellanic Cloud – LMC, has been proposed as a likely HMXB by Shtykovskiy & Gilfanov (2005). Palmer et al. (2007) found XMMU J054134.7-682550 in a flaring state during a routine scan of the Swift-BAT data on August 3, 2007 at a level of ≈50 mCrab. Subsequent RXTE observations on August 9, 2007 revealed X-ray pulsations ($P_s \approx 61.601 \pm 0.017$ s) and cyclotron features at 10 keV (Markwardt et al. 2007). Assuming that this source is a Be system having a (giant) type II outburst,

⋆ Based on observations obtained with XMM-Newton, an ESA science mission with instruments and contributions directly funded by ESA Member States and NASA.

Table 1. XMMU J054134.7-682550 observing runs. The table lists the initial time of the exposure, the exposure time, and the number of source counts. In the case of XMM-Newton, the number of counts is the sum obtained for both EPIC-MOS detectors.

Observation	XMM-Newton			RXTE		
	Start	Exposure (ks)	Counts	Start	Exposure (ks)	Counts
1	2007-07-06T23:32:48	10.4	15 241	–		
2	2007-08-21T15:12:12	7.5	33 184	2007-08-21T19:07:28	3.5	192 650
3	2007-10-05T23:50:15	17.0	22 576	2007-10-05T21:57:52	1.6	24 537
4	2007-11-24T22:06:15	19.3	4332	–		

Markwardt et al. (2007) estimated an orbital period of about 80 days (within a factor of ∼2) based on the Corbet diagram. The average PCA (Proportional Counter Array on board RXTE) spectrum could be fit with a cut-off power law, with photon index 0.47 and an e-folding cut-off energy of 16 keV (Markwardt et al. 2007).

In this paper we present XMM-Newton and RXTE data revealing a soft pulsed thermal emission. In Sect. 2, we present the observations and data reduction; in Sect. 3, the spectral and timing analysis. In Sect. 4, we discuss the source reprocessing geometry and summarize our results.

2. Observations and data reduction

2.1. Observations

Figure 1 displays the long-term RXTE/ASM light curve of XMMU J054134.7-682550, featuring an outburst with a duration of about 50 days (Markwardt et al. 2007). The four observing runs used in this work were carried out using the PCA on board the *Rossi X-ray Timing Experiment* (RXTE) and EPIC-MOS on board *XMM-Newton* (XMM) (Jansen et al. 2001). Table 1 lists the start time, exposure, and number of source counts for each observation. For observation 2 and 3 the XMM and RXTE exposures were performed quasi-simultaneously. RXTE/PCA data were not available for observations 1 and 4.

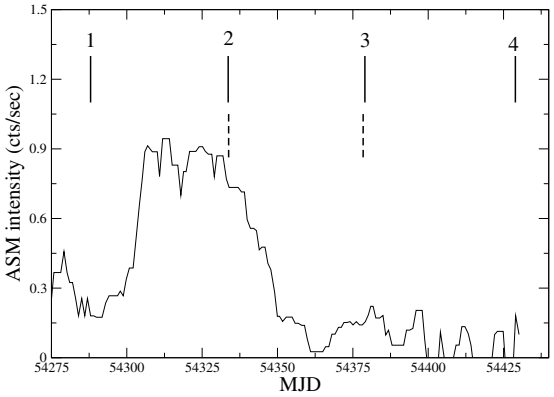

Fig. 1. RXTE/All-Sky-Monitor long term light-curve (2 days average) of XMMU J054134.7-682550. The pointed observations of XMM-Newton and RXTE are indicated by solid and dashed vertical lines, respectively.

2.2. Data reduction

Rossi X-ray Timing Experiment (RXTE)

We used data from RXTE obtained in late August 2007 and early October 2007 (Table 1). The PCA (Jahoda et al. 2006) instrument consists of 5 identical multianode Proportional Counter Units (PCU), operating in the 2−60 keV energy band, with an effective area of approximately 6500 cm^2 and a 1 degree FWHM field of view. PCA spectra and light-curves were extracted using standard FTOOLS (HEASOFT[1] version 6.3.1). Data were accumulated from Standard-2 mode[2]. The Bright Background model (>40 cts s^{-1} PCU^{-1}) was used for observation 2 at the peak of the outburst, and the Faint Background model was used for observation 3. We applied good time intervals (GTI) with an elevation greater than 10 degrees and a pointing offset angle less than 0.02 degrees. Response matrices were created using the tool `pcarsp`.

XMM-Newton

Serendipitous observations of XMMU J054134.7-682550 were performed by EPIC-MOS on board *XMM-Newton* for four epochs between July and November 2007 (obsID: 0500860301–0500860601, PI: Lanz). The Science Analysis Software (SAS) version 7.1.0 was used to produce event lists for the EPIC-MOS[12] (Turner et al. 2001) instrument running `emchain`. EPIC MOS was operated in small window mode for the pointed object, i.e. Cal 83. All the rest of the CCDs were operated in full frame mode providing a time resolution of 2.6 s. Significant pile-up effects were identified in obsevation 2 and 3 and were reduced by selecting data within an annular ring around the piled-up area, although out of time events were not identified. The source was outside the field of view of the other XMM-Newton instruments.

3. Data analysis

3.1. Outburst spectrum

The spectral analysis was performed using the XSPEC[3] package version 11.3.2 (Arnaud 1996). For the outburst spectrum quasi-simultaneous observations were available, i.e., observation 2. We selected data from EPIC/MOS1+2 and RXTE/PCA covering the energy band 0.2−10.0 keV and 5.0−30.0 keV, respectively. To fit the spectrum, we initially used a very simple model, made of three components: photoelectric absorption, a powerlaw with high energy exponential cutoff, and a cross-calibration factor, i.e., `const*wabs*cutoff`. The model failed to fit the data, providing $\chi^2_\nu \sim 3$ (Fig. 2). The residuals (Fig. 2, lower panel) indicate a clear soft excess below 1 keV and spectral features in the 7−20 keV energy range.

We added a fourth spectral component in order to account for the soft excess: either a blackbody (`bbody`) or a disk black body

[1] http://heasarc.gsfc.nasa.gov/lheasoft/
[2] http://heasarc.gsfc.nasa.gov/docs/xte/xtegof.html
[3] http://xspec.gsfc.nasa.gov/

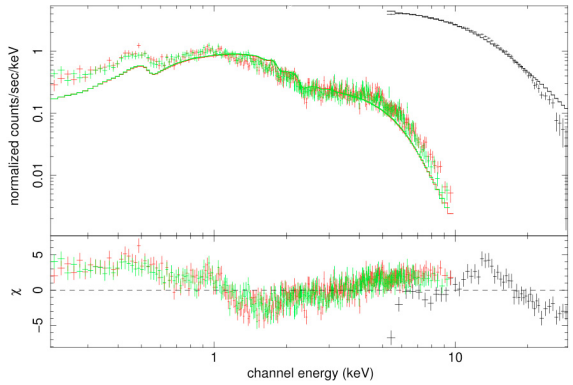

Fig. 2. Outburst spectrum obtained using EPIC/MOS1+2 and RXTE/PCA, fit with a simple absorbed cut-off powerlow model (const*wabs*cutoff).

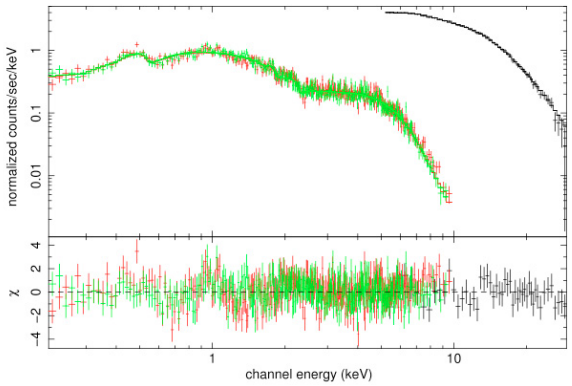

Fig. 3. The outburst spectrum is represented using a model invoking photoelectric absorption, a high-energy cutoff powerlaw, disk blackbody, a single blackbody, and a cyclotron-absorption line. We used EPIC/MOS1+2 and RXTE/PCA data.

(`diskbb`). This additional spectral component improves the fit very significantly, providing $\chi^2_\nu \sim 1.2$ for `diskBB` and $\chi^2_\nu \sim 1.5$ for `bbody`, and a cross-calibration factor of ∼0.9 in both cases.

The best fit column density $N_{\rm H} \sim 2.1 \times 10^{20}$ cm^{-2} is, however, less than the galactic value in the source direction $N_{\rm H^{gal}} \sim 6.32 \times 10^{20}$ cm^{-2} (Dickey & Lockman 1990). Fixing the column density to the galactic value, and using only one thermal model, an additional excess is observed below ∼0.5 keV, indicating that one thermal model is not adequate to represent the data. The model can be further improved by adding both disk and blackbody spectral components. To better constrain the parameters, we decided to fix the disk's inner radius to the radius of the magnetosphere, $R_{\rm m} \sim 1.3 \times 10^8$ cm, inferred from the cyclotron line. The disk component turned out to the softer (and cooler) than the single blackbody emitting region.

We finally added a sixth model component, a cyclotron line to account for the residuals observed around ∼10 keV. This model (`const*wabs*(cutoff*cyclabs+diskbb+bb)`) fits the data very well (Fig. 3) providing $\chi^2_\nu = 1.04$, and a cross-calibration factor ∼0.9. Table 2 lists the best fit parameters. The continuum, characterised by $\Gamma = 0.2$ and $E_C = 12$ keV, is typical for an accreting pulsar. The energy of the fundamental line (9.0 ± 0.4 keV) is consistent with the value derived from the RXTE data alone (Markwardt et al. 2007). We do not find evidence for cyclotron harmonic lines.

Figure 4 shows the $E \times f(E)$ model, unfolded spectrum, and the additive components of the model. The relative contribution of each component is also plotted. Above 5 keV the powerlaw cutoff component (blue dotted line) dominates the spectrum. At low energies, the blackbody (red dotted line) and the disk emission (green dotted line) dominates at 1 keV and below 0.5 keV, respectively.

Based on this model, we estimated the unabsorbed flux for each component in the energy range 0.2−30 keV as, $L^{\rm PL}_{0.2-30\ \rm keV} \sim 3 \times 10^{38}$ erg s^{-1}, $L^{\rm BB}_{0.2-30\ \rm keV} \sim 10^{37}$ erg s^{-1}, $L^{\rm DBB}_{0.2-30\ \rm keV} \sim 10^{37}$ erg s^{-1} given the distance to the LMC.

The residuals show some significant broad emission feature at 1 keV. Such features, possibly an Fe L line complex (Oosterbroek et al. 1997; McCray et al. 1982), have been detected in other X-ray binary pulsars (Endo et al. 2000).

Table 2. Best-fit parameters of the outburst spectrum (observation 2) for model: const ∗ wabs ∗ (cutoff ∗ cyclabs + diskbb + bbody). Errors are calculated at 90% confidence level independently for each parameter.

Parameters	Value	Unit
$N_{\rm H}$	6.32×10^{-2} (fixed)	10^{22} cm^{-2}
$kT_{\rm diskbb}$	0.088 ± 0.001	keV
$R^2_{\rm diskBB} \cos\theta$	70 000 (fixed)	km^2
$kT_{\rm bbody}$	0.22 ± 0.01	keV
Area	$(4.6 \pm 0.1) \times 10^4$	km^2
Γ	0.2 ± 0.1	
$E_{\rm cutoff}$	12 ± 1	keV
Norm$_{\rm cutoff}$	$(1.09^{+0.06}_{-0.1}) \times 10^{-2}$	ph keV^{-1} cm^{-2} s^{-1} at 1 keV
E_0	9.0 ± 0.4	keV
W_0	$2.1^{+0.7}_{-0.6}$	keV
τ_0	0.17 ± 0.03	
$C_{\rm MOS1}$	0.90 ± 0.03	
$C_{\rm MOS2}$	0.89 ± 0.03	
χ^2_ν/d.o.f.	1.04/666	

3.2. Spectral variability

To search for spectral variability during and outside of the outburst, we used a simple model to fit and compare the data of high and low signal to noise. To achieve this we removed the cyclotron line and the single black body component. The resulting model (`const*wabs*(diskbb+cutoff)`) was first fit to the outburst data with all parameters free except $N_{\rm H}$, fixed to the galactic value. For the pre- and post-outburst data several parameters were fixed to those obtained for the outburst spectrum: $kT_{\rm in} = 0.25$ keV, $\Gamma = 0.42$, and $E_C = 14$ keV, $C_{\rm MOS1} = 0.89$, and $C_{\rm MOS2} = 0.88$. The remaining free parameters are the normalization of the disk blackbody, and of the cut-off power law. Table 3 lists the results of our fits including the corresponging χ^2_ν and the relative strength of the soft and hard components in the 0.2−1 keV energy band. The latter peaked to a value of 3.2 for observation 2, during the outburst. The ratio was about 1.0 in observation 1 and 3 obtained close to the beginning and end of the outburst. Later on, during observation 4, this relative strength decreased to 0.4. The outburst is characterized by a global softening of the spectrum, signature of more efficient accretion.

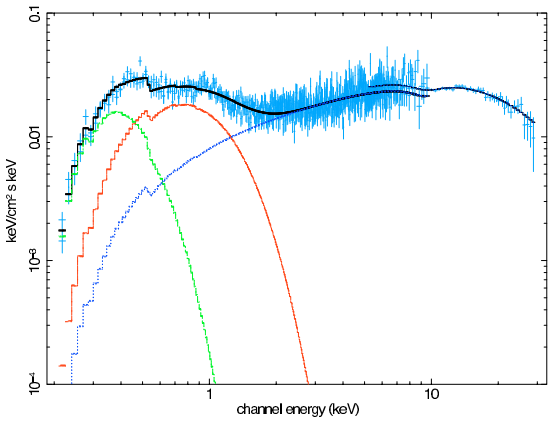

Fig. 4. $E \times f(E)$ outburst spectrum. The black solid line is the model described in the text. Cyan points are the unfolded spectrum. Blue, red, green dotted lines represent the cutoff powerlaw, hot blackbody and disk emission, respectively. For a color version see the electronic version of the paper.

Table 3. To search for spectral variability, all datasets were fit with a simple model (const*wabs*(cutoff+diskbb)). The normalization of the thermal and non-thermal components are listed below. $kT_{\rm in} = 0.25$ keV, $\Gamma = 0.42$, and $E_C = 14$ keV, $C_{\rm MOS1} = 0.89$, and $C_{\rm MOS1} = 0.88$ are fixed.

Obs.	Normalization `diskbb`	Normalization `cutoff` $\times 10^{-3}$	$\frac{F_{0.2-1(\rm BB)}}{F_{0.2-1(\rm PL)}}$	χ^2_ν (d.o.f.)
1	53 ± 4	2.51 ± 0.05	1.0 ± 0.1	1.20(445)
2	890 ± 20	13.7 ± 0.1	3.23 ± 0.1	1.26(675)
3	58 ± 4	2.77 ± 0.05	1.04 ± 0.1	1.34(614)
4	2 ± 1	0.23 ± 0.01	0.4 ± 0.2	1.05(147)

3.3. Timing analysis during the outburst

We produced lightcurves in the energy bands 5−30 keV (from RXTE standard-2 mode, i.e. 16 s resolution), 0.2−1 keV and 3−10 keV (from EPIC-MOS[1] event lists). Figure 5 shows the Lomb-Scargle periodogram, derived from the 5−30 keV lightcurve, with the power spectrum density distribution peaking at a period of 61.23 ± 0.06 s, and the corresponding folded lightcurve.

In order to derive the likely pulse shape for the thermal spectral components, we have corrected the soft lightcurve for the contamination of the hard component in the soft band using $LC^{\rm BB}_{\rm soft} = LC_{\rm soft} - \frac{C_{\rm S}}{C_{\rm H}} LC_{\rm Hard}$, where $\frac{C_{\rm S}}{C_{\rm H}}$ is the ratio of the counts predicted by the best fit model for both the soft and hard components, respectively.

Figure 6 shows the Lomb-Scargle periodograms obtained for the corrected "soft" 0.2−0.5 keV, 0.5−1 keV, and for the "hard" 3−10 keV lightcurves. The corresponding folded lightcurves, using a period of $P \approx 61.23$ s, are displayed in Fig. 7.

The power spectrum density distribution at $P = 61.23$ s increases with energy (Fig. 6). The pulsation is well detected above 0.5 keV and not significantly detected below 0.5 keV.

The shape of the peak in the folded 3−10 keV lightcurve is sharper and narrower than in the "soft" lightcurves (Fig. 7). The pulse starts simultaneously below 1 keV and above 3 keV, however the soft pulse appears to last twice the time.

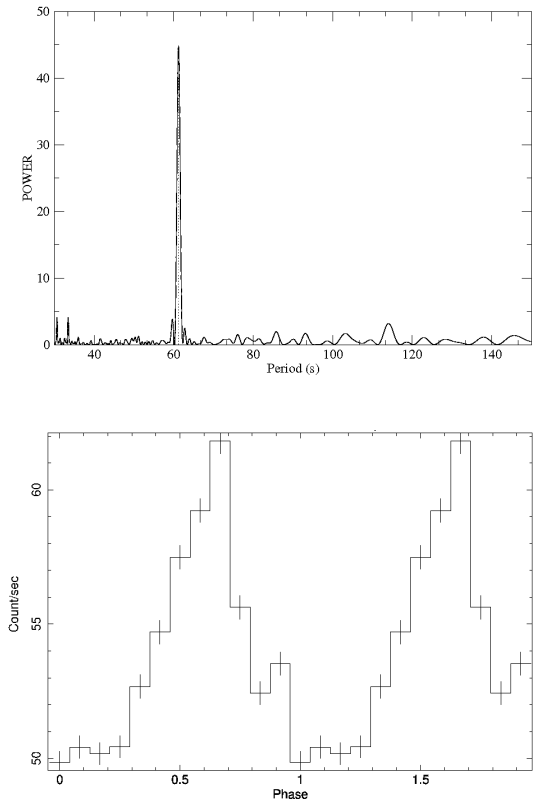

Fig. 5. *Top*: Lomb-Scargle periodogram for observation 2 using RXTE 5−30 keV data in standard-2 mode. The peak of the power spectrum density distribution is at $P \approx 61.23 \pm 0.06$ s. *Bottom*: folded lightcurve in the 5−30 keV energy band obtained with this period. The zero epoch was set to MJD 54 333.79882.

3.4. Variability of the spin period

Table 4 lists the periods derived for each observation in two energy bands, i.e. 0.2−10 keV (obtained from XMM/EPIC-MOS[1]) and 5−30 keV (obtained from RXTE/PCA). Between observation 1 and 3, the neutron star spinned up by $\Delta P = 1.54$ s over a period of $\Delta T \sim 50$ days. Assuming a massive OB star $M \sim 20\ M_\odot$ and circular orbit with a period of 80 days the Doppler effects can be neglected ($\sim 10^{-3}$).

3.5. Likely nearIR candidate

The SWIFT XRT position provided by Palmer et al. (2007) is compatible with the position we derive from the XMM-Newton MOS image (using SAS `edetect` task): $\alpha_{2000} = 5^{\rm h}41^{\rm m}34.33^{\rm s}$, $\delta_{2000} = -68°25'49.0''$ (systematic uncertainty of 2 arcsec). The XMM derived position is compatible with the optical counterpart detected by SWIFT UVOT (Palmer et al. 2007) corresponding to 2MASS 05413431−6825484 for which Cutri et al. (2003) provide $J = 13.84 \pm 0.03$, $H = 12.74 \pm 0.03$, $K = 13.63 \pm 0.05$ and Monet et al. (2003) provide $B2 = 13.76$, and $R2 = 13.84$.

The infrared-optical spectral energy distribution of the likely stellar counterpart was fitted with a blackbody of temperature ∼13 000 ± 1000 K suggesting a B star. Additional reddening would increase the temperature. An infrared excess detected

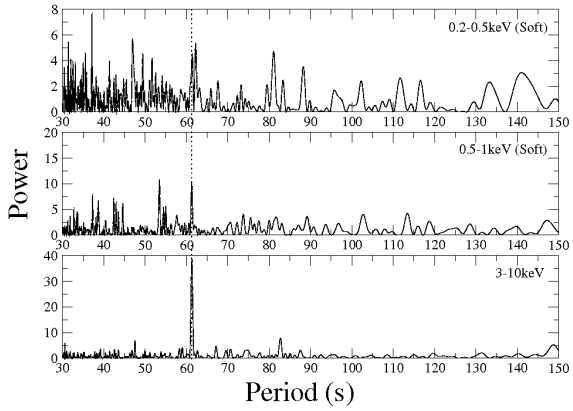

Fig. 6. Lomb-Scargle periodograms for observation 2 using XMM (EPIC/MOS[1]) data. The period of 61.23 s is indicated with a dashed line. The first two soft X-ray periodograms were constructed from lightcurves corrected for the contamination of the cutoff powerlaw component.

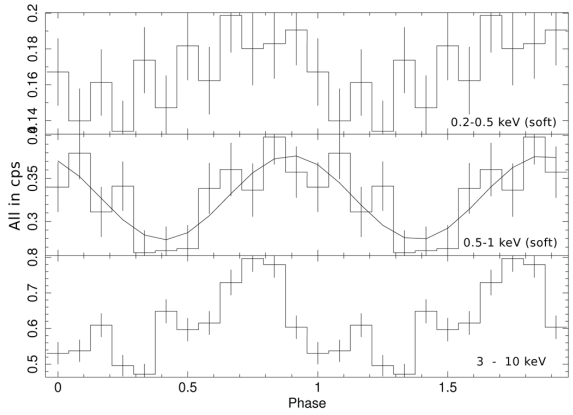

Fig. 7. Folded lightcurves obtained from EPIC/MOS[1] in the 0.2−0.5 keV (*top*), 0.5−1.0 keV (*middle*), and 3−10 keV (*bottom*) energy bands, using the best spin period ($P \approx 61.23$ s) found from RXTE/PCA data. The two soft lightcurves are corrected for the contamination of the cutoff powerlaw component. The solid curve in *the middle panel* shows a sinusoidal fit to the data. The zero epoch is set to MJD 54 333.5.

Table 4. The spin periods (in seconds) obtained from Lomb-Scargle periodograms, using data from *XMM-Newton* and *RXTE*.

Observation	0.2−10 keV	5−30 keV
1	62.19 ± 0.02	–
2	61.28 ± 0.02	61.23 ± 0.06
3	60.65 ± 0.01	60.62 ± 0.3
4	60.64 ± 0.01	–

above the blackbody fit (in the H band) may be an instrumental effect or the signature of a circumstellar disk (Wilson et al. 2005).

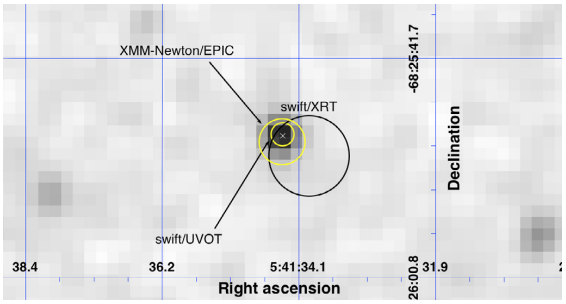

Fig. 8. K-band image (49″ × 26″) around XMMU J054134.7-682550 obtained using the 2MASS/IPAC image server. The circles indicate the source localization obtained by SWIFT/XRT (uncertainty 3.5″), and XMM/EPIC-MOS[1] (see text). The SWIFT/UVOT (uncertainty 1″) localization of the source is consistent with 2MASS 05413431−6825484.

4. Discussion

The fundamental cyclotron absorption line, located at ∼9 keV, indicates a magnetic field of $B = 8.6(1+z)E \times 10^{10}$ G $\approx 10^{12}$ G (where $z = 0.3$ is the gravitational redshift). The magnetospheric radius ($R_{\rm m} \sim 1.3 \times 10^8$ cm) can be obtained by equating the kinetic energy density of the accreted material to the magnetic energy density (White & Stella 1988).

The soft X-ray excess was modeled with a cold disk and a hot blackbody. The inner radius of the disk component was fixed to the radius of the magnetosphere. The surface emitting the hot blackbody component can be estimated from the spectral fit as 4.6×10^4 km^2. Assuming that this corresponds to a broadened inner disk, its thickness can be estimated as $h = (4\pi {R_{\rm BB}}^2)/(2\pi R_{\rm m}) \approx 75$ km.

If the inner disk is heated by the pulsar's hard X-ray emission, the covering factor can be estimated as $\frac{F_{\rm BB}}{F_{\rm PL}} \sim 0.03$, corresponding to $h \approx 45$ km. The hot blackbody could therefore indeed be produced by reproccessing of hard X-rays on a broadened accretion disk.

Spectral variability was studied by applying a simple model to all the datasets. During the outburst the thermal component is more enhanced than the powerlaw component, suggesting a more effective accretion ($\dot{M}/\dot{M}_{\rm Edd} \approx 0.8$) and/or a broadened accretion disk.

The cooling time scale of the hot blackbody component ($\sim 10^{-6}$ s) is much shorter than the pulse period. When the neutron star rotates, the maximum of the reprocessed hard X-ray emission will move along the inner edge of the accretion disk. Pulsations of the soft blackbody are therefore expected.

Figure 7 shows the different shapes of the folded lightcurves in the soft and hard energy bands (0.5−1 keV and 3−10 keV). The "hard" pulse ($\Delta\phi \sim 0.4 \pm 0.1$) is shorter than the the hot blackbody pulse ($\Delta\phi \sim 0.8 \pm 0.1$). The folded lightcurve of the hot blackbody component can in fact be represented by a sine curve (continuous line in the middle panel of Fig. 7) which could be expected in the very simplified source geometrical model represented in Fig. 9. In this model we assume that the hard X-rays are emitted preferentially towards the magnetic equator (Becker & Wolff 2007) of the neutron star and that these photons illuminate the inner edge of the accretion disk. The illuminated disk re-radiates at soft X-rays and features a sinusoidal modulation.

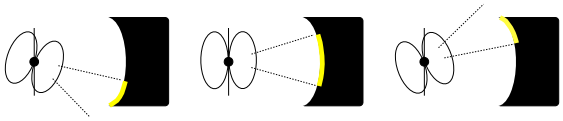

Fig. 9. Schematic representation of the reprocessing geometry in the accreting pulsar XMMU J054134.7-682550. The distance between the neutron star and the disk is not to scale. The vertical line represents the rotation axis of the neutron star. The yellow (grey) stripe indicates the reprocessing area on the inner edge of the accretion disk. The hard X-rays beam is indicated by dashed lines. *Left*: soft X-ray minimum. *Center*: soft X-ray maximum. *Right*: soft X-ray minimum.

We have also observed a significant spin-up of the pulsar ($\Delta P \sim 1.5$ s) over a period of ∼50 days, i.e. $\dot{P} \sim 3.5 \times 10^{-7} \sim 11$ s/yr and $\dot{P}/P \approx 6 \times 10^{-9}$ s$^{-1} \sim 0.18$ yr^{-1}.

Ghosh & Lamb (1979a,b) described the interaction between the accretion disk and the stellar magnetic field and calculated the effect of the accretion torque on the spin of the neutron star. A relation between the mass M and radius R of the neutron star can be estimated for a given magnetic field, luminosity, spin period, and period derivative observed during the outburst. Our observations indicate a relation $M/M_{\odot} \approx R/10$ km, which is compatible with a range of neutron star equations of state (Lattimer & Prakash 2001), and an accretion rate of $\sim 3 \times 10^{-8}\ M_{\odot}$ yr^{-1}.

2MASS 05413431−6825484 is the likely optical counterpart of XMMU J054134.7-682550. The available photometry suggests a temperature of 13 000 ± 1000 K, confirming a B stellar counterpart.

5. Conclusion

We report on XMM-Newton and RXTE observations of the X-ray binary pulsar XMMU J054134.7-682550, performed in August 2007, during a giant type II outburst lasting for roughly 50 days. The outburst spectrum was fit successfully with a power law modified by an exponentional high energy cutoff, a cyclotron absorption line, and two soft thermal components. We summarize our results as follows:

- The reprocessing region corresponds to the inner edge of the accretion disk broadened to ∼75 km.
- The soft X-ray pulse shape profile (0.5−1 keV) shows sinusoidal modulation, a signature of illumination of the broadened inner disk.
- The spin up of the pulsar and the enhancement of the disk emission during the outburst indicate a high accretion rate ($\dot{M}/\dot{M}_{\rm EDD} \approx 0.8$).
- The infrared-optical spectral energy distribution of the counterpart suggests a hot primary star of $T \sim 13\,000$ K, likely a B-type star.

Acknowledgements. M.A. acknowledges support from a Swiss National Science Foundation Professorship (PP002−110504). T. Lanz was supported by NASA grant NNX07AQ47G. This research has made use of NASA's Astrophysics Data System Bibliographic Service. The ASM lightcurve was obtained from the quick-look results provided by the ASM/RXTE team.

References

Arnaud, K. A. 1996, in Astronomical Data Analysis Software and Systems V, ed. G. H. Jacoby, & J. Barnes, ASP Conf. Ser., 101, 17
Becker, P. A., & Wolff, M. T. 2007, ApJ, 654, 435
Corbet, R. H. D. 1986, MNRAS, 220, 1047
Cutri, R. M., Skrutskie, M. F., van Dyk, S., et al. 2003, 2MASS All Sky Catalog of point sources, The IRSA 2MASS All-Sky Point Source Catalog, NASA/IPAC Infrared Science Archive, http://irsa.ipac.caltech.edu/applications/Gator/
Dickey, J. M., & Lockman, F. J. 1990, ARA&A, 28, 215
Endo, T., Nagase, F., & Mihara, T. 2000, PASJ, 52, 223
Finger, M. H., & Prince, T. A. 1997, in Proceedings of the Fourth Compton Symposium, ed. C. D. Dermer, M. S. Strickman, & J. D. Kurfess, AIP Conf. Ser., 410, 57
Finger, M. H., Bildsten, L., Chakrabarty, D., et al. 1999, ApJ, 517, 449
Ghosh, P., & Lamb, F. K. 1979a, ApJ, 232, 259
Ghosh, P., & Lamb, F. K. 1979b, ApJ, 234, 296
Hickox, R. C., Narayan, R., & Kallman, T. R. 2004, ApJ, 614, 881
Jahoda, K., Markwardt, C. B., Radeva, Y., et al. 2006, ApJS, 163, 401
Jansen, F., Lumb, D., Altieri, B., et al. 2001, A&A, 365, L1
Lattimer, J. M., & Prakash, M. 2001, ApJ, 550, 426
Markwardt, C. B., Swank, J. H., & Corbet, R. 2007, The Astronomer's Telegram, 1176, 1
McCray, R. A., Shull, J. M., Boynton, P. E., et al. 1982, ApJ, 262, 301
Monet, D. G., Levine, S. E., Canzian, B., et al. 2003, AJ, 125, 984
Oosterbroek, T., Parmar, A. N., Martin, D. D. E., & Lammers, U. 1997, A&A, 327, 215
Palmer, D. M., Grupe, D., & Krimm, H. A. 2007, The Astronomer's Telegram, 1169, 1
Paul, B., Nagase, F., Endo, T., et al. 2002, ApJ, 579, 411
Reig, P., & Roche, P. 1999, MNRAS, 306, 100
Shtykovskiy, P., & Gilfanov, M. 2005, A&A, 431, 597
Turner, M. J. L., Abbey, A., Arnaud, M., et al. 2001, A&A, 365, L27
Waters, L. B. F. M., & van Kerkwijk, M. H. 1989, A&A, 223, 196
White, N. E., & Stella, L. 1988, MNRAS, 231, 325
White, N. E., Swank, J. H., & Holt, S. S. 1983, ApJ, 270, 711
Wilson, C. A., Finger, M. H., Coe, M. J., & Negueruela, I. 2003, ApJ, 584, 996
Wilson, C. A., Weisskopf, M. C., Finger, M. H., et al. 2005, ApJ, 622, 1024

PART III:Other activities at ISDC

Chapter 9

INTEGRAL discovery of AX J1910.7+0917

9.1 Introduction

AX J1910.7+0917 is a relatively faint and poorly studied X-ray source discovered with ASCA during the survey of the Galactic plane. The ASCA spectrum showed an absorbed power-law model. The measured photon index was $\Gamma \sim 1$, for an absorption column density of N_H $\sim$1.4 10^{22} cm^{-2}. The estimated $0.7 - 10$ keV X-ray flux was 2.4×10^{-12} erg cm^{-2} s^{-1}. The source was also detected with INTEGRAL. The source maximum detection significance in the IBIS/ISGRI data is 8.3σ (18-60 keV), and the corresponding time-average flux is 0.4 ± 0.1 mCrab in the 20-40 keV and 0.6 ± 0.1 mCrab in 40-100 keV energy band. Based on the IR, optical and X-ray properties, the likely counterpart to AX J1910.7+0917 has been determined to be a new supergiant (Pavan *et al.* 2011).

9.2 Scientific Article on AX J1910.7+0917

A&A 526, A122 (2011)
DOI: 10.1051/0004-6361/201015561

Astronomy & Astrophysics

AX J1910.7+0917 and three newly discovered *INTEGRAL* sources

L. Pavan[1,2], E. Bozzo[1,2], C. Ferrigno[1,2], C. Ricci[1,2], A. Manousakis[1,2], R. Walter[1,2], and L. Stella[3]

[1] ISDC, INTEGRAL Science Data Centre, Université de Genève, Chemin d'Ecogia 16, 1290 Versoix, Switzerland
e-mail: lucia.pavan@unige.ch
[2] Observatoire de Genève, Université de Genève, Chemin des Maillettes 51, 1290 Sauverny, Switzerland
[3] INAF – Osservatorio Astronomico di Roma, via Frascati 33, 00044 Rome, Italy

Received 10 August 2010 / Accepted 27 November 2010

ABSTRACT

Aims. We take advantage of the high sensitivity of the IBIS/ISGRI telescope and the improvements in the data analysis software to investigate the nature of the still poorly known X-ray source AX J1910.7+0917, and search for closeby previously undetected objects.
Methods. We analyze all publicly available *INTEGRAL* data of AX J1910.7+0917, together with a number of archival observations that were carried out in the direction of the source with *Chandra*, *XMM-Newton*, and *ASCA*. In the IBIS/ISGRI field-of-view around AX J1910.7+0917, we discovered three new sources: IGR J19173+0747, IGR J19294+1327 and IGR J19149+1036; the latter is positionally coincident with the *Einstein* source 2E 1912.5+1031. For the first two sources, we also report the results of follow-up observations carried out with *Swift*/XRT.
Results. AX J1910.7+0917 features a clear variability in the X-rays. Its spectrum can be well described with an absorbed ($N_{\rm H} \sim 6 \times 10^{22}$ cm^{-2}) power-law ($\Gamma \simeq 1.5$) model plus an iron line at 6.4 keV. We also obtained a refined position and report on possible infrared counterparts.
Conclusions. The present data do not allow for a unique classification of the sources. Based on the property of its X-ray emission and the analysis of a likely infrared counterpart, we investigate different possibilities for the nature of AX J1910.7+0917.

Key words. X-rays: individuals: AX J1910.7+0917 – X-rays: individuals: IGR J19173+0747 – X-rays: individuals: IGR J19294+1327 – X-rays: individuals: IGR J19149+1036 – X-rays: individuals: 2E 1912.5+1031

1. Introduction

The wide field-of-view of the IBIS/ISGRI telescope (FOV, 19°×19°; Ubertini et al. 2003) onboard *INTEGRAL* (Winkler et al. 2003) and its unprecedented sensitivity in the hard X-ray domain (17−100 keV) have made this instrument particularly successful in the past few years in revealing new high-energy sources. The latest available IBIS/ISGRI catalog contains more than 700 objects (Bird et al. 2010) and an increasing number of sources are being discovered thanks to ongoing *INTEGRAL* surveys of the high-energy sky. Since 2003, the relatively large exposure time available (∼1−6 Ms) permitted to achieve in the galactic plane a limiting sensitivity of $\lesssim$1 mCrab in the 17−100 keV energy range and a point-source location accuracy of $\simeq$2−3 arcmin. Besides the increasing amount of observing time, the identification of a number of new hard X-ray sources has benefited from improvements in the data analysis software.

In this paper, we take advantage of the new version of the *INTEGRAL* OSA software released by the ISDC (Courvoisier et al. 2003) to investigate the nature of the still poorly known source AX J1910.7+0917, and search for nearby previously undetected faint X-ray sources in the field-of-view (FOV) around this source. In Sect. 2 we summarize all previous observations of AX J1910.7+0917 and the analysis of all the publicly available *INTEGRAL* data. We also carried out an analysis of all archival *Chandra*, *XMM-Newton*, and *ASCA*, observations that included AX J1910.7+0917 in the instruments' FOVs. The analysis of the *INTEGRAL* data also led to the discovery of three new hard X-ray sources in the IBIS/ISGRI FOV around AX J1910.7+0917, independently detected through data analysis also with the _ software (A. Segreto, priv. comm.). For two of these sources, we obtained follow-up observations with *Swift*/XRT and present these results in Sect. 3. Our discussion and conclusion are summarized in Sect. 4.

2. AX J1910.7+0917

AX J1910.7+0917 is a relatively faint and poorly known X-ray source discovered with *ASCA* during the survey of the Galactic plane. The best-determined position so far is $\alpha_{\rm J2000} = 19^{\rm h}10^{\rm m}47\overset{\rm s}{.}00$ and $\delta_{\rm J2000} = 09°17'06\overset{''}{.}0$, with an associated error of $57.6''$ (90% c.l., Sugizaki et al. 2001). The *ASCA* spectrum could be fitted with an absorbed power-law model ($\chi^2_{\rm red}$/d.o.f. = 0.72/10). The measured photon index was $\Gamma = 1.1^{+0.5}_{-0.4}$, for an absorption column density of $N_{\rm H} = (2.6^{+1.4}_{-1.0}) \times 10^{22}$ cm^{-2}. The estimated 0.7−10 keV X-ray flux was 2.4×10^{-12} erg/cm^{-2}/s. Sugizaki et al. (2001) associated AX J1910.7+0917 to the *Einstein* source 2E 1908.3+0911, which is characterized by an averaged X-ray flux of $(6.9 \pm 1.4) \times 10^{-13}$ erg/cm^2/s (0.2−3.5 keV, Hertz & Grindlay 1988). The source was also detected with *INTEGRAL*, and classified by Bird et al. (2010) as a likely variable source. The source maximum detection significance in the IBIS/ISGRI data is 8.3σ (18−60 keV), and the corresponding time-average flux is 0.4 ± 0.1 mCrab (0.6 ± 0.1 mCrab) in the 20−40 keV (40−100 keV) energy band (corresponding to 3.0×10^{-12} erg/cm^2/s and 5.7×10^{-12} erg/cm^2/s, respectively). No other detections and counterparts in different energy band have been reported so far.

A&A 526, A122 (2011)

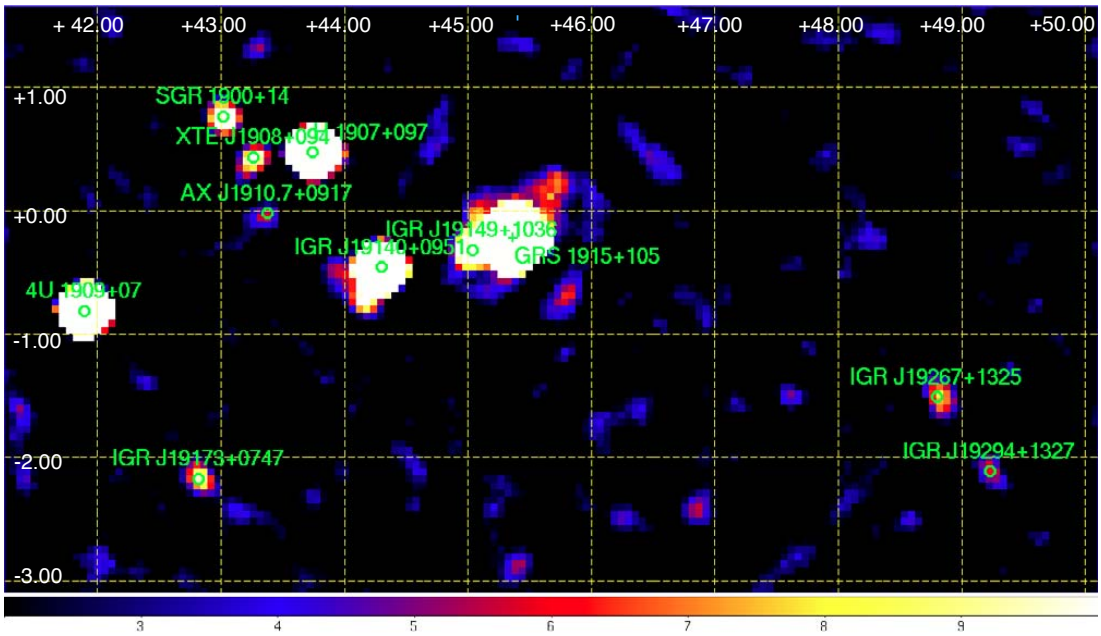

Fig. 1. IBIS/ISGRI mosaic around AX J1910.7+0917 (17–80 keV, significance map). We also show the newly discovered nearby sources (see Sect. 3 and the electronic version of the paper for the colored picture). The dashed grids denote galactic coordinates.

2.1. Data analysis and results

We analyzed all archival *INTEGRAL*, *ASCA*, *XMM-Newton*, and *Chandra* observations that included the position of AX J1910.7+0917 in their FOV. This is the first in-depth study of the emission from this source up to hard X-ray energies. In Sect. 2.1.1 we report the details of the *INTEGRAL* observations. A log of all other observations is given in Table 1. Throughout the paper, all uncertainties are given at 90% c.l. (unless otherwise stated).

2.1.1. *INTEGRAL*

INTEGRAL observations are commonly divided into ∼2–3 ks short pointings called "science windows" (SCWs). We considered all publicly available SCWs for the IBIS/ISGRI (17–80 keV, Lebrun et al. 2003) and for the two JEM-X telescopes (3–23 keV, Lund et al. 2003) that were performed in the direction of AX J1910.7+0917 from 2003 March 6 to 2009 April 15 (see Sect. 2). This permitted us to achieve an effective exposure time on the source of 4.8×10^2 ks and 2.7×10^3 ks for JEM-X and ISGRI respectively. All data, here and below, were analyzed with version 9.0 of the OSA software (Courvoisier et al. 2003).

The source was not detected in the JEM-X1 and JEM-X2 mosaics, and we derived an upper limit on the source X-ray flux by using the tool _ . From the JEM-X1 mosaic we derived a 3σ upper limit of 1.0×10^{-11} erg/cm^2/s, 5.8×10^{-12} erg/cm^2/s, and 9×10^{-12} erg/cm^2/s respectively in the energy bands 3–7 keV, 7–11 keV, and 11–19 keV. The corresponding 3σ upper limits derived from the JEM-X2 mosaic were 1.7×10^{-11} erg/cm^2/s, 1.2×10^{-11} erg/cm^2/s, and 1.8×10^{-11} erg/cm^2/s. These are compatible with the measured averaged *ASCA* flux reported in Sect. 1.

We produced an IBIS/ISGRI mosaic of the region around AX J1910.7+0917, using the energy band 17–80 keV to maximize the S/N. In this energy band AX J1910.7+0917 is detected with a significance of 5.8σ. A close view of the ISGRI mosaic is shown in Fig. 1. We checked that the best-fit position of the source obtained from the mosaic is compatible with both its *ASCA* and *XMM-Newton* refined position (see Sect. 2.1.2).

We derived a count rate of 0.09 ± 0.02 cts/s, corresponding to a flux of 0.31 ± 0.05 mCrab. This flux is higher than any contamination expected in the same energy band from the nearby supernova remnant (SNR, see Miceli et al. 2006, and Sect. 2.1.2).

We also performed a spectral analysis and extracted its lightcurve in the two energy bands 20–40 keV and 40–80 keV. The averaged IBIS/ISGRI spectrum of the source is shown in Fig. 5 and discussed in Sect. 2.1.2. We barycenter-correct the photon arrival times in the source lightcurves with the OSA9 tool . No evidence for a coherent periodicity could be found. This is also confirmed by the analysis of the data from *Swift*/BAT (Cusumano, priv. comm.), which operates in a similar energy band to that of IBIS/ISGRI.

2.1.2. *XMM-Newton*

AX J1910.7+0917 was serendipitously[1] observed in two *XMM-Newton* (Jansen et al. 2001) observations performed in 2004 April in the direction of the nearby SNR W49B (Miceli et al. 2006). We processed *XMM-Newton* observation data files (ODFs) to produce calibrated event lists using the and - tasks (Science Analysis System, SAS, v.10.0) for the Epic-pn and the MOS cameras. The event files of the two observations were filtered to exclude high background time intervals follow-

[1] AX J1910.7+0917 is named as 2XMM J191043.4+091629 in the *XMM-Newton* serendipitous source catalogue (Watson et al. 2009).

Table 1. Observation log of AX J1910.7+0917.

OBS ID	Instr	Date[a]	Exp[b] (ks)	N_H (10^{22} cm^{-2})	Γ	F_{obs}[c] (erg/cm^2/s)	$\chi 2_{red}$/d.o.f. (C-stat/d.o.f.)
ASCA							
50005000	GIS2+GIS3	1993-04-24	95	$4.8^{-1.5}_{+1.9}$	1.4±0.5	$8.2^{+0.7}_{-2.7}$	0.4/53
13000000[d]	GIS2	1993-05-03	2.3	4.8 (fixed)	1.4 (fixed)	<4.2	–
	GIS3	1993-05-03	2.3	4.8 (fixed)	1.4 (fixed)	<4.9	–
13000010[d]	GIS2	1993-05-03	2.3	4.8 (fixed)	1.4 (fixed)	<1.1	–
	GIS3	1993-05-03	2.3	4.8 (fixed)	1.4 (fixed)	<1.6	–
13000030[d]	GIS3	1993-05-03	1.4	4.8 (fixed)	1.4 (fixed)	<2.1	–
	GIS3	1993-05-03	1.4	4.8 (fixed)	1.4 (fixed)	<3.1	–
50005010[d]	GIS2	1993-10-16	12	4.8 (fixed)	1.4 (fixed)	<0.6	–
	GIS3	1993-10-16	12	4.8 (fixed)	1.4 (fixed)	<0.6	–
50005020[d]	GIS2	1993-10-17	20	4.8 (fixed)	1.4 (fixed)	<1.1	–
	GIS3	1993-10-17	20	4.8 (fixed)	1.4 (fixed)	<1.4	–
10020000	GIS2+GIS3	1993-11-03	26	$6.3^{+1.6}_{-1.4}$	2.3±0.5	$4.9^{-4.3}_{+0.4}$	(146.1/157)
10020010[d]	GIS2	1993-11-03	19	4.8 (fixed)	1.4 (fixed)	<2.1	–
	GIS3	1993-11-03	19	4.8 (fixed)	1.4 (fixed)	<2.3	–
57005050	GIS2+GIS3	1999-04-27	23	$5.0^{+3.4}_{-2.4}$	1.6±0.8	$2.5^{+0.2}_{-1.4}$	(70.7/59)
XMM-Newton							
0084100401	Epic-pn	2004-04-03	14.0	$6.3^{+0.5}_{-0.4}$	1.4±0.1	$17.1^{+1.0}_{-2.1}$	1.1/147
0084100501[e]	Epic-pn	2004-04-05	14.7	5.0±0.3	1.28±0.08	$24.3^{+1.2}_{-1.7}$	0.9/168
Chandra							
9615[f]	ACIS-S	2008-05-31	1.7	–	–	<0.4	–

Notes. [a] Format is YYYY-MM-DD; [b] Exp indicates the total exposure time of each observation; [c] observed flux in the 1−10 keV energy band in units of 10^{-12}; [d] 90% c.l. upper limit; [e] this fit includes also a Gaussian line at ∼6.4 keV, see text for details; [f] 68% c.l. upper limit.

ing the reccomandations of the SAS online analysis threads[2]. We excluded from further analysis time intervals in observation 0084100401 (0084100501) during which the count-rate of the entire detector FOV in the 10−12 keV energy band was higher than 0.2 (0.15) cts/s for the Epic-MOS and 0.35 (0.4) for the Epic-pn. We also carefully checked that none of these rises in the total field count-rate was due to a flare from AX J1910.7+0917.

In both observations 0084100401 and 0084100501, the three Epic cameras were operated in full frame and the source AX J1910.7+0917 was located at the rim of their FOV. In the Epic-MOS1 AX J1910.7+0917 lied on the border between two CCDs, and thus we excluded these data from the analysis. The total effective exposure time is of 14.0 ks (18.1 ks) for the Epic-pn (Epic-MOS2) in the observation 0084100401 and 14.7 ks (18.0 ks) in the observation 0084100501. In order to maximize S/N, source lightcurves and spectra were extracted by using an elliptical region (see Fig. 2). As we discuss also below in more detail, the elongated shape of the source is due to the off-axis point spread function of the *XMM-Newton* telescope for sources close to the border of the FOV[3]. Background lightcurves and spectra were extracted in the closest source-free region to AX J1910.7+0917. We checked that none of the results reported in this paper changed significantly by using different (reasonable) source and background extraction regions. We corrected all lightcurves for vignetting, bad pixels, point-spread-function (PSF) losses, and dead time with the SAS tool. All EPIC images and spectra were corrected for out of time events, according to the instructions provided by the SAS online analysis threads. Epic-pn and Epic-MOS spectra were rebinned before fitting so as to have at least 25 counts per bin and, at the same time, prevent oversampling the energy resolution by more than a factor of three. Given the relatively short exposure time and low X-ray flux of the source, we report below only results from the

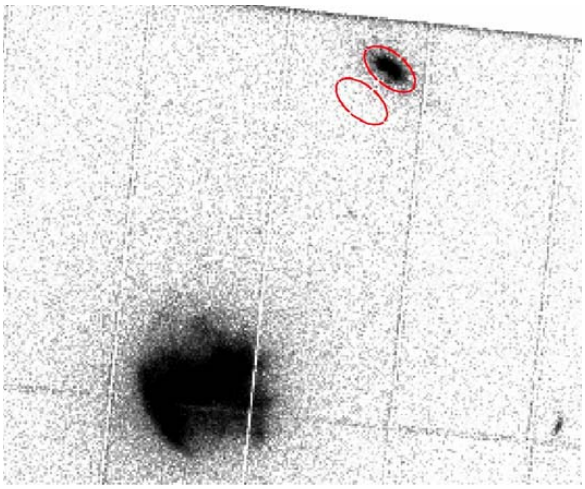

Fig. 2. Image of AX J1910.7+0917 as observed by the Epic-pn detector (0.5−12.0 keV). The extraction region for source and background are also shown. The bright object in the center is the SNR W49B.

[2] http://xmm.esac.esa.int/sas/documentation/threads/.

[3] See also http://xmm.esa.int/external/xmm_user_support/documentation/uhb/node18.html

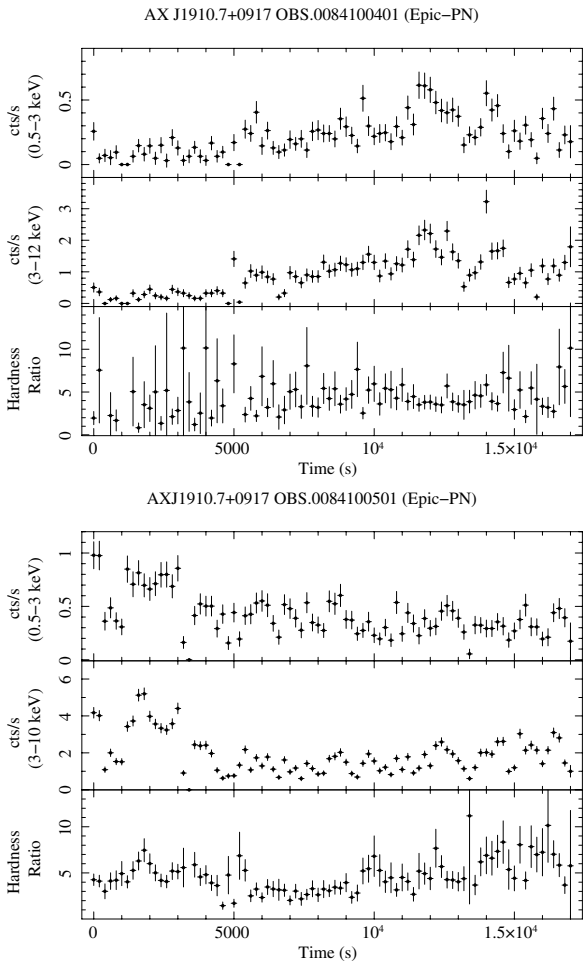

Fig. 3. *XMM-Newton* Epic-pn background-subtracted lightcurves of AX J1910.7+0917 extracted in the two energy bands 0.5−3 keV and 3−12 keV for the two observations 0084100401 (top) and 0084100501 (bottom). The hardness ratio is reported in the bottom panel of each figure. The time bin is 200 s.

Epic-pn analysis and checked that the Epic-MOS2 data would give compatible results in all cases.

In Fig. 3 we report the Epic-pn lightcurves of the source in the 0.5−3 keV and 3−12.0 keV energy bands, extracted from the two *XMM-Newton* observations. The hardness ratio, defined as the ratio of the count rate in the hard (3−12 keV) to soft (0.5−3 keV) energy band versus time, is also shown. A pronounced variability on timescales of hundreds of seconds is clearly visible from these lightcurves, but only marginal variations in the hardness ratio were measured (the most prominent feature is the increase of a factor ∼2 at the beginning of observation 0084100501, see Fig. 3). From the 0.5−12 keV Epic-pn lightcurves in observation 0084100401 (0084100501) we estimated a minimum source count rate of 0.25 ± 0.03 (0.6 ± 0.2) cts/s and a maximum source count rate of 5.6 ± 0.5 (6.2 ± 0.5) cts/s.

In order to search for spectral variations with the source intensity, we extracted from observation 0084100401 two *XMM-Newton* spectra by selecting time intervals in which the source count-rate in the 0.3−12 keV energy band was <2 and >2 cts/s. The first spectrum (effective exposure time 12 ks) could be reasonably well described ($\chi^2_{\rm red}$/d.o.f. = 1.2/125) by using an absorbed power-law (PL) model with $N_{\rm H} = (6.3^{+0.6}_{-0.5}) \times 10^{22}$ cm^{-2} and $\Gamma = 1.4^{+0.2}_{-0.1}$. The estimated 1−10 keV X-ray flux was 1.3×10^{-11} erg/cm^2/s. Alternatively, this spectrum could be well described ($\chi^2_{\rm red}$/d.o.f. = 1.0/125) by using a blackbody (BB) model with a temperature of $kT_{\rm BB} = (1.78 \pm 0.08)$ keV and a radius of $R_{\rm BB} = 0.42 \pm 0.03$ km (for an assumed distance of 10 kpc). The spectrum extracted at higher count-rates (effective exposure time 2 ks) could be reasonably well fitted by using the same models discussed above. This gave $N_{\rm H} = (6.2^{+0.9}_{-0.8}) \times 10^{22}$ cm^{-2}, and $\Gamma = 1.3 \pm 0.2$ for the PL model and $N_{\rm H} = (3.2 \pm 0.5) \times 10^{22}$ cm^{-2}, $kT_{\rm BB} = (2.0 \pm 0.2)$ keV, and $R_{\rm BB} = 0.60 \pm 0.07$ km for the BB model. In this case the estimated flux is 3.8×10^{-11} erg/cm^2/s (1−10 keV). This analysis did not reveal any significant change in the spectral parameters between the higher and lower count-rate spectra. We thus also extracted the average spectrum of this observation (see Fig. 4). This could be well fitted with an absorbed PL model, the parameters of the fit are reported in Table 1. A similar good fit ($\chi^2_{\rm red}$/d.o.f. = 0.9/147) could also be obtained by using a BB model ($kT_{\rm BB} = (1.85 \pm 0.07)$ keV, $R_{\rm BB} = 0.45 \pm 0.03$ km, $N_{\rm H} = (3.3 \pm 0.3) \times 10^{22}$ cm^{-2}).

We carried out a similar analysis for the observation 0084100501. The rate-resolved spectra were extracted during the time intervals in which the source count-rates were >2 and <2 cts/s (0.5−12 keV). We fitted both spectra with an absorbed power-law model and noticed that the residuals from these fits indicated the presence of an iron line at ∼6.4 keV (see Fig. 4). We therefore added a Gaussian line to the spectral model used for the fit. The spectrum extracted at higher count rates (effective exposure time 4.4 ks) gave ($\chi^2_{\rm red}$/d.o.f. = 1.1/134) a power-law photon index of $\Gamma = 1.3 \pm 0.1$, an absorption column density of $N_{\rm H} = (5.3 \pm 0.4) \times 10^{22}$ cm^{-2}, an energy for the iron line centroid of $E_{\rm line} = 6.45 \pm 0.06$ keV and an equivalent width of $EW = 0.06^{+0.04}_{-0.05}$ keV (errors on the EWs are given at 68% c.l. throughout the paper). The normalization of the line was $(3.8 \pm 2.4) \times 10^{-5}$, only yielding an indication of the presence of the line. For this spectrum the estimated 1−10 keV X-ray flux was $(4.3^{+0.1}_{-0.3}) \times 10^{-11}$ erg/cm^2/s. By using a BB model instead of a PL, we obtained $N_{\rm H} = (2.7 \pm 0.3) \times 10^{22}$ cm^{-2}, $kT_{\rm BB} = (1.95 \pm 0.08)$ keV, and $R_{\rm BB} = 0.63 \pm 0.04$ km.

The spectrum extracted at a lower count rate (effective exposure time 10.3 ks) gave $\Gamma = 1.4 \pm 0.1$, $N_{\rm H} = (4.6 \pm 0.4) \times 10^{22}$ cm^{-2}, $E_{\rm line} = 6.42 \pm 0.03$ keV, $EW = 0.14 \pm 0.06$ keV ($\chi^2_{\rm red}$/d.o.f. = 1.0/132), and a flux of $(1.7^{+0.1}_{-0.3}) \times 10^{-11}$ erg/cm^2/s (1−10 keV). The normalization of the line in this case was $(3.3 \pm 1.1) \times 10^{-5}$, thus indicating a detection significance >3σ. By using an absorbed BB instead of the PL component to fit the lower count-rate spectrum in the observation 0084100501 would give $N_{\rm H} = (2.2 \pm 0.2) \times 10^{22}$ cm^{-2}, $kT_{\rm BB} = 1.77 \pm 0.08$ keV, and $R_{\rm BB} = 0.44 \pm 0.03$ km. We also extracted the source spectrum by using the total exposure time of the observation 0084100501. This spectrum is shown in Fig. 4 and the best-fit parameters obtained with an absorbed PL model plus a Gaussian line are reported in Table 1. In this case we found $E_{\rm line} = 6.44 \pm 0.03$ keV and an $EW = 0.09 \pm 0.03$ keV. The normalization of the line was $(3.4 \pm 1.0) \times 10^{-5}$. By using a BB component instead of the PL for this spectrum would give $N_{\rm H} = (2.4 \pm 0.2) \times 10^{22}$ cm^{-2}, $kT_{\rm BB} = 1.85 \pm 0.06$ keV, $R_{\rm BB} = 0.51 \pm 0.03$ km, $\chi^2_{\rm red} = 1.0/168$ and parameters for the iron line fully in agreement (within the errors) with those reported above.

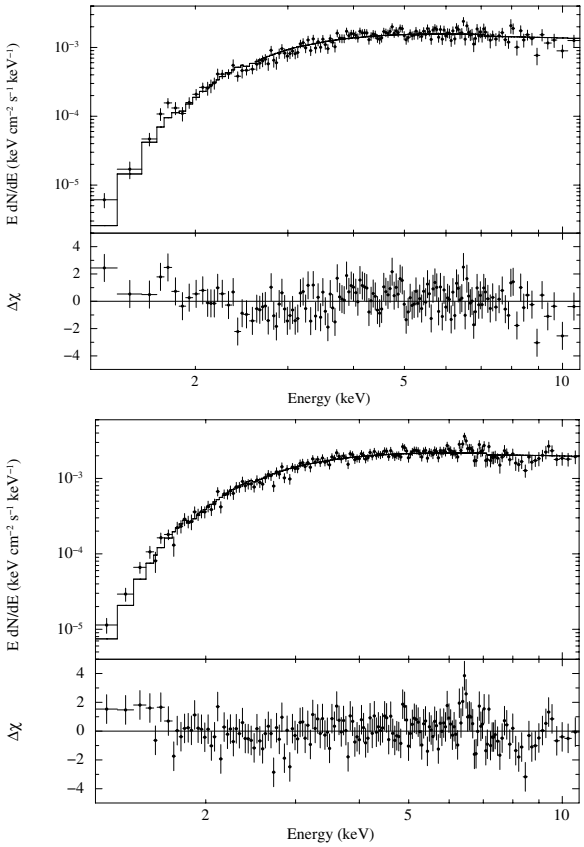

Fig. 4. Averaged *XMM-Newton* Epic-pn spectra of AX J1910.7+0917 extracted from the observations 0084100401 (*top*) and 0084100501 (*bottom*). In both cases we also show the best-fit model (an absorbed power-law) and the residuals from these fits. In the observation 0084100501 the residuals clearly showed an iron line at ∼6.4 keV.

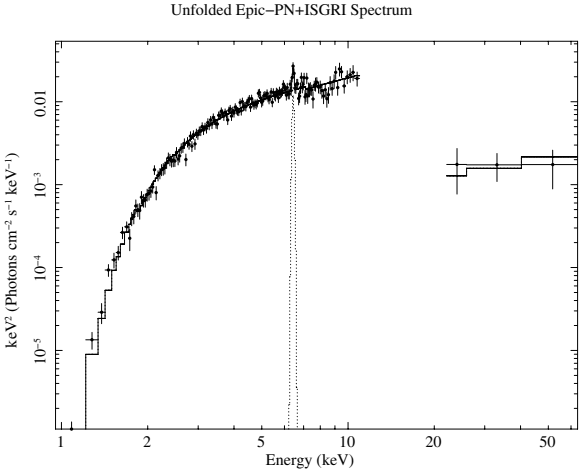

Fig. 5. Unfolded Epic-pn+ISGRI spectrum of AX J1910.7+0917. The best-fit model is obtained with an absorbed power-law model plus a Gaussian line at ∼6.4 keV (see text for details).

In order to compare the results found for the two *XMM-Newton* observations of AX J1910.7+0917, we added an iron line with a centroid energy fixed at 6.44 keV to the spectrum extracted by using the total exposure time of observation 0084100401 and determined the 90% c.l. upper limit on its normalization at 1.5×10^{-5}. This value is lower than the one measured in observation 0084100501, but still compatible with that expected due to the lower flux (∼40%) of the source in the observation 0084100401. We thus conclude that it is not possible to infer unambiguously from the present data a variation of the iron line parameters between the two observations. Even though no simultaneous *XMM-Newton* and *INTEGRAL* observation were available, we tried a fit to the combined averaged ISGRI spectrum and the Epic-pn averaged spectrum of the observation 0084100501. This spectrum could be well described with an absorbed power law model, and we introduced a normalization constant to take into account both the intercalibration between the Epic-pn and ISGRI instruments and the variability of the source. The values of the absorption column density and power-law photon index were found to be fully consistent with those of the averaged Epic-pn spectrum, but the normalization constant turned out to be 0.04 ± 0.02 (this value would be 0.06 ± 0.03 if the same fit were performed by using the *XMM-Newton* spectrum of the observation 0084100401). The relatively low value of the normalization constant between the two instruments indicates that on average the X-ray flux of the source is much lower than that measured during the *XMM-Newton* observations. This is consistent with the results reported in Table 1. The unfolded Epic-pn+ISGRI spectrum is shown in Fig. 5.

Finally, we also extracted for both *XMM-Newton* observations a spatially resolved X-ray spectrum by selecting different regions centered on the source in order to search for spectral shape variations and investigate a possible extended nature of the source. We did not find any evidence for a significant change in the spectral parameters, and concluded that the elongated shape of the source is most likely caused by distortion of the instrument PSF for sources close to the border of the FOV (see also above). Because of this problem, the determination of an improved source position requires some caution. We used the automatic *XMM-Newton* source-detection task - (with manually fine-tuned parameters), to have an estimate of the source position and error in the two *XMM-Newton* observations for both the Epic-pn and Epic-MOS2 cameras. In the observation 0084100401, the two best-determined positions are (i) $\alpha_{J2000} = 19^h10^m43\overset{s}{.}42$, $\delta_{J2000} = 09°16'29\overset{''}{.}3$ and (ii) $\alpha_{J2000} = 19^h10^m43\overset{s}{.}37$, $\delta_{J2000} = 09°16'29\overset{''}{.}3$, for the Epic-pn and the Epic-MOS2, respectively. The corresponding positions obtained in the observation 0084100501 were (i) $\alpha_{J2000} = 19^h10^m43\overset{s}{.}44$, $\delta_{J2000} = 09°16'30\overset{''}{.}7$ and (ii) $\alpha_{J2000} = 19^h10^m43\overset{s}{.}39$, $\delta_{J2000} = 09°16'30\overset{''}{.}0$. According to the latest calibration document available, the relative astrometry among all EPIC cameras is estimated to be better than 1.5″, and the absolute astrometric accuracy of any source in the *XMM-Newton* FOV is of ∼2″. Only for faint MOS sources near the detection limit this error can be as large as 4″ (90% c.l.). In the present case all results on the positions we obtained are consistent within 1.5″ as expected. Given the position of AX J1910.7+0917 at the very rim of the *XMM-Newton* detector, we assume in the following as the best determined position of the source: $\alpha_{J2000} = 19^h10^m43\overset{s}{.}39$, $\delta_{J2000} = 09°16'30\overset{''}{.}0$ (J2000), with a conservative associated error of 2″ (90% c.l.). In Sect. 2.1.5 we use this result to search for possible counterparts to AX J1910.7+0917.

A Fourier analysis of the *XMM-Newton* data of AX J1910.7+0917 did not reveal any indication for a possible coherent periodicity.

2.1.3. *ASCA*

AX J1910.7+0917 was serendipitously observed in several *ASCA* (Tanaka et al. 1994) observations performed in 1993 and 1999. A log of these observations is provided in Table 1. We used data from the two gas-imaging spectrometers (GIS2 and GIS3, Ohashi et al. 1996; Makishima et al. 1996) and applied standard screening criteria[4]. We extracted the source light curves and spectra from a circular region of 2′ radius. A larger extraction region could not be used because of the emission from the nearby SNR (see also Sect. 2.1.2). For the background, we used a similar extraction region, located in the same part of the FOV as the source events, as described in the *ASCA* ABC guide. Note that AX J1910.7+0917 is located well within the Galactic disk and thus we could not use the *ASCA* blank-sky observations (see p. 80 of the *ASCA* ABC guide). We used the latest available GIS2 and GIS3 instrument response files (gis2v4_0.rmf and gis3v4_0.rmf) and generated for each observation the corresponding ancillary file with the tool .

Only in observation 50 005 000 was the statistics sufficiently high to rebin the spectrum to have at least 20 photons per bin and perform a minimum χ^2 fitting. In all observations where the source was detected but the statistics was relatively poor, the C-statistics was used for the fits. We also determined a 90% c.l. upper limit on the source X-ray flux in all the observations in which AX J1910.7+0917 was not detected. In these cases, we obtained a source and background spectrum by using the same extraction regions adopted in the other observations, and fitted them with an absorbed PL model. The absorption column density and PL photon index were fixed to those of observation 50 005 000, and the 90% c.l. error on the model normalization was used to obtain an upper limit on the flux (1−10 keV energy band). All these results are reported in Table 1. Given the low S/N of the *ASCA* observations of AX J1910.7+0917, we did not investigate possible timing features in these data.

2.1.4. *Chandra*

A research in the data archive[5] revealed that AX J1910.7+0917 was also twice observed by the ACIS telescope on-board *Chandra* (Garmire et al. 2003). The first of these observations (ID. 117) was performed on 2001 July 8 and lasted for 54 ks. AX J1910.7+0917 was serendipitously observed in the ACIS-I2 chip, but not detected. Unfortunately, the analysis of this observation revealed the presence of a large number of poorly illuminated columns on the ACIS-I2 chip (most likely a read-out problem), and therefore we did not consider this observation in our subsequent analysis. In the second observation (ID. 9615), performed on 2008 May 31 and lasting 1.65 ks, AX J1910.7+0917 was observed in the FOV of the ACIS-S3 chip, but not detected.

We derived from these data an upper limit on the source X-ray flux by using both the task[6] available within the package (v.4.2) and by building a fluxed image of the ACIS-S3 chip[7]. The first method allowed us to derive a 68% c.l. upper limit on the source count rate of 0.012 cts/s (0.5−7 keV), which corresponds to a 1−10 keV X-ray flux of 4.0×10^{-13} erg/cm^2/s (we used the online tool [8] and assumed a PL model with $\Gamma = 1.4$ and $N_{\rm H} = 4.8 \times 10^{22}$ cm^{-2} to be consistent with the other upper limits derived, see Sect. 2.1.3). The second method permits us to directly calculate the energy flux in units of erg/cm^2/s for each event in the selected *Chandra* chip, taking into account the quantum efficiency and effective area as well. With this method we estimated a 3σ upper limit on the source X-ray flux of 5.4×10^{-13} erg/cm^2/s (0.5−7 keV) energy band, compatible with the limit derived with the first method.

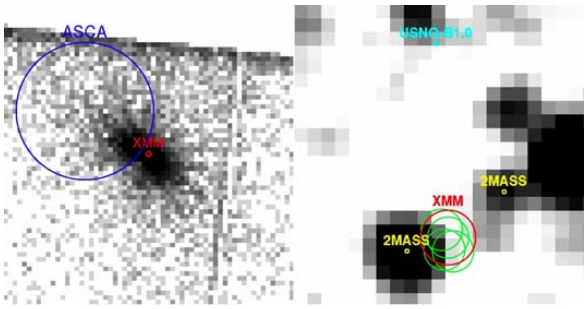

Fig. 6. *XMM-Newton* (*left*) and infrared (2MASS, *J* band, *right*) image of the region around AX J1910.7+0917. We show the error circles (green) associated with the determined positions in the 2 *XMM-Newton* observations for the Epic-pn and Epic-MOS2 cameras, and the best adopted source position (red circle, error 2″ at 90% c.l.). We also show in blue the previously determined *ASCA* position (only slightly outside the *XMM-Newton* error circle) and the closest 2MASS and USNO-B1.0 counterparts discussed in Sect. 2.1.5 (see the electronic version of the paper for the colored picture).

2.1.5. Counterparts of AX J1910.7+0917

We used the improved source position found from the *XMM-Newton* data to search for an infrared and/or optical counterpart to AX J1910.7+0917. In Fig. 6 we show the *XMM-Newton* FOV around AX J1910.7+0917, and the corresponding 2MASS image (Skrutskie et al. 2006). The four determined positions in the *XMM-Newton* observations (green circles) and the best adopted source position (red circle, error 2″ at 90% c.l.) are also shown. We found only one likely counterpart, 2MASS J19104360+0916291, which partly lies within the *XMM-Newton* error circle and has $J = 15.044 \pm 0.030$, $H = 13.000 \pm 0.022$, and $K = 11.808 \pm 0.023$. No cataloged optical counterparts were found within the *XMM-Newton* error circle. The closest object in the USNO-B1.0 catalog is shown in the figure but because of the relatively large separation from AX J1910.7+0917, it is very unlikely that it is associated with AX J1910.7+0917. We note that the lack of a clear optical counterpart is compatible with the high absorption in the direction of the source measured from the *XMM-Newton* observations (see Sect. 2.1.2). We also queried the FIRST Survey and the NVSS catalogs in search for a radio counterpart, but did not find any obvious candidate.

[4] See the ASCA ABC guide at http://heasarc.gsfc.nasa.gov/docs/asca/abc/abc.html.

[5] http://heasarc.gsfc.nasa.gov/.

[6] See the on-line thread: http://cxc.harvard.edu/ciao/threads/aprates/$\protect\kern-.1667em\relax$index.html#netcts.

[7] See the on-line thread: http://cxc.harvard.edu/ciao/threads/eff2evt.

[8] http://heasarc.nasa.gov/Tools/w3pimms.html

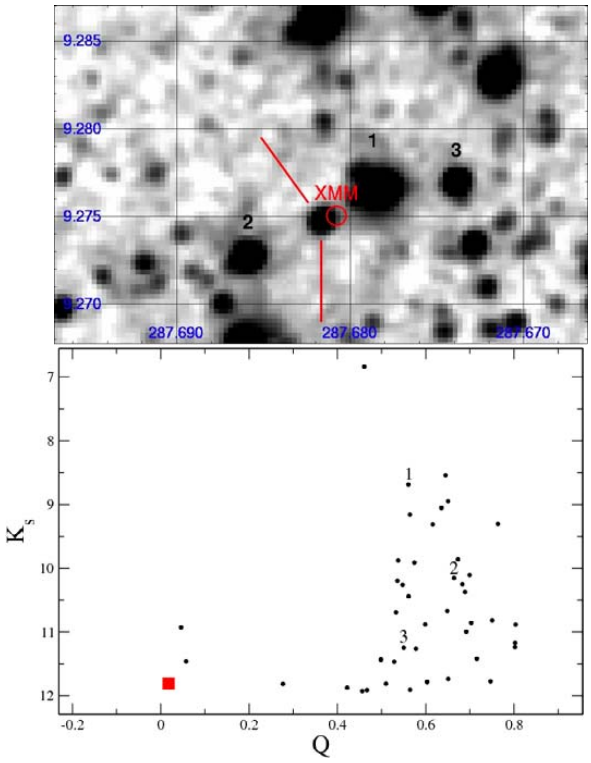

Fig. 7. *Top*: 2MASS image (K band, coordinates in Right Ascension and Declination) of the FOV around AX J1910.7+0917. The best-determined *XMM-Newton* position is marked in red, and a few nearby potential IR candidates are also displayed. *Bottom*: Plot of Q vs. K_s magnitudes for the 2MASS stars around the XMM position (see text for details). The square represents the likely IR counterpart to AX J1910.7+0917. Some of the nearby potential candidates are also shown.

To investigate the nature of the possible IR counterpart found above for AX J1910.7+0917 in more detail, we applied the analysis described in Negueruela & Schurch (2007) to the objects in the FOV of 2MASS J19104360+0916291. For each star represented in Fig. 7 we used 2MASS photometric data to obtain the values of their J, H, and K. Then, we calculated the quantity $Q = (J - H) - 1.70(H - K_s)$ for each object (here $K_s = K$) and plotted these values as a function of K_s in the bottom panel of Fig. 7. According to Negueruela & Schurch (2007), the objects characterized by $K_s \lesssim 11$ and $Q \lesssim 0.2$ are promising supergiant candidates. Even though this method does not provide a secure classification, it suggests that the nature of the source 2MASS J19104360+0916291 (red square in Fig. 7) would be compatible with being a supergiant star. We discuss this aspect further in Sect. 4.

3. New *INTEGRAL* sources

In the IBIS/ISGRI FOV around AX J1910.7+0917, we found three new sources that had previously remained undetected. These appeared to be the only excesses found independently both in the OSA9.0 mosaic and the mosaic obtained with the _ software (Segreto et al. 2008, 2010). A summary of the properties of the sources is given in Table 2. There we report the best values of the detection significance, source position, and the associated errors. The sources were named according to the standard *INTEGRAL* convention. A mosaic containing all the new sources is shown in Fig. 1.

Table 2. Newly discovered *INTEGRAL* sources around AX J1910.7+0917.

Name	RA (deg)	Dec (deg)	Err. (′)	Det.[a] (σ)	Counts[b]	Exp.[c] (Ms)
IGR J19173+0747	289.349	7.785	2.1	10.0	0.15 ± 0.02	3.0
IGR J19294+1327	292.367	13.459	3.4	6.8	0.12 ± 0.02	2.1
IGR J19149+1036	288.73[d]	10.61[d]	1.0[d]	~20[d]	~0.3[d]	2.6

Notes. [(a)] Detection significance in the IBIS/ISGRI mosaic (17–80 keV); [(b)] the count rates in cts/s estimated from the ISGRI mosaic. In this energy band 1 mCrab = 0.28 cts/s; [(c)] effective exposure time; [(d)] these values are affected by large systematic uncertainties related to the presence of GRS 1915-105.

We report in Table 2 only a first-order approximation for the values of IGR J19149+1036 because it is relatively close ($\lesssim$20 arcmin) to the brighter object GRS 1915-105 and a precise determination of the degree of contamination would require a much more detailed analysis. We note, though, that the inferred source position is coincident with the *Einstein* source 2E 1912.5+1031. For IGR J19173+0747 and IGR J19294+1327, we performed a spectral analysis. For IGR J19173+0747, the ISGRI spectrum was well described by a power-law model with $\Gamma = 3.3^{+0.9}_{-0.7}$ ($\chi^2_{\rm red}$/d.o.f. = 0.3/5) and flux of $F_{20-40\ \rm keV} = 5.6 \times 10^{-12}$ erg/cm^2/s. A similar analysis for IGR J19294+1327 gave $\Gamma = 2.6^{+0.8}_{-0.7}$, $F_{20-40\ \rm keV} = 6.5 \times 10^{-12}$ erg/cm^2/s and $\chi^2_{\rm red}$/d.o.f. = 0.4/4.

3.1. Swift/XRT follow-up of the newly discovered sources

Following the discovery of the three new sources reported in the previous section, we asked for follow-up observations (PI L. Stella) in the soft X-ray domain with *Swift*/XRT (0.3–10 keV; Gehrels et al. 2004). At the time of writing, only the follow-up observations in the direction of IGR J19173+0747 and IGR J19294+1327 were carried out. In order to search for the X-ray counterpart of these two sources, we used the best-determined positions and errors in Table 2. We processed all the *Swift*/XRT data with the and the latest calibration files available (caldb v.20091130). All observations were performed in photon-counting mode (PC). Filtering and screening criteria were applied by using (Heasoft v.6.9). We extracted source and background light curves and spectra by selecting event grades of 0–12 for the PC mode, and created the exposure maps for each observation through the task. We rebinned each spectrum where possible to have at least 20 photons per bin and used the latest spectral redistribution matrices available in the calibration database (v.011). Ancillary response files, accounting for different extraction regions, vignetting and PSF corrections, were generated with the task. For each of the two sources, we determined an improved source position by using the task.

3.1.1. IGR J19173+0747

IGR J19173+0747 was observed by *Swift*/XRT starting on 2010 February 22 at 08:07:00, for a total exposure time of 6 ks. An image of the source is shown in Fig. 8. Inside the *INTEGRAL* error circle there is only one soft X-ray source.

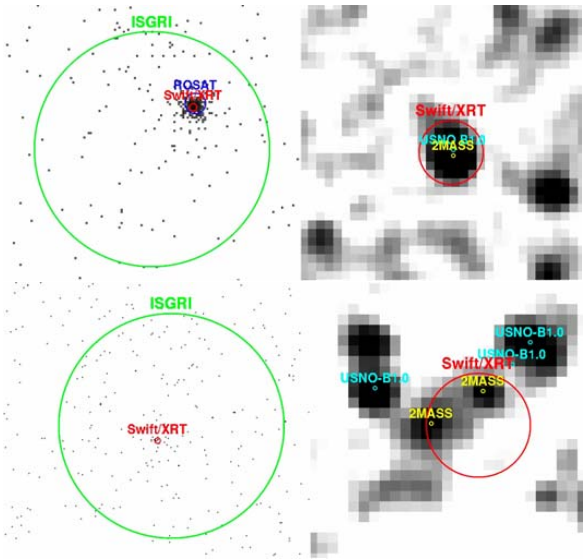

Fig. 8. *Swift*/XRT observations of the newly discovered *INTEGRAL* sources. *Top*: IGR J19173+0747. In this case only one soft X-ray source is found in *Swift*/XRT within the ISGRI error circle. We show on the right the 2MASS infrared image (J band) together with the *Swift*/XRT error circle and the position of the IR and optical counterpart. A positionally coincident *ROSAT* source is also shown. *Bottom*: for IGR J19294+1327 only one very faint soft X-ray excess has been found in the *Swift*/XRT observation (S/N = 3.7). Within the assumed XRT error circle there are two possible IR candidates, but no optical counterpart has been found (see the electronic version of the paper for the colored image).

The spectrum of the source could be well fitted by an absorbed power-law model. We estimated a PL photon index of $\Gamma = 0.6 \pm 0.2$ and obtained an upper limit on the absorption column density of $N_{\rm H} < 6 \times 10^{21}$ cm^{-2} (90% c.l.). The corresponding flux is $(6^{+1.0}_{-1.5}) \times 10^{-12}$ erg/cm^2/s (0.5−10 keV). Extrapolating this flux to the 20−40 keV band would predict a much higher flux ($\sim 2.8 \times 10^{-11}$ erg/cm^2/s) than the one observed with IBIS/ISGRI (5.6×10^{-12} erg/cm^2/s, see Sect. 3). This, together with the different photon index derived in the two energy ranges, suggests a break in the spectrum at energies between 10 and 20 keV, or alternatively a variability of the source. We obtained a refined source position at $\alpha_{\rm J2000}$ = 19$^{\rm h}$17$^{\rm m}$20$^{\rm s}$.8 and $\delta_{\rm J2000}$ = 07°47′51″.1, with an associated uncertainty of 3.8 arcsec (90% c.l.). This position is consistent with that of the *ROSAT* source 1RXS J191720.6+074755 (Voges et al. 1999). The count rate of the source is 0.04 ± 0.01 cts/s in the 0.1−2.4 keV band. By assuming the spectral shape determined above, we checked with the online tool that the *ROSAT* countrate would correspond to a flux compatible with that of *Swift*/XRT. Inside the *Swift*/XRT error circle we found only one possible NIR and optical counterpart. The NIR counterpart is 2MASS J19172078+0747506, characterized by J = 13.945 ± 0.031, H = 13.520 ± 0.030, and K = 13.311 ± 0.043. The optical counterpart is USNO-B1.0 0977-0532587 ($R1$ = 15.46, $B1$ = 16.91, $R2$ = 14.99, $B2$ = 16.14, I = 14.78). We queried the FIRST Survey and the NVSS catalogs in search for a radio counterpart, but did not find any obvious candidate.

3.1.2. IGR J19294+1327

IGR J19294+1327 was observed by *Swift*/XRT twice, on 2010 February 22 beginning at 23:59:01 and on 2010 February 26 beginning at 10:16:01. The total exposure time was 7.4 ks. In the *Swift*/XRT FOV only one very faint X-ray source is visible within the ISGRI error circle (S/N = 3.7, see Fig. 8). Given the relatively low S/N ratio, other observations are needed to confirm this detection. Assuming that this is the real counterpart of the *INTEGRAL* source, we estimated its best position at $\alpha_{\rm J2000}$ = 19$^{\rm h}$29$^{\rm m}$29$^{\rm s}$.80 and $\delta_{\rm J2000}$ = 13°27′05″.44 (associated error of 5.0 arcsec). The estimated source count rate was $(4.0 \pm 1.1) \times 10^{-3}$ cts/s, corresponding to an X-ray flux of 3×10^{-13} erg/cm^2/s (0.3−10 keV, we assumed $N_{\rm H} = 7.1 \times 10^{21}$ cm^{-2}, and Γ = 1.5). This low flux, compared to that measured in the 20−40 keV band, suggests that either the source is intrinsically very faint in the 0.3−10 keV range, or that it is a strongly variable source. Within the *Swift*/XRT error circle we found the two possible NIR counterparts 2MASS J19292976+1327087 (J = 16.075 ± 0.143, H = 15.187 ± 0.150, K = 14.761 ± 0.133) and 2MASS J19293011+1327056 (J = 16.018 ± 0.137, H = 14.725 ± 0.119, K = 13.803 ± 0.101). No cataloged optical or radio counterpart was found at these positions.

4. Discussion and conclusions

We reported on the analysis of all available X-ray observations carried out with *INTEGRAL*, *XMM-Newton*, *Chandra*, and *ASCA* that included AX J1910.7+0917 in the instruments' FOVs. The information we could extract from these data showed that in the soft X-ray energy band (0.5−10 keV) the source is clearly variable. The highest dynamic range in the X-ray flux we could investigate with all available observations and instruments is ≳60 (see Table 1). The highest flux was recorded during the *XMM-Newton* observations, which also provided an improved source position and the first detailed characterization of the spectrum of the source. In the *XMM-Newton* data, AX J1910.7+0917 appeared to be variable on a relatively short timescale (hundreds of seconds) and the 0.5−10 keV X-ray spectrum could be well fitted with an absorbed power-law model. In the second available *XMM-Newton* observation, we also found that an iron line was required to fit the spectrum of the source. The centroid of the line is at ∼6.4 keV, consistent with fluorescence origin from cold iron (likely due to iron material in a ionization state not higher that Fe XX). The absorption column density measured in the different X-ray observations showed only minor changes and remained always much higher than that expected in the direction of the source ($\sim 1.5 \times 10^{22}$ cm^{-2}). The power-law photon index was constant (to within the errors) in all data we analyzed. In the hard X-ray energy band (17−80 keV) the source was characterized by a mean X-ray flux of a few 10^{-12} erg/cm^2/s. No evidence was found in the *XMM-Newton* and *INTEGRAL* data for a coherent periodicity that could be associated with the spin period of a neutron star hosted in this system or an orbital period. The improved X-ray position obtained thanks to the *XMM-Newton* observations also allowed us to search for possible counterparts in different energy bands (optical, infrared, radio). In Sect. 2.1.5 we suggested a possible association between AX J1910.7+0917 and the object 2MASS J19104360+0916291, which is the closest classified object to the *XMM-Newton* position. No obvious counterpart in the optical and radio band could be identified.

The available X-ray data on AX J1910.7+0917 do not allow for an unambiguous classification of this source. Its position, relatively close to the Galactic plane, favors the

hypothesis of a Galactic source, and we discuss below a few different possibilities. A relevant feature for investigating the nature of AX J1910.7+0917 is the iron line visible in the *XMM-Newton* observations. The width and the centroid of the line are compatible with a fluorescence origin and thus suggest that AX J1910.7+0917 is likely part of a binary system. Similar iron lines are indeed unlikely to appear in the X-ray spectra of isolated compact objects and magnetars (see, e.g. Mereghetti 2008). The apparent lack of intrinsic broadening would also argue against AX J1910.7+0917 being a low-mass X-ray binary (Bhattacharyya & Strohmayer 2007, and references therein). Among the different subclasses of cataclysmic variables (for a review see Warner 1995, and references therein), polar systems are hardly detected in the ISGRI energy band. Furthermore, for these systems a variability in flux of order ∼60 is uncommon. Similar arguments apply to the intermediate polar case. These sources sometimes display emission above 20 keV, but they are known to be generally persistent objects in the soft energy band (0.5−10 keV). We also suggest that the X-ray properties of AX J1910.7+0917 are not compatible with those of novae sources (Warner 1995). A more likely possibility is that AX J1910.7+0917 is a new member of the high-mass X-ray binaries (HMXB) discovered by *INTEGRAL*. According to this interpretation, the iron line observed in the *XMM-Newton* spectrum could originate from irradiation of cold iron in the wind of a massive companion. The analysis conducted in Sect. 2.1.5 on the nature of the possible IR counterpart to AX J1910.7+0917 and the low Galactic latitude of the source would also support this interpretation. However, the association of AX J1910.7+0917 with the class of the HMXBs would still face some difficulties. Among the different subclasses of HMXBs observed by *INTEGRAL*, neither the classical supergiants (see e.g., Walter et al. 2006) nor the SFXT (Sguera et al. 2005) have a behavior fully compatible with that of AX J1910.7+0917. On the one hand, the variability in the X-ray flux reported in Table 1 for the different observations available clearly shows that AX J1910.7+0917 is not a persistent source as expected for the classical supergiant HMXBs. On the other hand, the non detection in the ISGRI data of some bright and short flares typical of the SFXT sources argues against this interpretation. Another possibility is that AX J1910.7+0917 is a Be X-ray binary, and the *XMM-Newton* observation luckily caught the source during an outburst. According to this interpretation we would expect a somewhat higher flux during this period in the *INTEGRAL* observations of AX J1910.7+0917. We checked that no simultaneous *INTEGRAL* and *XMM-Newton* observations were available, and in the closest ISGRI data (obtained about 7 days before and after the *XMM-Newton* observations) AX J1910.7+0917 was detected with a count rate compatible with the average one. We concluded that if the high flux measured in the *XMM-Newton* data corresponded to an outburst, then this should have lasted less than 10 days. This could still be compatible with the durations of the outbursts observed from Be systems. Extrapolating the *XMM-Newton* spectrum in the ISGRI energy band (17−80 keV), we estimated that a similar bright event should correspond to an ISGRI count rate of 1.5−2 cts/s. We searched for similar events in all available ISGRI data by using a 5-day binned lightcurve and found no evidence for such bursts. During the 2200 days spanned by the ISGRI data the source was effectively monitored for approximately 415 days. This suggests that AX J1910.7+0917 should spend <80% of the time in the bright X-ray state observed by *XMM-Newton*. Additional pointed observations in X-rays with *XMM-Newton* and *Chandra*, as well as follow-up observations in different energy bands, are required in order to firmly establish the nature of AX J1910.7+0917.

Besides carrying out a detailed study of AX J1910.7+0917 in X-rays, we also report the discovery of three new hard X-ray sources in the IBIS/ISGRI FOV around AX J1910.7+0917. These sources were independently detected with the OSAv9.0 and the _ software (Segreto, priv. comm.) and are the only excesses appearing in both the mosaics extracted around AX J1910.7+0917 with the two software packages. As we showed in Sect. 3, a detailed study of 2E 1912.5+1031 could not be carried out because of the likely contamination in the *INTEGRAL* data by the bright source GRS 1915-105 and the lack of proper follow-up with *Swift*. A more refined analysis of this source will be reported elsewhere. For the two new *INTEGRAL* sources IGR J19173+0747 and IGR J19294+1327, we identified a counterpart in the soft X-ray energy band (0.3−10 keV) thanks to dedicated *Swift* observations (see Sect. 3), and searched for possible cataloged optical and infrared counterparts. However, owing to the relative faintness of the sources in the hard X-ray band (<10^{11} erg/cm^2/s in the 17−80 keV band) and the short exposure time of the *Swift*/XRT observations, a clear classification of the two sources is still premature, and other observations are required in order to determine their nature.

Acknowledgements. We thank G. Cusumano for sharing the information on the *Swift*/BAT data on AX J1910.7+0917, A. Segreto for the information on the results obtained with _ software, and M. Falanga for useful discussions. We thank the referee P. R. den Hartog for his useful comments that improved the content of this paper. L.S. acknowledges financial support from ASI.

References

Bhattacharyya, S., & Strohmayer, T. E. 2007, ApJ, 664, L103
Bird, A. J., Bazzano, A., Bassani, L., et al. 2010, VizieR Online Data Catalog, 218, 60001
Courvoisier, T., Walter, R., Beckmann, V., et al. 2003, A&A, 411, L53
Garmire, G. P., Bautz, M. W., Ford, P. G., Nousek, J. A., & Ricker, Jr., G. R. 2003, in Society of Photo-Optical Instrumentation Engineers (SPIE) Conf. Ser., ed. J. E. Truemper, & H. D. Tananbaum, 4851, 28
Gehrels, N., Chincarini, G., Giommi, P., et al. 2004, ApJ, 611, 1005
Hertz, P., & Grindlay, J. E. 1988, AJ, 96, 233
Jansen, F., Lumb, D., Altieri, B., et al. 2001, A&A, 365, L1
Lebrun, F., Leray, J. P., Lavocat, P., et al. 2003, A&A, 411, L141
Lund, N., Budtz-Jørgensen, C., Westergaard, N. J., et al. 2003, A&A, 411, L231
Makishima, K., Tashiro, M., Ebisawa, K., et al. 1996, PASJ, 48, 171
Mereghetti, S. 2008, A&ARv, 15, 225
Miceli, M., Decourchelle, A., Ballet, J., et al. 2006, A&A, 453, 567
Negueruela, I., & Schurch, M. P. E. 2007, A&A, 461, 631
Ohashi, T., Ebisawa, K., Fukazawa, Y., et al. 1996, PASJ, 48, 157
Segreto, A., Cusumano, G., La Parola, V., et al. 2008, in Proceedings of the 7th INTEGRAL Workshop
Segreto, A., Cusumano, G., Ferrigno, C., et al. 2010, A&A, 510, A47
Sguera, V., Barlow, E. J., Bird, A. J., et al. 2005, A&A, 444, 221
Skrutskie, M. F., Cutri, R. M., Stiening, R., et al. 2006, AJ, 131, 1163
Sugizaki, M., Mitsuda, K., Kaneda, H., et al. 2001, ApJS, 134, 77
Tanaka, Y., Inoue, H., & Holt, S. S. 1994, PASJ, 46, L37
Ubertini, P., Lebrun, F., Di Cocco, G., et al. 2003, A&A, 411, L131
Voges, W., Aschenbach, B., Boller, T., et al. 1999, A&A, 349, 389
Walter, R., Zurita Heras, J., Bassani, L., et al. 2006, A&A, 453, 133
Warner, B. 1995, Cambridge Astrophysics Series, 28
Watson, M. G., Schröder, A. C., Fyfe, D., et al. 2009, A&A, 493, 339
Winkler, C., Courvoisier, T., Di Cocco, G., et al. 2003, A&A, 411, L1

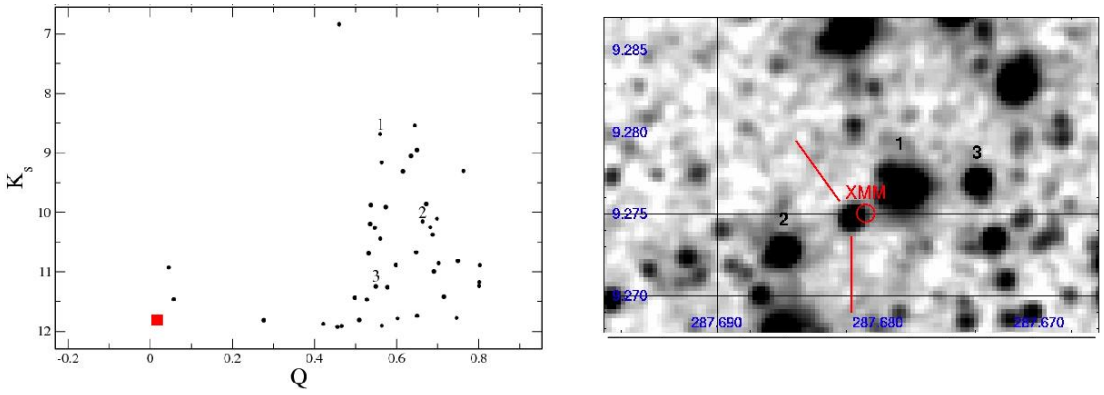

Figure 9.1: An plot of an IR Q values against K_s magnitude (left) and the field around the position of AX $J1910.7+0917$ (right).

9.3 IR Classification Scheme

INTEGRAL has a limited resolution for source localization and the error circle usually contain many stars. We define a reddening-free quantity $Q = (J-H) - 1.7(H-K_s)$. The intrinsic colors of early and late-type stars will lie clearly separated in a Q vs K_s diagram (Negueruela & Schurch 2007) For early-type Be or supergiants, several factors can affect their intrinsic colors, such as, variations in the extinction law and infrared excesses. Therefore searched the error circle of INTEGRAL for sources with the following criteria:

- $K_s < 11$ and $Q < 0.2$, for a possible OB supergiants.
- $K_s < 12$ and $Q < 0$ for a possible Be stars.

Figure 9.1 shows all the stars detected in the field in the Q vs K_s diagram. Three possible counterparts are detected. In addition, we rejected stars whose USNO B1 colors (B-V) were incompatible with a reddened OB star. As a reference, the standard reddening law implies $E(B-R) = 3.4E(J-K)$ and so an OB star should have $(B-R) > 3$ to be acceptable. Only one counterpart is revealed, 2MASS J19104360+0916291. The latter is a supergiant star with a position coinciding with the X-ray source detected by $XMM-Newton$.

Chapter 10

Scientist on duty and INTEGRAL operations

10.1 ISDC Shift team

A large fraction of the sources detected by *INTEGRAL* are X-ray binary systems. X-ray binaries are known to be highly variable. The scientist on duty is responsible for checking on a daily basis, sky images and light-curve of prominent sources. In addition, at the end of each revolution, similar tasks are performed on the mosaic images of the observed region. In the case of a new source or change of the state of a known source an Astronomer Telegram (ATel) is released. During my thesis I led the following ATels:

10.2 ATel on INTEGRAL hard X-ray detection of HMXB GX 304-1 and H 1417-624

ATel #1613; A. Manousakis, V. Beckmann (ISDC, Switzerland), V. Bianchin (INAF/IASF-Bologna), S. Brandt, J. Chenevez (DTU/NSI, Denmark), W. Hermsen (SRON & UvA, The Netherlands), A. von Kienlin (MPE, Germany), R. Krivonos (IKI, Moscow & MPA, Garching), M. Mas-Hesse (LAEFF, Madrid), A. Parmar (ESA/ESTEC, The Netherlands), V. Reglero (GACE, Valencia) on 10 Jul 2008; 18:19 UT Distributed as an Instant Email Notice Request For Observations

Subjects: X-ray, Request for Observations, Binary, Neutron Star, Transient, Pulsar

Referred to by ATel #: 2275, 2276, 2297, 3309, 3624

We report on the first detection of the Be star HMXBs GX 304-1 and H 1417-624 above 20 keV with the IBIS/ISGRI X-ray imager on board INTEGRAL. From 2008-06-24 to 2008-07-09, INTEGRAL performed monitoring observations of the Galactic plane around l=305 degrees for a total exposure time of 352 ksec.

GX 304-1 was detected in all spacecraft revolutions, and shows brightening with time. H 1417-624 was detected only in revolution 699 and 700 (2008-07-04 to 2008-07-09). The spectrum of this HMXB can be fitted either by a black body or by a simple power law. We see indication for softening of the 18-60 keV spectrum as the source brightens, with a power

law with photon index 2.3 ± 0.3 and 3.1 ± 0.5 for revolution 699 and 700, respectively. Both sources were also detected by JEM-X below 10 keV.

The evolution over the last revolutions is as follows (fluxes in mCrab in 20-40 keV, upper limits are 3 sigma values):

revolution	exposure [ksec]	GX 304-1 flux	H 1417-624 flux
695	54.5	3.1±0.6	< 2.3
696	66.5	5.0±0.6	< 3.1
698	73.1	3.8±0.7	< 3.8
699	78.7	5.0±0.6	7.8±0.7
700	79.2	6.9±0.6	11.3±1.3

INTEGRAL will continue to monitor these sources until 2008-07-23.

10.3 ATel on INTEGRAL observations of U Sco

ATel #2412; A. Manousakis (ISDC/Unige), M. Revnivtsev (IKI, Excellence Cluster Universe), R. Krivonos (MPA, IKI), E. Bozzo (ISDC/Unige) on 2 Feb 2010; 13:20 UT Distributed as an Instant Email Notice Novae

Subjects: Optical, X-ray, Gamma Ray, Nova

The recurrent Nova U Sco was discovered in outburst on 28 January 2010[1]. From 2010-01-28 17:01:43 to 2010-01-29 05:10:01 (exposure time 45 ks), INTEGRAL was observing the field around Sco X-1 (PI M. Revnivtsev), and U Sco was inside the IBIS/ISGRI and JEMX-2 fields of view.

The source was not detected by INTEGRAL X and gamma-ray instruments. We derived an 2 sigma upper limits on the source X-ray flux: 4 mCrab in the 20-40 keV energy band, 5 mCrab in the 40-80 keV energy band, 10 mCrab in 3-10 keV energy band.

Faintness of the source in X-ray energy band broadly resembles its behavior during outburst in 1999, and it likely caused by absence of enough amount of interstellar material, which can be shocked by outflowing shell to produce hot X-ray emitting plasma. Supersoft X-ray emission at energies lower than 0.5-0.7 keV, which might be expected from this source at later stages of the outburst can not be detected by INTEGRAL.

U Sco was instead detected by the Optical Monitor on-board INTEGRAL. The visual (V- band) magnitude of the source was V=8.76±0.01 on 2010-01-28 23:31 UTC. This result is in a good agreement with AAVSO announcement (see link above).

10.4 ATel on INTEGRAL observations of XTEJ1752-223

ATel #2530; Manousakis A., Ferrigno C. (ISDC-University of Geneva), Weidenspointner G. (MPE), Kuulkers E. (ESA/ESAC) Bozzo E. (ISDC-University of Geneva), Mereghetti S. (IASF-Mi/INAF), Gotz D. (CEA), Fiocchi M. (IASF-Rm/INAF), Watanabe K. (FGCU) Rothschild R. (UCSD), Kuiper L.M. (SRON), Chenevez J. (DTU Space), Caballero I. (CEA), Ducci L. (IASF-Mi/INAF) Bird A.J. (Southampton, UK), Puehlhofer G. (IAA

[1] http://www.aavso.org/publications/alerts/alert415.shtml

Tuebingen), Sanchez C. (ESA/ESAC), Del Santo M (IASF-Rm/INAF) Negueruela I. (Alicante), Bianchin V. (IASF-Bo/INAF), Prat L. (CEA), Paizis A. (IASF-Mi/INAF), Tarana A. (IASF-Rm/INAF), Panessa F. (IASF-Rm/INAF), Fiamma C. (IASF-Rm/INAF), Kreykenbohm I. (Dr. Karl Remeis Sternwarte Bamberg)) Terrier R. (APC) on 1 Apr 2010; 11:34 UT Distributed as an Instant Email Notice Transients

Subjects: Binary, Black Hole, Transient

Referred to by ATel #: 2775

The latest RXTE observations of XTEJ1752-223 detected this source in an intermediate state, and suggested that a spectral transition from the soft to the hard state was most likely taking place (Atel #2518). Following this announcement, we analyzed the INTEGRAL data of the latest revolutions in the direction of the source. In the period preceding the suspected spectral change, XTEJ1752-223 was inside the IBIS/ISGRI field of view from 2010-03-25 13:17 to 2010-03-27 02:08 (UTC). The source was detected at 6 sigma level in the 20-40 keV ISGRI mosaic (effective exposure time 21 ks), and the corresponding X-ray flux was of 7E-11 erg cm^{-2} s^{-1}. The ISGRI spectrum could be only poorly characterized and was compatible with a power-law of photon index 3±1. XTEJ1752-223 was again in the FOV of ISGRI after the announced spectral transition from 2010-03-27 at 10:03 to 2010-03-30 at 02:08 (UTC). The source was detected at 21 sigma in the 20-40 keV ISGRI mosaic, and the corresponding X-ray flux was 2.8E-10 erg cm^{-2} s^{-1}(effective exposure time 36 ks). The ISGRI spectrum could be described by a power law with a photon index of 2.8+/-0.3 above 23 keV. Further observations of the source took place from 2010-03-30 09:52 to 2010-03-30 13:33 (UTC). The source was detected at 15 sigma in the 20-40 keV ISGRI mosaic (effective exposure time 7.3 ks), and the corresponding X-ray flux was 3.2E-10 erg cm^{-2} s^{-1}. The ISGRI spectrum above 25 keV could be roughly modeled with a power-law of photon index 1.7±0.5. The measured change in the spectral photon index of XTEJ1752-223 supports the idea that this source is presently undergoing a spectral state transition. XTEJ1752-223 was outside the JEMX2 FOV for the entire observational period.

PART IV: Concluding remarks

Chapter 11

Conclusions and future perspectives

Since the launch of *INTEGRAL*, our view of supergiant High Mass X-ray Binaries (sgHMXBs) has changed considerably. *INTEGRAL* revealed two new classes of objects: the highly obscured and the fast X-ray transient systems. This variety indicates that the characteristics of the winds of massive stars are more diverse than previously thought.

The newly discovered persistent and heavily obscured sgHMXBs show much more X-ray absorption than the classical sgHMXBs. That absorption cannot be explained by smooth stellar winds. We have observed one of these systems, IGR $J17252-3616$, with XMM-Newton at several orbital phases. Significant variations of the absorbing column density and of the Fe Kα line have been observed and characterized. We have proposed an ad hoc model to reproduce these observations. The model consist of i) a smooth stellar wind, ii) an hydrodynamical 'tail' trailing the neutron star, and iii) a dense cocoon of material close to the neutron star. The main results is that a rather slow wind terminal velocity is required. If this would be confirmed in other systems, it may turn out that half of the persistent sgHMXBs exhibits slow stellar winds.

To confirm this model we have simulated the system using the hydrodynamic code VH1. It turns out that a slow wind is indeed required to reproduce the variability of the absorbing column density with orbital phase. For a slow wind, the distribution does not only depend on the wind and geometry parameters but also on the gravitational effect of the neutron star. More massive neutron star will have a larger hydrodynamical impact on the wind. Detailed comparison between the observation and the model allows to measure the neutron star mass, independently from the dynamical estimates. A new method of mass determination is important as it could be used to constrain the equation-of-state of hyper-dense matter.

Besides IGR $J17252-3616$, another obscured sgHMXB, IGR $J18027-2016$, showing eclipses, will be of particular interest to test the method and optimize the hydrodynamical simulations. These simulations will also need to be refined by inclusion of more physical mechanisms (e.g. heating/cooling). It is also interesting to notice that the simulations produce off-states that should be compared with these discovered in Vela X-1 by *INTEGRAL*.

During this thesis, we have analyzed a type II outburst of a Be/X-ray binary XMMU $J054134.7-682550$, located in LMC. The low interstellar absorption allowed us to see a remarkable soft excess, below 2 keV, featuring variability. These events are rare and only

a couple of sources (e.g. LMC X-1, SMC X-1, Her X-1) have shown such remarkable soft excess in the past. The variations of the soft excess have been interpreted as reprocessing of the hard X-rays by the inner edge of the accretion disk, which allowed to determine the thickness of the accretion disk, thanks to the magnetospheric radius determined from the observed cyclotron feature. Future instruments, such as *Athena*, will allow to study the response of the accretion disk to type II flares in much greater details.

For the last 4 years, during my Ph. D. at the ISDC, I have learned many techniques: data analysis with XMM, RXTE and INTEGRAL, timing and spectral analysis techniques, tuning and running of hydrodynamical code, and the comparison between observations and simulations and their interpretation. I also learned about the physics of stellar winds and accretion onto compact objects. I also had the opportunity to initiate collaboration with new colleagues. In particular, with John Blondin at NCSU, to use his hydrodynamical code. After all these years, diving into an international research environment, I feel confident to pursue research.

List of publications

2011

- **Manousakis, A.** et al. *Hydro-dynamical simulation of heavily absorbed HMXBs.* in preparation.

- **Manousakis, A.** & Walter, R. *X-ray wind tomography of the highly absorbed HMXB IGR J17252-3616*, A&A, (2011), **526** , 62

- Pavan, L., Bozzo, E., Ferrigno, C., Ricci, C.,**Manousakis, A.**, Walter, R., Stella, L. *AX J1910.7+0917 and three newly discovered INTEGRAL sources*, A&A, (2011), **526**, 122

⋆ **Manousakis, A.** & Walter, R. *The nature of the absorber in the INTEGRAL highly obscured sgHMXB IGR J17252-3616*, 8th INTEGRAL Workshop Proceedings, (2011) `ArXiV/1105.1988`

⋆ Pavan, L., Bozzo, E., Ferrigno, C., Ricci, C.,**Manousakis, A.**, Walter, R., Stella, L. *Study of the X-ray/gamma source AX J1910.7+0917 and three newly discovered INTEGRAL sources*,8th INTEGRAL Workshop Proceedings, (2011) `ArXiV/1104.5102`

2010

⋆ **Manousakis, A.**, Walter, R., Audar, M., Lanz, T. *Pulsed Thermal Emission from the Accreting Pulsar XMMU J054134.7-682550*, 9th International Conference of the Hellenic Astronomical Society proceedings, Publications Astronomical Society of the Pacific 2010

⋆ **Manousakis, A.**, Walter, R. *X-Ray Wind Tomography of IGR J17252-3616*, X-Ray Astronomy 2009: Present status, multi-wavelength approach and future perspectives, AIP Conference Proceedings 2010

♢ **Manousakis, A.**, Ferrigno, C., Weidenspointner, G., Kuulkers, E., Bozzo, E., Mereghetti, S., Gotz, D., Fiocchi, M., Watanabe, K., Rothschild, R., Kuiper, L. M., Chenevez, J., Caballero, I., Ducci, L., Bird, A. J., Puehlhofer, G., Sanchez, C., Del Santo, M., Negueruela, I., Bianchin, V., Prat, L., Paizis, A., Tarana, F., Panessa, F., Fiamma, C., Kreykenbohm, I., Terrier, R. *INTEGRAL observations of XTEJ1752-223*, ATel. **#2530**, 2010

♢ **Manousakis, A.**, Revnivtsev, M., Krivonos, R., Bozzo, E. *INTEGRAL observations of U Sco*, ATel. **#2512**, 2010

2009

- **Manousakis, A.** & Walter, R., Audard, M., Lanz, T *Pulsed thermal emission from the accreting pulsar XMMU J054134.7-682550*, A&A, (2009), **498**, 217

⋆ **Manousakis, A.**, Walter, R., Audard, M., Lanz, T. *Pulsed Thermal Emission from the Accreting Pulsar XMMU J054134.7-682550*, SIMBOX-X: Focusing on the hard X-Ray universe, AIP Conference Proceedings 2009

♢ Bozzo, E., Ferrigno, C., **Manousakis, A.**, Del Santo, M. *Swift follow-up of the new integral source IGRJ16442-554*, ATel. **#2188**, 2009

♢ Produit, N., Beckmann, V., **Manousakis, A.**, Bianchin, V., Budtz-Jorgensen, C., Domingo, A., Kuulkers, E., Lutovinov, A., Mandrou, P., Paul, J., Tarana, A., von Kienlin, A. *INTEGRAL observes outburst from 1A 0535+262*, ATel. **#2146**, 2009

2008

♢ **Manousakis, A.**, Beckmann, V. Bianchin, V. Brandt, S. Chenevez, J. Hermsen, W. von Kienlin, A. Krivonos, R. Mas-Hesse, M. Parmar, A. Reglero, V. *INTEGRAL hard X-ray detection of HMXB GX 304-1 and H 1417-624*, ATel. **#1613**, 2008

♢ Gotz, D., Paizis, A., Mereghetti, S., Beckmann, V., Beck, M., **Manousakis, A.**, Borkowski, J. *GRB 080723B : a long GRB detected with INTEGRAL*, GCN **8002**, 2008

♢ Mereghetti, S., Paizis, A., Gotz, D., **Manousakis, A.**, Beckmann, V., Beck, M., Borkowski, J. *GRB 080120: a long GRB detected by INTEGRAL*, GCN **7194**, 2008

N.B.: Bullet (•) indicates refereed publication in a scientific journal, star (⋆) indicates conference contribution (oral or poster), and diamond (♢) indicates astronomers′ telegram (ATel) or GCN reports.

Bibliography

Abbott D. C. (1978). The terminal velocities of stellar winds from early-type stars. *ApJ*, **225**, 893–901. [36]

Abbott D. C. (1982). The theory of radiatively driven stellar winds. II - The line acceleration. *ApJ*, **259**, 282–301. [36]

Arnaud K. A. (1996). XSPEC: The First Ten Years. In G. H. Jacoby & J. Barnes, editors, *Astronomical Data Analysis Software and Systems V*, volume 101 of *Astronomical Society of the Pacific Conference Series*, pages 17–+. [70]

Becker P. A. & Wolff M. T. (2007). Thermal and Bulk Comptonization in Accretion-powered X-Ray Pulsars. *ApJ*, **654**, 435–457. [27, 28]

Beckmann V., Kennea J. A., Markwardt C., Paizis A., Soldi S., Rodriguez J., Barthelmy S. D., Burrows D. N., Chester M., Gehrels N., Mowlavi N. & Nousek J. (2005). Swift, INTEGRAL, RXTE, and Spitzer Reveal IGR J16283-4838. *ApJ*, **631**, 506–510. [53, 57]

Binney J. & Merrifield M. (1998). *Galactic Astronomy*. Prienceton University Press. [51]

Blondin J. M., Kallman T. R., Fryxell B. A. & Taam R. E. (1990). Hydrodynamic simulations of stellar wind disruption by a compact X-ray source. *ApJ*, **356**, 591–608. [52, 75, 76, 79, 81]

Blondin J. M., Stevens I. R. & Kallman T. R. (1991). Enhanced winds and tidal streams in massive X-ray binaries. *ApJ*, **371**, 684–695. [52, 79]

Bodaghee A., Walter R., Zurita Heras J. A., Bird A. J., Courvoisier T. J.-L., Malizia A., Terrier R. & Ubertini P. (2006). IGR J16393-4643: a new heavily-obscured X-ray pulsar. *A&A*, **447**, 1027–1034. [54, 57]

Bodaghee A., Courvoisier T. J.-L., Rodriguez J., Beckmann V., Produit N., Hannikainen D., Kuulkers E., Willis D. R. & Wendt G. (2007). A description of sources detected by INTEGRAL during the first 4 years of observations. *A&A*, **467**, 585–596. [51]

Bodaghee A., Tomsick J. A., Rodriguez J., Chaty S., Pottschmidt K. & Walter R. (2010). Broadband Suzaku Observations of IGR J16207-5129. *ApJ*, **719**, 451–458. [54]

Bodaghee A., Tomsick J. A., Rodriguez J., Chaty S., Pottschmidt K., Walter R. & Romano P. (2011). Suzaku Observes Weak Flares from IGR J17391-3021 Representing a Common Low-activity State in this Supergiant Fast X-ray Transient. *ApJ*, **727**, 59–+. [56]

Bondi H. & Hoyle F. (1944). On the mechanism of accretion by stars. *MNRAS*, **104**, 273–+. [15, 20]

Bouret J.-C., Lanz T. & Hillier D. J. (2005a). Lower Mass Loss Rates in O Stars. In *American Astronomical Society Meeting Abstracts*, volume 37 of *Bulletin of the American Astronomical Society*, page 182.23. [1]

Bouret J.-C., Lanz T. & Hillier D. J. (2005b). Lower mass loss rates in O-type stars:

Spectral signatures of dense clumps in the wind of two Galactic O4 stars. *A&A*, **438**, 301–316. [46]

Bozzo E., Falanga M. & Stella L. (2008). Are There Magnetars in High-Mass X-Ray Binaries? The Case of Supergiant Fast X-Ray Transients. *ApJ*, **683**, 1031–1044. [56]

Bozzo E., Stella L., Ferrigno C., Giunta A., Falanga M., Campana S., Israel G. & Leyder J. C. (2010). The supergiant fast X-ray transients XTE J1739-302 and IGR J08408-4503 in quiescence with XMM-Newton. *A&A*, **519**, A6+. [54]

Bozzo E., Giunta A., Cusumano G., Ferrigno C., Walter R., Campana S., Falanga M., Israel G. & Stella L. (2011). XMM-Newton observations of IGR J18410-0535: the ingestion of a clump by a supergiant fast X-ray transient. *A&A*, **531**, A130+. [55]

Castor J. I., Abbott D. C. & Klein R. I. (1975). Radiation-driven winds in Of stars. *ApJ*, **195**, 157–174. [34, 43, 44]

Chaty S., Rahoui F., Foellmi C., Tomsick J. A., Rodriguez J. & Walter R. (2008). Multi-wavelength observations of Galactic hard X-ray sources discovered by INTEGRAL. I. The nature of the companion star. *A&A*, **484**, 783–800. [51, 52, 53, 54, 55]

Cherepashchuk A. M., Khaliullin K. F. & Eaton J. A. (1984). Ultraviolet photometry from the Orbiting Astronomical Observatory. XXXIX - The structure of the eclipsing Wolf-Rayet binary V444 Cygni as derived from light curves between 2460 A and 3. 5 microns. *ApJ*, **281**, 774–788. [44]

Coburn W., Heindl W. A., Rothschild R. E., Gruber D. E., Kreykenbohm I., Wilms J., Kretschmar P. & Staubert R. (2002). Magnetic Fields of Accreting X-Ray Pulsars with the Rossi X-Ray Timing Explorer. *ApJ*, **580**, 394–412. [27, 31]

Colella P. & Woodward P. R. (1984). The Piecewise Parabolic Method (PPM) for Gas-Dynamical Simulations. *Journal of Computational Physics*, **54**, 174–201. [75]

Corbet R., Barbier L., Barthelmy S., Cummings J., Fenimore E., Gehrels N., Hullinger D., Krimm H., Markwardt C., Palmer D., Parsons A., Sakamoto T., Sato G., Tueller J. & The Swift-Survey Team (2005). Swift/BAT Discovery of the Orbital Period of IGR J16320-4751. *The Astronomer's Telegram*, **649**, 1–+. [53, 57]

Corbet R. H. D. (1986). The three types of high-mass X-ray pulsator. *MNRAS*, **220**, 1047–1056. [7]

Corbet R. H. D., Markwardt C. B. & Swank J. H. (2005). Rossi X-Ray Timing Explorer Observations of the X-Ray Pulsar EXO 1722-363: A Candidate Eclipsing Supergiant System. *ApJ*, **633**, 377–383. [58]

Corbet R. H. D., Barthelmy S. D., Baumgartner W. H., Krimm H. A., Markwardt C. B., Skinner G. K. & Tueller J. (2010a). A 10 Day Period in IGR J16328-4726 from Swift/BAT Observations. *The Astronomer's Telegram*, **2588**, 1–+. [56]

Corbet R. H. D., Krimm H. A., Barthelmy S. D., Baumgartner W. H., Markwardt C. B., Skinner G. K. & Tueller J. (2010b). A 4.2 Day Period in the X-ray Pulsar IGR J16393-4643 from Swift/BAT and RXTE/PCA Observations. *The Astronomer's Telegram*, **2570**, 1–+. [54]

Courvoisier T., Walter R., Beckmann V., Dean A. J., Dubath P., Hudec R., Kretschmar P., Mereghetti S., Montmerle T., Mowlavi N., Paltani S., Preite Martinez A., Produit N., Staubert R., Strong A. W., Swings J., Westergaard N. J., White N., Winkler C. & Zdziarski A. A. (2003). The INTEGRAL Science Data Centre (ISDC). *A&A*, **411**, L53–L57. [12]

Davidson K. (1973). Accretion at a Magnetic Pole of a Neutron Star. *Nature*, **246**, 1–+. [28]

Demorest P. B., Pennucci T., Ransom S. M., Roberts M. S. E. & Hessels J. W. T. (2010). A two-solar-mass neutron star measured using Shapiro delay. *Nature*, **467**, 1081–1083. [82, 89]

den Hartog P. R., Hermsen W., Kuiper L., Vink J., in't Zand J. J. M. & Collmar W. (2006). INTEGRAL survey of the Cassiopeia region in hard X rays. *A&A*, **451**, 587–602. [53]

Dickey J. M. & Lockman F. J. (1990). H I in the Galaxy. *ARA&A*, **28**, 215–261. [70]

Drave S. P., Clark D. J., Bird A. J., McBride V. A., Hill A. B., Sguera V., Scaringi S. & Bazzano A. (2010). Discovery of the 51.47-d orbital period in the supergiant fast X-ray transient XTE J1739-302 with INTEGRAL. *MNRAS*, **409**, 1220–1226. [56, 57]

Ducci L., Sidoli L. & Paizis A. (2010). INTEGRAL results on supergiant fast X-ray transients and accretion mechanism interpretation: ionization effect and formation of transient accretion discs. *MNRAS*, **408**, 1540–1550. [56]

Dupree A. K., Gursky H., Black J. H., Davis R. J., Hartmann L., Matilsky T., Raymond J. C., Hammerschlag-Hensberge G., van den Heuvel E. P. J., Burger M., Lamers H. J. G. L. M., Vanden Bout P. A., Morton D. C., De Loore C., van Dessel E. L., Menzies J. W., Whitelock P. A., Watson M., Sanford P. W. & Pollard G. S. G. (1980). Simultaneous ultraviolet, optical, and X-ray observations of the X-ray source VELA X-1 /HD 77581/. *ApJ*, **238**, 969–981. [79]

Eggleton P. P. (1983). Approximations to the radii of Roche lobes. *ApJ*, **268**, 368–+. [18]

Eversberg T., Lepine S. & Moffat A. F. J. (1998). Outmoving Clumps in the Wind of the Hot O Supergiant zeta Puppis. *ApJ*, **494**, 799. [45]

Filliatre P. & Chaty S. (2004). The Optical/Near-Infrared Counterpart of the INTEGRAL Obscured Source IGR J16318-4848: An sgB[e] in a High-Mass X-Ray Binary? *ApJ*, **616**, 469–484. [54]

Fiocchi M., Sguera V., Bazzano A., Bassani L., Bird A. J., Natalucci L. & Ubertini P. (2010). IGR J16328-4726: A New Candidate Supergiant Fast X-ray Transient. *ApJ*, **725**, L68–L72. [56]

Frank J., King A. & Raine D. (1992). *Accretion power in astrophysics.* Cambridge University Press. [15, 17, 18, 21, 22, 24]

Fransson C. & Fabian A. C. (1980). X-ray induced shocks in stellar winds. *A&A*, **87**, 102–108. [82]

Ghosh P. (2007). *Rotation and Accretion Powered Pulsars*. World Scientific Publishing Co. [20]

Ghosh P. & Lamb F. K. (1979a). Accretion by rotating magnetic neutron stars. II - Radial and vertical structure of the transition zone in disk accretion. *ApJ*, **232**, 259–276. [25]

Ghosh P. & Lamb F. K. (1979b). Accretion by rotating magnetic neutron stars. III - Accretion torques and period changes in pulsating X-ray sources. *ApJ*, **234**, 296–316. [25, 27]

Ghosh P., Pethick C. J. & Lamb F. K. (1977). Accretion by rotating magnetic neutron stars. I - Flow of matter inside the magnetosphere and its implications for spin-up and spin-down of the star. *ApJ*, **217**, 578–596. [25]

Giacconi R., Gursky H., Paolini F. R. & Rossi B. B. (1962). Evidence for x Rays From

Sources Outside the Solar System. *Physical Review Letters*, **9**, 439–443. [3]

Giunta A., Bozzo E., Bernardini F., Israel G., Stella L., Falanga M., Campana S., Bazzano A., Dean A. J. & Mendez M. (2009). The supergiant fast X-ray transient IGRJ18483-0311 in quiescence: XMM-Newton, Swift and Chandra observations. *MNRAS*, **399**, 744–749. [55]

Godunov S. K. (1959). A difference method for numerical calculation of discontinuous solutions of the equations of hydrodynamics. *Mat. Sb. (N.S.)*, **47 (89)**, 271–306. [74, 75]

González-Riestra R., Oosterbroek T., Kuulkers E., Orr A. & Parmar A. N. (2004). XMM-Newton observations of the INTEGRAL X-ray transient IGR J17544-2619. *A&A*, **420**, 589–594. [55, 57]

Hannikainen D. C., Rawlings M. G., Muhli P., Vilhu O., Schultz J. & Rodriguez J. (2007). The nature of the infrared counterpart of IGR J19140+0951. *MNRAS*, **380**, 665–668. [53]

Hanuschik R. W. (1996). On the structure of Be star disks. *A&A*, **308**, 170–179. [3]

Hatchett S. & McCray R. (1977). X-ray sources in stellar winds. *ApJ*, **211**, 552–561. [20]

Hickox R. C., Narayan R. & Kallman T. R. (2004). Origin of the Soft Excess in X-Ray Pulsars. *ApJ*, **614**, 881–896. [29, 33, 90, 91]

Hill A. B., Walter R., Knigge C., Bazzano A., Bélanger G., Bird A. J., Dean A. J., Galache J. L., Malizia A., Renaud M., Stephen J. & Ubertini P. (2005). The 1-50 keV spectral and timing analysis of IGR J18027-2016: an eclipsing, high mass X-ray binary. *A&A*, **439**, 255–263. [52, 57]

Ibarra A., Matt G., Guainazzi M., Kuulkers E., Jiménez-Bailón E., Rodriguez J., Nicastro F. & Walter R. (2007). The XMM-Newton/INTEGRAL monitoring campaign of IGR J16318-4848. *A&A*, **465**, 501–507. [54, 57]

in't Zand J. J. M. (2005). Chandra observation of the fast X-ray transient IGR J17544-2619: evidence for a neutron star? *A&A*, **441**, L1–L4. [44, 54, 56]

in't Zand J. J. M., Jonker P. G., Nelemans G., Steeghs D. & O'Brien K. (2006). Optical identification of IGR J19140+0951. *A&A*, **448**, 1101–1106. [53]

in't Zand J. J. M., Kuiper L., den Hartog P. R., Hermsen W. & Corbet R. H. D. (2007). A probable accretion-powered X-ray pulsar in IGR J00370+6122. *A&A*, **469**, 1063–1068. [53]

Jahoda K., Swank J. H., Giles A. B., Stark M. J., Strohmayer T., Zhang W. & Morgan E. H. (1996). In-orbit performance and calibration of the Rossi X-ray Timing Explorer (RXTE) Proportional Counter Array (PCA). In O. H. Siegmund & M. A. Gummin, editor, *Society of Photo-Optical Instrumentation Engineers (SPIE) Conference Series*, volume 2808 of *Society of Photo-Optical Instrumentation Engineers (SPIE) Conference Series*, pages 59–70. [12]

Jahoda K., Markwardt C. B., Radeva Y., Rots A. H., Stark M. J., Swank J. H., Strohmayer T. E. & Zhang W. (2006). Calibration of the Rossi X-Ray Timing Explorer Proportional Counter Array. *ApJS*, **163**, 401–423. [12]

Jain C., Paul B. & Dutta A. (2009). Discovery of a short orbital period in the Supergiant Fast X-ray Transient IGR J16479-4514. *MNRAS*, **397**, L11–L15. [54]

Jansen F., Lumb D., Altieri B., Clavel J., Ehle M., Erd C., Gabriel C., Guainazzi M., Gondoin P., Much R., Munoz R., Santos M., Schartel N., Texier D. & Vacanti G. (2001).

XMM-Newton observatory. I. The spacecraft and operations. *A&A*, **365**, L1–L6. [9]

Joss P. C. & Rappaport S. A. (1984). Neutron Stars in Interacting Binary Systems. *ARA&A*, **22**, 537–592. [19]

Kallman T. R. & McCray R. (1982). X-ray nebular models. *ApJS*, **50**, 263–317. [71, 75, 78]

Kallman T. R., Palmeri P., Bautista M. A., Mendoza C. & Krolik J. H. (2004). Photoionization Modeling and the K Lines of Iron. *ApJS*, **155**, 675–701. [29, 71]

Koh D. T., Bildsten L., Chakrabarty D., Nelson R. W., Prince T. A., Vaughan B. A., Finger M. H., Wilson R. B. & Rubin B. C. (1997). Rapid Spin-up Episodes in the Wind-fed Accreting Pulsar GX 301-2. *ApJ*, **479**, 933–+. [5]

Kreykenbohm I., Mowlavi N., Produit N., Soldi S., Walter R., Dubath P., Lubiński P., Türler M., Coburn W., Santangelo A., Rothschild R. E. & Staubert R. (2005). INTEGRAL observation of V 0332+53 in outburst. *A&A*, **433**, L45–L48. [28, 32]

Kreykenbohm I., Wilms J., Kretschmar P., Torrejón J. M., Pottschmidt K., Hanke M., Santangelo A., Ferrigno C. & Staubert R. (2008). High variability in Vela X-1: giant flares and off states. *A&A*, **492**, 511–525. [79]

Kudritzki R. & Puls J. (2000). Winds from Hot Stars. *ARA&A*, **38**, 613–666. [36, 37, 38]

Labanti C., Di Cocco G., Ferro G., Gianotti F., Mauri A., Rossi E., Stephen J. B., Traci A. & Trifoglio M. (2003). The Ibis-Picsit detector onboard Integral. *A&A*, **411**, L149–L152. [12]

Lamers H. J. G. L. M. & Cassinelli J. P. (1999). *Introduction to Stellar Winds*. Cambridge University Press. [40, 43, 77]

Lattimer J. M. & Prakash M. (2007). Neutron star observations: Prognosis for equation of state constraints. *Phys. Rep.*, **442**, 109–165. [82]

Leahy D. A. & Kostka M. (2008). Stellar wind accretion in GX 301-2: evidence for a high-density stream. *MNRAS*, **384**, 747–754. [5]

Lebrun F., Leray J. P., Lavocat P., Crétolle J., Arquès M., Blondel C., Bonnin C., Bouère A., Cara C., Chaleil T., Daly F., Desages F., Dzitko H., Horeau B., Laurent P., Limousin O., Mathy F., Mauguen V., Meignier F., Molinié F., Poindron E., Rouger M., Sauvageon A. & Tourrette T. (2003). ISGRI: The INTEGRAL Soft Gamma-Ray Imager. *A&A*, **411**, L141–L148. [11]

Leitherer C. (1988). H-alpha as a tracer of mass loss from OB stars. *ApJ*, **326**, 356–367. [36]

Lépine S. & Moffat A. F. J. (2008). Direct Spectroscopic Observations of Clumping in O-Star Winds. *AJ*, **136**, 548–553. [45]

Levine A. M., Bradt H., Cui W., Jernigan J. G., Morgan E. H., Remillard R., Shirey R. E. & Smith D. A. (1996). First Results from the All-Sky Monitor on the Rossi X-Ray Timing Explorer. *ApJ*, **469**, L33. [13]

Leyder J.-C., Walter R., Lazos M., Masetti N. & Produit N. (2007). Hard X-ray flares in ¡ASTROBJ¿IGR J08408-4503¡/ASTROBJ¿ unveil clumpy stellar winds. *A&A*, **465**, L35–L38. [54]

Liu Q. Z., van Paradijs J. & van den Heuvel E. P. J. (2006). Catalogue of high-mass X-ray binaries in the Galaxy (4th edition). *A&A*, **455**, 1165–1168. [5]

Lund N., Budtz-Jørgensen C., Westergaard N. J., Brandt S., Rasmussen I. L., Hornstrup

A., Oxborrow C. A., Chenevez J., Jensen P. A., Laursen S., Andersen K. H., Mogensen P. B., Rasmussen I., Omø K., Pedersen S. M., Polny J., Andersson H., Andersson T., Kämäräinen V., Vilhu O., Huovelin J., Maisala S., Morawski M., Juchnikowski G., Costa E., Feroci M., Rubini A., Rapisarda M., Morelli E., Carassiti V., Frontera F., Pelliciari C., Loffredo G., Martínez Núñez S., Reglero V., Velasco T., Larsson S., Svensson R., Zdziarski A. A., Castro-Tirado A., Attina P., Goria M., Giulianelli G., Cordero F., Rezazad M., Schmidt M., Carli R., Gomez C., Jensen P. L., Sarri G., Tiemon A., Orr A., Much R., Kretschmar P. & Schnopper H. W. (2003). JEM-X: The X-ray monitor aboard INTEGRAL. *A&A*, **411**, L231–L238. [12]

Lutovinov A., Rodriguez J., Revnivtsev M. & Shtykovskiy P. (2005). Discovery of X-ray pulsations from IGR J16320-4751 = AX J1631.9-4752. *A&A*, **433**, L41–L44. [53, 54, 57]

Makishima K. (1986). Iron Lines from Galactic and Extragalactic X-ray Sources. In K. O. Mason, M. G. Watson, & N. E. White, editor, *The Physics of Accretion onto Compact Objects*, volume 266 of *Lecture Notes in Physics, Berlin Springer Verlag*, pages 249–+. [72]

Manousakis A. & Walter R. (2011). X-ray wind tomography of the highly absorbed HMXB IGR J17252-3616. *A&A*, **526**, A62+. [52, 57, 79, 80, 84, 89]

Manousakis A., Walter R., Audard M. & Lanz T. (2009). Pulsed thermal emission from the accreting pulsar XMMU J054134.7-682550. *A&A*, **498**, 217–222. [91]

Markova N., Puls J., Repolust T. & Markov H. (2004). Bright OB stars in the Galaxy. I. Mass-loss and wind-momentum rates of O-type stars: A pure H\alpha analysis accounting for line-blanketing. *A&A*, **413**, 693–709. [45]

Markwardt C. B., Swank J. H. & Smith E. (2005). RXTE Observations of IGR J16283-4838 and IGR J16493-4348. *The Astronomer's Telegram*, **465**, 1–+. [53]

Markwardt C. B., Swank J. H. & Corbet R. (2007). XMMU J054134.7-682550 is a 61 s X-ray Pulsar with Cyclotron Features. *The Astronomer's Telegram*, **1176**, 1–+. [90]

Mas-Hesse J. M., Giménez A., Culhane J. L., Jamar C., McBreen B., Torra J., Hudec R., Fabregat J., Meurs E., Swings J. P., Alcacera M. A., Balado A., Beiztegui R., Belenguer T., Bradley L., Caballero M. D., Cabo P., Defise J. M., Díaz E., Domingo A., Figueras F., Figueroa I., Hanlon L., Hroch F., Hudcova V., García T., Jordan B., Jordi C., Kretschmar P., Laviada C., March M., Martín E., Mazy E., Menéndez M., Mi J. M., de Miguel E., Muñoz T., Nolan K., Olmedo R., Plesseria J. Y., Polcar J., Reina M., Renotte E., Rochus P., Sánchez A., San Martín J. C., Smith A., Soldan J., Thomas P., Timón V. & Walton D. (2003). OMC: An Optical Monitoring Camera for INTEGRAL. Instrument description and performance. *A&A*, **411**, L261–L268. [12]

Masetti N. (2006). Unveiling the Nature of INTEGRAL Sources Through Optical Spectroscopy. *Chinese Journal of Astronomy and Astrophysics Supplement*, **6**(1), 010000–148. [51]

Masetti N., Mason E., Bassani L., Bird A. J., Maiorano E., Malizia A., Palazzi E., Stephen J. B., Bazzano A., Dean A. J., Ubertini P. & Walter R. (2006a). Unveiling the nature of INTEGRAL objects through optical spectroscopy. II. The nature of four unidentified sources. *A&A*, **448**, 547–556. [51]

Masetti N., Pretorius M. L., Palazzi E., Bassani L., Bazzano A., Bird A. J., Charles P. A., Dean A. J., Malizia A., Nkundabakura P., Stephen J. B. & Ubertini P. (2006b). Unveiling the nature of INTEGRAL objects through optical spectroscopy. III. Observations

of seven southern sources. *A&A*, **449**, 1139–1149. [51]

Masetti N., Bassani L., Bazzano A., Bird A. J., Dean A. J., Malizia A., Norci L., Palazzi E., Schwope A. D., Stephen J. B., Ubertini P. & Walter R. (2006c). Unveiling the nature of INTEGRAL objects through optical spectroscopy. IV. A study of six new hard X-ray sources. *A&A*, **455**, 11–19. [51]

Masetti N., Morelli L., Palazzi E., Galaz G., Bassani L., Bazzano A., Bird A. J., Dean A. J., Israel G. L., Landi R., Malizia A., Minniti D., Schiavone F., Stephen J. B., Ubertini P. & Walter R. (2006d). Unveiling the nature of INTEGRAL objects through optical spectroscopy. V. Identification and properties of 21 southern hard X-ray sources. *A&A*, **459**, 21–30. [51]

Masetti N., Mason E., Morelli L., Cellone S. A., McBride V. A., Palazzi E., Bassani L., Bazzano A., Bird A. J., Charles P. A., Dean A. J., Galaz G., Gehrels N., Landi R., Malizia A., Minniti D., Panessa F., Romero G. E., Stephen J. B., Ubertini P. & Walter R. (2008). Unveiling the nature of INTEGRAL objects through optical spectroscopy. VI. A multi-observatory identification campaign. *A&A*, **482**, 113–132. [51]

Masetti N., Parisi P., Palazzi E., Jiménez-Bailón E., Morelli L., Chavushyan V., Mason E., McBride V. A., Bassani L., Bazzano A., Bird A. J., Dean A. J., Galaz G., Gehrels N., Landi R., Malizia A., Minniti D., Schiavone F., Stephen J. B. & Ubertini P. (2009). Unveiling the nature of INTEGRAL objects through optical spectroscopy. VII. Identification of 20 Galactic and extragalactic hard X-ray sources. *A&A*, **495**, 121–135. [51]

Masetti N., Parisi P., Palazzi E., Jiménez-Bailón E., Chavushyan V., Bassani L., Bazzano A., Bird A. J., Dean A. J., Charles P. A., Galaz G., Landi R., Malizia A., Mason E., McBride V. A., Minniti D., Morelli L., Schiavone F., Stephen J. B. & Ubertini P. (2010). Unveiling the nature of INTEGRAL objects through optical spectroscopy. VIII. Identification of 44 newly detected hard X-ray sources. *A&A*, **519**, A96+. [51]

Mason A. B., Norton A. J., Clark J. S., Negueruela I. & Roche P. (2009a). Preliminary determinations of the masses of the neutron star and mass donor in the High Mass X-ray Binary system EXO 1722-363. *ArXiv e-prints*. [52, 58, 80]

Mason A. B., Clark J. S., Norton A. J., Negueruela I. & Roche P. (2009b). Spectral classification of the mass donors in the high-mass X-ray binaries EXO 1722-363 and OAO 1657-415. *A&A*, **505**, 281–286. [79, 80]

Mason A. B., Norton A. J., Clark J. S., Negueruela I. & Roche P. (2011). The masses of the neutron and donor star in the high-mass X-ray binary IGR J18027-2016. *A&A*, **532**, A124+. [53]

Matt G. (2002). The iron Kα Compton shoulder in transmitted and reflected spectra. *MNRAS*, **337**, 147–150. [72]

Müller H. & Serot B. D. (1996). Relativistic mean-field theory and the high-density nuclear equation of state. *Nuclear Physics A*, **606**(3-4), 508 – 537. [82]

Negueruela I. & Schurch M. P. E. (2007). A search for counterparts to massive X-ray binaries using photometric catalogues. *A&A*, **461**, 631–639. [53, 111]

Nespoli E., Fabregat J. & Mennickent R. E. (2008). Unveiling the nature of six HMXBs through IR spectroscopy. *A&A*, **486**, 911–917. [54, 55]

Olson G. L. & Ebbets D. (1981). Mass-loss rates in early-type stars determined by fitting Balmer alpha profiles. *ApJ*, **248**, 1021–1030. [36]

Oskinova L. M., Feldmeier A. & Hamann W.-R. (2006). High-resolution X-ray spec-

troscopy of bright O-type stars. *MNRAS*, **372**, 313–326. [45]

Osterbrock D. & Flather E. (1959). Electron Densities in the Orion NEBULA.II. *ApJ*, **129**, 26–+. [44]

Owocki S. (2004). Stellar wind mechanisms and instabilities. In M. Heydari-Malayeri, P. Stee, & J.-P. Zahn, editor, *EAS Publications Series*, volume 13 of *EAS Publications Series*, pages 163–250. [46]

Owocki S. P. (1994). Theory review: Line-driven instability and other causes of structure and variability in hot-star winds. *Ap&SS*, **221**, 3–23. [46]

Owocki S. P., Castor J. I. & Rybicki G. B. (1988). Time-dependent models of radiatively driven stellar winds. I - Nonlinear evolution of instabilities for a pure absorption model. *ApJ*, **335**, 914–930. [46]

Palmer D. M., Grupe D. & Krimm H. A. (2007). Outburst of XMMU J054134.7-682550 in the LMC. *The Astronomer's Telegram*, **1169**, 1–+. [90]

Pavan L., Bozzo E., Ferrigno C., Ricci C., Manousakis A., Walter R. & Stella L. (2011). AX J1910.7+0917 and three newly discovered INTEGRAL sources. *A&A*, **526**, A122. [100]

Pellizza L. J., Chaty S. & Negueruela I. (2006). ¡ASTROBJ¿IGR J17544-2619¡/ASTROBJ¿: a new supergiant fast X-ray transient revealed by optical/infrared observations. *A&A*, **455**, 653–658. [55]

Pellizza L. J., Chaty S. & Chisari N. E. (2011). Unveiling the nature of IGR J16283-4838. *A&A*, **526**, A15+. [53]

Perna R., Bozzo E. & Stella L. (2006). On the Spin-up/Spin-down Transitions in Accreting X-Ray Binaries. *ApJ*, **639**, 363–376. [27]

Prat L., Rodriguez J., Hannikainen D. C. & Shaw S. E. (2008). Peering through the stellar wind of IGR J19140+0951 with simultaneous INTEGRAL/RXTE observations. *MNRAS*, **389**, 301–310. [53]

Pravdo S. H., Becker R. H., Boldt E. A., Holt S. S., Serlemitsos P. J. & Swank J. H. (1977). X-ray spectra of Hercules X-1. I - Iron line fluorescence from a subrelativistic shell. *ApJ*, **215**, L61–L64. [29]

Press W. H. & Rybicki G. B. (1989). Fast algorithm for spectral analysis of unevenly sampled data. *Astrophysical Journal*, **338**, 277. [69]

Prinja R. K. & Massa D. L. (2010). Signature of wide-spread clumping in B supergiant winds. *A&A*, **521**, L55+. [79]

Quaintrell H., Norton A. J., Ash T. D. C., Roche P., Willems B., Bedding T. R., Baldry I. K. & Fender R. P. (2003). The mass of the neutron star in Vela X-1 and tidally induced non-radial oscillations in GP Vel. *A&A*, **401**, 313–323. [79]

Rahoui F., Chaty S., Lagage P. & Pantin E. (2008). Multi-wavelength observations of Galactic hard X-ray sources discovered by INTEGRAL. II. The environment of the companion star. *A&A*, **484**, 801–813. [51, 53, 54, 55]

Rampy R. A., Smith D. M. & Negueruela I. (2009). IGR J17544-2619 in Depth With Suzaku: Direct Evidence for Clumpy Winds in a Supergiant Fast X-ray Transient. *ApJ*, **707**, 243–249. [55]

Reig P. (2011). Be/X-ray binaries. *Ap&SS*, **332**, 1–29. [7]

Roche P., Larionov V., Tarasov A. E., Fabregat J., Clark J. S., Coe M. J., Kalv P., Larionova L., Negueruela I., Norton A. J. & Reig P. (1997). Observations of the recent

disc loss in X Persei: photometry and polarimetry. *A&A*, **322**, 139–146. [4]

Rodriguez J., Tomsick J. A., Foschini L., Walter R., Goldwurm A., Corbel S. & Kaaret P. (2003). An XMM-Newton observation of IGR J16320-4751 = AX J1631.9-4752. *A&A*, **407**, L41–L45. [53]

Rodriguez J., Bodaghee A., Kaaret P., Tomsick J. A., Kuulkers E., Malaguti G., Petrucci P.-O., Cabanac C., Chernyakova M., Corbel S., Deluit S., Di Cocco G., Ebisawa K., Goldwurm A., Henri G., Lebrun F., Paizis A., Walter R. & Foschini L. (2006). INTEGRAL and XMM-Newton observations of the X-ray pulsar IGR J16320-4751/AX J1631.9-4752. *MNRAS*, **366**, 274–282. [53]

Rodriguez J., Tomsick J. A., Bodaghee A., Zurita Heras J.-A., Chaty S., Paizis A. & Corbel S. (2009). The nature of the X-ray binary ¡ASTROBJ¿IGR J19294+1816¡/ASTROBJ¿ from INTEGRAL, RXTE, and Swift observations. *A&A*, **508**, 889–894. [7]

Romano P., Sidoli L., Cusumano G., La Parola V., Vercellone S., Pagani C., Ducci L., Mangano V., Cummings J., Krimm H. A., Guidorzi C., Kennea J. A., Hoversten E. A., Burrows D. N. & Gehrels N. (2009). Monitoring supergiant fast X-ray transients with Swift: results from the first year. *MNRAS*, **399**, 2021–2032. [54, 55]

Rothschild R. E., Blanco P. R., Gruber D. E., Heindl W. A., MacDonald D. R., Marsden D. C., Pelling M. R., Wayne L. R. & Hink P. L. (1998). In-Flight Performance of the High-Energy X-Ray Timing Experiment on the Rossi X-Ray Timing Explorer. *ApJ*, **496**, 538. [12]

Schulz N. S., Canizares C. R., Lee J. C. & Sako M. (2002). The Ionized Stellar Wind in Vela X-1 during Eclipse. *ApJ*, **564**, L21–L25. [30]

Sguera V., Barlow E. J., Bird A. J., Clark D. J., Dean A. J., Hill A. B., Moran L., Shaw S. E., Willis D. R., Bazzano A., Ubertini P. & Malizia A. (2005). INTEGRAL observations of recurrent fast X-ray transient sources. *A&A*, **444**, 221–231. [55]

Sguera V., Hill A. B., Bird A. J., Dean A. J., Bazzano A., Ubertini P., Masetti N., Landi R., Malizia A., Clark D. J. & Molina M. (2007a). IGR J18483-0311: an accreting X-ray pulsar observed by INTEGRAL. *A&A*, **467**, 249–257. [55]

Sguera V., Bird A. J., Dean A. J., Bazzano A., Ubertini P., Landi R., Malizia A., Barlow E. J., Clark D. J., Hill A. B. & Molina M. (2007b). INTEGRAL and Swift observations of the supergiant fast X-ray transient AX J1845.0-0433 = IGR J18450-0435. *A&A*, **462**, 695–698. [55]

Shakura N. I. & Sunyaev R. A. (1973). Black holes in binary systems. Observational appearance. *A&A*, **24**, 337–355. [23]

Shapiro I. I. (1964). Fourth Test of General Relativity. *Physical Review Letters*, **13**, 789–791. [82]

Shtykovskiy P. & Gilfanov M. (2005). High mass X-ray binaries in the LMC: Dependence on the stellar population age and the "propeller" effect. *A&A*, **431**, 597–614. [90]

Sidoli L., Romano P., Mereghetti S., Paizis A., Vercellone S., Mangano V. & Götz D. (2007). An alternative hypothesis for the outburst mechanism in supergiant fast X-ray transients: the case of IGR J11215-5952. *A&A*, **476**, 1307–1315. [56]

Sidoli L., Romano P., Mangano V., Pellizzoni A., Kennea J. A., Cusumano G., Vercellone S., Paizis A., Burrows D. N. & Gehrels N. (2008). Monitoring Supergiant Fast X-Ray Transients with Swift. I. Behavior outside Outbursts. *ApJ*, **687**, 1230–1235. [54, 55, 57]

Slettebak A. (1988). The Be stars. *PASP*, **100**, 770–784. [3]

Stevens I. R. (1991). X-ray-illuminated stellar winds - Optically thick wind models for massive X-ray binaries. *ApJ*, **379**, 310–326. [82]

Stevens I. R. & Kallman T. R. (1990). X-ray illuminated stellar winds - Ionization effects in the radiative driving of stellar winds in massive X-ray binary systems. *ApJ*, **365**, 321–331. [82]

Strüder L., Briel U., Dennerl K., Hartmann R., Kendziorra E., Meidinger N., Pfeffermann E., Reppin C., Aschenbach B., Bornemann W., Bräuninger H., Burkert W., Elender M., Freyberg M., Haberl F., Hartner G., Heuschmann F., Hippmann H., Kastelic E., Kemmer S., Kettenring G., Kink W., Krause N., Müller S., Oppitz A., Pietsch W., Popp M., Predehl P., Read A., Stephan K. H., Stötter D., Trümper J., Holl P., Kemmer J., Soltau H., Stötter R., Weber U., Weichert U., von Zanthier C., Carathanassis D., Lutz G., Richter R. H., Solc P., Böttcher H., Kuster M., Staubert R., Abbey A., Holland A., Turner M., Balasini M., Bignami G. F., La Palombara N., Villa G., Buttler W., Gianini F., Lainé R., Lumb D. & Dhez P. (2001). The European Photon Imaging Camera on XMM-Newton: The pn-CCD camera. *A&A*, **365**, L18–L26. [9]

Swank J. H. & Markwardt C. B. (2003). RXTE PCA Snapshots of IGR J16318-4848 and IGR J19140+098. *The Astronomer's Telegram*, **128**, 1–+. [53]

Takeuchi Y., Koyama K. & Warwick R. S. (1990). Further GINGA observations of the new X-ray pulsar X1722-36. *PASJ*, **42**, 287–293. [58, 79]

Tauris T. M. & van den Heuvel E. P. J. (2006). *Formation and evolution of compact stellar X-ray sources*, pages 623–665. Cambridge University Press. [3, 5, 7, 8]

Tawara Y., Yamauchi S., Awaki H., Kii T., Koyama K. & Nagase F. (1989). Discovery of 413.9-second x-ray pulsation from x1722-36. *Astronomical Society of Japan*, **41**, 473. [58]

Thompson T. W. J., Tomsick J. A., Rothschild R. E., in't Zand J. J. M. & Walter R. (2006). Orbital Parameters for the X-Ray Pulsar IGR J16393-4643. *ApJ*, **649**, 373–381. [54]

Thompson T. W. J., Tomsick J. A., in 't Zand J. J. M., Rothschild R. E. & Walter R. (2007). The Orbit of the Eclipsing X-Ray Pulsar EXO 1722-363. *ApJ*, **661**, 447–457. [52, 58]

Tomsick J. A., Chaty S., Rodriguez J., Foschini L., Walter R. & Kaaret P. (2006). Identifications of Four INTEGRAL Sources in the Galactic Plane via Chandra Localizations. *ApJ*, **647**, 1309–1322. [53, 57]

Tomsick J. A., Chaty S., Rodriguez J., Walter R., Kaaret P. & Tovmassian G. (2009). An XMM-Newton Spectral and Timing Study of IGR J16207 - 5129: An Obscured and Non-Pulsating HMXB. *ApJ*, **694**, 344–353. [54]

Torrejón J. M., Schulz N. S., Nowak M. A. & Kallman T. R. (2010a). A Chandra Survey of Fluorescence Fe Lines in X-ray Binaries at High Resolution. *ApJ*, **715**, 947–958. [29, 33]

Torrejón J. M., Negueruela I., Smith D. M. & Harrison T. E. (2010b). Near-infrared survey of high mass X-ray binary candidates. *A&A*, **510**, A61+. [53, 55]

Truemper J., Pietsch W., Reppin C., Voges W., Staubert R. & Kendziorra E. (1978). Evidence for strong cyclotron line emission in the hard X-ray spectrum of Hercules X-1. *ApJ*, **219**, L105–L110. [28]

Turner M. J. L., Abbey A., Arnaud M., Balasini M., Barbera M., Belsole E., Bennie P. J., Bernard J. P., Bignami G. F., Boer M., Briel U., Butler I., Cara C., Chabaud C., Cole R., Collura A., Conte M., Cros A., Denby M., Dhez P., Di Coco G., Dowson J., Ferrando P., Ghizzardi S., Gianotti F., Goodall C. V., Gretton L., Griffiths R. G., Hainaut O., Hochedez J. F., Holland A. D., Jourdain E., Kendziorra E., Lagostina A., Laine R., La Palombara N., Lortholary M., Lumb D., Marty P., Molendi S., Pigot C., Poindron E., Pounds K. A., Reeves J. N., Reppin C., Rothenflug R., Salvetat P., Sauvageot J. L., Schmitt D., Sembay S., Short A. D. T., Spragg J., Stephen J., Strüder L., Tiengo A., Trifoglio M., Trümper J., Vercellone S., Vigroux L., Villa G., Ward M. J., Whitehead S. & Zonca E. (2001). The European Photon Imaging Camera on XMM-Newton: The MOS cameras : The MOS cameras. *A&A*, **365**, L27–L35. [9]

Ubertini P., Lebrun F., Di Cocco G., Bazzano A., Bird A. J., Broenstad K., Goldwurm A., La Rosa G., Labanti C., Laurent P., Mirabel I. F., Quadrini E. M., Ramsey B., Reglero V., Sabau L., Sacco B., Staubert R., Vigroux L., Weisskopf M. C. & Zdziarski A. A. (2003). IBIS: The Imager on-board INTEGRAL. *A&A*, **411**, L131–L139. [11]

van Kerkwijk M. H., van Paradijs J., Zuiderwijk E. J., Hammerschlag-Hensberge G., Kaper L. & Sterken C. (1995). Spectroscopy of HD77581 and the mass of VELA X-1. *A&A*, **303**, 483–+. [79]

Vedrenne G., Roques J.-P., Schönfelder V., Mandrou P., Lichti G. G., von Kienlin A., Cordier B., Schanne S., Knödlseder J., Skinner G., Jean P., Sanchez F., Caraveo P., Teegarden B., von Ballmoos P., Bouchet L., Paul P., Matteson J., Boggs S., Wunderer C., Leleux P., Weidenspointner G., Durouchoux P., Diehl R., Strong A., Cassé M., Clair M. A. & André Y. (2003). SPI: The spectrometer aboard INTEGRAL. *A&A*, **411**, L63–L70. [12]

Walter R. & Zurita Heras J. (2007). Probing clumpy stellar winds with a neutron star. *A&A*, **476**, 335–340. [44, 56]

Walter R., Rodriguez J., Foschini L., de Plaa J., Corbel S., Courvoisier T. J.-L., den Hartog P. R., Lebrun F., Parmar A. N., Tomsick J. A. & Ubertini P. (2003). INTEGRAL discovery of a bright highly obscured galactic X-ray binary source IGR J16318-4848. *A&A*, **411**, L427–L432. [54]

Walter R., Zurita Heras J., Bassani L., Bazzano A., Bodaghee A., Dean A., Dubath P., Parmar A. N., Renaud M. & Ubertini P. (2006). XMM-Newton and INTEGRAL observations of new absorbed supergiant high-mass X-ray binaries. *A&A*, **453**, 133–143. [52, 54, 57]

Watanabe S., Sako M., Ishida M., Ishisaki Y., Kahn S. M., Kohmura T., Nagase F., Paerels F. & Takahashi T. (2006). X-Ray Spectral Study of the Photoionized Stellar Wind in Vela X-1. *ApJ*, **651**, 421–437. [4, 30, 52]

Waters L. B. F. M. & van Kerkwijk M. H. (1989). The relation between orbital and spin periods in massive X-ray binaries. *A&A*, **223**, 196–206. [6]

Wen L., Levine A. M., Corbet R. H. D. & Bradt H. V. (2006). A Systematic Search for Periodicities in RXTE ASM Data. *ApJS*, **163**, 372–392. [53, 57]

White N. E. & Stella L. (1988). The radius of a magnetosphere in the radiation pressure dominated region of an accretion disk. *MNRAS*, **231**, 325–331. [24]

White N. E., Swank J. H. & Holt S. S. (1983). Accretion powered X-ray pulsars. *ApJ*, **270**, 711–734. [27]

White N. E., Nagase F. & Parmar A. N. (1995). The properties of X-ray binaries. In

X-ray Binaries, pages 1–57. [3, 27]

Winkler C., Courvoisier T., Di Cocco G., Gehrels N., Giménez A., Grebenev S., Hermsen W., Mas-Hesse J. M., Lebrun F., Lund N., Palumbo G. G. C., Paul J., Roques J., Schnopper H., Schönfelder V., Sunyaev R., Teegarden B., Ubertini P., Vedrenne G. & Dean A. J. (2003). The INTEGRAL mission. *A&A*, **411**, L1–L6. [11]

Zurita Heras J. A. & Walter R. (2009). INTEGRAL and XMM-Newton observations of AX J1845.0-0433. *A&A*, **494**, 1013–1019. [55]

Zurita Heras J. A., de Cesare G., Walter R., Bodaghee A., Bélanger G., Courvoisier T., Shaw S. E. & Stephen J. B. (2006). IGR J17252-3616: an accreting pulsar observed by INTEGRAL and XMM-Newton. *A&A*, **448**, 261–270. [52, 57, 58]